

Anomaly Detection using Fuzzy Q-learning Algorithm

Shahaboddin Shamshirband¹, Nor Badrul Anuar², Miss Laiha Mat Kiah², Sanjay Misra³

¹Department of Computer Science, Chalous Branch, Islamic Azad University (IAU), 46615-397, Chalous, Iran, e-mail: shamshirband@um.edu.my

²Faculty of Computer Science and Information Technology, University of Malaya, 50603 Kuala Lumpur, Malaysia, e-mails: badrul@um.edu.my, misslaiha@um.edu.my

³Department of Computer Engineering, Atilim University, 06836-Incek, Ankara Turkey, e-mail: smisra@atilim.edu.tr

Abstract: Wireless networks are increasingly overwhelmed by Distributed Denial of Service (DDoS) attacks by generating flooding packets that exhaust critical computing and communication resources of a victim's mobile device within a very short period of time. This must be protected. Effective detection of DDoS attacks requires an adaptive learning classifier, with less computational complexity, and an accurate decision making to stunt such attacks. In this paper, we propose an intrusion detection system called Fuzzy Q-learning (FQL) algorithm to protect wireless nodes within the network and target nodes from DDoS attacks to identify the attack patterns and take appropriate countermeasures. The FQL algorithm was trained and tested to establish its performance by generating attacks from the NSL-KDD and CAIDA DDoS Attack datasets during the simulation experiments. Experimental results show that the proposed FQL IDS has higher accuracy of detection rate than Fuzzy Logic Controller and Q-learning algorithm alone.

Keywords: Intrusion detection; Fuzzy system; Reinforcement learning; Multi Agent System

1 Introduction

Recent advances in wireless communication and digital electronic have enabled the development of low-cost, low-power, multifunctional nodes which are small in size and which communicate with each other using radio frequencies [1]. A single node has limited capability in sensing and it is only capable of collecting data from a limited region within its range. Therefore, in order to gather useful information from an entire of Wireless Sensor Networks (WSNs), the data must be collected through the collective work of a number of sensor nodes.

The application designs for wireless sensors such as natural disaster relief [2], health monitoring [3], and hazardous events [4], afford greater flexibility in establishing communications and increase system automation, though lack in security and privacy [5]. The core weaknesses with these sensor nodes lie in the limited-resource devices, i.e. power and processing units. For this reason, vulnerability to various security threats is notably high. Meanwhile, an adversary possesses passive and active abilities. It may thus implicate sensor nodes through access to secret information such as keys stored in the compromised node in addition to the potential to eavesdrop and exhaust the sensor node resources [6]. Therefore, security is still a major design goal in WSNs.

In 2012, a report by Gartner reveals that a sophisticated class of DDoS attack sent an attack command to hundreds or even thousands of mobile agents, which then launched flooding attacks to access multiple websites [7]. Different types of DDoS attacks have been developed, which can be classified as TCP flood, UDP flood, ICMP flood, smurf, distributed reflector attack and distributed reflector attack are discussed [8]. During the distributed SYN flood attack, the compromised systems (“zombies”) are led to send SYN packets with an invalid source IP address, to create an instance of a half-open connection data structure on the target server. It can be concluded that the memory stack on the victim’s system is filled up and no new demands can be handled [9].

The problem of DDoS attacks has already been addressed in many studies. Fuzzy logic controller as a soft computing (SC) technique enables decision making when the values are mostly estimated or the available information is incomplete or ambiguous especially in systems that deliver tedious mathematical models [10, 11]. Fuzzy logic based detection systems are capable of calculating with availability of only ambiguous information; these systems are suitable for describing their decisions but the rules they utilize to generate decisions cannot be obtained automatically. To improve the drawbacks of unknown behavior detection, fuzzy logic combined with neural network in terms of adaptive neuro fuzzy to identify the abnormal behavior by tuning the fuzzy rules [12, 13]. The most remarkable advantages of the neuro fuzzy classifier are robustness and flexibility, but consume massive computing resources when performing fuzzy alarm correlation in large scale wireless network [14].

Reinforcement Learning [15] appears to be a greatly significant method of wireless network security due to its capability to autonomously learn new attacks via online, unsupervised learning, as well as to modify new policies without complex mathematical approaches [14]. It has been proven to be effective, especially in real time fault detection and when no prior system’s behavior information is assumed. A disadvantage of reinforcement learning is the lack of memory to sustain the agent’s data [16]. These limitations have been our motivation for the creating of intelligent systems where fuzzy logic systems utilized reinforcement learning algorithms to overcome the problem of memory and accuracy of detection.

To improve the accuracy of detection, Intrusion Detection System (IDS) proposed to identify the type of possible attacks [17]. Munoz et al. [18] utilized fuzzy Q-learning for congestion detection to drop packets that differs from normal features. Fuzzy Q-learning algorithms proposed by Munoz improved the accuracy of detection and consumed minimum resources, due to an increase in the high volume of traffic. The approach we have used in this study aims to design a hybrid intrusion detection system called a Fuzzy Q-Learning (FQL) to enhance the learning ability of attack detection. Our research work, fuzzy logic controller utilized fuzzy min-max strategy to provide the action selection policy. The Q-learning algorithm adjusts their parameters (i.e, state, action) based on fuzzy functions to reduce the complexity of states and action as well as speed up the decision process.

This paper will discuss how DDoS attacks launched in wireless network can be modeled through fuzzy Q-learning algorithms. The purposes of developing such models are manifold:

- 1) To evaluate whether resources of a given system are vulnerable to certain types of attacks.
- 2) To understand whether we can possibly detect DDoS, by observing fuzzy behavior of network traffic and other observable data.
- 3) To develop methodologies and formulate machine learning algorithms that can detect DDoS attacks in wireless network.

The remainder of this paper is organized as follows: in Section 2, we discuss related studies. In Section 3, we proposed the system model. In section 4, we describe the self-tuning scheme of the model, incorporating Fuzzy Logic Controller (FLC) with Q-learning algorithm into the IDS of a WSN. Section 5 presents simulation results. Finally, the paper concludes in Section 6.

2 Related Studies

2.1. DDoS Attack Dataset

The most significant challenge for an appraisal of a DDoS attack detection algorithm is the lack of proper public DDoS attack dataset. Since 2000, the two classes of publicly accessible datasets for IDS are Network-based IDS (NIDS) and Wireless-based IDS (WIDS) datasets.

The KDD Cup dataset was produced by processing the tcpdump portions of the 1998 DARPA Intrusion Detection System (IDS) evaluation dataset [19]. The data is not synthetic and does not reflect contemporary attacks. NSL-KDD datasets [20] were selected to mitigate the difficulties incurred by KDD'99 datasets. NSL-

KDD is significant in that it contains fewer redundant, duplicate records in the training and test phases of learning-based detection, making the evaluation process of the learning system more efficient. CAIDA dataset consists of DDoS attack dataset 2007, which can be availed by user's request. CAIDA DDoS attack dataset [21] consist of an hour of anonymized traffic traces from a DDoS attack.

2.2. Real Time Feature Extraction

Online feature extraction methods based on per flow analysis are expensive, not scalable, and thus prohibitive for large scale networks. An increase in the number of features led to better accuracy but computation of a larger number of features in real time causes more overhead and time consumption. As a result, fewer feature selection is suitable for better pattern classification in real time.

The detailed analysis on DDoS attacks, available attack tools and defense mechanisms [22] indicate that the DDoS attack has the following features.

- Source and Destination IP address and port numbers of the packets are spoofed.
- Window size, sequence number, and packet length are fixed during the attacks.
- Flags in the TCP and UDP protocols are manipulated.
- Roundtrip time is measured from the server response.
- Routing table of host or gateway is changed.
- DNS transaction IDs (reply packet) are flooded.
- HTTP requests are flooded through port 80.

Our objective is to differentiate the DDoS attack and normal traffic. In this research work, the 'duration' feature or response time has been used to identify the incomplete length time of the connection due to handshake. Most of the attacks target the victims' servers through legitimate ports such as 80, 53, 443, etc. Hence, the 'Protocol_type' feature from clients over a time window was used to monitor the legitimate port. DDoS attacks send flooding packets to victims in order to consume the resources such as memory and CPU. The "Src_bytes and Dst_bytes" features used, in terms of 'buffer size or packet size ', to identify the number of data bytes from source to destination and destination to source. The number of connections to the same host is the key features of DDoS attack. The 'Count' feature is used to monitor the number of connections to the same host during specified time window.

In our data selection method, the NSL-KDD dataset combined with CADIA dataset in order to create a new set of attack dataset that reveals the characteristics of DDoS attack. By processing the continuous flow of the packets which propagates from mixed dataset, key characteristics of network activity can be

achieved between hosts. From the dataset attributes, five features, as shown in Table 1, have been selected for accurate detection of DDoS attacks. These attributes mostly consist of spoofed source address and contain half-open connections.

Table 1
List of features of the DDoS attacks

Feature name	Feature Description
Time response	Variance of time difference between two connections during specific time window
Protocol_type	Type of the protocol, e.g., TCP, UDP, etc.
Src_bytes	number of data bytes from source to destination
Dst_bytes	number of data bytes from destination to source
Count	number of connections to the same host during specified time window

2.3. Fuzzy Q-learning Detection - Motivation

To detect the type of attack a node may face in the future; this research optimized the Fuzzy Logic Controller (FLC) by Q-learning algorithm to enhance the self-learning ability of the detector agent. The fuzzification process converts the variables $x \in X$, where X is the set of possible input variables to fuzzy linguistic variables by applying the corresponding membership functions. The Inference Engine (IE) maps input and output fuzzy sets to Q-value. The Q-value and its eligibility updates by fuzzy rules. Defuzzification computes a crisp value to adopt an action in terms of the action policy. Such an adaptation of Q-Learning allows to process continuous state and action spaces by a simple discretization of the action-value policy. Figure 1 demonstrates the proposed Fuzzy Q-learning (FQL) architecture.

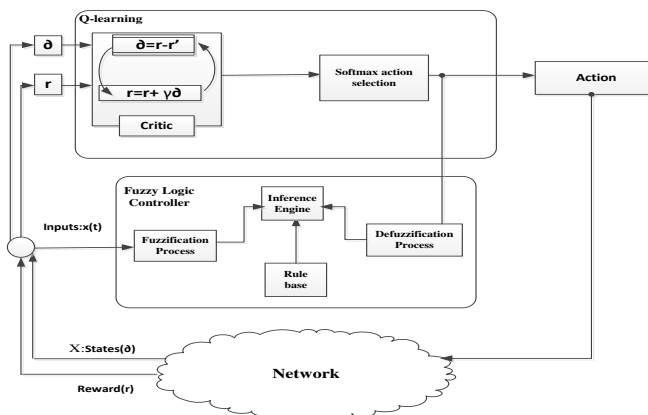


Figure 1
Block diagram of the Fuzzy Q-learning architecture

FQL-based detection instead of adding a new input to the FLC, the learning algorithm enables to control this performance indicator by the ‘trial-and-error’ methodology to avoid complex rules. The disadvantage of the FQL is that of the operator as fuzzy rules is fixed. For instance, IDS in a very congested network should be conservative as detection receives much more anomaly. Another special situation is when there is a small overlap between normal and abnormal states; the FQL produces an extreme change in the IDS margin that significantly increases the detection rate. In all cases the risk of resource consumption is higher when modifying FLC margins.

In our scheme, we modified the FQL algorithm by applying min-max action selection instead of ϵ -greedy action-selection and softmax action selection rule. The main drawback of ϵ -greedy action-selection is that when it explores it selects equally among all actions. The worst performing actions may be happened. To solve this problem, softmax method uses a Boltzmann distribution. The greedy action is given the highest selection probability according to their value estimates. The adjusting parameters of action selection methods must be set manually that decreases the speed of algorithm in training. To solve the problem of manually adjusting the action selection parameters, decrease the false alarm rate and increase the accuracy of attack detection, we used dynamic fuzzy min-max action selection method to improve the performance of algorithm.

2.4. Utility Function

To appraise the efficacy of the associations determined by the FQL and to determine the applicability of the rule at every point in time, Eq. 1 was utilized in this work, as suggested by Huang *et al.* [23]. In Table 2 the parameters of the utility function are described:

$$U = \rho * SP - \beta * FN - \theta * FP \quad (1)$$

Table 2
Utility function parameters

Parameters	Explanation
U	Is a utility
ρ	Symbolizes the weight of effective prediction, $q = 0.75$
SP	Characterizes the true confidence rate of attack patterns.
β	Signifies the weight of failed estimates (attack but no defense), $b = 1$
FN	Represents false negative of attack patterns - there are attacks but no defense
θ	Denotes the weight of failed predictions (defense but no attack), $h = 1$
FP	Represents false positive of attack patterns - there is defense but no attack

The fuzzy Q-learning principle approach entails detection accuracy with low time complexity, which only afterward begins to formulate a shield policy. The major drawback of the FQL theory is that if attacks are recurring over a short period, a

considerable amount of time is consumed in the detection phase, something that weakens the defense. It can be said that the detection precision may be low while the false alert rate is high. This problem is a worst-case scenario but can be addressed using the modified FQL proposed by [14]. Its principal contribution is identifying the probability of future attacks aimed at a wireless sensor node. For frequent attacks occurring over a short time, multi agent-based FQL was adopted to deal with the excessive time spent on detection. The aim of the proposed FQL is to obtain high detection accuracy with a low false alarm rate.

3 Proposed Model

3.1. WSN Model

In the present research study, Figure 2 illustrates the network model with hierarchical routing, which consists of clusters (C), their coordinators, or Cluster Heads (CHs), as well as the member sensor nodes (S). In the current scheme, the Cluster Head (CH) is assumed to be a Sink Node (SN) in a cluster. The SN monitors the behavior of sensor nodes by collecting data from the member sensor nodes and transmitting the critical status - the attack information of the sensor nodes, to a Base Station (BS).

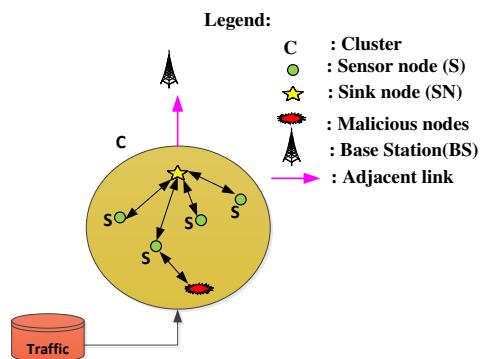


Figure 2

A network system perspective of a WSN

The route from a sensor node to a BS is deemed a hierarchical path that creates a hierarchical system with numerous routes, which is the main feature of cluster-based WSNs [24]. Figure 2 illustrates how sensor nodes send collected data from a sink node to a BS via other adjacent sink nodes, and the BS receives data only if SN within the routing formation are actively functioning. Attacks in this scenario can target the WSN in multiple ways, with DDoS attacks potentially originating either from the Internet or neighboring wireless sensor sources.

3.2. Methodologies and Techniques Used

The fuzzy Q-learning-based detection and defense mechanism operate to detect DDoS attacks, where the sink node and base station adapt to select the best strategy of detecting an immediate attack and respond to it. Regardless of whether the attacks are carried out on a regular or irregular basis, the IDS can adjust its learning parameters through fuzzy Q-learning to identify future attacks. Figure 3 depicts the proposed architecture of Fuzzy Q-learning Detection System (FQL).

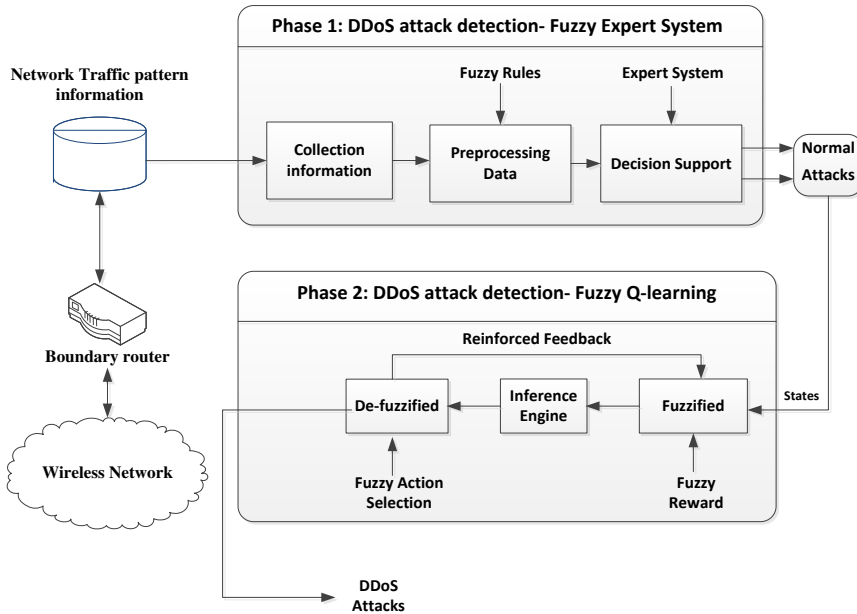


Figure 3

Architecture of Fuzzy Q-learning based Wireless Intrusion Detection System(FQL-WIDS)

In the first phase of proposed FQL architecture, Fuzzy Expert System (FES) concentrates to audit the attack records received from the traffic. When FES detects the possible attacks then send the new set of traffic dataset to the next layer. In the second phase, the FLC optimized by Q-learning to discover and detect the security treats captured by FES. The architecture of the proposed FQL-IDS is dual, that is, it has two phases (Figure 3).

- **Expert Policy:** It uses Expert System (ES) to decrease the state space for sink node due to increase in look-up table or Q-table. This policy broadcast the gain of ES engine (i.e. Abnormal, normal) through Base Station (BS).
- **Fuzzy Q-learning (FQL) policy:** It adopts to mitigate the possible faults escaped from Expert System policy. This learning policy identifies the anomalous data by optimizing Fuzzy Logic Controller based Q-learning.

4 Self-Tuning Scheme

In this section, we describe the FQL-based WIDS setup; define a primary detection based on an fuzzy expert system, express the FLC utilized Q-learning. We demonstrate how to optimize FLC based on a Q-learning algorithm. The process discovers six attributes: 1) Protocol type: ES chooses only TCP connection; 2) Source and destination IP: ES selects the IP range of acceptable by default; 3) Source and destination port: IDS pick out the corresponding port. 4) Time response: It deals with the time duration of response between sensor nodes. 5) Buffer size: It relies on the size of the buffer on processor storage. 6) Count: the number of connections to the same host at current connection in a past two second.

4.1. Fuzzy Expert System for DDoS Attack Detection

To fully exploit the suspicious level at the first phase, Expert System (ES) utilized Fuzzy Rules Base (FRB) to identify the anomaly conditions received from the traffic. The Fuzzy Expert System (FES) employed to decrease the record of anomalous data through fuzzy logic controller. We designed FES consists of the following components: the traffic capture, the feature extractor, the fuzzification, the fuzzy inference engine, the knowledge base, the defuzzification, and the expert analyzer. Figure 4 shows the details of component of the proposed Fuzzy Expert detection system architecture.

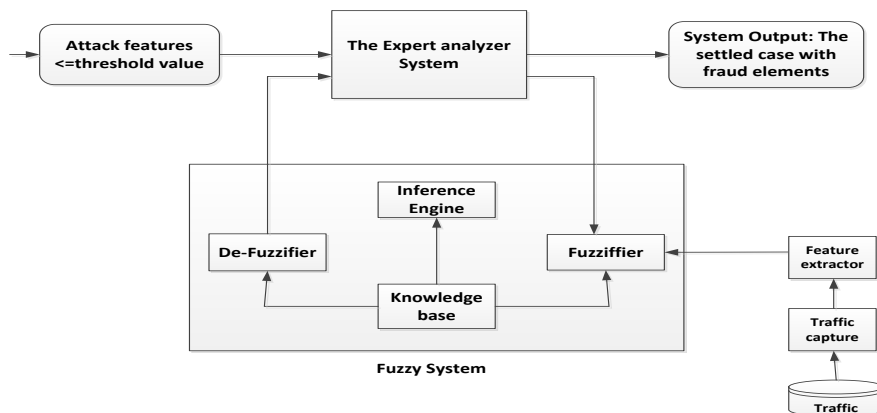


Figure 4

The architecture of the proposed fuzzy expert system

4.1.1. The Traffic Capture

The traffic capture component collects the traffic records and prepared the base information for traffic analysis. Currently the traffic capture is based on the popular network and hosts' intrusion detection tools and other scanning tools:

Snort, Sniffer, and Wireshark. These different forensic tools real-time collect network attack traffics and intrusion host's information. In this research work, we utilized Wireshark packet analyzer tools to pre-processed DDoS attacks data and their features.

4.1.2. The Feature Extractor

The feature extractor performs extracting features on the "network traffic" captured by the traffic capture component. Under the network and system environment, there are many traffic features that can be used for attack detection and analysis.

Definition 1:

Attack data source: The attack data source can be defined as a 5-tuple $ADS = \{Pt, Dp, Tr, Bs, Co\}$ according to the vulnerability scanning information, where Pt denotes as the type of protocol (TCP=1, UDP=2); Dp denotes as the destination port; Tr denotes as the variance of time difference between two connections during specific time window, Bs denotes as the length of packet from source to destination, Co denotes as the number of connections to the same host as the current connection in the past two seconds. Table 2 denotes as the major forensic parameters of DDoS attack data source.

4.1.3. The Fuzzification

Each input variable's sharp (crisp) value needs to be first fuzzified into linguistic values before the fuzzy decision processes with the rule base. The characteristic function of a fuzzy set is assigned to values between 0 and 1, which denotes the degree of membership of an element in a given set. Table 3 displays the linguistic terms and their fuzzy numbers used for evaluating the attack data source for time response, buffer size, and Count. Figure 5 indicates the membership functions for time response.

Table 3
Fuzzy rating for occurrence of attack traffic in ADS

Linguistic variables	Fuzzy number		
	Tr	Bs	Co
Low (L)	(-inf,-inf,0,40)	(-inf,0,2,3)	(-inf,0,1,1.5)
Medium (M)	(20,40,80,100)	(2,3,5,6)	(1,1.5,2,2.5)
High (H)	(80,120,inf,inf)	(5,6,8,inf)	(2,2.5,3,inf)

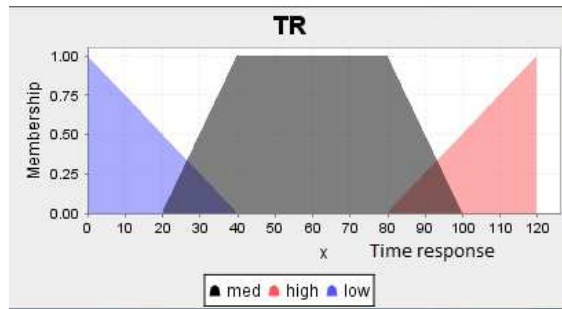


Figure 5

The membership functions of linguistic variables for attack data source Tr

4.1.4. The Fuzzy Inference Engine and Knowledge Base

Knowledge base stores the fuzzy rules which are used by the fuzzy inference engine to get a new fact from. The pseudo code of proposed FES is shown in Table 4 in parallel of Figure 6.

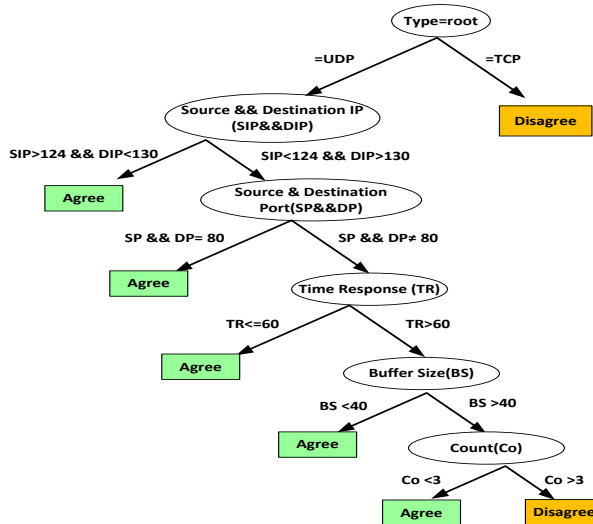


Figure 6

The state of decision fuzzy expert system to reach the goal

4.1.5. The Expert Analyzer

The expert analyzer decides the influence result from defuzzification whether inspected packets are attacks or not. If the crisp value is disparate than threshold value of the detection attack rule, then it adopts that an attack has occurred. The process of manually extracting rules may be time consuming and the rules may be approximate. Because these methods are off-line in nature, if a very large set of

data is involved, it can become expensive and impractical, and can not real-time detect the novel attacks. In order to overcome this problem, we propose a hybrid soft computing methods to identify DDoS attacks.

4.2. Fuzzy Q-Learning Algorithm for Anomaly Detection

To mitigate the learning time process FLC is optimized by Q-learning algorithm developed in. In this section, we optimized the FLC for anomaly detection by using the Q-Learning algorithm. Three fuzzy sets have been defined for the input of FQL to represent three different situations as a state space of Q-learning: These inputs are named as TBC. Time response deals with the time duration of response between sensor nodes, the Buffer Size relies on the size of the buffer for processor storage in sensor node by sending a huge number of fake messages. Count is the number of connections to the same host at current connection in a past two second. Figure 7 demonstrates block diagram of the optimization scheme for anomaly based-FQL.

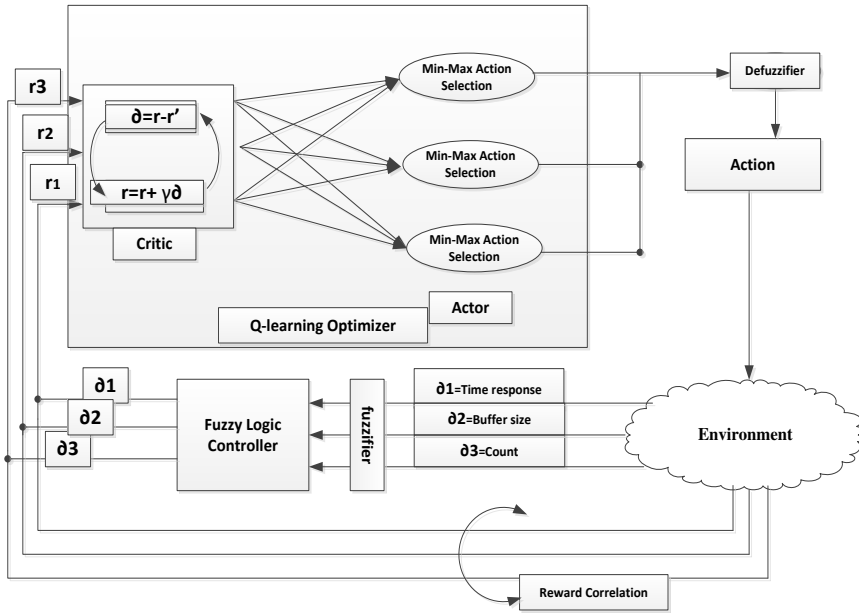


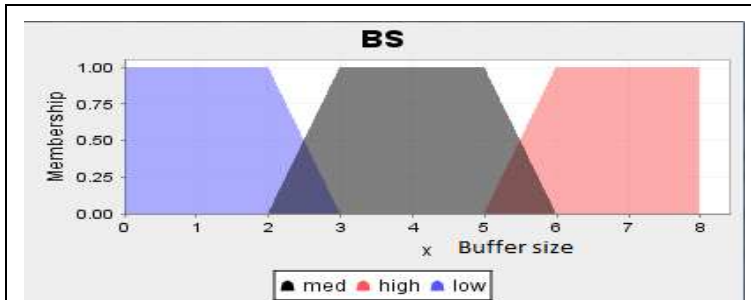
Figure 7

Block diagram of the optimization scheme for FQL

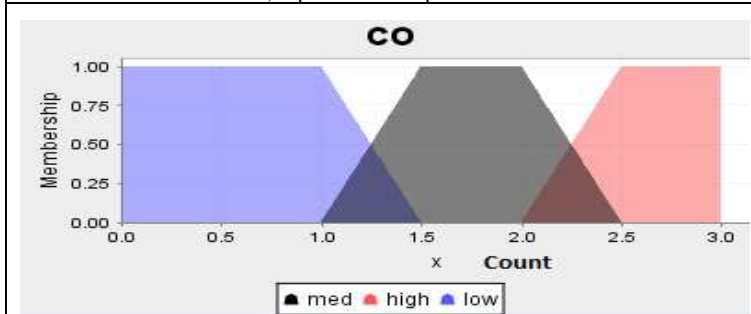
The FLC output, given by the Time response (Tr), Buffer size (Bs) and Count (Co), correspond to the fuzzy state of the network $S(t)$,

$$\bullet \quad S(t) = [Time\ response, Buffer\ size, Count] = [Tr, Bs, Co] \quad (2)$$

The FLC output, given by the increment in the states, represents the action of the sink node, $A(t)$. The reward signal, $R(t)$, is built from the FLC, is measured in both modes of the adjacency in order to test if the sensors are experiencing attacks. The linguistic variables of Time response (Tr), Buffer size (Bs), and Count (Co) act as inputs and the Detect Confidence (DC) acts as an output are used in the experiments. Figure. 8 (a, and b) indicates the membership function for the input and Figure. 9 indicates the output variable of fuzzy systems.



a) Input membership function



b) Input membership function

Figure 8

(a), and (b), Input Membership function design in Java-fuzzy toolbox [25]

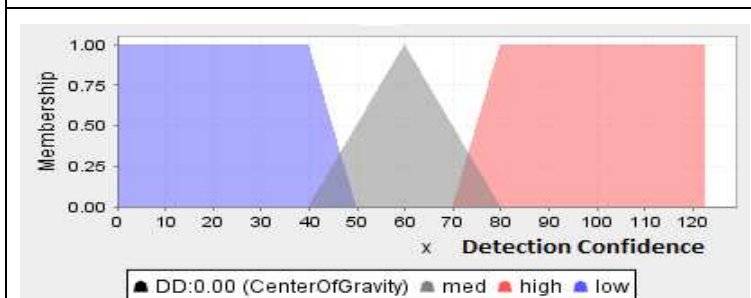


Figure 9

Output Membership function

Three fuzzy sets are identified in the current Buffer size (Bs), whose linguistic terms are ‘Low’ (L), ‘Medium’ (M), and ‘High’ (H). These three fuzzy sets discriminate the cases when Bs is less than (3k), which has been defined the length of packet received from source during specified time window. The output linguistic variable represents the system’s Detect Confidence (DC) in the presence of abnormal behavior. To illustrate, if the confidence value is higher than 80, then the system is more than 80% certain that there is an abnormal entity, if the detection confidence is smaller than 40, it is more likely that there is no abnormality. However, input and output variables give us a notion of how traffic connection is changing. Figure. 8 (a, and b) indicates the membership function for the input variables of buffer size and count and Figure. 9 indicates the output variable of fuzzy systems. The membership functions are triangular or trapezoidal.

The number of selected rules in this section is smaller, resulting in a lower number of fuzzy rules. A small number of rules speed up the convergence of the Q-Learning algorithm since fewer states have to be visited during the exploration phase. The interpretation of each rule defined in this work is described as follows:

- **Rule 1:** It is activated when there is a high value in Tr and the Bs margin has a ‘high’ value and the number of connections to the same host has a high percentage, which is opposite to the desired value. A large increment in the linguistic variables should be necessary in this case to increase the grade of detection of anomalies. Thus, the consequent of rule 1 is set to ‘high’.
- **Rule 2:** It is similar to rule 1 but with the difference that the Tr has a low value. The consequences of that rule should be a moderate change such as ‘High’.
- **Rule 3:** The activation of rule 3 occurs when there is a medium Tr difference in the adjacency from the source to the destination but the Bs and Count margins have an appropriate (‘low’) value to monitor the traffic. For those reasons, the consequent for rule 3 is set to ‘medium’.
- **Rule 4:** It is activated when the Tr has medium and the Bs margin has a ‘high’ value and Count is high. The selected consequent for rule 4 has been set to ‘high’.

Each state defines by Time response, Buffer size and Count (TBC). The valuable range of TBC adopts the fuzzy membership function to represent the function of Q-learning.

In order to find the optimal action, the reinforcement signal $r(t)$ used Eq.(2). FQL agent assigns a weight to all possible next states based on FLC. Associated to the threshold value, the optimal cost may be achieved. Thus, those FLC actions that lead to a Detect Confidence (DC) less than DC_{th} should be rewarded with a positive value, while those actions producing a DC higher than DC_{th} should be punished with a negative value. Formally, the reinforcement signal used in this work is defined by:

$$\bullet \quad r(t+1) = \begin{cases} 100, & \text{if } DC_{\text{measured}}^k(t) < DC_{\text{th}} \\ -100, & \text{otherwise} \end{cases} \quad (2)$$

Where $r(t+1)$ is the reinforcement signal for the K^{th} sink node in iteration $t+1$. The value of $DC_{\text{measured}}^k(t)$ is calculated as the min-max weighted average:

$$\text{Detect Confidence} = \text{output}(C_j) = (\sum_{j=1}^N \alpha_j c_j) / (\sum_{j=1}^N \alpha_j) \quad (3)$$

$$\alpha_j = [\mu_j(x_0) * \mu_j(y_0)] \quad (4).$$

Where N is the number of rules, α_j is the degree of truth for the rule j and c_j is the selected output constant value for the same rule. The sufficient rules generate by look up table and shows in the Table 5.

Table 5
Fuzzy rules provide by a lookup table

Rule1: IF Tr = high AND Bs = high AND Co =High THEN output = Abnormal
Rule2: IF Tr = high AND Bs = low AND Co =med THEN output = Abnormal
Rule3: IF Tr = low AND Bs = low AND Co =low THEN output = Normal
Rule4: IF Tr = low AND Bs = high AND Co =low THEN output = Normal

These rules are typical of control applications in that the antecedents consist of the logical combination of the time response, buffer size and count signals, while the consequent is a control pattern output. The rule outputs can be defuzzified using a discrete centroid computation based on Eq. (3). Table 6 demonstrates the results of applying one of possible action selection for FQ- Learning algorithm.

Table 6
Possible action selection by FQL

Input variables state i			Input variables state j			Output desirable	Action(Min-Max)
Tr	Bs	Count	Tr	Bs	Count	Pattern	
Low (0.2)	High (0.8)	Low (0.2)	High (0.8)	High (0.8)	High (0.8)	Abnormal (0.8)	Min Sj (0.8, 0.8, 0.8) =0.8
			High (0.8)	Low (0.2)	High (0.8)	Abnormal (0.8)	Min Sj (0.8, 0.2, 0.8) =0.2
			Low (0.2)	Low (0.2)	Low (0.4)	Normal (0.2)	Min Sj (0.2, 0.2, 0.4) =0.2
			Low (0.2)	High (0.8)	Low (0.4)	Normal (0.2)	Min Sj (0.2, 0.8, 0.4) =0.2

Abnormal: Max (0.8,0.2) =0.8
 Normal: Max (0.2, 0.2) =0.2
 Threshold
 0.8 > 0.2 → Abnormal > normal

Example

Consider the FQL is at start state ($\partial 1$) with the degree of membership function for parameter of TR to Low is 0.2, the degree of membership of BS to high 0.8 and the value of count is 0.2, so it is going to move to the goal state S_j (i. e $\partial 9$ in state diagram) with Tr=high, Bs=high and Count=high. It allocates a weighed fuzzy label for all next states by using fuzzy max min. Finally the simple threshold which compares the consequent is used to choose the best action.

5 Experimental Results

Three sets of experiments were conducted to examine the effects of attack detection accuracy based on Fuzzy Logic Controller (D1), Q-learning algorithm (D2), and Fuzzy Q-learning (D3). D3 is derived by taking D1+D2 functionality to produce a sophisticated attack detection algorithm. Table 7 shows the comparison of the proposed ensemble FQL detection algorithm versus the other existing standalone algorithms.

Table 7
 Comparison of existing ensemble algorithms with proposed algorithm

Algorithm / Features	Fuzzy Logic Controller (D1)	Q-learning (D2)	Fuzzy Q-learning (D3)
Prior knowledge of data distribution	Required	Not Required	Not Required
Method used to combine classifiers	Fuzzy Classifiers	Markov Decision Process	Fuzzy rule base and Q-learning
Drawbacks	Work for small subset	Sensitive to noise and outliers, High cost consumption,	Limited by one classifier, The low speed of detection, Fail to high volume of traffic
Advantages	Simple to implement with good performance	Capable of handling multi-class attack detection	Prior knowledge of data distribution no needed,

We used FLC, which utilized min-max fuzzy method for improving classification scheme. If the new sets of fuzzy rules agree on the same class, that class is the final classification decision. If the fuzzy classifiers disagree, then class chosen by the second sets of fuzzy rules classifier is the final decision. The min-max fuzzy

classifiers show the good performance in reduced dataset, but inaccurate by increasing the high volume of traffics that fuzzy IDS may be crashed. In addition, prior knowledge of data distribution is required for fuzzy IDS algorithm. We also, modified the Q-learning algorithm to identify the DDoS attacks. The Q-learning based DDoS attack detection is capable of handling the minor class of DDoS attacks detection, but the multi objective procedure or major features of DDoS attack consumes maximum resources, especially in real time environment. In addition, the convergence of Q-learning takes much time. In Q-learning algorithm the observation is limited by one single classifier. Therefore, this algorithm fails due to high volume of real time traffic. To overcome the problem of accuracy of detection, false alarm rate and time complexity, we combine Q-learning algorithm with fuzzy logic controller to reach high accuracy of detection and low false alarm rate, especially in real time traffic.

Three investigates were carried out on publicly available datasets such as NSL-KDD dataset and CAIDA DDoS dataset, and mixed dataset using the Castalia and the results are discussed in Section 5.1, 5.2, and 5.3.

5.1. Performance Verification

Our proposed classification algorithm with cost per sample function is compared with existing soft computing methods D1, D2, in terms of accuracy of detection per sample on three dataset NSL-KDD, CAIDA, and mixed dataset of attacks. Comparing the false positive rate of FQL with cost minimization, it can be seen that FQL algorithm with cost minimization yields an improvement of 20% $\left(\frac{3.50-2.80}{3.50} * 100\right)$ over Q-Learning algorithm as shown in Table 8. Moreover, it can be inferred from Figure.10 that cost per percentage of samples or anomalous is less for FQL algorithm than the other methods.

The proposed Fuzzy Q-learning (FQL) algorithm with the cost function $U = \rho * SP - \beta * FN - \theta * FP$ was compared with existing soft computing methods (Fuzzy Logic Controller, and Q-learning) with respect to the attack detection precision of modeled Denial-of-Service attacks on three dataset NSL-KDD, CAIDA, and mixed dataset. A comparison between the average utility function and FQL with cost maximization indicates that the latter yielded an improvement of 20% $\left(\frac{3.50-2.80}{3.50} * 100\right)$ over Q-Learning algorithm as shown in Table 8. Moreover, it can be inferred from Figure 10 that cost per percentage of samples or anomalous is less for FQL algorithm than the other methods.

Table 8
Simulation result of detection algorithm for NSL-KDD dataset

Percentage of anomalous	FLC			Q-learning			FQL		
	True Positive (%)	False positive (%)	UF	True Positive (%)	False positive (%)	UF	True Positive (%)	False positive (%)	UF
1	70.20	1.80	50.85	75.20	1.40	55.00	80.10	1.20	58.88
5	71.50	2.20	51.43	76.70	1.60	55.93	81.20	1.40	59.50
10	73.20	2.80	52.10	76.90	1.90	55.78	82.50	1.90	59.98
15	75.40	3.20	53.35	77.60	2.10	56.10	83.70	2.10	60.68
20	75.90	3.70	53.23	78.50	2.40	56.48	83.90	2.40	60.53
25	76.10	4.10	52.98	79.80	3.10	56.75	84.20	2.60	60.55
30	77.10	4.60	53.23	80.10	3.40	56.68	85.80	2.80	61.55
35	80.10	4.90	55.18	82.30	3.90	57.83	86.40	2.90	61.90
40	81.90	5.10	56.33	83.60	4.20	58.50	87.70	3.20	62.58
45	78.20	5.30	53.35	79.80	4.90	54.95	88.50	3.40	62.98
50	76.80	5.90	51.70	78.90	5.20	53.98	89.60	3.90	63.30
55	75.60	6.10	50.60	79.30	5.60	53.88	90.40	4.10	63.70
60	74.80	6.20	49.90	80.00	5.80	54.20	92.40	4.50	64.80
Average	75.91	5.77	52.63	79.13	3.5	55.85	85.88	2.8	61.61

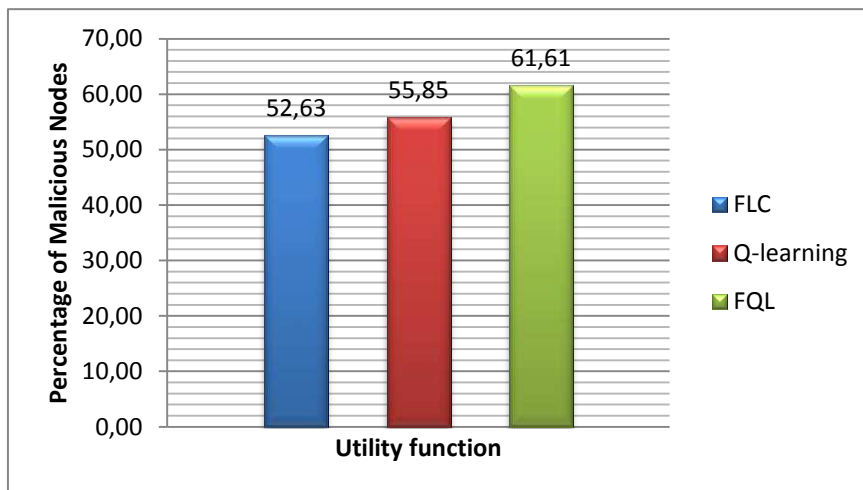


Figure 10
Cost per sample for existing DDoS detection and FQL from NSL-KDD attack source

The next tryout was conducted for CAIDA traffic. From Table 9, it can be seen that the detection accuracy is 78.59% with 5.79% false positive rate. Comparing the false positive rate, FQL algorithm with minimum cost function, it can be seen that FQL yields an improvement over Q-learning, and FLC. It can be inferred from Figure 11 that cost per samples is less for FQL algorithm than other methods.

Table 9
Simulation result of detection algorithm for CAIDA dataset

Percentage of	FLC			Q-learning			FQL		
	True Positive (%)	False positive (%)	UF	True Positive (%)	False positive (%)	UF	True Positive (%)	False positive (%)	UF
1	73.50	1.80	53.33	74.20	1.40	54.25	82.70	1.20	61.73
5	73.90	2.20	53.23	74.70	1.60	54.43	84.70	1.34	63.19
10	74.20	2.80	52.85	75.40	1.90	54.65	85.40	1.50	63.68
15	74.80	3.20	52.90	75.90	2.10	54.83	85.90	2.10	63.90
20	75.10	3.70	52.63	78.60	2.40	56.55	86.60	2.30	64.38
25	75.40	4.10	52.45	78.80	3.10	56.00	87.70	2.80	65.08
30	75.60	4.60	52.10	79.40	3.40	56.15	88.80	3.60	65.70
35	76.10	4.90	52.18	79.90	3.90	56.03	89.40	3.90	66.08
40	76.80	5.10	52.50	80.40	4.20	56.10	90.70	4.50	66.90
45	79.20	5.30	54.10	81.80	4.90	56.45	91.40	4.60	67.40
50	79.50	5.90	53.73	82.80	5.20	56.90	92.50	4.70	68.20
55	80.30	6.10	54.13	83.70	5.60	57.18	93.80	4.90	69.13
60	80.60	6.20	54.25	84.50	5.80	57.58	94.40	5.00	69.55
Average	76.54	6.43	53.10	79.24	5.85	55.93	78.59	5.79	65.76

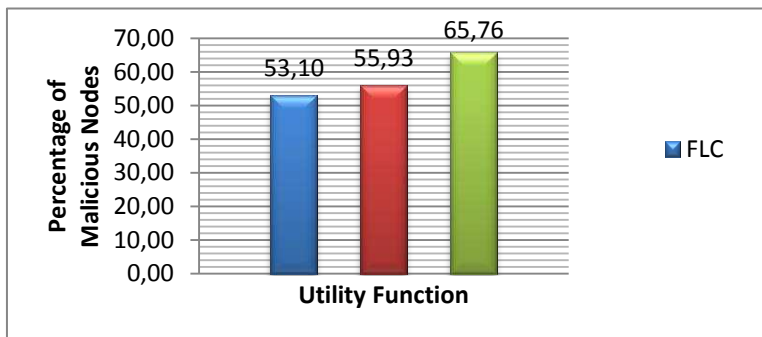


Figure 11

Cost per sample for existing DDoS detection and FQL from CAIDA attack source

Experiment 3 was performed in mixed dataset. From Table 10, it is evidence that the trained FQL algorithm was able to detect DDoS attack with high accuracy of detection, low false positive rate and minimum cost function. Figure 12 indicated the cost per sample of FQL.

Table 10
Simulation result of detection algorithm for Mixed dataset

Percentage of	FLC			Q-learning			FQL		
	True Positive (%)	False positive (%)	UF	True Positive (%)	False positive (%)	UF	True Positive (%)	False positive (%)	UF
1	78.20	1.80	56.85	78.70	1.34	57.69	82.70	1.00	61.03
5	78.60	2.40	56.55	79.20	1.47	57.93	84.70	1.10	62.43
10	79.00	2.80	56.45	79.40	2.10	57.45	85.40	1.30	62.75
15	79.30	3.50	55.98	79.80	2.80	57.05	85.90	1.80	62.63
20	80.10	3.90	56.18	80.10	2.40	57.68	86.60	2.10	62.85
25	80.60	4.30	56.15	80.50	2.92	57.46	87.70	2.40	63.38
30	81.30	4.60	56.38	81.30	3.40	57.58	88.80	2.70	63.90
35	82.10	4.90	56.68	81.80	3.90	57.45	89.40	2.90	64.15
40	82.50	5.10	56.78	82.70	4.20	57.83	90.70	3.00	65.03
45	83.10	5.30	57.03	83.90	4.90	58.03	91.40	3.30	65.25
50	83.40	5.90	56.65	84.60	5.20	58.25	92.50	3.60	65.78
55	84.10	6.10	56.98	85.90	5.60	58.83	93.80	3.70	66.65
60	84.20	6.20	56.95	86.60	5.80	59.15	94.40	3.90	66.90
Average			56.58			57.87			64.05

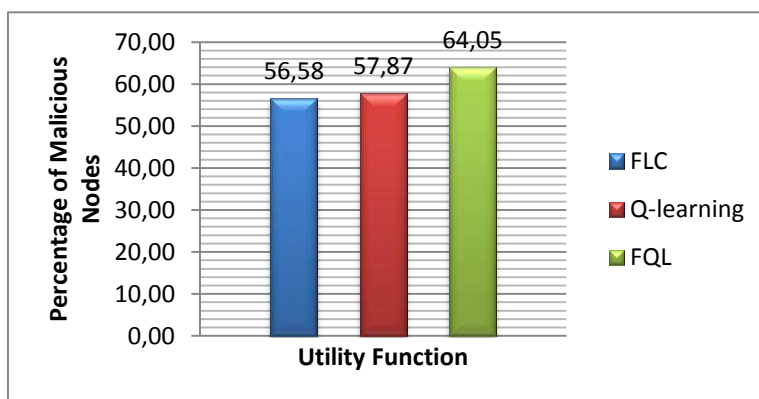


Figure 13

Cost per sample for existing DDoS detection and FQL from Mixed attack source

5.2. Computational Time of FQL Algorithm

Preprocessing time includes the time spent in feature extraction and normalization. The training time depends on the number of times the classifier needs training which in turn depends on the mean square error between iterations reaching goal minimum. Testing time includes the time spent in testing the unlabeled instances by weighted mean. Table 11 shows the performance comparison of the FQL in terms of consuming time obtained during the experiments. From Table 11, it can be realized that the training time of FQL is higher to QL, but it consumes more testing time than the FLC, Q-learning. Also, the computational time was calculated on Intel 3.10 GHz, Core i-5 Processor, 4 GB RAM computer.

Table 11

Performance comparison of Co-FQL with existing machine learning methods in terms of consuming time

Dataset	Algorithms	Training time (seconds)	Testing time (seconds)
Mixed Dataset	Fuzzy Logic Controller (D1)	3.10	1.30
	Q-learning (D2)	3.14	1.36
	Fuzzy Q-learning (D3)	3.22	1.40

Testing time of the proposed FQL method is a little high due to the ensemble output combination methods such as fuzzy logic controller with Q-learning algorithm, but more detection accuracy was achieved in FQL. The speedup of FQL can be improved when a hybrid classifier is executed in parallel processors. Thus, all the modules can be processed in parallel by different engines in order to reduce the overall processing time considerably.

Conclusions and Future Research

Development of the machine learning algorithmic technique for online IDS by modifying Fuzzy Q-learning mechanism detects DDoS attack with 85.88% accuracy, which is far superior to Fuzzy Logic Controller, and Q-learning algorithm by themselves. Reducing complexity and dimensionality of the selected feature set is learnt to reach to the goal state. In our research work discretization, feature selection and accuracy calculation are handled simultaneously, which reduces computational cost and build the detection in a comprehensive way. It has been observed that for detection of continuous attack attribute by fuzzy Q-learning, if different parameters are applied to all attributes, classification accuracy yields best result. The proposed method is tested with differently correlated data sets such as NSL-KDD, CAIDA, and Mixed datasets, showing effectiveness of the system in real time intrusion detection environment. It has been observed that the proposed method achieves higher classification by 88.77% accuracy and minimum cost function by 65.76% in CAIDA dataset compared to other existing detection methods (i.e., fuzzy logic controller, and Q-learning,) applied in the wireless networks.

Given the huge types and amounts of DDoS attacks, their optimum classification is very important for rapid detection, in which other performance indicators such as processing rate, energy consumption rate and accuracy of response would be needed to estimate the quality of the IDS. Novel detection of attacks is an important research area in security domain and has immense importance for IDPS. The characteristics of attacks changing with time and space and so handling of such attacks by using existing knowledge opens new avenue of research. Designing of classifiers using different approaches and then fusing those classifiers surely improve classification accuracy in IDPS. However, its deployment in real life operational environment is a huge challenge that still needs to be further researched.

Acknowledgement

This work is supported by the University of Malaya, Malaysia, under Research Grant RG108-12ICT.

References

- [1] I. F. Akyildiz, W. Su, Y. Sankarasubramaniam, E. Cayirci, *Wireless Sensor Networks: a Survey*, *J. Comput. Netw*, 38 (2002) 393-422
- [2] Y. E. Aslan, I. Korpeoglu, Ö. Ulusoy, *A Framework for Use of Wireless Sensor Networks in Forest Fire Detection and Monitoring*, *Computers, Environment and Urban Systems* (2012)
- [3] J. M. L. P. Caldeira, J. J. P. C. Rodrigues, P. Lorenz, *Toward Ubiquitous Mobility Solutions for Body Sensor Networks on Healthcare*, *Communications Magazine, IEEE*, 50 (2012) 108-115
- [4] A. Bonastre, J.V. Capella, R. Ors, M. Peris, *In-line Monitoring of Chemical-Analysis Processes Using Wireless Sensor Networks*, *TrAC Trends in Analytical Chemistry*, 34 (2012) 111-125
- [5] N. Li, N. Zhang, S. K. Das, B. Thuraisingham, *Privacy Preservation in Wireless Sensor Networks: A State-of-The-Art Survey*, *Ad Hoc Networks*, 7 (2009) 1501-1514
- [6] P. Schaffer, K. Farkas, Á. Horváth, T. Holczer, L. Buttyán, *Secure and Reliable Clustering in Wireless Sensor Networks: A Critical Survey*, *Computer Networks*, 56 (2012) 2726-2741
- [7] *DDOS Attacks against U.S. Banks Continue – LINKAGES Explored*, Available from [www.gartner.com/], (2012)
- [8] A. D. Wood, J. A. Stankovic, *Denial of Service in Sensor Networks*, *Computer*, 35 (2002) 54-62
- [9] C. V. Zhou, C. Leckie, S. Karunasekera, *A Survey of Coordinated Attacks and Collaborative Intrusion Detection*, *Computers & Security*, 29 (2010) 124-140

- [10] S. Shamshirband, S. Kalantari, Z. Bakhshandeh, Designing a Smart Multi-Agent System Based on Fuzzy Logic to Improve the Gas Consumption Pattern, *Sci Res Essays*, 5 (2010) 592-605
- [11] A. Feizollah, S. Shamshirband, N. Anuar, R. Salleh, M. Mat Kiah, Anomaly Detection Using Cooperative Fuzzy Logic Controller, in: K. Omar, M. Nordin, P. Vadakkepat, A. Prabuwono, S. Abdullah, J. Baltes, S. Amin, W. Hassan, M. Nasrudin (Eds.) *Intelligent Robotics Systems: Inspiring the NEXT*, Springer Berlin Heidelberg, 2013, pp. 220-231
- [12] D. Petković, N. T. Pavlović, S. Shamshirband, M. L. Mat Kiah, N. Badrul Anuar, M. Y. Idna Idris, Adaptive Neuro-Fuzzy Estimation of Optimal Lens System Parameters, *Optics and Lasers in Engineering*, 55 (2014) 84-93
- [13] D. Petković, Ž. Čojbašić, V. Nikolić, S. Shamshirband, M. L. Mat Kiah, N. B. Anuar, A. W. Abdul Wahab, Adaptive Neuro-Fuzzy Maximal Power Extraction of Wind Turbine with Continuously Variable Transmission, *Energy*, 64 (2014) 868-874
- [14] S. Shamshirband, N. B. Anuar, M. L. M. Kiah, A. Patel, An Appraisal and Design of a Multi-Agent System-based Cooperative Wireless Intrusion Detection Computational Intelligence Technique, *Engineering Applications of Artificial Intelligence*, 26 (2013) 2105-2127
- [15] X. Xu, T. Xie, A Reinforcement Learning Approach for Host-based Intrusion Detection Using Sequences of System Calls, *Advances in Intelligent Computing*, (2005) 995-1003
- [16] S. S. Shamshirband, H. Shirgahi, S. Setayeshi, Designing of Rescue Multi Agent System Based on Soft Computing Techniques, *Advances in Electrical and Computer Engineering*, 10 (2010) 79-83
- [17] S. A. Razak, S. M. Furnell, N. L. Clarke, P. J. Brooke, Friend-assisted Intrusion Detection and Response Mechanisms for Mobile Ad Hoc Networks, *Ad Hoc Networks*, 6 (2008) 1151-1167
- [18] P. Muñoz, R. Barco, I. de la Bandera, Optimization of Load Balancing Using Fuzzy Q-Learning for Next Generation Wireless Networks, *Expert Systems with Applications*, 40 (2013) 984-994
- [19] Kdd cup 1999 data, UCI KDD Archive [<http://kdd.ics.uci.edu/databases/kddcup99/kddcup99.html>] (1999)
- [20] E. Çayirci, C. Rong, Front Matter, in: *Security in Wireless Ad Hoc and Sensor Networks*, John Wiley & Sons, Ltd, 2009, pp. i-xxiii
- [21] The CAIDA DDoS Attack 2007 Dataset, Available from [http://www.caida.org/data/passive/ddos-20070804_dataset.xml] (2007)

- [22] P. A. Raj Kumar, S. Selvakumar, Distributed Denial of Service Attack Detection Using an Ensemble of Neural Classifier, *Computer Communications*, 34 (2011) 1328-1341
- [23] J.-Y. Huang, I. E. Liao, Y.-F. Chung, K.-T. Chen, Shielding Wireless Sensor Network Using Markovian Intrusion Detection System with Attack Pattern Mining, *Information Sciences*, 231 (2013) 32-44
- [24] M. Eslaminejad, S. A. Razak, Fundamental Lifetime Mechanisms in Routing Protocols for Wireless Sensor Networks: A Survey and Open Issues, *Sensors*, 12 (2012) 13508-13544
- [25] P. Cingolani, J. Alcalá-Fdez, jFuzzyLogic: a Robust and Flexible Fuzzy-Logic Inference System Language Implementation, in: *Fuzzy Systems (FUZZ-IEEE) 2012 IEEE International Conference on*, 2012, pp. 1-8

Optimisation of Computer-aided Screen Printing Design

Eszter Horvath, Adam Torok, Peter Ficzer, Istvan Zador, Pal Racz

Department of Electronics Technology, Budapest University of Technology and Economics, Egy József u 18, H-1111 Budapest, Hungary, horvathe@ett.bme.hu;

Department of Transport Technology and Economics, Budapest University of Technology and Economics, Sztoczek u. 2, H-1111 Budapest, Hungary, atorok@kgazd.bme.hu;

Department of Vehicle Elements and Vehicle-Structure Analysis; Budapest University of Technology. and Economics; Stoczek u. 2, H-1111 Budapest, Hungary, ficzere@kge.bme.hu;

Kogát Ltd., Eperjes u. 16, H-4400 Nyíregyháza, Hungary, istvan.zador@kogat.hu

Bánki Donát Faculty of Mechanical and Safety Engineering, Óbuda University, Népszínház u. 8, H-1081 Budapest, Hungary, racz.pal@bgk.uni-obuda.hu

Abstract: Computer-aided screen printing is a widely used technology in several fields like the production of textiles, decorative signs and displays and in printed electronics, including circuit board printing and thick film technology. Even though there have been many developments in the technology, it is still being improved. This paper deals with the optimisation of the screen printing process. The layer deposition and the manufacturing process parameters strongly affect the quality of the prints. During this process the paste is printed by a rubber squeegee onto the surface of the substrate through a stainless steel metal screen masked by photolithographic emulsion. The off-contact screen printing method is considered in this paper because it allows better printing quality than the contact one. In our research a Finite Element Model (FEM) was created in ANSYS Multiphysics software to investigate the screen deformation and to reduce the stress in the screen in order to extend its life cycle. An individual deformation measuring setup was designed to validate the FEM model of the screen. By modification of the geometric parameters of the squeegee the maximal and the average stress in the screen can be reduced. Furthermore the tension of the screen is decreasing in its life cycle which results in worse printing quality. The compensation of this reducing tension and the modified shape of squeegee are described in this paper. Using this approach the life cycle of the screen could be extended by decreased mechanical stress and optimised off-contact.

Keywords: screen printing; FEM; optimisation

1 Introduction

Screen printing is the most widespread and common additive layer deposition and patterning method because of its ability to print on many kinds of substrates with the widest range of inks and because, considering any modern print process, it can deposit the greatest thickness of ink film [1]. Although this technology has been used since the beginning of the 2nd millennium it is still under development and there have been many innovations with the technology in the last 50 years [2].

Screen printing technology provides the most cost effective facility for applying and patterning the different layers for hybrid electronics industry as well, since a thick film circuit usually contains printed conductive lines, resistive and dielectric layers. Due to its simple technology and relative cheapness it is still widely used in the mass assembly of recent electronic circuits. The technology has a large application field extending to decal fabrication, balloon and cloths patterning, textile production, producing signs and displays, decorative automobile trim and truck signs and last but not least use in printed electronics [3]. Screen-printing is ideal as a manufacturing approach for microfluidic elements also used in the field of clinical, environmental or industrial analysis [4], in sensors [5] and in solar cells [6].

In general, the layers are designed using computer-assisted design (CAD) software [7]. Paste printing is carried out by a screen printer machine. The screen is strained onto an aluminium frame and the ink is pressed onto the substrate through the screen not covered by emulsion by a printing squeegee. The squeegee has constant speed and pushes the screen with a contact force. The material of the screen can be stainless steel or polymer. The design of the printed layer is realized with a negative emulsion mask on the screens. There are two main techniques of screen printing:

- off-contact, where the screen is warped with a given tension above the substrate;
- contact, where the screen is in full contact with the substrate.

Contact screen-printing is less advantageous in general, because due to the lift off of the screen it often causes the damage of the high resolution pattern.

In case of off-contact screen-printing, some paste is applied on top of the screen in the front of the polymer squeegee. While the squeegee is moving forward, it pushes the screen downwards until it comes into contact with the substrate beneath. The paste is pushed along in front of the squeegee and pushed through the screen not covered by emulsion pattern onto the substrate. The screen and substrate separate behind the squeegee. The off-contact screen printing process is demonstrated in Fig. 1.

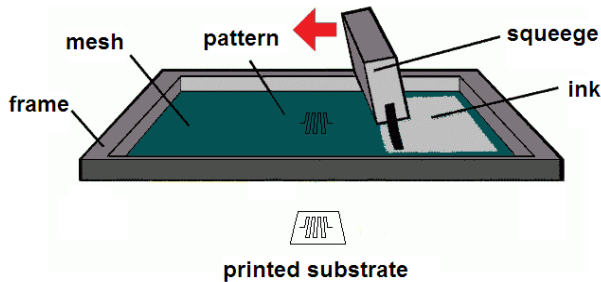


Figure 1

The squeegee pushes the paste on the screen and presses it through the openings

Since the 1960s several experiments and models of the printing process have been evaluated. The optimisation of screen printing was mainly achieved by experimental evaluation without the advantage of numerical models. The empirical optimisation method is described by *Kobs* and *Voigt* [8] in 1970, they appointed more than 50 variables and combined the most important ones in almost 300 different ways and also compared the effects of them. These investigations offer an enormous empirical database but general rules for screen-printing cannot be created from this without models. *Miller* [9] has investigated the amount of paste printed on the substrate in the function of paste rheology, mesh size and line width. Others have examined the influence of squeegee angle and squeegee blade characteristic on the thickness of the deposited paste [10] and the effect of the screen on fine scale printed patterns [11]. In general, the best solution for optimising a process can be achieved by parameter optimisation based on a theoretical model [12].

The first efforts to achieve a theoretical description of the screen printing process were made by *Riemer* more than 20 years ago [13-15]. His mathematical models of the screen-printing process were based fundamentally on the Newtonian viscous fluid scraping model [16]. This model was extended by others [17-18], although they did not take into account the flexibility of the screen, which is a feature influencing the process essentially. Neither of these models deals with the effect of geometry in the screen printing process. The repetitive behaviour of the printing process requires taking into consideration the effect of the cyclic load. In this work, a mechanical model is presented with similar geometry to the off-contact screen printing process. In this model, instead of the paste deposition phase, the mechanical behaviour of the screen is in the focus. Furthermore, our model effectively considers the geometry of the knife. The aim of this paper is to improve the technical solutions and in increase the performances without harming reliability as defined at *Morariu* [26].

2 Experimental Setup

2.1 Material Parameters of Screen

The first step of the model construction is to define the geometries and obtain the mechanical parameters of the screen [27]. The geometric features and the initial strain – which warps it onto an aluminium frame – are realised by the manufacturing process.

In order to decrease screen tension deviation during the print the screen is tightened onto the aluminium frame with the thread orientation of 45° to the printing direction. Therefore the load distribution is more homogeneous between the threads.

The elastic (Young) modulus of the screen was determined using the modified Voigt expression:

$$E_c = \eta \cdot E_f \cdot V_f + E_m \cdot (1 - V_f) \quad (1)$$

where

$E_m = 690$ MPa is the elastic modulus of the emulsion,

$E_f = 193$ GPa is the elastic modulus of the stainless steel,

V_f is the volume fraction of the stainless steel and

η is the Krenchel efficiency factor [19], [20].

In case of $\theta_1 = \theta_2 = 45^\circ$ thread orientation in the frame:

$$\eta = 0.5 \cdot \cos^4 \theta_1 + 0.5 \cdot \cos^4 \theta_2 = 0.25 \quad (2)$$

The Poisson ratio can be expressed as:

$$\nu_{xy} = \nu_f \cdot V_f + \nu_m \cdot V_m \quad (3)$$

where

ν_f is the Poisson's ratio of stainless steel (0.28) and

ν_m is the Poisson ratio of emulsion (0.43) [21].

In our study SD75/36 stainless steel screen was utilised with the mesh number of 230 and open area of 46%. The schematic view of screen cross section is shown in Fig. 2,

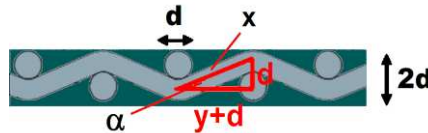


Figure 2

A sketch of the SD75/36 screen cross section with the main parameters

where
 d is the diameter of the thread,
 α is the bending angle,
 x is the element length of the thread.

$$x = \frac{d}{\sin \alpha} \quad (4)$$

Using Eq.4. the volume fraction of the stainless steel can be calculated:

$$V_f = 2 \cdot \frac{d^2 \cdot \pi}{4} \cdot l \cdot \frac{l}{l+d} \cdot \frac{d}{\sin \alpha} = 0.27 \quad (5)$$

Substituting Eq. 5. into Eq. 1. the elastic modulus of the screen turned out to be 13 GPa. The sizes of the screen are 298 mm in width, 328 mm in length and the thickness of it was 72 μm . These parameters were utilised in the finite element model.

2.2 Measuring the Friction Force between the Screen and the Squeegee

The paste we have applied in our experiment was PC 3000 conductive adhesive paste from Heraeus. In the process of screen printing the friction force between the screen and the squeegee plays an important role. While the squeegee passes the screen due to the friction force the position of the mask shifts. The individual friction force measuring setup is shown in Fig. 3.

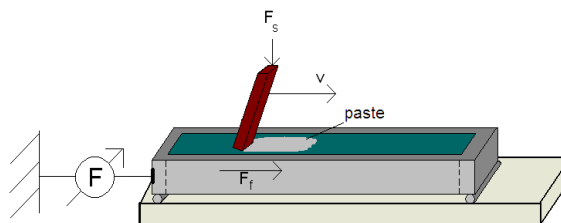


Figure 3

Measurement setup for determining the friction force between the squeegee

By this measurement the relationship between the friction force (F_f) and the printing speed (v) and squeegee force (F_s) was estimated. Every thick film paste is viscous and has a non-Newtonian rheology suitable for screen printing. The shear stress, τ , for this kind of fluids can be described by the Ostwald de Waele relationship:

$$\tau = K \left(\frac{dv}{dy} \right)^n \quad (6)$$

where

K is the flow consistency coefficient ($\text{Pa}\cdot\text{s}^n$),

$\partial v/\partial y$ is the shear rate or the velocity gradient perpendicular to the plane of shear (s^{-1}),

n is the flow behaviour index (-) [22].

Fig. 4 shows the shear stress and paste velocity during screen printing. Thick film paste is a shear-thinning fluid, thus n is positive but lower than 1.

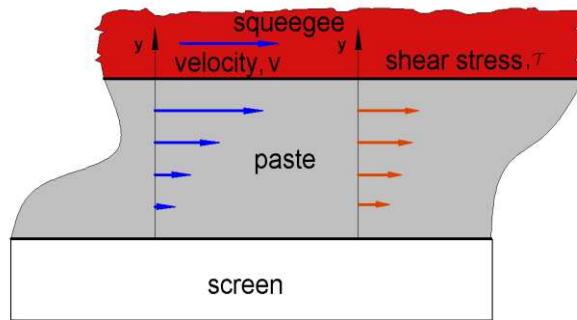


Figure 4

Appared shear stress and the velocity of paste during screen printing.

In addition the elongation of the screen – which is greater if the off-contact is greater – results in image shift as well [23]. The effect of these lateral shifts demonstrated in Fig. 5 has also to be taken into account.

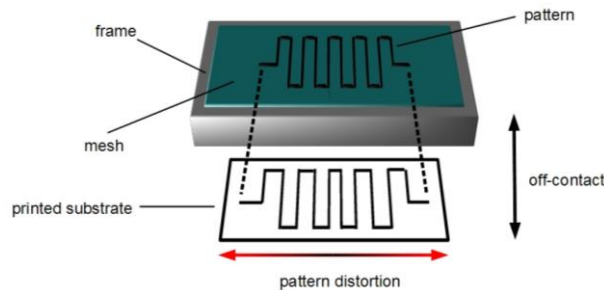


Figure 5

Deformed paste deposition is the result of the screen elongation

The image shift was examined, where the screen tension was in the region of 2–3.3 N/mm, the off-contact was 0.9–1.5 mm, and the applied friction force was based on the measurement. The reduction of screen tension can affect the quality of the printing in other respects. The deflection force of the screen is decreasing,

so the separation of the substrate and the screen cannot start right after the squeegee passes on the screen. This off-contact distance has to be modified in the function of screen tension to keep the screen from sticking to the substrate during printing because adhesion causes many separation problems that damage the quality of the printed film.

2.3 Principles of the Mechanical Model

Equations for mechanical simulations are based on the stress strain relationship for linear material [24]:

$$\sigma_{ij} = C_{ijkl} \varepsilon_{kl} \quad (7)$$

where

σ is the stress tensor,

C is fourth order elasticity tensor and

ε is the elastic strain tensor.

The stiffness matrix can be reduced to a simpler form because the material is symmetric in the x and y direction. The elastic stiffness matrix has the following form:

$$D = \frac{E}{(1+\nu) \cdot (1-2\nu)} \begin{bmatrix} 1-\nu & \nu & 0 \\ \nu & 1-\nu & 0 \\ 0 & 0 & \frac{1-2\nu}{2} \end{bmatrix} \quad (8)$$

where

E is the Young modulus,

ν is Poisson ratio.

As a consequence of the squeegee load the screen bends and gets large displacement or so called geometric nonlinearity. The resulting strains are calculated by using Green-Lagrange strains, where that is defined with reference to the undeformed geometry. Green-Lagrangian strain components, E_{ij} , can be expressed as:

$$E_{ij} = \frac{1}{2} \left(\frac{\partial u_i}{\partial x_j} + \frac{\partial u_j}{\partial x_i} + \frac{\partial u_k}{\partial x_i} \cdot \frac{\partial u_k}{\partial x_j} \right) \quad (9)$$

where \mathbf{u} is the displacements vector.

2.4 Constructing and Verifying the Finite Element Model

For the screen model SHELL 93 element was selected because it handles nonlinear geometry in large strain/deflection and in stress stiffening. These two types of geometric nonlinearities are playing significant role in modelling the mechanical description of the screen. SHELL93 element has six DOF (degrees of freedom) at every node. The first step in modelling the screen was to determine the initial strain in the screen without additional load, due to the fact that it tightens on the frame. These loads were applied on two perpendicular edges of the screen, while the two others were fixed in the direction of the load acting at the opposite edge. The schematic view of the sizes ($x=328$ mm, $y=298$ mm), edge loads (σ_x , σ_y) and constraints can be seen on Fig. 6.

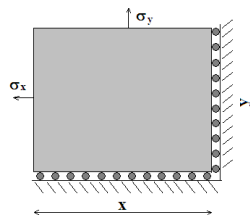


Figure 6

Layout of the pre-stress condition

In the second model – in which the bending of the screen is calculated in the function of load value and position – the screen tightness is given by a displacement constraint calculated in the model before. As boundary conditions, fixed screen edges (in all direction the displacements and rotations are zero) with the calculated displacement conditions were given. Taking into consideration that the printing process is slow enough, it can be handled stationary in each moment while the screen is in force equilibrium. The width of the squeegee was 180 mm. Rectangular elements were used and the mesh density was gradually increasing only towards the load area of the squeegee for faster convergence. The aim of this simulation was to examine how the model describes the real process. In order to compare the FEM calculation to the real situation a measurement set-up was designed and realised (Fig. 7).

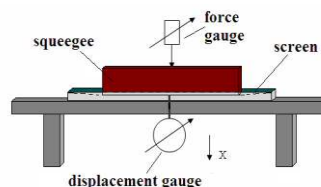


Figure 7

A sketch of the equipment for measuring deformation of the screen

The screen was loaded at 11 different positions, where the distances from the centre range from 0 mm to 100 mm with 10 mm step sizes, represented in Fig. 8. The load was 40-80 N in 10 N step sizes. These parameters give 55 different measurement points. At one measurement point five measurements were recorded.

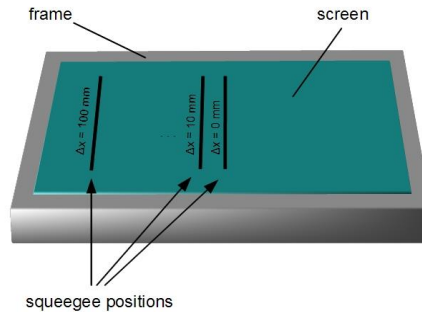


Figure 8

The squeegee line locations on the screen during the measurement

In the model of screen-printing, the displacement of the screen at the load place in direction z was maximised according to the industrial standards of distance (about 1 mm) between the screen and the substrate (off-contact) [25]. The original construction of the screen printing is shown in Fig. 9.

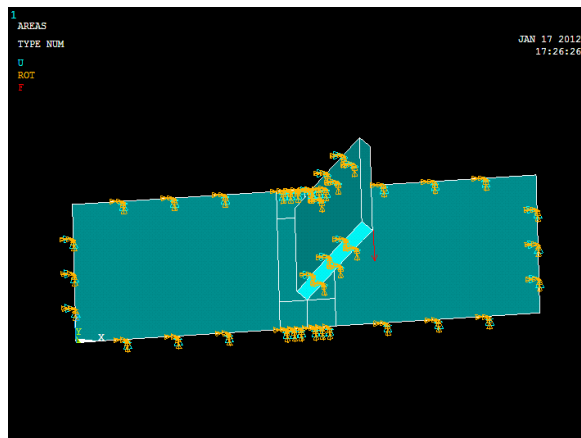


Figure 9

The original construction of screen printing in FEM model with the constraints

As boundary conditions, fixed screen edges (motion is zero in all possible direction) were set with the displacement load in x and y direction which corresponds to the screen tension. A finer mesh was created in that area where the squeegee acts and a coarser mesh for the rest of the model (Fig. 10).

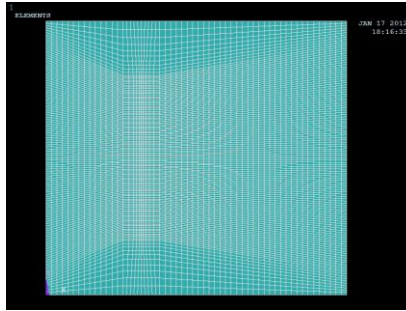


Figure 10

Meshed screen in FEM; the mesh is densified at the load area of the squeegee.

The finer-meshed area ensures accuracy the coarser-meshed area provides faster run time.

3 Results and Discussion

3.1 Modelling of Stress Distribution in the Screen

In the first model of the screen the initial strain – caused by the stretching on the frame – was determined. For the initial stress of $\sigma_x = \sigma_y = 2.65 \text{ N/mm}$ the displacements in direction x and y were -0.6209 mm and 0.5641 mm respectively. In the second model the screen tightness is given by this displacement constraint calculated in the model before. In this model the screen was loaded at 11 different positions and five different loads were applied according to the measurements. Compared to the simulation results and measurements the screen deformation can be seen in Fig. 11 for 55 different conditions.

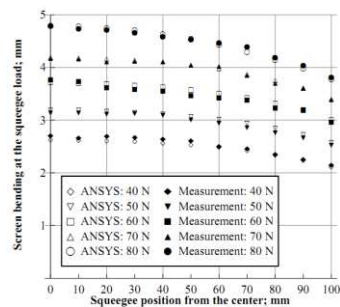


Figure 11

Measured and simulated bending of the screen at load line

In the model of screen printing – where the maximal displacement of the screen in direction z was 1 mm – the stress was concentrated at the ends of the load area (Fig. 12).

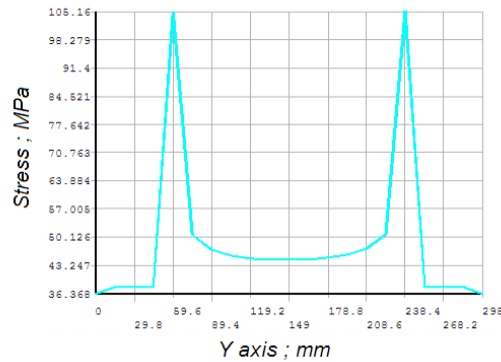


Figure 12

Von Mises equivalent stress distribution in the screen along the line, where the load is applied

The maximal stress in the screen (105 MPa) appeared around the load edge while the average stress in the screen was only about 38 MPa. This phenomenon occurred due to the squeegee shape ending in a point so the corners of the squeegee generate stress concentration in the screen. The surface quality of a used screen (5000 cycles) was examined by optical microscope to detect the damage caused by these high stress peaks (Fig. 13). Investigation shows that the screen area, where the edges of the squeegee passed the filaments are abraded, while the middle part is intact.

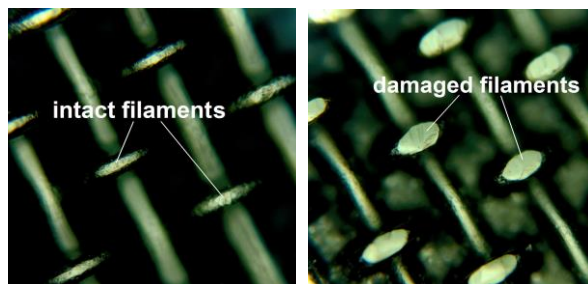


Figure 13

The middle part of the screen is intact but where the squeegee edges act the filaments are abraded

In order to reduce this relative high stress peak in the material the shape of the squeegee was modified (Fig. 14). The two parameters of the rounding are R and f , the radius of the circle and the width of the rounded squeegee segment respectively.

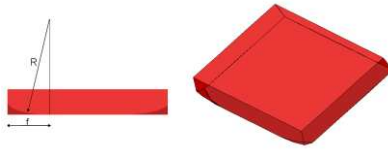


Figure 14

Squeegee rounding scheme with the radius of the circle and the width of the rounded squeegee segment

The optimal radius can be obtained from the extrema (in this case the minimum) of the $\sigma(R)$ stress-radius function (Fig. 15).

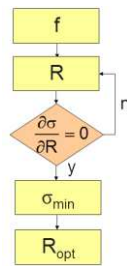


Figure 15

Process flow of the squeegee – rounding optimisation

As the result of the rounded squeegee, in case of $f = 40$ mm with the optimal R of 1900 mm, the maximal stress in the screen reduces to half (Fig. 16).

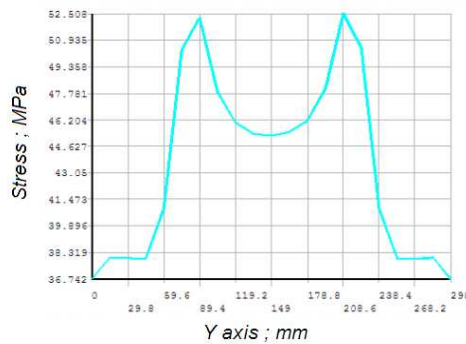


Figure 16

Von Mises equivalent stress distribution in the screen along the line, where the load is applied

The value of f should be as high as the screen mask allows, because larger rounded area results in lower stress concentration. During screen printing the geometry of the squeegee, so the shape of the curvature can be changed.

Therefore, further simulation was carried out to determine the deformation of the squeegee for different loads. Fig. 17 shows the deformation of the squeegee in direction Z (vertical axis that perpendicular to basic surface):

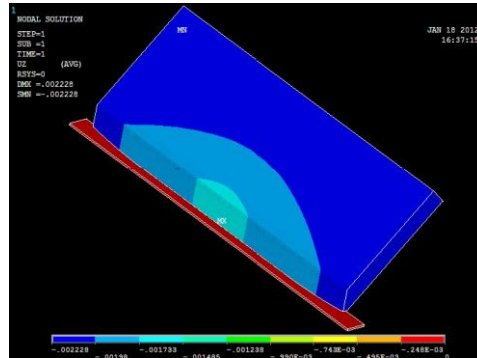


Figure 17

Displacement of the squeegee in direction Z in case of the load of 50 N

The result of the simulation shows that the maximal deformation of the squeegee is equal to the squeegee shape with a cutting process accuracy of ± 0.02 mm so this can be neglected in the final model.

3.2 Effect of the Friction Force and Screen Tension in the Quality of Screen Printing

The model was supplemented by the friction force (see Section 2.2) in order to determine the shift of the patterned screen. *Table 1* summarises the friction force between the screen and the squeegee as a function of the squeegee force and speed.

Table 1

The friction force between the screen and the squeegee*

Squeegee pressure [N]	Speed [mm/s]							
	20	40	60	80	100	120	140	160
10	2.2	3.4	4	4.6	4.6	5.2	5.6	5.6
20	2.6	4	4.4	5.2	5.4	5.6	6	6.2
30	3.4	4	4.6	5.2	5.6	5.8	6.8	6.6
40	3.6	4.2	5	5.4	5.8	6	6.8	7
50	3.6	4.6	5	5.4	5.8	6.2	7	7
60	3.8	4.6	5.2	6	5.8	6.4	7.2	7.4
70	4.6	5	5.6	6.2	6.2	6.6	7.4	8
80	4.8	5.6	5.8	6.6	6.6	6.9	8.4	8.4

* at different squeegee force and speed

Evaluating the results of *Table 1* it can be determined by regression of least squares method, that n is between 0.2 and 0.4 in Eq. 6 for this type of adhesive paste. Even if the applied friction force was 8.4 N, the off-contact was 1.5 mm and the tension of the screen is reduced to only 2 N/mm the resulted shift is less than 2.7 μm . The image deformation arising from the elongation of the screen is less than 0.5 μm in the printing area of the screen in case of 1.5 mm off-contact. Obviously it is lower if the off-contact is lower. Accordingly the deposition shift is negligible under 1.5 mm off-contact and if the friction force is in this region. However, if there is not enough paste on the screen the friction force can be multiplied, so the shift can reach 10 μm . On the other hand the quality of the printing is maintainable if the reduction of screen tension is compensated. The screen tension is reducing in the screen caused by repetitive printing – which can be handled as a cyclic mechanical load – when the elongation of the screen is increasing. As the tension is decreasing the deflection force of the screen is also decreasing, so the screen usually adheres to the substrate and the separation cannot start right after when the squeegee has passed on the screen. The deflection force is maintainable if the off-contact distance is modified. In our study the initial screen tension was 3 N/mm and the off-contact was the industrial standard (1 mm) which resulted in adequate printing quality. In order to avoid adhering, the off-contact has to be increased according to Fig. 18.

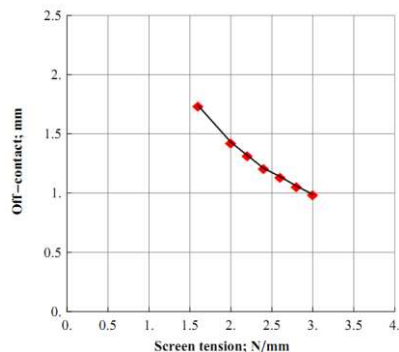


Figure 18

Off-contact compensation in the function of screen tension

As the squeegee force has not been changed, the paste is being printed with the same pressure, and due to the modified off-contact the elastic force resulting from screen deflection and the paste adhesion has the same force condition as at the initial screen tension and off-contact.

Conclusion

A finite element model was created and verified to describe the stress distribution in the screen due to squeegee load. The boundary displacement condition was determined in the first step by the preliminary model. Using these results a model was constituted to simulate the bend of the screen due to different loads acting at

different positions. A measurement set-up was designed and realised to verify the model. Comparing the measured and simulated results it can be clearly concluded that the model gives good approximation of the bending values. In the model of screen printing – where the maximal displacement of the screen in direction z was 1 mm – the stress was determined. The maximums appeared at the ends of the load area. The geometric parameters of the squeegee were modified to reduce the stress in the screen in order to extend its life cycle. By this the maximal and average stress in the screen could be reduced. Furthermore the decreasing screen tension was compensated by modifying the value of the off-contact which leads to sustainable screen-printing quality. Therefore the life cycle of the screen could be extended by decreased mechanical stress and increased off-contact.

Acknowledgement

This work is connected to the scientific program of the ‘*Development of quality oriented and harmonized R+D+I strategy and functional model at BME*’ project. These projects are supported by the New Szechenyi Development Plan (Project ID: TÁMOP-4.2.1/B-09/1/KMR-2010-0002). The author would like to express their sincere appreciation to Dr. Gábor Várhegyi, for his advice throughout the kinetic research and to Dávid Vékony to his suggestions in statistical data analysis. The authors are grateful to the support of Bólyai János Research fellowship of HAS (Hungarian Academy of Science). and Prof. Dr. Florian Heinitz, Director of Transport and Spatial Planning Institute in Erfurt, Germany.

References

- [1] Anderson J., Forecasting the Future of Screen-Printing Technology, *Screen Printing Magazine*, October, 2003
- [2] Kosloff A., Photographic Screen Printing, *ST Publications*, Cincinnati, Ohio, 1987
- [3] Selejdak J., Stasiak-Betlejewska R., Determinants of Quality of Printing on Foil, *Journal of Machine Engineering*, Vol. 7, No. 2, 2007, pp. 111-117
- [4] Albareda-Sirvent, M., A. Merkoçi, and S. Alegret, Configurations used in the Design of Screen-printed Enzymatic Biosensors. A review. *Sensors and Actuators B: Chemical*, 2000, 69(1-2) pp. 153-163
- [5] Viricelle J. P., Compatibility of Screen-Printing Technology with Microhotplate for Gas Sensor and Solid Oxide Micro Fuel Cell Development. *Sensors and Actuators B: Chemical*, 2006, 118(1-2) pp. 263-268
- [6] Krebs F. C., Large Area Plastic Solar Cell Modules. *Materials Science and Engineering: B*, 2007, 138(2), pp. 106-111
- [7] Nùria Ibàñez-García, Julián Alonso, Cynthia S. Martínez-Cisneros, Francisco Valdés, Green-Tape Ceramics. New Technological Approach for Integrating Electronics and Fluidics in Microsystems, *Trends in Analytical Chemistry*, Volume 27, Issue 1, January 2008, pp. 24-33

-
- [8] D. R. Kobs and D. R. Voigt, Parametric Dependencies in Thick Film Screening. *Proc. ISHM* 18, 1970, pp. 1-10
- [9] Miller L. F., Paste Transfer in the Screening Process, *Solid State Technology*, 1969, pp. 46-52
- [10] Benson M. Austin, Thick-Film Screen Printing, *Solid State Technology*, 1969, pp. 53-58
- [11] Bacher J. Rudolph, High Resolution Thick Film Printing, *Proceedings of the International Symposium on Microelectronics*, 1986, pp. 576-581
- [12] Dyakov I., Prentkovskis O., Optimization Problems in Designing Automobiles, *Transport*, Vol. 23(4), 2008, pp. 316-322
- [13] Riemer E. Dietrich, Analytical Model of the Screen Printing Process: Part 2. *Solid State Technology* 9, 1988, pp. 85-90
- [14] Riemer E. Dietrich. Analytical Model of the Screen Printing Process: Part 1. *Solid State Technology* 8, 1988, pp. 107-111
- [15] Riemer E. Dietrich, The Theoretical Fundamentals of the Screen Printing Process. *Hybrid Circuits* 18, 1989, pp. 8-17
- [16] Taylor G. I., On Scraping Viscous fluid from a Plane Surface. *Miszallangen Angewandten Mechanik*, 1962, pp. 313-315
- [17] Riedler J., Viscous flow in Corner Regions with a Moving Wall and Leakage of fluid. *Acta Mechanica* 48, 1983, pp. 95-102
- [18] Jeong J., Kim M., Slow Viscous Flow Due to Sliding of a Semi-Infinite Plate over a Plane, *Journal of Physics Society*, 54, 1985, pp. 1789-1799
- [19] Cox H. L., The Elasticity and Strength of Paper and Other Fibrous Materials, *British Journal of Applied Physics*, 3, 1952, pp. 72-79
- [20] Krenchel H., Fibre Reinforcement, *Akademisk Forlag*, 1964, Copenhagen, Denmark
- [21] Irgens F., *Continuum Mechanics*, Springer, 2008
- [22] Blair Scott G. W., Hening, J. C., Wagstaff A.: The Flow of Cream through Narrow Glass Tubes, *Journal of Physical Chemistry* (1939) 43 (7) 853-864
- [23] Hohl Dawn: Controlling Off-Contact", 1997, *Specialty Graphic Imaging Association Journal*, Vol. 4, pp. 5-11
- [24] K-J Bathe, *Finite Element Procedures*, Prentice Hall, 1996
- [25] G. S. White, C. J. W. Breward, P. D. Howell, A Model for the Screen-Printing of Newtonian Fluids, *Journal of Engineering Mathematics*, 2006, 54, pp. 49-70
- [26] C. O. Morariu et al.: A New Method for Determining the Reliability Testing Period Using Weibull Distribution, *Acta Polytechnica Hungarica*, 2013, 10/7, pp. 171-186
- [27] János Kundrák, Zoltán Pálmai: Application of General Tool-life Function under Changing Cutting Conditions, *Acta Polytechnica Hungarica*, 2014, 11/2, pp. 61-76

Stability of the Robotic System with Time Delay in Open Kinematic Chain Configuration

Ivan Buzurovic

Division of Medical Physics and Biophysics, Harvard Medical School, 75 Francis Street, ASB1, L2, Boston, MA 02115, USA;
ibuzurovic@lroc.harvard.edu

Dragutin Lj. Debeljkovic

Department of Control Engineering, School of Mechanical Engineering, University of Belgrade, Kraljice Marije 16, 11120 Belgrade, Serbia;
ddebeljkovic@mas.bg.ac.rs33

Vladimir Mistic

Division of Medical Physics, University of Pittsburgh Medical Center, 200 Lothrop St, Pittsburgh, PA 15213, USA; misticv@upmc.edu

Goran Simeunovic

Innovation Center, School of Mechanical Engineering, University of Belgrade, Kraljice Marije 16, 11120 Belgrade, Serbia; gsimeunovic@mas.bg.ac.rs

Abstract: In this article, stability of the robotic manipulator with time delay in open kinematic chain configuration was analyzed. The dynamic equations of motions were derived for one five-degree-of-freedom (DOF) robotic system with system latency. The mathematical model includes the model of the actuators to define the parameters of the actuators that can stabilize such a system. Investigation of the system stability was performed using novel stability conditions. The system state responses and the system stability were analyzed for different time delays. The proposed control methodology was shown to be appropriate to maintain the stability of the robotic system during tracking tasks. To analyze the concept, we presented a numerical example together with an extensive system simulation. The stability analysis showed the full compliance of the system behavior with the desired system dynamics. The proposed method can be used for the stability analysis of any robotic system with state delays in the open kinematic chain configuration.

Keywords: stability; stability conditions; robotic systems; time delay

1 Introduction

Time delay plays an important role in the dynamics of robotic systems in some applications. For instance, accurate tracking might be challenging if time delay exists. The fact is especially pronounced in the medical, even in some industrial, applications where high accuracy and positioning are strictly demanded. Furthermore, in repeatable motions, time delay might influence the phase shifting, and consequently, increases the errors. In some cases, the system instability might appear as an unwanted consequence of neglecting the time delay of systems.

The influence of time delay on robotic systems was previously analyzed in literature [2, 3, 6, 10, 17-20, 22, 24, 25, and 35]. Different types of latencies have been analyzed in conjunction with system stability, such as mechanical latency, signal processing (transmission) latency, communication latency etc. Signal transmission latency was shown to be able to affect the robotic effective force-reflecting system, [24]. A large group of teleoperation robotic systems is affected by time delay due to communication drifts. The overview of telemanipulators with constant transmission time delay and control challenges was presented in [25]. The instability of the systems can often be caused by time delay. Many control strategies have been reported to solve this problem [4, 6, 17-18, 22, 24-25, 30, 35]. A control strategy for a robotic system where instability was caused by time delay was proposed to overcome instability, [2]. An adaptive tracking controller was introduced to solve the instability problem. A study [17] showed the advantages of the compliant control over the force feedback control for one six-DOF robotic system within the wide range of time delay. The stability analysis for multiple manipulators capable of sensing latency was analyzed in [22]. Some robotic manipulators use video feedback [18], and the delay appears in the image processing module. In these situations, the discrete time modeling [6], adaptive motion and force control [35] can be used to overcome the suboptimal results in operations. In some cases, the existing time delay can be neglected in the analysis, as in [30]. However, a broader approach, such as the robust control, was used for tracking control. Consequently, the latency problem does not need to be analyzed separately; it should rather be analyzed within a more general set of uncertainties which acts on the systems [4].

The initial approach presented in [2, 3, 6, 17-20, 22, 24, 25, and 35] took the system delay into account, which potentially could destabilize the system and degrade the performances. The group of stability criteria that take time delay into account for investigations is named delay-dependent conditions [40]. Different control methodologies were developed based on the delay-dependent criteria. The latest research results on this topic are presented in the sequel. In [8, 9], robust tracking tasks for robotic manipulators were performed using a gradient estimator and an adaptive compensator, respectively. The system trajectory control i.e. tracking task in [27, 28] was performed using time delayed control which was proven to be robust against nonlinearities in the robotic dynamic system. Tracking

of industrial robotic systems with time delay was analyzed in [12-14] from different aspects. The control methodology included the time delay estimation to decrease nonlinearities, velocity feedback, and sliding mode control to converge time delay errors. Another sliding mode controller together with the impedance control was used in [33] for position tracking. Uncertain disturbances and time delay can pose a problem in the modeling of robotic systems [11]; the linearization procedure and application of the linear matrix inequalities were found suitable in this case. A teleoperated mobile robot with latency was presented in [29] where the usage of a sensor was recommended as a solution for the fulfillment of the desired tasks, similar to [26].

An overview of the stability problems, when the time delay is present in the systems, is analyzed in [41]. Another theoretic approach to the asymptotic stability for robotic systems with time delay was proposed in [1]. It was noticed that the stability of systems with time delay is often related to complicated numerical calculations that can make the stability criteria inapplicable. The numerical calculations of the system stability under the influence of latency were analyzed in [42]. In some articles, this approach was solved using delay-independent criteria [40]. The method avoided using complicated computations of the inverse system dynamics; a time delay estimation was used to obtain the adequate dynamics and local disturbances. The trajectory tracking problem for the analyzed class of robotic systems was solved using a neural network controller, as described in [31].

In this article, it is of interest to analyze trajectory tracking problems. The article [21] analyzed the control of a space robotic system with time delay to track the desired trajectory in the inertial space with several uncontrolled variables, such as the position of the base and vertical coordinates. The nonlinear feedback control law was applied. A discrete time control of a mobile robot with transport latency was suggested in [32], instead of the continuous time control strategy. A tracking control algorithm for an industrial six-DOF robot was proposed in [23]. The maximum value of time delay was estimated to maintain the desired tracking performances. Some of the latest classical and new theoretical results that include the control of robots, application, servos, and actuators are presented in [34], [36-39].

In this article, we analyzed the stability of a five-DOF robotic system with time delay. An extensive computer simulation was presented for the evaluation of the system behavior. In order to be able to perform a high precision contour tracking, we modeled the system with latency. Moreover, it was requested that the system end-effector should be in the repeatable desired positions in the equidistant time interval. Consequently, latency in the mechanical part of the system or in signal processing can significantly influence the fulfillment of the desired tasks.

Due to the specified requirements, the innovative modeling procedure that includes the mathematical modeling of both the robotic systems and the actuators was derived. The time delay was incorporated in the generalized coordinates. The

novel stability conditions were presented to investigate the stability of the robotic system. Furthermore, the calculation of the control gains was proposed in the article. This method can be used for the stabilization of this class of systems, irrespective of the number of joints within the manipulators, as long as they are in the open kinematic chain configuration. To evaluate the efficacy of the novel controller, we compared it to a classical proportional-integral-derivative (PID) controller and investigated the stability with respect to the time delay.

2 Mathematical Framework

The second section describes the mathematical modeling procedure for a robotic system with time delay, which is used for the simulation. The detailed modeling procedure for the system without latency and time delay stability conditions can be found in [5, 7].

2.1 Preliminaries

A general representation of the nonlinear control systems with time delay can be written as:

$$\begin{aligned}\dot{\mathbf{x}}(t) &= \mathbf{f}(t, \mathbf{x}(t), \mathbf{x}(t-\tau), \mathbf{u}(t)), \quad t \geq 0 \\ \mathbf{x}(t) &= \boldsymbol{\varphi}(t), \quad -\tau \leq t \leq 0\end{aligned}\tag{1}$$

where $\mathbf{x}(t) \in \mathfrak{R}^n$ is a state-space vector, $\mathbf{u}(t) \in \mathfrak{R}^m$ is a control law vector, $\boldsymbol{\varphi} \in \mathfrak{N}([-\tau, 0], \mathfrak{R}^n)$ is an admissible functional of the initial states, $\mathfrak{N} = \mathfrak{N}([-\tau, 0], \mathfrak{R}^n)$ is the continuous state-space function which maps interval $[-\tau, 0]$ to \mathfrak{R}^n , where \mathfrak{R} is a real vector space. Vector function \mathbf{f} satisfies the following condition:

$$\mathbf{f} : \mathfrak{T} \times \mathfrak{R}^n \times \mathfrak{R}^n \times \mathfrak{R}^m \rightarrow \mathfrak{R}^n.\tag{2}$$

Function \mathbf{f} is assumed to be smooth to guarantee the existence and uniqueness of the solutions on time interval defines as

$$\mathfrak{T} = [t_0, (t_0 + \tau)] \in \mathfrak{R}_+.\tag{3}$$

Quantity τ can be a positive real number or $+\infty$. The initial state of the function $\mathbf{f} = (t, \mathbf{0}, \mathbf{0})$ does not need to be equal to 0, which means that the origin does not need to be identical as an equilibrium state.

2.2 Mathematical Modeling

Fig. 1 represents a kinematic structure of the 5 DOF robotic system analyzed in this article. As shown in Fig. 1, generalized coordinates $(q_1, q_2, q_3, q_4, q_5)$ were adopted to characterize the motion of the individual joints. A stationary coordinate frame was denoted as O_0 , and the coordinate frames of the joints were marked as $O_i, i = 1, \dots, 5$. $D_i, i = 1, \dots, 5$, denote distances between the origins O_i . The coordinate systems were marked as $x_i, y_i, z_i, i = 0, 1, \dots, 5$.

With the use of the energy-based Lagrange-Euler approach, the dynamic equation of the motion can be written as

$$\sum_{\alpha=1}^n a_{\alpha\gamma}(q)\ddot{q}^\alpha + \sum_{\alpha=1}^n \sum_{\beta=1}^n \Gamma_{\alpha\beta,\gamma}(q)\dot{q}^\alpha \dot{q}^\beta = Q_\gamma^g + Q_\gamma^u, \tag{4}$$

where $\gamma = 1, \dots, 5$. $a_{\alpha\gamma}(q)$ represents the tensor coefficients, $\Gamma_{\alpha\beta,\gamma}(q)$ denotes the matrix coefficients, Q^g and Q^u are the major components of the generalized torque. Q^g represents the gravitation forces, and Q^u corresponds to the generalized torque, produced by the actuators.

A mathematical description of the actuators, Fig. 2, is given as in equation (5).

$$N_V N_m J_M \ddot{\theta} + F \dot{\theta} + M = C_n N_m I_R, \tag{5}$$

where θ is the rotation angle, M is the output torque of the actuator, equal to the sum of Q^g and Q^u . I_R is the current of the rotor, L_R is the inductance of the actuator, and U is the voltage of the actuator.

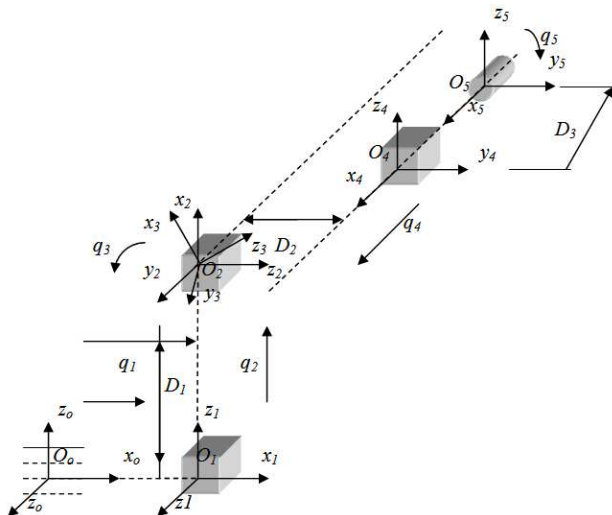


Figure 1

Model of the robotic system containing three translational and two rotational joints

The coefficient in equation (5) is denoted as follows: N_V is the reduction coefficient (ratio of the output velocity and input rotational velocity); N_m is the torque reduction coefficient (ratio of the input and output torques); J_M is the torque coefficient; F is the motor friction coefficient; C_n is the mechanical constant of the motor; R_R is the rotor circuit resistance; and C_E is the counter-electromotive force coefficient.

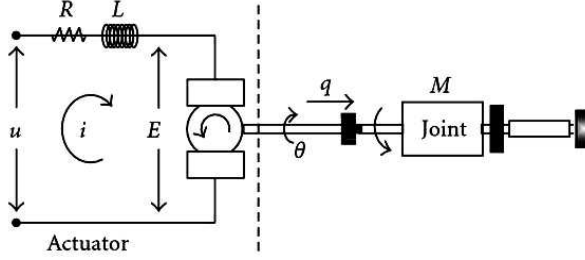


Figure 2

Schema of an actuator. Robotic joints are governed by the presented actuator.

Without the loss of any precession, it can be assumed that the inductance is $L_R \approx 0$. If the state-space vector for the motors is adopted as $x = (\theta, \dot{\theta}, I_R)^T$, it can be concluded that the order of the mathematical model of the actuators is equal to two. Consequently, the state-space equation of each actuator is as follows

$$\dot{x}_i = A_i x_i + B_i u_i + d_i M_i \quad (6)$$

where A_i , b_i and d_i are the matrices defined as:

$$A_i = \begin{bmatrix} 0 & 1 \\ 1 & -\frac{1}{J_M} \left(\frac{F_i}{N_V N_M} + \frac{C_M C_E}{R_R} \right) \end{bmatrix}, b_i = \begin{bmatrix} 0 \\ \frac{C_M}{N_V J_M R_R} \end{bmatrix}, d_i = \begin{bmatrix} 0 \\ -\frac{1}{N_V J_M N_m} \end{bmatrix} \quad (7)$$

The correlation between the robotic system and the actuator is established via generalized coordinates and torques in the following way: $\theta_i = t_i q_i$, where t_i is a transfer coefficient vector for the individual joint i . The generalized torques on the actuators are defined as $M_i = \tau_{geni}$. A matrix representation of the coefficient is $T = \text{diag}(T_i)$, $T_i = (0 \ t_i)$. Equation (4) can now be written as follows,

$$H(q)\ddot{q} + h(q, \dot{q}) = \tau_{gen} \quad (8)$$

In equation (8), H represents an inertia matrix; h is a matrix that represents both the centrifugal and Coriolis effects, as well as the gravity. The relation between the state space vector and the generalized coordinates is adopted as $\mathbf{x} = T^{-1} \dot{q}_d$. The time delay joint variables are defined as:

$$\begin{aligned} q_d(t) &= q(t - \tau) \\ \dot{q}_d(t) &= \dot{q}(t - \tau) \end{aligned} \quad (9)$$

where τ is the system latency. When (4), (6) and (9) are combined with (8), the nonlinear dynamic equations of the robotic systems governed by the actuators can be written as:

$$\dot{\mathbf{x}} = A_n(\mathbf{x}) + B_n(\mathbf{x})\mathbf{u}, \quad (10)$$

where \mathbf{x} and \mathbf{u} are the state-space and control vectors, respectively. $\mathbf{x} = (q_1, q'_1, \dots, q_5, q'_5)$, and $\mathbf{u} = (U_1, \dots, U_5)$, where U_i is the voltage on each actuator. Nonlinear matrices A_n and B_n are calculated as:

$$\begin{aligned} A_n(\mathbf{x}) &= [A + F(I_n - H(\mathbf{x})TF)^{-1}H(\mathbf{x})TA]\mathbf{x} + \\ &F(I_n - H(\mathbf{x})TF)^{-1}h(\mathbf{x}), \end{aligned} \quad (11)$$

$$B_n(\mathbf{x}) = B + F(I_n - H(\mathbf{x})TF)^{-1}H(\mathbf{x})TB$$

where $A = \text{diag}(A_i)$, $B = \text{diag}(B_i)$, $F = \text{diag}(d_i)$. Equation (12) can be obtained through the derivation of equation (10) in the second order Taylor series around the nominal point. For derivation purposes, the deviation of the generalized coordinates due to time delay was expressed as $\Delta q_d(t) = q(t) - q(t - \tau)$.

$$\dot{\mathbf{x}}(t) = A_{L0}\mathbf{x}(t) + A_{L1}\mathbf{x}(t - \tau) + B_L\mathbf{u}(t) \quad (12)$$

where matrices $A_L = (A_{L0} \ A_{L1})^T$ and B_L have the following form:

$$\begin{aligned} A_L &= A + F(I_n - HTF)^{-1} \frac{\partial H}{\partial \mathbf{x}} TF(I_n - HTF)^{-1} [HTA\mathbf{x}_0 + HTB\mathbf{u}_0 + h] + \\ &F(I_n - HTF)^{-1} \left[\frac{\partial H}{\partial \mathbf{x}} (TA\mathbf{x}_0 + TB\mathbf{u}_0) + HTA + \frac{\partial h}{\partial \mathbf{x}} \right] \\ B_L &= B_n(\mathbf{x}_0, 0) \end{aligned} \quad (13)$$

3 Control Synthesis

In this part, the ability of the robotic system to guarantee the desired trajectory tracking within the strictly predefined time interval was investigated. Consequently, it was necessary to find the control law which will supply the actuator with appropriate control signals to perform the motion of the links according to the predefined trajectories within a specified time frame.

The analyzed latency includes latency in mechanical parts, signal processing latency and latency due to the unmeasured disturbances. The overall system latency affects the generalized coordinates and consequently, the system states.

The proposed control method deals with the latency of any source that can cause delay in the system states.

The objective of the control was to minimize the error Δq between the real generalized coordinates and the generalized coordinates (positions and velocities) under the influence of latency. The errors due to time delay can be presented as:

$$\begin{aligned}\Delta q_d(t) &= q(t) - q(t - \tau) \\ \Delta \dot{q}_d(t) &= \dot{q}(t) - \dot{q}(t - \tau) \\ \Delta \ddot{q}_d(t) &= \ddot{q}(t) - \ddot{q}(t - \tau)\end{aligned}\quad (14)$$

Equation (8) is rewritten as:

$$H(q)\ddot{q} + V(q, \dot{q})\dot{q} + G(q) = \mathfrak{I}.\quad (15)$$

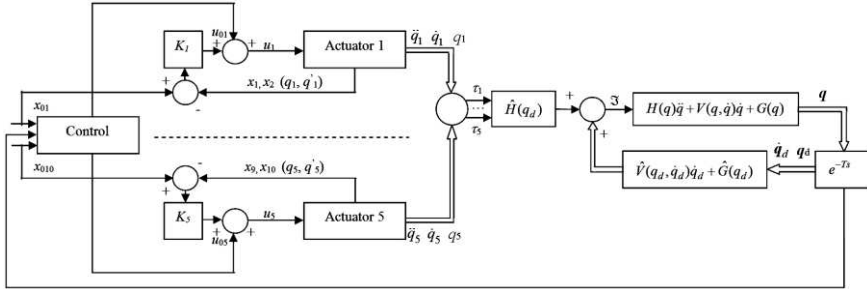


Figure 3

Control schema of the manipulator with time delay

Through the introduction of the estimated values of the system parameters, such as the estimated inertia matrix $\hat{H}(q)$, the estimated Coriolis and centrifugal matrix $\hat{V}(q, \dot{q})$, and the estimated gravitational vector $\hat{G}(q)$, the generalized form of equation (15) can be written as

$$\hat{H}(q)[\ddot{q} + K_v \Delta \dot{q} + K_p \Delta q] + \hat{V}(q, \dot{q})\dot{q} + \hat{G}(q) = \mathfrak{I},\quad (16)$$

where K_v and K_p are the derivative and proportional gain matrices. Including (14), the controller equation for the system with time delay can be written as

$$\hat{H}(q_d)[\ddot{q}_d + K_v \Delta \dot{q}_d + K_p \Delta q_d] + \hat{V}(q_d, \dot{q}_d)\dot{q}_d + \hat{G}(q_d) = \mathfrak{I}\quad (17)$$

The proposed control methodology guarantees the asymptotic reduction of errors introduced by time delay. A block diagram of the proposed approach was presented in Fig. 3.

The control law used in the described case can be expressed as

$$\mathbf{u} = -K\mathbf{C}\mathbf{x},\quad (18)$$

where C is the output system matrix and K is the gain matrix, $K = \text{diag}(K_p, K_v)$. The values of the proportional and derivative gains were calculated for each link according to the following formula:

$$\begin{aligned} K_p &< ((0.5\omega_0)^2 (H_{ii} + N_v N_m J_m) R_R) / N_m C_M \\ K_v &= 2(K_p (H_{ii} + N_v N_m J_m) R_R - F R_R)^{1/2} / N_m C_M - N_v C_E \end{aligned} \quad (19)$$

By recalculating the control law for trajectory tracking with respect to the actuators and using equation (6), one can obtain:

$$\mathbf{u}(t) = (\dot{\mathbf{x}}_v(t) - A_i \mathbf{x}_v(t) - d_i \tau_{gen}(t)) B_i^{-1}, \quad (20)$$

where \mathbf{x}_v denotes the velocity components of the state values, with matrices defined as in (6).

4 Stability Analysis

In this part, a brief stability analysis for such systems is presented. To evaluate the stability of the system described here, we performed an evaluation using a novel approach. System (12) in the free working regime was analyzed

$$\dot{\mathbf{x}}(t) = A_{L0} \mathbf{x}(t) + A_{L1} \mathbf{x}(t - \tau), \quad (21)$$

with an initial vector function as

$$\mathbf{x}(t) = \boldsymbol{\varphi}_x(t), \quad -\tau \leq t \leq 0. \quad (22)$$

While the analyzed class of the systems is kept in mind, the following definitions are presented. The theorem presented here was used to evaluate the stability of system (21).

Definition 1: System (21) is stable with respect to $\{\alpha, \beta, -\tau, T, \|\mathbf{x}\|\}$, $\alpha \leq \beta$ if for any trajectory $\mathbf{x}(t)$ condition $\|\mathbf{x}_0\| < \alpha$ implies $\|\mathbf{x}(t)\| < \beta$, $\forall t \in [-\Delta, T]$, $\Delta = \tau_{\max}$, [7].

Definition 2: Autonomous system (21) is contractively stable with respect to $\{\alpha, \beta, \gamma, T, \|\mathbf{x}\|\}$, $\gamma < \alpha < \beta$, if for any trajectory $\mathbf{x}(t)$ with condition $\|\mathbf{x}_0\| < \alpha$, implies:

(i) stability with respect to $\{\alpha, \beta, -\tau, T, \|\mathbf{x}\|\}$,

(ii) there exists $t^* \in]0, T[$ such that $\|\mathbf{x}(t)\| < \gamma$, for all $\forall t \in]t^*, T[$, [7].

Definition 3: System (21) satisfying initial condition (22) is finite time stable with respect to $\{\zeta(t), \beta, \mathfrak{T}\}$ if and only if $\boldsymbol{\varphi}_x(t) < \zeta(t)$, implies $\|\mathbf{x}(t)\| < \beta$, $t \in \mathfrak{R}$, $\zeta(t)$ is a scalar function with the property $0 < \zeta(t) \leq \alpha$, $-\tau \leq t \leq 0$, where α is a real positive number and $\beta \in \mathfrak{R}_+$ and $\beta > \alpha$, [7].

Theorem 1: Suppose that the matrix defined as $\Pi = (A_{L0}^T + A_{L0} + A_{Ll}^T A_{Ll} + I)$ is positive definite. Then the autonomous system (21) with initial function (22) is finite time stable with respect to $\{\alpha, \beta, \tau, \mathfrak{I}\}$, if $\alpha < \beta$, such that the following condition holds

$$(1 + \tau)e^{\lambda_{\max}(\Pi)\tau} < \beta / \alpha, \quad \forall t \in \mathfrak{I}, \quad (23)$$

where λ_{\max} is the maximum eigenvalue of the specific matrix, and \mathfrak{I} is a finite time interval.

Proof: Let us consider the following Lyapunov-like, aggregation function:

$$V(\mathbf{x}(t)) = \mathbf{x}^T(t)\mathbf{x}(t) + \int_{t-\tau}^t \mathbf{x}^T(\vartheta)\mathbf{x}(\vartheta)d\vartheta, \quad (24)$$

Denote by $\dot{V}(\mathbf{x}(t))$ time derivative of $V(\mathbf{x}(t))$ along the trajectory of system (21), so one can obtain:

$$\begin{aligned} \dot{V}(\mathbf{x}(t)) &= \dot{\mathbf{x}}^T(t)\mathbf{x}(t) + \mathbf{x}^T(t)\dot{\mathbf{x}}(t) + \frac{d}{dt} \int_{t-\tau}^t \mathbf{x}^T(\vartheta)\mathbf{x}(\vartheta)d\vartheta \\ &= \mathbf{x}^T(t)(A_0^T + A_0)\mathbf{x}(t) + 2\mathbf{x}^T(t)A_1\mathbf{x}(t-\tau) \\ &\quad + \mathbf{x}^T(t)\mathbf{x}(t) - \mathbf{x}^T(t-\tau)\mathbf{x}(t-\tau) \end{aligned} \quad (25)$$

Based on the known inequality¹, and with the particular choice:

$$\mathbf{x}^T(t)\Gamma\mathbf{x}(t) = \mathbf{x}^T(t)I\mathbf{x}(t) > 0, \quad \forall \mathbf{x}(t) \in \mathcal{S}_\beta, \quad (26)$$

so that:

$$\begin{aligned} \dot{V}(\mathbf{x}(t)) &\leq \mathbf{x}^T(t)(A_0^T + A_0 + A_1A_1^T + I)\mathbf{x}(t) \\ &\leq \mathbf{x}^T(t)\Pi\mathbf{x}(t), \\ &\leq \lambda_{\max}(\Pi)\mathbf{x}^T\mathbf{x}(t) \end{aligned} \quad (27)$$

under the assumption given in *Theorem 1*. Moreover, it can be calculated:

$$\begin{aligned} \dot{V}(\mathbf{x}(t)) &< \lambda_{\max}(\Pi)\mathbf{x}^T\mathbf{x}(t) + \lambda_{\max}(\Pi) \int_{t-\tau}^t \mathbf{x}^T(\vartheta)\mathbf{x}(\vartheta)d\vartheta \\ &< \lambda_{\max}(\Pi) \left(\mathbf{x}^T\mathbf{x}(t) + \int_{t-\tau}^t \mathbf{x}^T(\vartheta)\mathbf{x}(\vartheta)d\vartheta \right) < \lambda_{\max}(\Pi)V(\mathbf{x}(t)) \end{aligned} \quad (28)$$

since $\int_{t-\tau}^t \mathbf{x}^T(\vartheta)\mathbf{x}(\vartheta)d\vartheta > 0$ and $\lambda_{\max}(\Pi) > 0$.

¹ $2\mathbf{u}^T(t)\mathbf{v}(t-\tau) \leq \mathbf{u}^T(t)\Gamma^{-1}\mathbf{u}(t) + \mathbf{v}^T(t-\tau)\Gamma\mathbf{v}(t-\tau)$, $\Gamma > 0$

Multiplying (28) with $e^{-\lambda_{\max}(\Pi)t}$, one can obtain:

$$\frac{d}{dt} \left(e^{-\lambda_{\max}(\Pi)t} V(\mathbf{x}(t)) \right) < 0. \quad (29)$$

Integrating (29) from 0 to t , with $t \in \mathfrak{T}$, we have:

$$V(\mathbf{x}(t)) < e^{\lambda_{\max}(\Pi)t} \cdot V(0). \quad (30)$$

From (24), it can be seen:

$$\begin{aligned} V(0) = \mathbf{x}^T(0)\mathbf{x}(0) + \int_{-\tau}^0 \boldsymbol{\varphi}^T(0)\boldsymbol{\varphi}(0)d\vartheta \leq \mathbf{x}^T(0)\mathbf{x}(0) + \\ \boldsymbol{\varphi}^T(0)\boldsymbol{\varphi}(0) \int_{-\tau}^0 d\vartheta \leq \alpha + \alpha \cdot \tau = \alpha(1+\tau) \end{aligned} \quad (31)$$

Combining (30) and (31) leads to:

$$V(\mathbf{x}(t)) < \alpha(1+\tau) \cdot e^{\lambda_{\max}(\Pi)t} \quad (32)$$

On the other hand:

$$\mathbf{x}^T(t)\mathbf{x}(t) < \mathbf{x}^T(t)\mathbf{x}(t) + \int_{t-\tau}^t \mathbf{x}^T(\vartheta)\mathbf{x}(\vartheta)d\vartheta = V(\mathbf{x}(t)) < \alpha(1+\tau) \cdot e^{\lambda_{\max}(\Pi)t}, \quad (33)$$

Condition (24) and the above inequality imply:

$$\mathbf{x}^T(t)\mathbf{x}(t) < \alpha(1+\tau) \cdot e^{\lambda_{\max}(\Pi)t} < \beta, \quad \forall t \in \mathfrak{T}, \quad (34)$$

which was to be proven.

5 Numerical Example and Simulation

For the purpose of the simulations of such systems, the desired trajectory in the Cartesian space was defined as in Fig. 4.

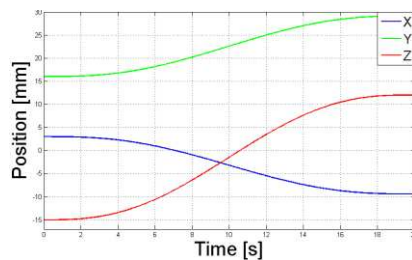


Figure 4

Tracking (desired) trajectories in the Cartesian space

It was requested that the coordinates of the absolute end-effector should follow the predefined trajectories within a time frame of 20 s and should maintain the stability in the interval.

Due to the described task, it is necessary to investigate the finite time stability of the time delay system.

Table 1
Geometric characteristics of the system and masses

Value/Joint	1	2	3	4	5
m (kg)	0.2	0.2	0.5	0.1	0.01
\bar{p}_{ii} (m)	(-0.2 0 0) ^T	(0 0.18 0) ^T	(0 0 -0.17) ^T	(0 0 -0.165) ^T	(0 0 -0.2) ^T
\bar{p}_i (m)	(0.1 0 0) ^T	(0 -0.09 0) ^T	(0 0 0.1) ^T	(0 0 0.1) ^T	(0 0 0.1) ^T
\bar{e}_i	(1 0 0) ^T	(0 1 0) ^T	(1 0 0) ^T	(0 0 1) ^T	(0 0 1) ^T

Table 2
Numerical values of the parameters of the actuators

Value/Joint	1	2	3	4	5
R_r	8.40	8.40	84.30	2.10	16
J	6.50E-06	6.50E-06	5.40E-07	6.50E-06	9.00E-09
N_v	473	473	247	994	2100
C_m	2.02E+04	2.02E+04	74200	9800	2000
C_e	2.12E-03	2.12E-03	4.04E-04	4.04E-04	3.00E-03
N_m	115	115	111	111	870

In relation to Figure 1, the geometric characteristics of the system and the mass of the joints are presented in Table 1.

Table 3
Elements of the matrices

Actuator	a_{22}	b_2	d_2
1	-7.825e+05	7.822e+05	1.610e-02
2	-7.825e+05	7.822e+05	1.610e-02
3	-6.593e+04	6.588e+04	1.009e-01
4	-2.901e+05	7.371e+05	1.612e-02
5	-4.167e+07	6.614e+06	2.646e+01

Table 2 represents the numerical values of the parameters described in equation (5) and Figure 2.

The variables described in equation (6) which were used to determine control gains (19) are presented in Table 3. The coefficients a_{22} , b_2 , and d_2 are the diagonal elements of the matrices (7).

K is the diagonal matrix and their elements are the position and velocity gains, $K = \text{diag}\{K_p, K_v\}$. The gain values for each segment can be calculated using equation (19) and the values in Table 2.

Table 4
Gain elements

Joint	K_p	K_v
1	1.306E-02	1.164E+03
2	1.306E-02	1.164E+03
3	3.690E-01	7.461E+03
4	6.999E-03	2.143E+02
5	1.839E+00	2.488E+03

The detailed explanations for this procedure can be found in [18]. Using the control law (29), (4) and (30), it is possible to calculate the eigenvalues of system (5). The control gains are presented in Table 4.

Fig. 5 represents q_i , $i=(1,2,\dots,5)$ trajectories in the joint space. The values on the y axis are in mm for joints 1, 2, and 4, and in rad/s for joints 3 and 5. The initial condition (22) transformed to the initial generalized coordinates in the joint space can be described as $\mathbf{q}_0=[0 \ -17 \ 0 \ 1 \ 0]^T$, as in Fig. 5. At this point, it is of interest to investigate the influence of time delay on the system stability.

For that purpose, the comparison between the two control strategies applied for system (12) was performed. The first one includes the classical approach using a PID controller. The second one includes the proposed methodology, as in (18) and Fig. 3. The comparison was presented in Fig. 6 and Fig. 7. The figures represent the step and sinusoidal responses of the system.

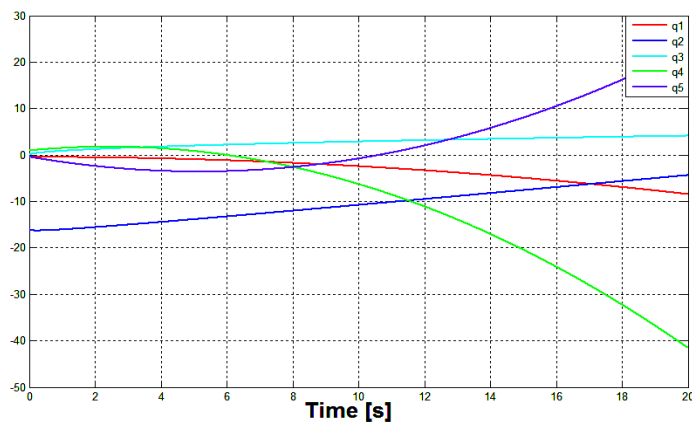


Figure 5
Generalized trajectories in the joint space

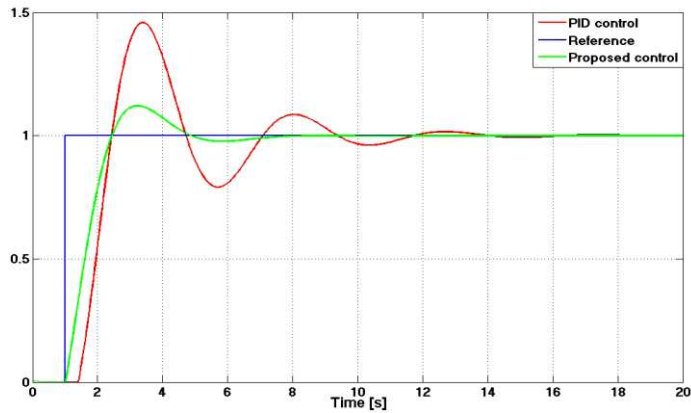


Figure 6

Step responses of the system for both PID and proposed control methodology vs. reference input signal

It was observed that the time delay had a significant influence on the dynamic behavior of system (12) when the PID controller was used. However, the proposed methodology in this article solved the latency problem of the system output, as shown in Figs. 6-7.

In the sequel, the stability of the robotic system represented by equation (21) with initial vector function (22) graphically presented in Fig. 4 was investigated. For the numerical stability analysis, *Theorem 1* was used.

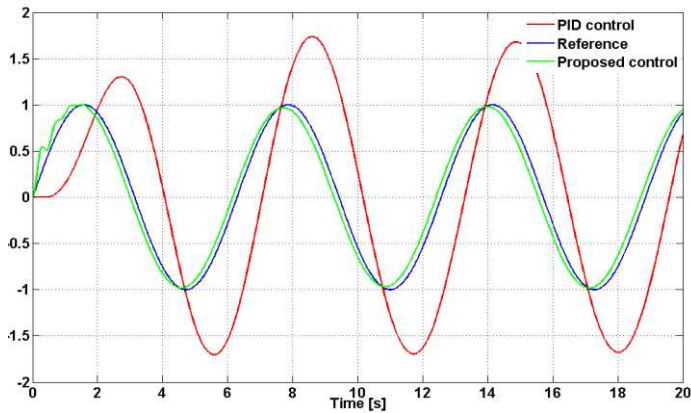


Figure 7

Sinusoidal responses of the system for both PID and proposed control methodology vs. reference input signal

The numerical values of matrices A_{L0} and A_{L1} are as follows, as in (35-36):

$$A_{L0} = \begin{bmatrix} 0 & 1 & 0 & 0 & 0 & 0 & 0 & 0 & 0 & 0 \\ 0 & -3.9e6 & 0 & 0 & 0 & 0 & 0 & 0 & 0 & 0 \\ 0 & 0 & 0 & 1 & 0 & 0 & 0 & 0 & 0 & 0 \\ 0 & 0 & 0 & -3.9e6 & 8.42 & -26.92 & -1.5e-4 & 0 & 0 & 0 \\ 0 & 0 & 0 & 0 & 0 & 1 & 0 & 0 & 0 & 0 \\ 0 & 0 & 0 & -3.27e3 & 2.8e-2 & -4.6e4 & -0.24 & 0 & 0 & 0 \\ 0 & 0 & 0 & 0 & 0 & 0 & 0 & 1 & 0 & 0 \\ 0 & 0 & 0 & 0 & -4.1e-2 & 0 & 4.4e-3 & -2.9e5 & 0 & 0 \\ 0 & 0 & 0 & 0 & 0 & 0 & 0 & 0 & 0 & 1 \\ 0 & 0 & 0 & 0 & 0 & 0 & 0 & 0 & 0 & -4.2e6 \end{bmatrix}, \quad (35)$$

$$A_{L1} = \begin{bmatrix} 0 & 1 & 0 & 0 & 0 & 0 & 0 & 0 & 0 & 0 \\ 0 & -2.33e5 & 0 & 0 & 0 & 0 & 0 & 0 & 0 & 0 \\ 0 & 0 & 0 & 1 & 0 & 0 & 0 & 0 & 0 & 0 \\ 0 & 0 & 0 & -2.3e3 & 8.42 & -4.28 & -1.5e-3 & 0 & 0 & 0 \\ 0 & 0 & 0 & 0 & 0 & 1 & 0 & 0 & 0 & 0 \\ 0 & 0 & 0 & -3.3e4 & 0.18e-1 & -4.6e4 & -0.32 & 0 & 0 & 0 \\ 0 & 0 & 0 & 0 & 0 & 0 & 0 & 1 & 0 & 0 \\ 0 & 0 & 0 & 0 & -0.44e-1 & 0 & 2.4e-2 & -2.3e4 & 0 & 0 \\ 0 & 0 & 0 & 0 & 0 & 0 & 0 & 0 & 0 & 1 \\ 0 & 0 & 0 & 0 & 0 & 0 & 0 & 0 & 0 & -3.2e5 \end{bmatrix}. \quad (36)$$

System matrices A_{L0} and A_{L1} were calculated for the system with feedback, as in Fig. 3. For this example, the following was adopted: $\alpha = 2.5$, $\beta = 3$, and $\tau = 200$ ms. With the use of equation $\Pi = (A_{L0}^T + A_{L0} + A_{L1}^T A_{L1} + I)$, it was calculated that matrix Π is a positive definite matrix, i.e. $\Pi > 0$. The eigenvalues of the matrix were denoted as $\sigma(\Pi) = \{\lambda_1, \dots, \lambda_{10}\}$.

The eigenvalues of the system were calculated using equation (37)

$$\det(A_L - KC - sE) = K \prod_{j=1}^N (s_j^0 - s) = \det\left(\left(A_{0L} + A_{1L}e^{-s\tau}\right) - CK - sE\right) = \det\left(\left(A_{0L} + \bar{A}_{1L}\right) - CK - sE\right) \quad (37)$$

where $A_L = (A_{0L} + \bar{A}_{1L})$ is a decomposition of matrix A^L . After calculation, it was obtained: $\sigma(\Pi) = \{8.3, 2.8e5, 7.2e5, 1.2, 6.4e5, 1245, 12,4, 2.4e5, 4234, 4.1e6\}$.

It can be seen that $\lambda_{\max}(\Pi) = 4.1e7$. Now it is possible to calculate condition (23) and to estimate T_{est} - time after the system is stable under the influence of control feedback. $(1 + \tau)e^{\lambda_{\max}(\Pi)\tau} = (1 + 0.2)e^{4.1e7 \cdot 0.2} < 1.2$. For this specific case, it was calculated that system (21) with control feedback (20) would obtain and maintain stability after $T_{\text{est}} = 3.9e-8$.

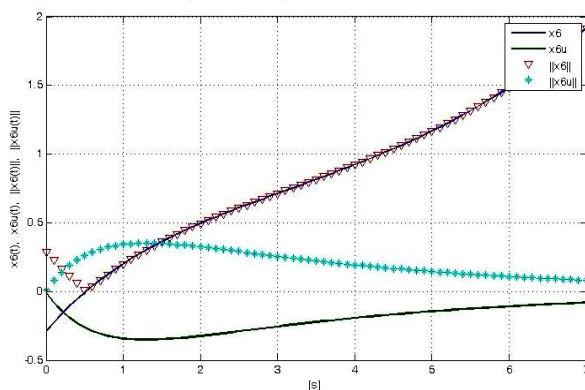


Figure 8

Trajectory and square norms of the representative state trajectory for the controlled and uncontrolled system

Fig. 8 represents the result graphically. The figure shows the trajectory and norm of the trajectory for controlled and uncontrolled systems. The norm of the representative state trajectory was presented to depict its convergence to the stable zero state during the time interval of interest.

Conclusions

In this article, a mathematical modeling procedure of the robotic system with time delay was presented. This procedure includes the mathematical model of the actuators, and it can be used for any robotic system in the open kinematic configuration. The time delay was included in the mathematical model. A time delay controller capable of system stabilization under the influence of the time delay was developed. The novel stability conditions were derived for the investigation of the stability of the system. These conditions were used to evaluate the proposed controller under the influence of system latency. The comparative results for both the PID and the time delay controller were presented. The proposed control methodology resulted in a stable dynamic behavior of the system. It was observed that the proposed controller could nullify the latency presented in each link. Consequently, the time delay did not influence the overall system performances. The performance investigation of the system using novel stability conditions showed the full compliance of the system behavior with the desired system dynamics. The future work of this study will include further rigorous dynamic analyses and the influence of the specific value of time delay on the system, and it will also define the stability boundaries for such a system.

References

- [1] Ailon A.: Asymptotic Stability in Flexible-Joint Robots with Multiple Time Delays, Proc. of the IEEE Conference on Decision and Control (CDC), 2003, pp. 4375-4380

-
- [2] Anderson R. J., Spong M. W.: Asymptotic Stability for Force Reflecting Teleoperators with Time Delay, *International Journal of Robotics Research* Vol. 11, No. 2, 1992, pp. 135-149
- [3] Llama M. A., Santibanez V., Flores J.: A Passivity-based Stability Analysis for a Fuzzy PD+ Control for Robot Manipulators, *Proc. of 18th IEEE International Conference of the North American*, New York, NY, USA June, 1999, pp. 665-669
- [4] Buzurovic I. M., Debeljkovic D. Lj.: Robust Control for Parallel Robotic Platforms, *Proc. of 16th IEEE International Symposium on Intelligent Systems and Informatics (INES)*, Lisbon, Portugal, 2012, pp. 45-50
- [5] Buzurovic I., Podder T. K., Yu Y.: Force Prediction and Tracking for Image-guided Robotic System using Neural Network Approach: *IEEE Biomedical Circuits and Systems Conference (BioCAS)*, Baltimore, MA, USA, November, 2008, 41-44
- [6] Debeljkovic D. Lj., Buzurovic I. M., Nestorovic T., Popov D.: A New Approach to the Stability of Discrete Descriptor Time Delay Systems in the Sense of Non-Lyapunov Delay Independent Conditions, *Proc. of 24th IEEE Chinese Control and Decision Conference (CCDC)*, Taiyuan, China, May 23-25, 2012, pp. 1155-1160
- [7] Debeljkovic D. Lj., Buzurovic I. M., Simeunovic G. V., Mistic M.: Asymptotic Practical Stability of Time Delay Systems, *Proc. of 10th IEEE International Symposium on Intelligent Systems and Informatics (SISY)*, Subotica, Serbia, September 20-22, 2012, pp. 379-384
- [8] Han D. K., Chang P. H., Jin M.: Robust Trajectory Control of Robot Manipulators using Time Delay Control with Adaptive Compensator, *IFAC Proc. Vol.*, 2008, pp. 2276-2281
- [9] Han D. K., Chang P.: Robust Tracking of Robot Manipulator with Nonlinear Friction using Time Delay Control with Gradient Estimator, *Journal of Mechanical Science and Technology*, Vol. 24, No. 8, 2010, pp. 1743-1752
- [10] Gu K., Chen J., Kharitonov V.: *Stability of Time-Delay Systems*, Springer-Verlag, Berlin, Heidelberg, New York, 2003
- [11] Jiang W.: Robust H_∞ Controller Design for Wheeled Mobile Robot with Time-Delay, *Proc. of International Conference on Intelligent Computation Technology and Automation (ICICTA)*, 2008, pp. 450-454
- [12] Jin M., Jin Y., Chang P. H., Choi C.: High-Accuracy Trajectory Tracking of Industrial Robot Manipulators using Time Delay Estimation and Terminal Sliding Mode, *IECON Proc. on Industrial Electronics Conference*, 2009, pp. 3095-3099

- [13] Jin M., Jin Y., Chang P. H., Choi C.: High-Accuracy Tracking Control of Robot Manipulators using Time Delay Estimation and Terminal Sliding Mode, *International Journal of Advanced Robotic Systems*, Vol. 8, No. 4, 2011, pp. 65-78
- [14] Jin M., Kang S. H., Chang P. H.: A Robust Compliant Motion Control of Robot with Certain Hard Nonlinearities using Time Delay Estimation, *IEEE International Symposium on Industrial Electronics*, 2006, pp. 311-316
- [15] Precup R. E., Doboli S., Preitl S.: Stability Analysis and Development of a Class of Fuzzy Control Systems, *Engineering Applications of Artificial Intelligence*, Vol. 13, No. 3, 2000, pp. 237-247
- [16] Zhang W., Cai X. S., Han Z. Z.: Robust Stability Criteria for Systems with Interval Time-Varying Delay and Nonlinear Perturbations, *Journal of Computational and Applied Mathematics*, Vol. 234, Vol. 1, 2010, pp. 174-180
- [17] Kim W. S., Hannaford B., Fejczy, A. K.: Force-Reflection and Shared Compliant Control in Operating Telemanipulators with Time Delay, *IEEE Transactions on Robotics and Automation*, Vol. 8, No. 2, 1992, 176-185
- [18] Koivo A. J., Houshangi N.: Real-Time Vision Feedback for Servoing Robotic Manipulator with Self-Tuning Controller, *IEEE Transactions on Systems, Man and Cybernetics*, Vol. 21, No. 1, 1991, pp. 134-142
- [19] Galambos P., Baranyi P.: Representing the Model of Impedance Controlled Robot Interaction with Feedback Delay in Polytopic LPV Form: TP Model Transformation based Approach, *Acta Polytechnica Hungarica*, Vol. 10, No. 1, 2013, pp. 139-157
- [20] Kuti J., Galambos P., Baranyi P.: Delay and Stiffness Dependent Polytopic LPV Modelling of Impedance Controlled Robot Interaction, in: *Issues and Challenges of Intelligent Systems and Computational Intelligence*, Springer International Publishing, 2014, pp. 163-174
- [21] Liang J., Chen L.: Improved Nonlinear Feedback Control for Free-Floating Space-based Robot with Time-Delay Based on Predictive and Approximation of Taylor Series, *Hangkong Xuebao/Acta Aeronautica et Astronautica Sinica*, Vol. 33, No. 1, 2012, pp. 163-169
- [22] Liu Y., Passino K. M., Polycarpou M. M.: Stability Analysis of M-Dimensional Asynchronous Swarms with a Fixed Communication Topology, *IEEE Transactions on Automatic Control*, Vol. 48, No. 1, 2003, pp. 76-95
- [23] Liu H., Zhang T.: Tracking Control of Industrial Robot Based on Time Delay Estimation and Robust H_∞ Control, *Huanan Ligong Daxue Xuebao/Journal of South China University of Technology (Natural Science)* Vol. 40, No. 1, 2012, pp. 77-81

-
- [24] Niemeyer G., Slotine J. E.: Stable Adaptive Teleoperation, IEEE Journal of Oceanic Engineering, Vol. 16, No. 1, 1991, pp. 152-162
- [25] Niemeyer G., Slotine J. E.: Telemanipulation with Time Delays, International Journal of Robotics Research, Vol. 23, No. 9, 2004, pp. 873-890
- [26] Ogaki F., Suzuki K.: Adaptive Teleoperation of a Mobile Robot under Communication Time Delay, Proc. of ROSE 2007 - International Workshop on Robotic and Sensor Environments, 2007, pp. 1-6
- [27] Park J., Cho B., Lee J.: Trajectory Control of Underwater Robot Using Time Delay Control, Transactions of the Korean Society of Mechanical Engineers, A, Vol. 32, No. 8, 2008, pp. 685-692
- [28] Park J., Cho B., Lee J.: Trajectory-Tracking Control of Underwater Inspection Robot for Nuclear Reactor Internals Using Time Delay Control, Nuclear Engineering and Design, Vol. 239, No. 11, 2009, pp. 2543-2550
- [29] Sanders D.: Analysis of the Effects of Time Delays on the Teleoperation of a Mobile Robot in Various Modes of Operation, Industrial Robot, Vol. 36, No. 6, 2009, pp. 570-584
- [30] Slotine J. E.: Robust Control of Robot Manipulators, International Journal of Robotics Research, Vol. 4, No. 2, 1985, pp. 49-64
- [31] Sree Krishna Chaitanya V., Srinivas Reddy M.: A Neural Network Controller for the Path Tracking Control of a Hopping Robot Involving Time Delays, International Journal of Neural Systems, Vol. 16, No. 1, 2006, pp. 47-62
- [32] Velasco-Villa M., Alvarez-Aguirre A., Rivera-Zago G.: Discrete-Time Control of an Omnidirectional Mobile Robot Subject to Transport Delay, Proc. of the American Control Conference, 2007, pp. 2171-2176
- [33] Zeng Q., Xu T., Xu J., Song A., Tian X.: Predictive Control for Force Telepresence Teleoperation Robot System with Time Delay, Dongnan Daxue Xuebao (Ziran Kexue Ban)/Journal of Southeast University (Natural Science Edition), Vol. 34, 2004, pp. 160-164
- [34] Juang J. G., Yu C. L., Lin C. M., Yeh R. G., Rudas I. J.: Real-Time Image Recognition and Path Tracking of a Wheeled Mobile Robot for Taking an Elevator, Acta Polytechnica Hungarica, Vol. 10, No. 6, 2013, pp. 5-23
- [35] Zhu W., Salcudean S. E.: Stability Guaranteed Teleoperation: an Adaptive Motion/Force Control Approach, IEEE Transactions on Automatic Control, Vol. 45, No. 11, 2000, pp. 1951-1969
- [36] Baranyi P., Yam Y.: TP Model Transformation Based Observer Design to 2-D Aeroelastic System, Acta Polytechnica Hungarica, Vol. 1, No. 2, 2004, pp. 63-78

- [37] Preitl S., Precup R. E., Fodor J., Bede B.: Iterative Feedback Tuning in Fuzzy Control Systems. Theory and Applications, Acta Polytechnica Hungarica, Vol. 3, No. 3, 2006, pp. 81-96
- [38] Petra M. I., DeSilva L. C.: Implementation of Folding Architecture Neural Networks into an FPGA for an Optimized Inverse Kinematics Solution of a Six-Legged Robot, International Journal of Artificial Intelligence, Vol. 10, No. S13, 2013, pp. 123-138
- [39] Triharminto H. H., Adji T. B., Setiawan N. A.: 3D Dynamic UAV Path Planning for Interception of Moving Target in Cluttered Environment, International Journal of Artificial Intelligence, Vol. 10, No. S13, 2013, pp. 154-163
- [40] Debeljkovic D. Lj., Nestorovic T., Buzurovic I. M., Dimitrijevic N. J.: A New Approach to the Stability of Time-Delay Systems in the Sense of Non-Lyapunov Delay-Independent and Delay-Dependent Criteria, Proc. of 8th IEEE International Symposium on Intelligent Systems and Informatics (SISY) Subotica, Serbia, September, 2010, pp. 213-218
- [41] Debeljkovic D. Lj., Buzurovic I. M.: Dynamics of Singular and Descriptive Time Delayed Control Systems: Stability, Robustness, Optimization, Stabilizability and Robustness Stabilizability, University of Belgrade, Serbia, ISBN: 978-86-7083-77, 2013
- [42] Buzurovic I., Debeljkovic D. Lj., Jovanovic A. M.: An Efficient Method for Finite Time Stability Calculation of Continuous Time Delay Systems, Proc. of IEEE Asian Control Conference (ASCC), Istanbul, Turkey, June, 2013, pp. 1-5

A Dynamic File Replication and Consistency Mechanism for Efficient Data Center Operation and its Formal Verification

Manu Vardhan, Dharmender Singh Kushwaha

Department of Computer Science and Engineering
Motilal Nehru National Institute of Technology Allahabad, India
{rcs1002, dsk}@mnnit.ac.in

Abstract: Data centers are built to provide a highly available and scalable infrastructure on which the applications run. As enterprises grow, so do their application need, along with resources required for additional application-specific services. This increase in bottom line expense heightens the overall resource requirement. This paper provides solution to mitigate the impact of these expenses by proposing a file replication and consistency maintenance mechanism that enhances the manageability, scalability, and high availability of resource in these environments. To keep files consistent, changes made at one replica of the file are reflected on other replicas in minimum possible time. File replica is updated on-demand by only propagating the required partial updates. The results show that as compared to Google File System (GFS), the proposed partial write rate shows an improvement of 38.62% while updating the stale replicas. Time required for invalidating the replicas decreases by 34.04% and the time required to update the replica on FRS reduces by 61.75%. Process algebraic approach has been used to establish the relationship between the formal aspect of the file replicating server and its architectural model.

Keywords: Cluster Computing; Consistency; File Replication; Process algebra

1 Introduction

Data centers are emerging and finding acceptability due to convergence of several trends including the high performance microprocessors, high speed network, standard tools and availability with economical commodity-off-the-shelf components. This comprises of several servers and networking infrastructure. The server portion of the infrastructure is now far down the road of commoditization, and low-cost servers have replaced the high-end enterprise-class servers. Driven by the PC commoditization economics, the operating theme is “scaling out instead of scaling up”. Thus, data centers seem to gain popularity day by day. Data center based distributed systems provide a cost-effective solution to applications intended for High Performance Computing (HPC) [1]. It leads to the evolution of power-

ful Computer Supported Cooperative Working (CSCW) [2] environment that enables improving availability of resources and load sharing.

Replication is a practical and effective method to achieve efficient file access, and increasing the file availability. File replication is done to achieve high availability of resources. It is achieved by replicating the file and redirecting the requests of busy nodes to lighter ones. Optimal performance is achieved by replicating the resource among different clusters. This helps in reducing file access latency, and network congestion in order to enable the system to handle more requests. Replication of files and replica placement demand an effective and optimized replication approach so that neither remote nor local file request is dropped. Replicating critical data serves as the basis for disaster recovery.

The proposed File Replication approach tries to resolve the following issues: (1) Prevent the creation of file replica if a copy of the requested file is available on the other node. (2) In case of node failure, file request is redirected to other FRS, without any user intervention. (3) Limit the number of queries for a particular file below the threshold. (4) New request for a particular file will never be served, once the threshold value for that particular file has been reached. (5) Avoids unnecessary file replication. (6) Maintains consistency of replicated files.

Every node has an optimal capability of handling file requests. If the file request count for a particular file on any FRS reaches the threshold value, it replicates the file on other FRS's. The location of new replica is intimated to the requesting node. This maximizes the resource utilization by minimizing the message exchanges overhead, thus increasing the overall system performance.

Replication becomes mandatory in cluster computing, whenever there is an increase in number of requests (that a system can handle), for a particular resource. Buyya [4], discusses the major performance issue in large-scale decentralized distributed systems, such as grids, along with mechanisms to minimize latency in the presence of resource performance fluctuations. Buyya [5] addresses the problem of transferring huge amount of data among federated systems, thus facilitating a better way to support critical applications while minimizing the total number of rejected requests. Google's MapReduce [6] system runs on top of the Google File System [7], within which data is loaded, partitioned into chunks, and each chunk is replicated. Google by default replicates the data at three locations. The Google File System (GFS) enables the files to be moved transparently in order to balance the load that is in line with the proposed File Replication. Unlike GFS, proposed approach avoids the creation of redundant replicas on the same node and consumes less raw storage than GFS. By default GFS stores, three replicas of a file, but proposed approach creates replicas as and when demand arises. Proposed approach reclaims the physical storage only when the need arises, in case there is not sufficient storage space to store a file being replicated. GFS does this lazily during regular garbage collection. In contrast to the system like xFS [8], AFS [9], Intermezzo [10] and Frangipani [11], GFS and the approach proposed in this paper, does not provide any caching below the file system interface. Unlike GFS, in

order to increase reliability and gain flexibility proposed approach does not maintain any centralized master replica for maintaining file consistency and management. Rather it uses a distributed architecture that manages the assignment of the role of master replica to the latest updated replica dynamically and propagates the same to the secondary replicas on-demand. This overcomes the issue of single point failure. Scalability and high availability (for read) are achieved by adding new servers as and when the need arises without affecting the current ongoing processing. Like proposed approach, GFS also addresses a problem similar to Lustre [12] in terms of delivering aggregate performance to a large number of clients. Bigtable [13] relies on a highly-available and persistent distributed lock service called Chubby [14]. A Chubby service consists of five active replicas, one of which is elected to be the master and actively serve requests. The service is live when a majority of the replicas are running and can communicate with each other. Chubby uses the Paxos algorithm [15], Lamport [16] to keep its replicas consistent in the face of failure. Each directory or file can be used as a lock, and reads and writes to a file are atomic. The Chubby client library provides consistent caching of Chubby files. Each Chubby client maintains a session with a Chubby service. A client's session expires if it is unable to renew its session lease within the lease expiration time. When a client's session expires, it loses any locks and open handles. Chubby clients can also register callbacks on Chubby files and directories for notification of changes or session expiration. The master is responsible for assigning tablets to tablet servers, detecting the addition and expiration of tablet servers, balancing tablet-server load, and garbage collection of files in GFS. Bigtable clients do not rely on the master for tablet location information; most clients never communicate with the master. As a result, the master is lightly loaded in practice. Primary-copy (master-slave) approach for updating the replicas says that only one copy could be updated (the master); secondary copies are updated by the changes propagated from the master. There is only one replica, which always has all the updates. Consequently the load on the primary copy is huge. Domenici [17] discusses several data consistency solutions, including Eager (Synchronous) replication and Lazy (Asynchronous) replication, Single-Master and Multi-Master Model, and pull-based and push-based. Guy [18] proposes a replica modification approach where a replica is designated either a master or a secondary. Only master replica is allowed to be modified whereas secondary replica is treated as read-only, i.e., modification permission on secondary replica is denied. A secondary replica is updated in accordance with the master replica if master replica is modified. Sun [19] proposes two coherence protocols viz., Lazy-copy and Aggressive-copy. Replicas are only updated as needed if accessed by the Lazy-copy protocol. For the aggressive-copy protocol, replicas are always updated immediately when the original file is modified. Compared with Lazy-copy, access delay time can be reduced by Aggressive-copy protocol without suffering from long updating time during each replica access. However, proposed approach has simplified the problem significantly by focusing on the application needs rather than building a POSIX-compliant file system. Most of the replication strategies are capitalized by

GFS, but there are some areas that leave ample scope for future work as discussed in this work. The next section discusses the proposed approach.

In order to ascertain architecture and framework of the proposed model, modeling and evaluation is necessary, before implementing a system to a large scale. The dynamic but complex behavior of the proposed model is analyzed by underlying communication protocol and characteristics of their components. The proposed model is verified through Calculus of Communicating System (CCS).

CCS [3] is a formal language for describing patterns of interaction in the concurrent systems. It allows the description of system in terms of sub processes that include primitives for describing composition and interaction among these, through message passing. Therefore, the motivation for using process algebra is to simplify the specification part and to verify the design structure of model while meeting its ultimate goal, i.e., file replication.

2 Proposed Approach

A scenario of three participating Cluster is considered. These clusters could be part of one organization or three different private clusters of a different organization. It is assumed that the nodes in these different clusters trust each other. The same is illustrated in Fig. 2. The proposed architecture is discussed below.

2.1 Architecture

A scenario is presented, though on a smaller scale where geographically disparate clusters interact with each other for information sharing through replication. One node in each cluster is designated as File Replicating Server (FRS). FRS can also be replicated on some other node in the cluster for backup and recovery. It consists of loosely coupled systems, capable of providing various kinds of services like replication, storage, I/O specific, computation specific and discovery of resources. Based on the application requirement, the resources are made available to other nodes.

2.2 Architecture Description

Fig. 1 shows a mini data center where each server is catering its services to the connected workstations. These workstations can be reorganized so as to form a cluster of nodes as shown in Fig. 2; it shows a network of three clusters that are connected to each other via intercommunication network. Each cluster consists of a group of trusted Requesting Nodes (RN) and a File Replicating Server (FRS) assigned to these nodes. Each node can presume the role of FRS. A FRS can be *local* or *remote*.

A file Replicating Server (FRS) assigned to a cluster having some nodes is known as local FRS, and FRS positioned outside that cluster, will be called as remote FRS. Each subset of nodes (denoted as requesting nodes) receives the list of IP-address of remote FRS's from the local FRS, but the nodes of a cluster will send the file request only to the local FRS. In case, if the local FRS fails to serve the request, it is automatically routed to a remote FRS in a transparent manner, and the remote FRS fulfills the request of the requesting node. This makes the model robust and capable of handling crashes in case local or even remote FRS fails. Each FRS maintains two tables: (1) File request count table with the following attributes: <file_id, file_name, request_count, metadata>. (2) FRS table with the following attributes: <FRS_IP, FRS_PORT>.

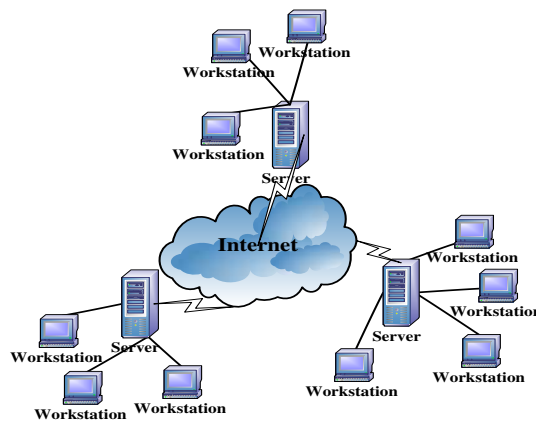


Figure 1

An abstract view of data center

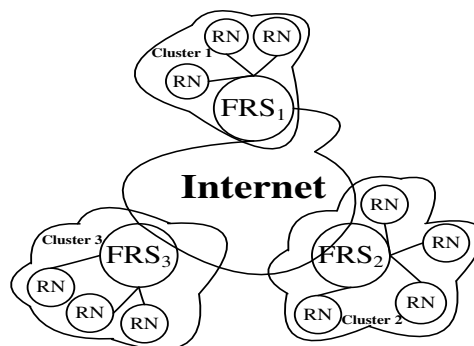


Figure 2

Architecture of file replicating server

Each FRS is informed whenever a new FRS is added to the network, so as to update its FRS table. FRS does not monitor the status of remote FRS periodically, instead FRS requests for the current status of remote FRSs on-demand. FRS status

can either be *busy*, *ready* or *File not available*. *Busy* signifies that the *request count* is greater than file threshold value. *Request count* is described in section 3.5. *Ready* signifies that the *request count* is less than file threshold value. *File not available* indicates that the requested file is not available on the cluster. Number of thread a server can handle, and the server load balancing aspects are left on the application developer and deployment environment.

2.3 Description of File Replication Mechanism

Each local FRS is responsible for accepting the file request from the Requesting Node (RN). Local FRS checks its status against the requested file and redirects the request depending on its status in the following manner: (1) If the status of local FRS is *ready*, the local FRS will fulfill the request. (2) If the status of local FRS is *file not available*, the local FRS looks for remote FRS that can fulfill the file request as discussed below in 2(a) & 2(c). Otherwise, (3) In case, status of local FRS is *busy*, it looks for a remote FRS that can handle the request, by one of the following manner, described as under:

(a) Local FRS sends a message only to those FRSs that are present in the *replica location* field of the data structure for file request count table (Table 1) and requests for their status against the requested file. The local FRS redirects the request to the remote FRS having the status as *ready*. This remote FRS fulfills the request of the RN. (b) If not so, the local FRS contacts those remote FRS's on which the requested file is not available. In this case, file replication will be initiated, by the local FRS of the cluster and the file replica is created on the remote FRS having the status as *file not available*. (c) For both the cases mentioned above, IP address of the remote FRS that can handle the request will be sent by the local FRS to the requesting node. Now, the request is redirected to the remote FRS and RN shall receive the file, without any user intervention. Thus, the overhead of polling and broadcasting is reduced.

2.4 File Replication Strategy

Fig. 3 shows each FRS as a part of different cluster. To differentiate between the remote FRS and local FRS, dotted and solid lines are used. All FRS are logically interconnected with each other and update their FRS table as soon as a new FRS is added. Node N_1 is the Requesting Node (RN) that sends the file request to FRS. Fig. 3 shows the replication scenario for a file replicating server S_1 .

FRS S_1 on successfully connecting to N_1 sends the list of remote FRS ($S_2, S_3, S_4 \dots S_{i-1}, S_i$) to node N_1 . Now, node N_1 sends file request to the local FRS, i.e., S_1 . As FRS S_1 has reached the threshold, it cannot handle this request. FRS S_1 looks for a remote FRS that can handle the request. While looking for a FRS that can fulfill the request, some FRS's send their status as *busy*, and the rest of the FRS may not hold the requested file, i.e., file not available (*fna*). Now, local FRS will

initiate the replication process for the requested file on the remote FRS. Replica will always be created on the FRS that does not contain the requested file. On successfully creating the replica of the requested file on a remote FRS, local FRS will send the IP-address of remote FRS to N_1 and request gets redirected and fulfilled by remote FRS.

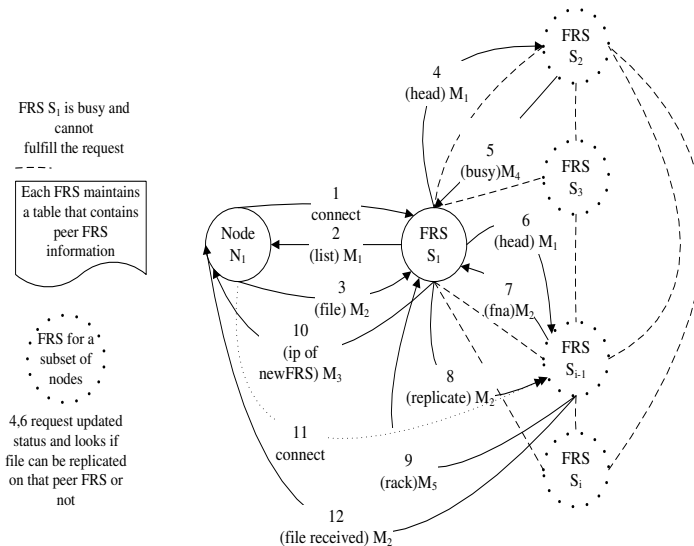


Figure 3

Replication scenario of a file replicating server

2.5 Data Structures Used

Each node maintains Table 1 to handle dynamic on-demand file replication and consistency mechanism. Table 1 keeps the following information about the files requested by the requesting nodes: (1) *File ID*: uniquely identifies the requested file. (2) *Filename*: name of the file requested by the node. (3) *Request Count*: is the number of request for a particular file that the FRS is currently handling. This count is incremented by one, whenever the FRS initiates the file transfer operation that is intended for the requesting node. As soon as the request is fulfilled this count is decremented by one. (4) *Metadata*: stores the data that identify the various file attributes. (5) *Valid*: It is a Boolean variable that signifies whether the file is stale or updated. (6) *Lock*: It is an integer variable that signifies that a FRS has acquired lock on the file and the file is being modified. (7) *Owner FRS*: It is a string variable. This field contains the IP address of the FRS that has most recently modified the file. (8) *Replica Location*: It is an integer variable. This specifies the node ID (FRS and requesting node) on which the file replica is present. (9) *Timestamp (t_f)*: It is a string variable. It stores the timestamps of the file that is present on the node (FRS and requesting node).

Table 2 represents the format of the table maintained by each FRS, which contains the <IP address and port number> of FRS. FRS IP denotes the IP address of the FRS and FRS PORT denotes the port number of the FRS to which the network messages are forwarded.

2.6 Message Definitions for Proposed Approach

The proposed approach consists of following messages viz., M_1 , M_2 , M_3 , M_4 and M_5 . M_1 is request for sending or receiving a file. It consists of three tuples, which include the following details: (1) Machine Type (either Requesting Node or FRS) (a) Requesting Node requests a file from the file replicating server (FRS). (b) FRS uses the *head message* to initiate the replication request. (2) Request Type (either “get” or “put” or “list”), list will provide the IP address of the remote FRS. (3) Filename. Message M_2 Copies the file or list contents from FRS to Requesting Node or other FRS, in accordance with the type of request, i.e., whether file request is made by FRS for file replication or by requesting node. M_3 responds to the request based on the local FRS current status, namely: (1) It informs the requesting node if the local FRS is ready to serve the request, i.e., N_{ready} . Or, (2) If the local FRS is busy, it sends the IP and port address of the remote FRS having the requested file. M_4 informs the local FRS about the current status of the remote FRS, namely: (1) *Busy*: remote FRS is busy, so it cannot handle the current request. (2) *Ready*: file is present and remote FRS is ready to serve the request. (3) *File Not Available*: if the file does not exist on the remote FRS, this remote FRS will become the potential node for file replication. M_5 is reply acknowledgement message, i.e., “RACK” is sent to the local FRS, when file is transferred completely. M_6 is a multicast message for sending a request for the modification file to owner FRS. M_7 sends the modification file to those FRSs that has the replica of the modified file f . M_8 is the ACK message send by remote FRSs to FRS_{*i*}. M_9 grants permission to node N_i to modify the file.

File Replication approach discussed in section 3.4, 3.5 and 3.6 ensures that, implicit addressing is used, to fulfill the nodes request, for a logical resource and maintains the access, migration and performance transparency of the system.

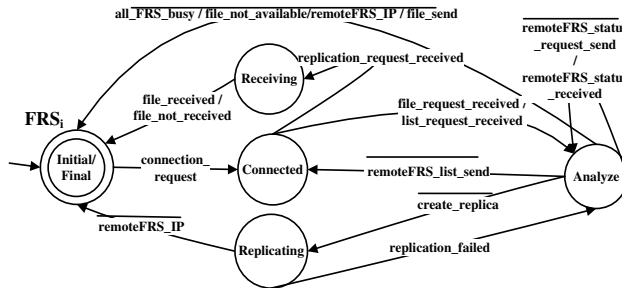


Figure 4

File replicating server (FRS) model

The various states of the file replication model are shown in Fig. 4. Here, the state *Connected* represents the state after the connection has been established between the Requesting Node (RN) and FRS_i . FRS_i can change its state either to *Receiving* or *Analyze* as follow: (a) In *Connected* state FRS_i accepts the file request, requested by RN and changes its state from *Connected* to *Analyze*. Also, FRS_i becomes the destination FRS if a remote FRS needs to replicate a file on this FRS_i . FRS_i on receiving the replication request changes its state from *Connected* to *Receiving*. After the state *Receiving* has been reached, the transition will only be made to *Final* state, which indicates that the connection has been closed. (b) FRS_i on changing its state from *Connected* to *Analyze*, depending on the FRS (local and remote) status the transition will take place either to *Final* state or *Replicating* state. In the state *Replicating*, if failure signal is received, the transition will be made to *Analyze* state, and other remote FRS will be selected for replication. When no failure signal is received, transition will be made to *Final* state.

The process algebraic approach is used to verify the correctness of proposed file replication model. It is a mathematical technique used for the verification of software and hardware systems. This is required, to confirm whether the proposed model is meeting the specifications or not.

2.7 Hybrid Consistency Mechanism Using Partial Update Propagation

The proposed consistency mechanism is called hybrid because the replica of the modified file is updated on FRS using partial update propagation and the write invalidate message is send to the requesting nodes having the replica of the modified file, as shown in Fig. 6. A Requesting Node (RN_i) requests to modify a file (f) present on File Replicating Server (FRS_i). It is assumed that the clocks of all FRSs are synchronized with each other, and all RNs synchronize their clocks with local FRS. In partial update propagation, write update is performed using modification file on FRS's and these FRS's perform write invalidate on RN's. During write update using modification file, owner FRS sends the modification file only to those FRSs that has the replica of the modified file. Now, each FRS on which the replica has been updated, will send an invalidate message to those requesting nodes that have the replica of the modified file.

Owner node is any FRS_j that has most recently modified the file (f) and contains the latest updated (valid) copy of file f , and FRS_j is not a centralized entity. A modification file contains the changes that have been performed on the original file. These changes include the line number on which the change has been made and the content of that line.

When a file on any FRS_i has to be modified by a RN, this FRS_i generates a request to acquire the lock on file (f). If FRS_i is the owner of file (f), it performs a check whether or not file (f) is locked by any other RN on FRS_i . If yes, it waits for the write operation to get completed. Once the write operation is completed, lock is

released and the write permission is granted to the requesting node RN_i . If FRS_i is not the owner of file (f), FRS_i multicasts a message for acquiring the lock on file (f) called $RW(f)$ message, to other FRSs. FRS_i multicasts the message only to those FRSs that are present in the *replica location* field of the data structure. On receiving this message if FRS_j has not locked file (f) it sends an acknowledgement for acquiring lock to FRS_i . If FRS_j has locked file (f), it waits for completion and responds by sending modification files. FRS_i updates the stale copy of (f) by patching it with the modification file. FRS_i acquire write lock on file (f) and gives write permission to requesting node RN_i . After modifying the file, the RN will update the file on its local FRS_i by sending the modification file. Now FRS_i will update the file using Hybrid consistency mechanism and becomes the owner of the file. Other FRSs makes an entry in the *Owner* field of the data structure that new file owner of file (f) is FRS_i . Now, these FRSs in turn send an invalidate message to the RN 's having the replica of the modified file. If any of the RN 's have to use the file later, these RN update their replica by sending a request for modification files to its local FRS as and when the need arises. Flow diagram is shown in Fig. 5.

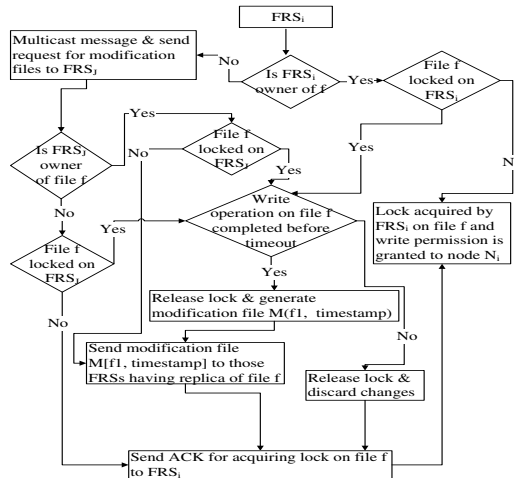


Figure 5

Flow diagram for acquiring lock by FRS on the file and replica update & consistency maintenance mechanism on FRS using modification files

As discussed above, in case the file is modified, the replica is updated or invalidated on other nodes (FRSs and requesting nodes) using the above discussed hybrid consistency mechanism. Depending on the number of FRS on which the replica is updated, and the number of requesting nodes on which the replica is invalidated there arises two cases as follow: *Best case*: When only few FRS and requesting nodes have the replica of the file that has been modified file. *Worst case*: When all the FRSs and the requesting nodes have the file replica of the modified file, this is considered as the worst case scenario.

Consider a scenario as shown in Fig. 6, in which the file replica is present on FRS_1 , FRS_2 , FRS_3 , RN_3 , RN_6 and RN_9 . Now, RN_9 makes a request to modify a file present on FRS_3 . FRS_3 checks whether or not the requested file is locked by some other RN using the file locking mechanism, as discussed above. Fig. 6 shows the hybrid consistency mechanism in which the file is updated on those FRSs having the replica of the modified file by using the modification file and these FRSs in turn send the invalidate message to the requesting nodes having the replica of the file that has been modified.

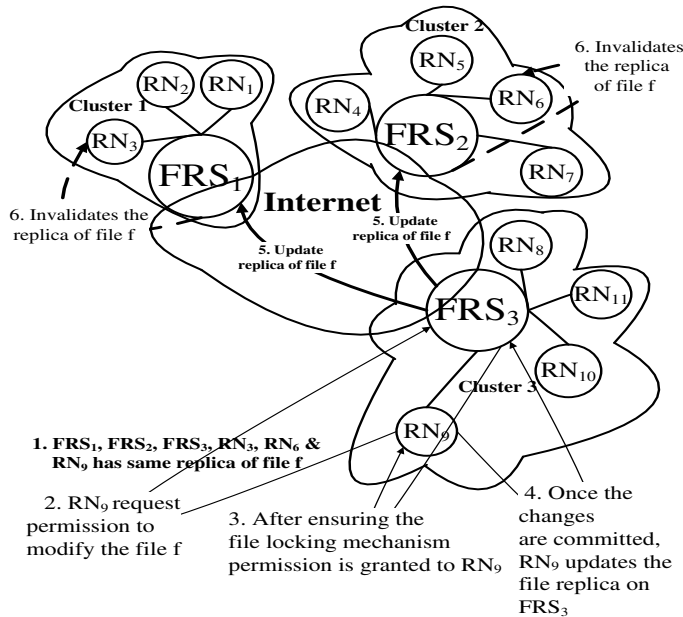


Figure 6

Hybrid consistency mechanism

If the owner FRS_j is down, FRS_i selects a remote FRS from the *Replica location* field of Table 1 as described in section 3.5 and checks the validity of file on that remote FRS. File validity is checked from the *Valid* field of Table 1. As soon as validity of file on the remote FRS is confirmed, that remote FRS becomes the new owner of that file.

3 Stability Analysis

Stability analysis of File Replication Model (FRM) using a process algebraic approach is carried out in this section.

3.1 Transition System Definition

Transition systems [20] are considered to perform external and internal actions. External actions are defined as observable actions, which are seen by the observer. However, an unobservable action is considered as an internal action which the observer cannot see. According to Milner [21], an agent C is a cell which may hold a single data item. It has two ports; an empty cell may accept an item or value from its left hand port labeled in ; while it may deliver a value from its right hand port labeled out as shown in Fig. 7.

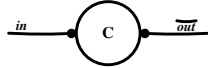


Figure 7
Labelled transition

3.2 File Replication Model (FRM) in Process Algebraic Framework

In the proposed formal model, the components of a system are identified as communicating agents. In the flow diagram as shown in Fig. 8, circle represents the communicating agents, i.e., Requesting Node (RN), i.e., N_{fr} and file replicating server (FRS). These are considered as communicating agent. The communication between agents is represented through transition graph. Transmission line (*trans*) is used to transfer messages from one node to other. The FRS receiving the file request (M_1) is termed as File Replicating Server (FRS), i.e., N_{frs} and is denoted by S_i . FRS S_i^r or S_{i-1}^r is the server on which file replica is either created or previously available. The RN, i.e., N_{fr} raises a file requisition via message \overline{M}_1 and receives its corresponding reply via M_2 or M_3 , depending on the FRSs status. M_4/\overline{M}_4 shows the status of FRS as busy (N_{busy}) or ready (N_{ready}). Status of FRS depends on the number of request a FRS is currently serving for a meticulous file. FRSs having the status as busy cannot fulfill the file request. Ready FRS (N_{ready}) represents that FRS is ready to handle the file request. In case FRS S_i is busy, it requests the status information of remote FRSs and redirects the request to the FRS having the status as ready (N_{ready}) that can handle the request. If no such FRS is present, replica is created on FRS S_i^r or S_{i-1}^r that has the status as N_{fna} , i.e., file not available.

After the file is replicated on FRS S_i^r or S_{i-1}^r an acknowledgement message M_5 or \overline{M}_5 is sent by FRS S_i^r or S_{i-1}^r to FRS S_i , the file request gets redirected and fulfilled by FRS S_i^r or S_{i-1}^r .

The value of file threshold index prohibits the behavior of nodes as busy and ready. Similarly, the file availability index gives information about the file availability on that node. Here arise two scenarios, discussed as below: (1) Replica available (2) Replica created.

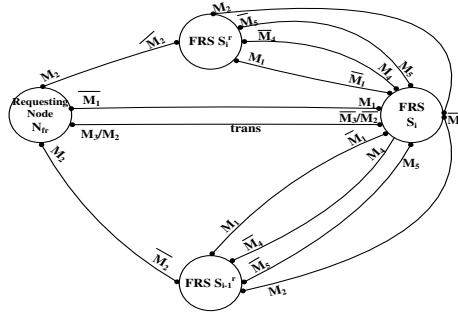


Figure 8

Flow graph for file replication model in process algebraic approach

Replica Available: FRS S_i , which receives the file request from the requesting node, fulfills it if and only if, its status is *ready*, i.e., N_{ready} . This means that, the requested file is present on S_i and it can handle the file request. If S_i is not able to fulfill the request, it looks for any S_i^r or S_{i-1}^r that has the requested file and status as N_{ready} . In this case, there is no need to create a replica of the requested file. *Replica created:* if all FRS, i.e., S_i , S_i^r or S_{i-1}^r having the copy of the requested file are busy, then its replica needs to be created. Replica will always be created, on the FRS S_i^r or S_{i-1}^r whose status is N_{fna} , i.e., file not available. The formal specification of two scenarios is described below:

Set of agents can be denoted by \mathfrak{A} . Hence,

$$\mathfrak{A} \in \{N, N_{fr}, N_{frs}, S, D, FRS\}$$

Equ. (1) shows different status of FRS:

$$N_{status} \stackrel{\text{def}}{=} (N_{busy} \mid N_{fna} \mid N_{ready}) \quad (1)$$

FRS status depends on the number of requests a FRS is currently serving for the requested file known as file request load. If the file request load \geq the file threshold value, the requested file is replicated on remote FRS, i.e., S_i^r or S_{i-1}^r .

Equ. (2), a node requesting for a file, hence called as Requesting Node (N_{fr}) denoted by S .

$$N_{fr} \stackrel{\text{def}}{=} S \quad (2)$$

Equ. (3), FRS S_i receives file request. S_i responds to the requesting node via message \overline{M}_3 or \overline{M}_2 , depending on the FRSs status, the state transition will take place.

$$N_{frs} \stackrel{\text{def}}{=} (\overline{file_request_received}). (\overline{frs_status} + \overline{file_send}). N_{frs} \quad (3)$$

Equ. (4), FRS that affirms its status as N_{ready} will fulfill file request and is denoted by D .

$$N_{ready} \stackrel{\text{def}}{=} D \quad (4)$$

$$D \stackrel{\text{def}}{=} \overline{\text{file_request_received}}.\overline{\text{file_send}}.D \quad (5)$$

$$S \stackrel{\text{def}}{=} \overline{\text{file_request_send}}.\text{file_received}.S \quad (6)$$

According to Robin Milner [21] a labeled transition system can be thought of as an automaton without any Initial/Final state.

3.2.1 Language Specification for Replica Available (FRM_{ra}) Scenario

Now, a scenario of file replication model, i.e., replica available is discussed. Here, the file request is fulfilled by the available copy of the requested file on a remote FRS. Thus, unnecessary replica creation is avoided.

3.2.1.1 Language Specification for Local FRS

The language specification for the local FRS that can be described as follow: (1) State transition takes place from one state to the other depending upon the interrupt received by the current state. (2) After receiving the file request from the requesting node, the local FRS S_i fulfills the request if and only if its' status is N_{ready} . Otherwise, S_i checks with the remote FRS, i.e., S_i^r or S_{i-1}^r that can handle the request. (3) If a remote FRS is busy, it will not accept the file request and sends its status as busy to the local FRS S_i . (4) If S_i status is not marked as ready, this means, either S_i status is N_{fna} or N_{busy} , refer to equ. (8). In case, those FRSs having the replica of the requested file are busy, requested file is replicated on that remote FRS having the status as N_{fna} . (5) State LocalFRS' is reached after the connection with requesting node is closed.

$$\text{LocalFRS} \stackrel{\text{def}}{=} (\text{list_request_received} + \text{file_request_received}).\text{Analyze} \quad (7)$$

$$\begin{aligned} & \overline{\text{Analyze}} \stackrel{\text{def}}{=} \\ & \overline{\text{remoteFRS_status_request}}.\overline{\text{Analyzing}} + \overline{\text{send_remoteFRS_list}}.\text{LocalFRS} + \\ & (\text{all_FRS_busy} + \text{file_not_available} + \text{file_send}).\text{LocalFRS}' \end{aligned} \quad (8)$$

$$\begin{aligned} & \overline{\text{Analyzing}} \stackrel{\text{def}}{=} \\ & (\overline{\text{remoteFRS_busy}} + \overline{\text{remoteFRS_fna}}).\overline{\text{Analyze}} + \overline{\text{remoteFRS_IPaddress}}.\text{LocalFRS}' \end{aligned} \quad (9)$$

3.2.1.2 Corresponding Language Specification for Requesting Node

The behavior of the requesting node that sends the request to FRS for a file is represented by equ. (10). Requesting node after sending the file request to FRS, changes its state from N_{fr} to N_{fr}' . In this state, the requesting node will wait for the reply from the FRS S_i . Once the response is received the transition is made to state N_{fr}'' .

$$N_{fr} \stackrel{\text{def}}{=} (\overline{\text{list_request_send}} + \overline{\text{file_request_send}}).N_{fr}' \quad (10)$$

$$\begin{aligned} & N_{fr}' \stackrel{\text{def}}{=} (\overline{\text{list_received}} + \overline{\text{file_received}}).N_{fr} + (\overline{\text{remoteFRS_IP}} + \overline{\text{all_FRS_busy}} + \overline{\text{file_not_available}} + \\ & \overline{\text{remoteFRS_list_not_received}}).N_{fr}'' \end{aligned} \quad (11)$$

$$N_{fr}'' \stackrel{\text{def}}{=} (\text{requesting_node_crashes} + \text{no_remoteFRS_available}). N_{fr}'' \quad (12)$$

$$FRM_{(ra)} \stackrel{\text{def}}{=} \text{RequestingNode} \parallel \text{FRS} \parallel \text{Destination} \quad (13)$$

3.2.2 Language Specification for Replica Created (FRM_{rc}) Scenario

Now, second scenario of file replication model, i.e., replica creation will be discussed. It symbolizes a communicating system that consists of *Replicate* and *Receiving* agents, which represents the replication mechanism of file replicating server. Replicate agent is the FRS that creates the replica of the file on remote FRS. This remote FRS is known as receiving agent. *Replicate (F)*: A file request is sent through the transmission line (*Trans*) by the requesting node and it is received by FRS. On receiving the request, FRS changes its state to *Replicate*, which denotes that the FRS is busy, and the requested file needs to be replicated, refer to (14) & (15). *Receiving (F)*: The receiving agent, i.e., remote FRS that receives file request through the transmission line (*Trans*) and reaches the state FRS', on successful completion of file transmission. *FRS'*: state FRS' is the final state after the file transfer is complete.

$$FRS \stackrel{\text{def}}{=} \text{replication_request_received}. \text{Receiving} + \text{file_request_received}. \text{Replicate} \quad (14)$$

$$\text{Replicate} \stackrel{\text{def}}{=} \overline{\text{replication_request_send}}. \text{Replicating} \quad (15)$$

$$\text{Receiving} \stackrel{\text{def}}{=} \text{replica_created}. \text{FRS}' \quad (16)$$

$$\text{Replicating} \stackrel{\text{def}}{=} \text{replication_failed}. \text{Replicate} + \overline{\text{replica_created}}. \text{FRS}' \quad (17)$$

$$FRM_{(rc)} \stackrel{\text{def}}{=} \text{Replicate} \parallel \text{Trans}(\epsilon) \parallel \text{Replica_created} \quad (18)$$

Where *Trans* (ϵ) denotes initially empty transmission line and \parallel denotes restricted composition. From equation (13) and (18), it is proved that replication mechanism of file replication model meets its specification with $FRM_{(ra)}$ and $FRM_{(rc)}$. Hence, $FRM_{(ra)} \approx FRM_{(rc)}$.

3.2.3 Bisimulation Proof for FRM_(ra) and FRM_(rc)

The transition graph for local FRS and requesting node, refer to equ. (5) and (6). Equation shows the different FRS states (14), Replicate (15), Replicating (16) and Receiving (17). Fig. 9 shows the bisimulation graph by linking the related states of both the models on a state transition graph. Observations show that bisimulation graph represents the one to one transition of different state as per above mentioned equations.

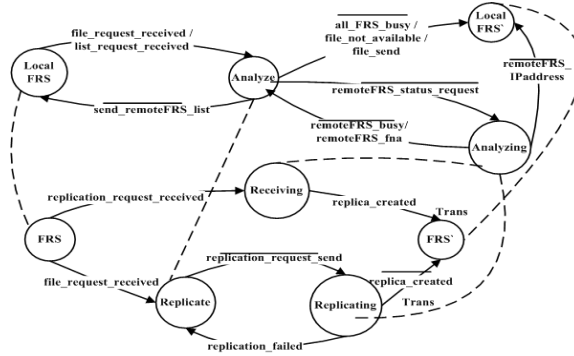


Figure 9

Bisimulation graph by linking the related states on a transition graph

Requesting node (N_{fr}) sends a file request to the local FRS (S_i), refer equ. (10) and receives the status from S_i followed either by the requested file or the IP address of the remote FRS having the copy of the requested file, refer equ. (11). In this case, the request is fulfilled by the available copy of the requested file either by the local FRS itself (8) or by remote FRS having a copy of that file (9). Remote FRS discards the file request in case the status of remote FRS against the requested file is N_{busy} or N_{fna} , refer equ. (9). If the status of any FRS is marked as *ready*, i.e., N_{ready} , the request gets redirected and fulfilled by this FRS, equ. (8).

State ‘Replicate’ represents that, the file replication is required as the status of the FRSs that have the replica of the requested file is busy N_{busy} . Intermediate state is represented by *Replicating* and FRS’ represents the final state after the replication has been done, i.e., file has been transferred completely, and the connection has been closed. State FRS represents that the connection has been established between two nodes. State *Receiving* represents the intermediate state. The output would be sent from the transmission line (*Trans*).

4 Simulation and Results

The proposed model is simulated on JAVA platform. Threshold is fixed in accordance to the constraints and demands, depending on the application requirement. Experimental system configuration is illustrated in Table 4. Table 3 shows the request completion time in seconds for replicating the file of size 64.1 MB. Table 3 shows the worst case scenario, in which 100 requesting nodes send request for the file f simultaneously.

The first few requests handled by FRS takes more time because this time is inclusive of replication overhead from FRS1 to FRS2, and FRS1 to FRS3, but subsequently the service time taken by FRSs drops from 281.62 seconds to 245.62 seconds. The average request completion time decreases by 12.78%.

Table 3
Average request completion time (seconds)

Number of FRSs/ Number of Request- ing Nodes →	1-20	21-40	41-60	61-80	81-100	Average
2 FRS	400.75	265.86	220.67	300.15	220.67	281.62
3 FRS	292.21	251.55	148.51	252.35	283.51	245.62

In replication scenario, all available FRS's are utilized to fulfill the request. As shown in Table 3, service time for requesting node 41-60 in case of 3 FRS is very less, this is because, by the time FRS receives this request, some of the previous requests gets completed, same is shown in Fig. 10. When the local FRS reaches the file threshold value and replicates the file on some other FRS, the replication overhead is compensated by the following benefits: (1) Avoid retransmission of request by the requesting node. (2) Reduces latency in case of load above threshold.

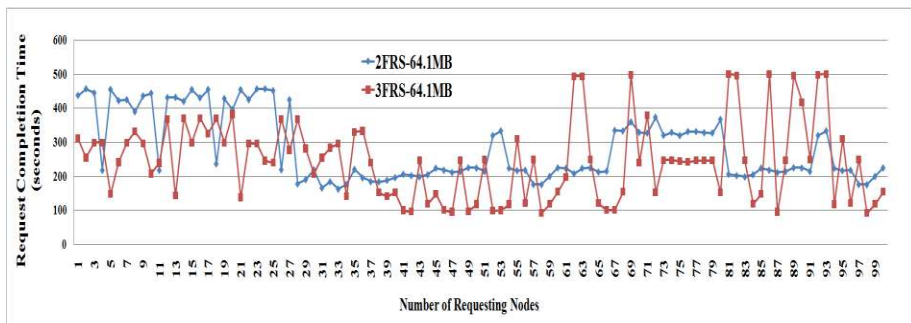


Figure 10
Request Completion Time for 64.1MB file

Fig. 11 shows the time taken by the local FRS, to invalidate the replica available on the Requesting Nodes (RNs) that are connected to this local FRS. Size of invalidate message is 15 bytes. The invalidate message to RNs is sent by the local FRS. Two cases are shown in the figure viz., Best case and Worst case. In the best case, replica does not exist on all the RNs. It is considered that out of 30RNs connected to the local FRS, 70% of the RNs have the replica of the modified file. In the worst case, replica of the modified file is available on all the RNs.

The average time required for invalidating the replicas using hybrid consistency approach in the best case is 13.43 msec and in the worst case is 20.36 msec. For some RNs, it is observed that there is a delay in the message delivery, due to which there is the formation of the crest as shown in the figure.

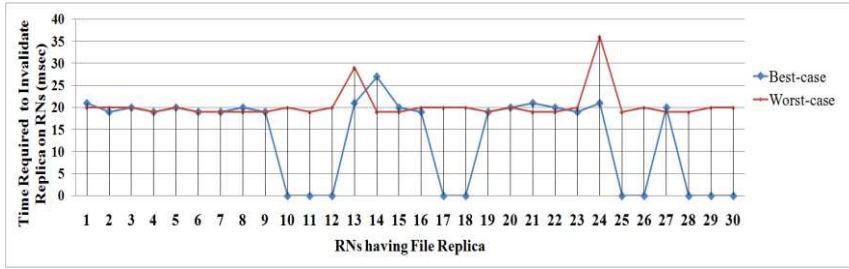


Figure 11

Time required for invalidating stale replica on requesting node

Fig. 12 shows the time required to update the replica on the FRS for file size of 128 kb, 677 kb, and 3.1 mb. Two cases that are shown in the figure are Complete File Transfer (CFT) and Hybrid approach. In CFT, complete file that has been modified is sent to the FRS having the replica of that file. In case of hybrid approach, only the modification that has been done is sent to the FRS having the replica of that file. Time required for updating replicas using hybrid consistency approach reduces from 153.33 msec to 58.64 msec.

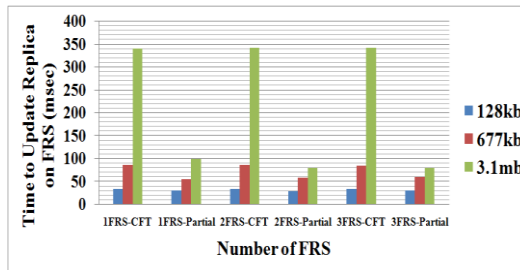


Figure 12

Time required for updating stale replica on FRSs

4.1 How Proposed Approach Weighs against Existing Approaches

The configuration used by the Google File System (GFS), and the proposed scheme is shown in the Table 4.

Table 4
Experiment configuration table

	Processor	Memory	Hard Disk	Ethernet Connection	Switch
GFS	Dual 1.4 GHz PIII	2 GB	Two 80 GB 5400 rpm	100 Mb/s full-duplex	1 Gb/s link
Proposed	3.6 GHz P IV	1 GB	80 GB 5400 rpm	-	100Mb/s

In case, N clients write simultaneously to N distinct files. Fig. 13 shows that with GFS the average write rate reaches 21.8 MB/s for 10 clients and with the proposed Partial Write scheme the average write rate is 35.52 MB/s. The proposed partial write rate shows the improvement of 38.62% as compared to GFS write rate.

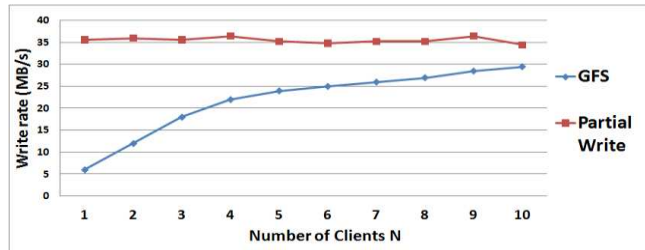


Figure 13

Write rate as the number of replicas to be updated increases (MB/s)

Fig. 14 shows that when N clients read simultaneously from a file, GFS average read rate reaches 44.5 MB/s for 10 clients and with the proposed scheme the average read rate is 14.57 MB/s. GFS read rate is 67.23% better than the proposed scheme. This is due to the system configuration as described in Table 4.

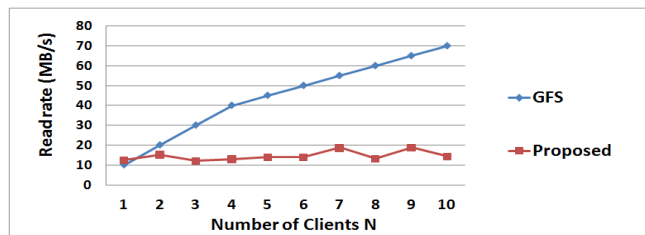


Figure 14

Read rate with an increasing number of readers (MB/s)

Conclusion

This paper makes an attempt to propose and establish the threshold based file replication approach in the distributed cluster computing environment, having a mini data centric view. Proposed file replication and consistency maintenance mechanism, autonomously determines the need for file replication based on the file threshold and availability of files on the nodes of cluster environment. The decentralized architecture for the proposed model eliminates the possibility of single point failure. Proposed approach ensures automatic retransmission of request to the remote FRS, in case the local FRS fails. The hybrid consistency mechanism that reduces the time for updating multiple replicas of a file by using modification propagation is also proposed. Experimental results show that as compared to Google File System (GFS), the proposed partial write rate shows an improvement of 38.62% while updating stale replicas. Time required for invalidating the replicas decreases by 34.04% and the time required to update the replica

on FRS reduces by 61.75%. The replication overhead is compensated by the benefits like avoiding retransmission of request by the requesting node, and reducing file access latency.

Finally, a relationship between the formal aspect of file replication server and its architectural model, i.e., proposed file replication model is established through process algebraic approach. The stability and reliability analysis ensure that the system will run in the finite sequences of interaction and transitions. On the basis of these properties, a transparent, reliable and safe file replication model is built.

References

- [1] R. Buyya, High Performance Cluster Computing, Vol. 1, Pearson Education, 2008
- [2] J. Grudin, "Computer-Supported Cooperative Work: History and Focus". *Computer* 27 (5), 1994, pp. 19-26
- [3] R. A. Milner, Calculus for Communicating System, in: Lecture notes in Computer Science, Vol. 272, Springer, 1980
- [4] Rajkumar Buyya and Rajiv Ranjan, Federated Resource Management in Grid and Cloud Computing Systems, Future Generation Computer Systems, Volume 26, No. 8, ISSN: 0167-739X, Elsevier Press, Amsterdam, The Netherlands, Oct. 2010
- [5] Ivona Brandic and Rajkumar Buyya, Recent Advances in Utility and Cloud Computing, Future Generation Computer Systems, Volume 28, No. 1, ISSN: 0167-739X, Elsevier Press, Amsterdam, The Netherlands, Jan. 2012
- [6] Jeffrey Dean and Sanjay Ghemawat, MapReduce: Simplified Data Processing on Large Clusters, In Sixth Symposium on Operating System Design and Implementation (OSDI'04), San Francisco, CA, Dec. 2004
- [7] S. Ghemawat, H. Gobioff and S. T. Leung, "The Google file system," *SI-GOPS Oper. Syst. Rev.*, Vol. 37, pp. 29-43, 2003
- [8] Thomas Anderson, Michael Dahlin, Jeanna Neefe, David Patterson, Drew Roselli, and Randolph Wang. Serverless networkfile systems. In Proceedings of the 15th ACM Symposium on Operating System Principles, pages 109-126, Copper Mountain Resort, Colorado, Dec. 1995
- [9] John Howard, Michael Kazar, Sherri Menees, David Nichols, Mahadev Satyanarayanan, Robert Sidebotham, and Michael West. Scale and performance in a distributed file system. *ACM Transactions on Computer Systems*, 6(1):51-81, February 1988
- [10] InterMezzo. <http://www.inter-mezzo.org>, 2003, accessed on 20 July 2012
- [11] Chandramohan A. Thekkath, Timothy Mann, and Edward K. Lee. Frangipani: A scalable distributed file system. In Proceedings of the 16th ACM Symposium on Operating System Principles, pp. 224-237, Saint-Malo,

France, October 1997

- [12] Lustre. <http://www.lustre.org>, 2003, accessed on 20 July 2012
- [13] F. Chang, J. Dean, S. Ghemawat, W. C. Hsieh, D. A. Wallach, M. Burrows, T. Chandra, A. Fikes, and R. E. Gruber, “Bigtable: a distributed storage system for structured data,” in Proceedings of OSDI 2006, Seattle, WA, 2004
- [14] M. Burrows, “The Chubby Lock Service for Loosely-coupled Distributed Systems,” in Proceedings of OSDI’06: Seventh Symposium on Operating System Design and Implementation, Seattle, WA, November 2006
- [15] Jun Rao, Eugene J. Shekita, and Sandeep Tata. 2011. Using Paxos to Build a Scalable, Consistent, and Highly Available Datastore. Proc. VLDB Endow. 4, 4 (January 2011), pp. 243-254
- [16] Lamport, L. The part-time parliament. ACM TOCS 16, 2 (1998), 133-169
- [17] Andrea Domenici, Flavia Donno, Gianni Pucciani, Heinz Stockinger, Kurt Stockinger, “Replica Consistency in a Data Grid,” Nuclear Instruments and methods in Physics Research Section A: Accelerators, Spectrometers, Detectors and Associated Equipment, Volume 534, Issues 1-2, pp. 24-28, 21 November 2004
- [18] L. Guy, P. Kunszt, E. Laure, H. Stockinger and K. Stockinger “Replica Management in Data Grids”, Technical report, GGF5 Working Draft, Edinburgh, Scotland, July 2002
- [19] Yuzhong Sun and Zhiwei Xu, “Grid Replication Coherence Protocol”, The 18th International Parallel and Distributed Processing Symposium (IPDPS’04) - Workshop, Santa Fe, USA, pp.232-239. April 2004
- [20] A. Y. Zomaya (Ed.), Parallel and Distributed Handbook, McGraw Hill Professionals, pp. 60-68, 1995
- [21] R. Milner, Communication and Concurrency, Prentice Hall 1989
- [22] S. Mishra, D. S. Kushwaha, A. K. Misra, “Hybrid Reliable Load Balancing with MOSIX as Middleware and its Formal Verification using Process Algebra,” Future Generation Computer Systems, Volume 27, Issue 5, pp. 506-526, May 2011

Thermoelectric Power Study of Nitride Precipitation and Recrystallization in Continuously-heated Low Carbon Al-killed Steels

András Mucsi

Óbuda University, Donát Bánki Faculty of Mechanical and Safety Engineering,
Népszínház u. 8, H-1081 Budapest, Hungary
mucsi.andras@bgk.uni-obuda.hu

Abstract: This paper deals with the metallurgical phenomena occurring in aluminium-killed low carbon steels during industrial batch annealing process. The formability of these steels is strongly influenced by the nitride precipitation – recrystallization interaction during the batch annealing stage of the production technology. The accurate precipitation kinetics of nitrides is not clearly described yet because of the difficult evaluation of precipitated fraction of nitrides in cold rolled state steels. The aim of this study is to present a methodology for measuring the precipitated nitride fraction in cold rolled state, moreover to investigate the precipitation – recrystallization sequence during batch annealing process. Another purpose of this study is to give the conditions of the development of good deep-drawable microstructure. The nitride precipitation process in cold rolled and annealed state is measured using a special thermoelectric power test based methodology. On the basis of the experimental work, it is concluded that good formable microstructure develops if the precipitated nitride fraction reaches at least ~40% at the beginning of the recrystallization. This condition can be satisfied if the heating rate is held between 30 and 45 °C/h during the industrial batch annealing process.

Keywords: Al-killed low carbon steel; nitride precipitation; thermoelectric power

1 Introduction

1.1 Basics of Industrial Processing of Al-killed Low Carbon Steels

Aluminium killed low carbon steels are widely used for deep-drawing purposes due to their excellent formability. These grades of steels consist of elements in w.t. %: 0.02...0.05 C, 0.15...0.3 Mn, ~ 0.01 Si, 0.03-0.06 Al, 0.004...0.006 N,

0.015...0.02 Cr, 0.01...0.03 Cu, and low amount of Ti, Mo, Ni, Nb. In the manufacturing process of these steels it is essential to control the nitrogen content in liquid as well as in solid state [1]. It is recommended to avoid alloying with Ti and Nb. In this case, there is no possibility to form stable TiN particles, moreover the NbC particles will not increase the yield strength. Additionally, it is advantageous, if the Mn content of the steel is held around 0.17...0.2 w.t. %. Steels with larger Mn content exhibit lower deep-drawability. Some other important condition exists for producing good formable sheet, which can be satisfied with the proper thermomechanical processing of the steel. The time-temperature diagram of the production technology is shown in Fig. 1.

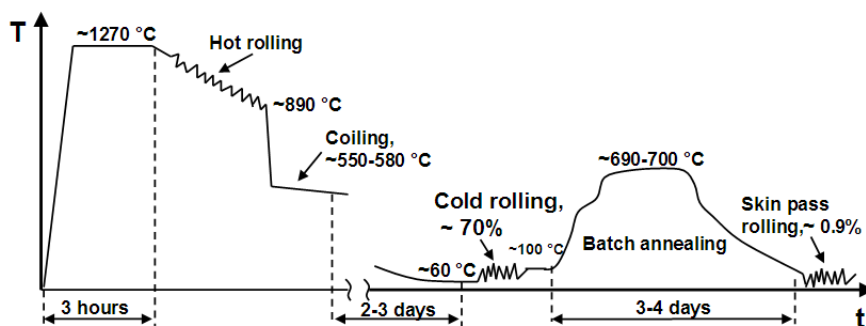


Figure 1

Production technology of Al-killed low carbon steels for deep-drawing purposes [1]

The production technology starts with the reheating of the slab to 1270 °C. It is followed by hot rolling in the austenite region with 890 °C average finishing temperature. At this point the strip is cooled down with water sprays to the coiling temperature. In order to keep the nitrogen in solid solution, the cooling rate after hot rolling must be fast enough and the coiling temperature must be low. Therefore the usual temperature range is 550-580 °C for coiling. The hot strip coil cools very slowly, with about 15-30 °C/hours cooling rate, depending on the position in the coil. The next step in the production technology is the cold rolling to around 70% thickness reduction, and it is followed by 3-4 day long batch annealing. According to the practical experience, if the free nitrogen precipitates in the form of aluminium and complex nitrides during the heating-up stage of the batch annealing process, then a good deep drawable microstructure develops [2]. Since the nitrides forming in cold rolled sheets are not only aluminium-nitrides but complex nitrides [3], moreover they can transform into other nitrides during heating [4], the term “nitride” will be used in this study. There are two advantageous effects of nitrides in the cold rolled sheet [5]:

1) If small, disperse nitride precipitates are present in the vicinity of dislocations and grain boundaries, the so-called pancake type microstructure develops, which decreases the sensitivity of the sheet to thinning.

2) During the recrystallization process, if small nitride precipitations are present in the cold rolled microstructure, then a good deep-drawable {111} texture will form.

It is not entirely clarified either complete or partial nitride precipitation should occur before the recrystallization starts. A possible change in the heating rate during the heating up stage of the batch annealing process largely influences the formability of the end product. The heating rate could be different even due to the large dimensions of the coil, so, in an indirect manner the formability and the mechanical properties could change significantly along the length of the strip. The knowledge of the nitride precipitation process in cold rolled state would be advantageous for the optimization of the batch annealing process.

The nitride precipitation in steels can be measured using different methods (chemical dissolution techniques [6], internal friction [4], resistivity [5], and numerous other methods [3]), but most of them provide inappropriate results if small, disperse nitride precipitations are present [3]. It was demonstrated that the measurement of thermoelectric power can be successfully applied to follow the nitride precipitation even in the case of small precipitates. Therefore in this study a special thermoelectric power test was used for determining the precipitated nitride fractions.

1.2 The Thermoelectric Power of Metals

The measurement of thermoelectric power (TEP) is a powerful method to quantify the microstructural changes occurring in metals. It can be used for investigating the effect of cold working [7], recovery and recrystallization [8], precipitation and dissolution processes [9-11]. It can provide the quantitative evaluation of free interstitial content of steels [12], so, in an indirect manner nitride- and carbide precipitation processes can be evaluated. The general set-up for measuring thermoelectric power of materials is shown in Figure 2 [4, 9].

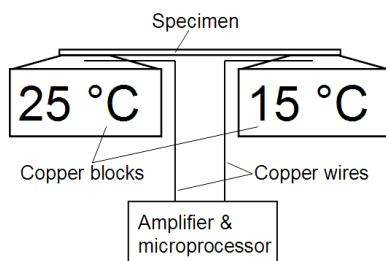


Figure 2
General set-up of a thermoelectric power measuring device

The sample under investigation is placed between two blocks made of high specific thermal capacity metal (usually copper blocks are used). The temperature of one of the blocks is held at 25 °C, whilst the temperature of the other one is cooled to 15 °C. Because of the temperature difference ($\Delta T=10$ °C) between the two blocks, a temperature gradient develops in the specimen and in this way a thermoelectric voltage (U) is arising between the two copper blocks. This voltage is measured using a low noise nanovoltmeter. The ratio of the voltage (U) generated and the temperature difference (ΔT) is called thermoelectric power (TEP) and denoted by S [11]:

$$S = U / \Delta T . \quad (1)$$

The thermoelectric power strongly depends on the microstructural state of the given material. It is generally accepted that the larger is the distortion of the crystal lattice the smaller is the numerical value of the thermoelectric power [4, 7-9]. Thus, cold working, dissolution of precipitations into the matrix and cold working decrease the value of TEP, whilst recovery, recrystallization and precipitation of elements from solid solution increase it. It is necessary to know the effect of the amount of elements in solid solution on TEP. The change in thermoelectric power (ΔS) due to alloying elements in solid solution is described by the Nordheim-Gorter law [13]:

$$\Delta S = \sum K_i \cdot x_{ss,i} , \quad (2)$$

where K_i is a coefficient linking the amount of element i in solid solution ($x_{ss,i}$) with the change ΔS in TEP. Coefficients K_i for some elements are given in Table 1 [4].

Table 1
Values of coefficients K_i in Nordheim-Gorter law for different elements [4]

Element	C	N	Al	Cu	Mn
K_i $\mu V/(K \cdot wt\%)$	-45	-24	-30	-2	-3

The evaluation of amount of precipitated nitrogen in steels is based either on the measurement of the amount of precipitated nitrides or on the estimation of the amount of free nitrogen [3]. Using the thermoelectric power method, the latter can be applied. The precipitation kinetics in hot rolled (in low dislocation density) material can be followed by a special TEP methodology, which will be outlined in the next section.

1.3 Measurement of Free Nitrogen Content in Hot Rolled State

Massardier et al. [4] have developed a thermoelectric power based methodology, by which the free nitrogen content and thus the amount of precipitated nitrides can be quantified in soft (low dislocation density) material. Their methodology is based on the aging phenomenon occurring in steels. During aging, free interstitials are moving from solid solution to the vicinity of dislocations and grain boundaries, where they cause less distortion in the crystal lattice, so aging also changes the thermoelectric power. On the basis of this phenomenon, the free interstitial content (C and N) can be accurately (within 2-3 ppm precision) measured. In this way, the amount of nitride or carbide precipitations can be evaluated on the basis of the change of the free interstitial content. It was also verified by comparison of thermoelectric power and internal friction measurements that the effect of free nitrogen and carbon on thermoelectric power can be separated [4]. The principle of this methodology is illustrated in Figure 3. The aim of the methodology was to evaluate the precipitated nitride fraction after heat treatment of steel specimens at temperatures $T_p=600\dots700$ °C for different times t_p .

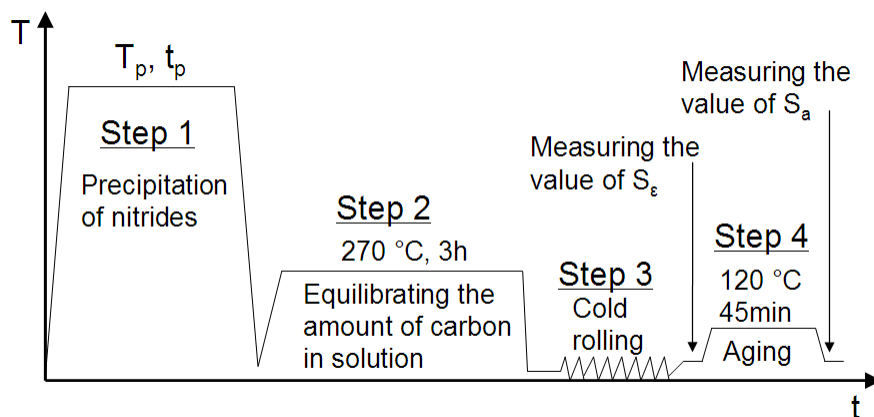


Figure 3

Method for measuring the nitride precipitation kinetics in hot rolled state [4]

It is obvious that after heat treatment at temperature T_p for any time t_p the amount of dissolved carbon and precipitated nitrogen can be quite different in each specimen. In order to ensure equal amount of carbon in solid solution for each sample, a low temperature treatment at 270 °C for 3 hours and water quenching was performed (Step 2). After this operation only a little amount of carbon (it is called residual carbon) remains in interstitial state (usually about 10-15 ppm) and according to the earlier studies [4, 12] this amount seems to be equal in all samples regardless to the prior treatment temperature (T_p) and time (t_p).

It is not possible of forming iron-nitride at this low temperature (270 °C) if the total nitrogen content of the steel is smaller than 0.01 w.t. % [14]. Moreover the precipitation of aluminium- and other nitrides is also unlikely because of the low diffusion rate of substitutional elements [3]. Another role of this treatment is to precipitate as much carbon from solid solution as possible, and ensure a reference state for all samples. The water quenching after the treatment at 270 °C results in a supersaturated solid solution of carbon and free nitrogen in steel. The next steps are designated to make visible the dissolved nitrogen and carbon. In the third step cold rolling has been followed by 75% reduction in thickness, this causes a large dislocation density microstructure. In this state the thermoelectric power of the samples denoted by S_e was measured. The fourth step is an aging at 120 °C for 45 minutes, which causes the elimination of carbon and nitrogen from solid solution and transfers the interstitials to the vicinity of dislocations. It was proved that all of the nitrogen can be eliminated from solid solution by aging if the dislocation density is large enough [4]. In order to trap all of the free nitrogen in the vicinity of dislocations during aging, the cold reduction in Step 3 should be larger than 50%. If the nitrogen and carbon atoms are completely eliminated from solid solution, then they are invisible by TEP [4, 12]. After the aging operation the thermoelectric power of the specimens denoted by S_a was measured. The difference between the S_e and S_a ($\Delta S_a = S_a - S_e$) gives information about the free interstitial content of the steel. Using the Nordheim-Gorter law [13], the difference ΔS_a can be expressed as:

$$\Delta S_a = S_a - S_e = K_C \cdot x_C + K_N \cdot x_N. \quad (3)$$

If all of the nitrogen has been precipitated (after treatment at high T_p temperature for long time), only the dissolved carbon atoms move from solid solution to the vicinity of dislocations. This means that only the so-called residual carbon contributes to the value of ΔS_a . In this case the amount of dissolved carbon at 270 °C can be calculated as:

$$x_C = \Delta S_a / K_C. \quad (4)$$

If the nitrogen is not completely precipitated as nitrides, the amount of free nitrogen can be expressed as:

$$x_N = (\Delta S_a - K_C \cdot x_C) / K_N. \quad (5)$$

Based on the above concept the precipitated fraction (Y) of nitrides can be evaluated as:

$$Y = 1 - x_t / x_M, \quad (6)$$

where x_t is the amount of free nitrogen at treatment time t_p , and x_M is the maximal free nitrogen content of the steel.

The aim of this study is to present a methodology for measuring the precipitated nitride fraction during continuous heating of the cold rolled strip, and to determine the general conditions for producing good formable sheets. Another purpose of this study is to present the effect of the degree of overlapping between the nitride precipitation and recrystallization on the cold formability.

2 Experimental

2.1 Material

The material investigated in this study is an aluminium killed low carbon steel having the following composition (in w.t. %): 0.044 C, 0.261 Mn, 0.009 Si, 0.008 P, 0.009 S, 0.028 Cu, 0.018 Cr, 0.015 Ni, 0.031 Al, 0.006 N, 0.001 Ti. The industrial processing of the steel started with the reheating of the slab to 1270 °C, which was followed by hot rolling to 4 mm thickness. The average finish temperature of hot rolling was 883 °C, whilst the average coiling temperature was 565 °C. After that the hot rolled strip was cold rolled to 1 mm thickness. Due to the low coiling temperature, most of the nitrogen content of the steel is expected to be in solid solution [1].

The free nitrogen content of the steel was measured in hot rolled state according to the concept presented in Fig. 3 and a value of 49 ppm was obtained.

2.2 Evaluation of Free Nitrogen Content in Cold Rolled and Partially Recrystallized State

To measure the free nitrogen in cold rolled or partially recrystallized state the methodology of Massardier et al. has been modified. The modified methodology is demonstrated in Figure 5. During the batch annealing process, 20-60 °C/hour heating rate is usual [1, 2]; therefore the first step of the modified methodology is heating up the cold rolled specimens with constant heating rate (20, 55 and 120 °C/h) up to temperature $T_i = 50 \dots 700$ °C. Then specimens were cooled down from every applied T_i temperatures with 10 °C/min cooling rate. After cooling down, the thermoelectric power of the specimens denoted by S_T was determined.

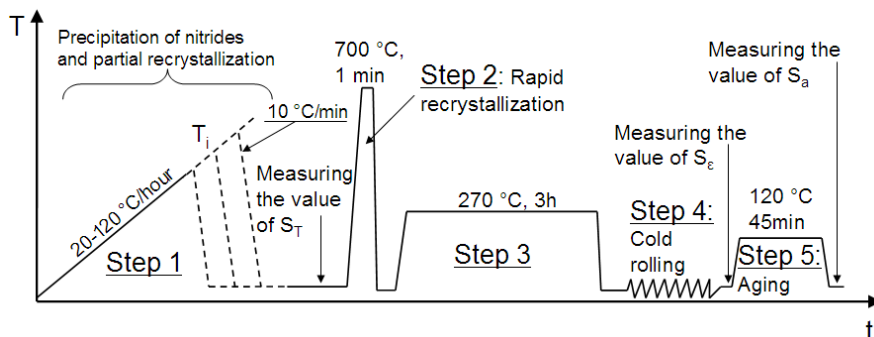


Figure 5

Method for measuring the nitride precipitation kinetics in cold rolled or partially recrystallized state

The specimens are either in cold rolled or in partially recrystallized state after the first treatment. In this state almost all of the free nitrogen and carbon in the steel is located in the vicinity of dislocations, so, a heat treatment at 270 °C would be ineffective for the amount of interstitials in solid solution.

Therefore an additional step, a heat treatment at 700 °C for 1 min was inserted in order to lower the dislocation density of the specimens. During this step, the recrystallization finishes completely, but the precipitated fraction of nitrides increases only with negligible amount. This fact is proved by measurement of free nitrogen content of the steel in hot and in cold rolled state. Approximately the same results were obtained in both microstructural states; it means that the rapid recrystallization (700 °C, 1 min) does not influence significantly the free nitrogen content of the steel. After the rapid recrystallization treatment, the specimens have a similar dislocation density as the hot rolled specimens after isothermal treatment at temperature T_p for time t_p (see Fig. 4). Therefore from this point the evaluation of free nitrogen content of the steel is exactly the same as in hot rolled state (see Fig. 4). The third step of the modified methodology is a heat treatment at 270 °C for 3 h, which was followed by a second cold rolling and aging (the fourth and fifth steps). The thermoelectric power of the specimens was measured before and after the aging treatment, and the free nitrogen content of the steel was determined by the same way as it was outlined in Section 1.3. The method described in this study provides the evaluation of the amount of precipitated nitrides 1-2 ppm precision, which can be advantageously used for estimating the uncertainty in various mathematical models [15].

2.3 Investigation of recrystallization process

In order to investigate the recrystallization process, the Vickers-hardness of the specimens was measured at room temperature after Step 1 (see Fig. 5) using a load of 70.63 N (7.2 kg). The hardness was measured in the midthickness of the sheet.

After the metallographic preparation of the samples, the recrystallized fraction has been also determined using the conventional point-counting method in the centre of the sheet.

2.4 Testing of Formability of Heat-treated Sheets

The formability is characterized with the plastic strain ratio (r -value) estimated from tensile tests and using Erichsen cupping tests. The r -value was measured on tensile test specimens prepared perpendicular to the rolling direction according to ISO 10113:2006 [16]. Square-shaped pieces were prepared to investigate their formability with Erichsen tests according to ISO 20482:2003 [17]. The cold rolled samples were heated with heating rate 20, 30, 55, 85 and 120 °C/h to 690 °C and held at this temperature for six hours. After cooling, three Erichsen and three tensile tests were performed on each group of specimens.

3 Results and Discussion

3.1 The Change of Hardness during Continuous Heating

Diagrams in Figure 6 show the change of hardness against temperature after heat treatment with different heating rates and final heating temperatures.

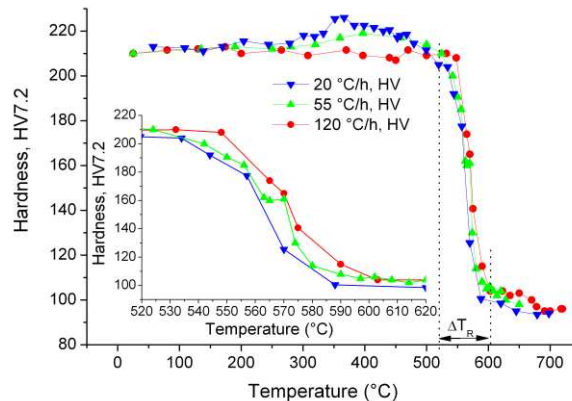


Figure 6

The hardness of cold rolled samples heated with different heating rate

As it can be seen in Figure 6, the heating rate influences the change of the hardness. At 20 and 55 °C/hour heating rate, the hardness increases in the temperature interval $T=300\text{...}450$ °C. The hardness change in this temperature

interval is found to be $14 (\pm 2)$ and $7 (\pm 2)$ HV7.2 at heating rate 20 and 55 °C/h, respectively. In spite of that, no hardness change was detected at heating rate 120 °C/h between 300 and 450 °C. The hardness increase could be explained with the nitride precipitation process, which can occur at low heating rates (20-55 °/h), but it is not able to proceed significantly at large (120 °C/h) heating rate. This phenomenon will be explained in Section 3.3.

In the temperature interval ($\Delta T_R=525-600$ °C) recrystallization occurs at all heating rate. The temperature range of recrystallization is shown in Fig. 6 and denoted by ΔT_R , whilst the start temperature of recrystallization is denoted by T_R . The shift of the temperature at 50 % recrystallized fraction due to the heating rate change from 20 to 120 °C/h is approximately 15 °C. The recrystallized fraction was measured by the generally used point-counting method after metallographic preparation of partially recrystallized samples. The relation between the hardness and recrystallized fraction is shown in Fig. 7.

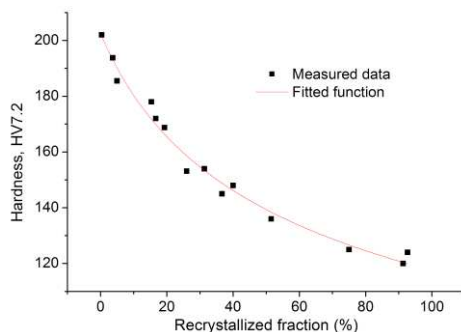


Figure 7

The relation between hardness and recrystallized fraction

In order to establish a mathematical relation between hardness and recrystallized fraction, a simple power function was fitted on the measured data:

$$HV = 212 - 12.2 \cdot X^{0.45} \quad (7)$$

where X is the recrystallized fraction. At the initiation of the recrystallization process ($X=0$) 212 HV7.2 hardness was measured, which equals to the hardness of the cold rolled sheet.

3.2 The Change of Thermoelectric Power during Continuous Heating

The thermoelectric power of specimens after Step 1 (see Fig. 5) denoted by S_T was measured for each sample. The change of TEP and hardness are plotted together against temperature in Fig. 8.

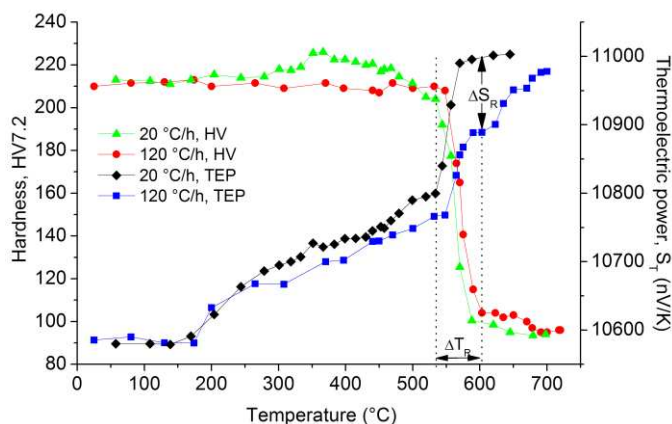


Figure 8

The relation between hardness and recrystallized fraction

No hardness and TEP change was detected below 200 °C. In temperature range 200...525 °C the TEP of specimens increases, but the change is more intensive at 20 °C/h than at 120 °C/h. In the temperature interval of recrystallization ($\Delta T_R=525-600$ °C) the TEP significantly increases. At the end of the recrystallization process, a TEP difference denoted by ΔS_R (≈ 110 nV/K) appears between the specimens heated at 20 and 120 °C/h. This difference is attributed to the fact that at 20 °C/h heating rate much more metallurgical processes occur, which decrease more intensively the distortion of the crystal lattice. As it will be presented in the next section, the nitride precipitation process also contributes to difference ΔS_R . In the temperature range 600...700 °C (after recrystallization), the TEP of specimens heated at 120 °C/h increases, whilst at heating rate 20 °C/h no TEP change was obtained. The hardness of specimens after recrystallization is found to be a little bit larger (~ 105 HV7.2) at 120 °C/h than at 20 °C/h. The increase in hardness and TEP in temperature interval 600...700 °C is also attributed to the effect of nitride precipitation process.

3.3 The Change of Free Nitrogen Content of the Steel

The free nitrogen content of the specimens was measured according to the method outlined in Section 2.2 and demonstrated in Fig. 5. The change of the free nitrogen content of the steel is shown in Fig. 9.

In Fig 9, the temperature interval of recrystallization (ΔT_R) also indicated. The amount of free nitrogen at low temperatures (100-200 °C) equals the amount of it in hot rolled state (~ 49 ppm). This means that the rapid recrystallization operation (Step 2, 700 °C, 1 min, see Fig. 5) does not change the significantly the amount nitrogen in solid solution.

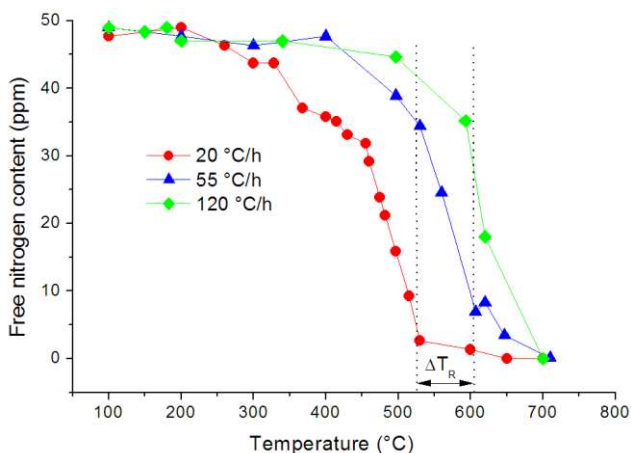


Figure 9

The change of free nitrogen content in continuously heated specimens

The nitride precipitation process precedes the recrystallization at 20 °C/h heating rate. At 55 °C/h, the precipitation and recrystallization occur concurrently, and a slight retardation in the recrystallisation can be also observed between 560 and 575 °C (See Fig. 6). At 120 °C/h the nitride precipitation proceeds mainly after the recrystallization finished. The difference ΔS_R in TEP after recrystallization (see Fig. 8) can be explained by the amount of free nitrogen and substitutionals in solid solution. After recrystallization, at heating rate 120 °C/h much more nitrogen (~30 ppm) is remained in solid solution than at 20 °C/h heating rate. Due to the crystal lattice distortion caused by the solute atoms, a lower TEP was measured at 120 °C/h heating rate after recrystallization. This solute nitrogen precipitates in the temperature interval 600-700 °C at heating rate 120 °C/h, which causes a TEP and a slight (7 ± 2 HV7.2) hardness increase (see Fig. 8).

For the better understanding, the change of free nitrogen content of the steel is plotted together with the hardness change for the experiments performed at 20 °C/h heating rate in Fig. 10.

At heating rate 20 °C/h the nitrogen precipitates mainly in cold rolled state in the temperature interval 250...520 °C. Between 250 and 450 °C, the third part of the free nitrogen precipitates as nitrides, this causes a slight hardness increase ($\sim 14 \pm 2$ HV7.2). At temperatures larger than 450 °C, the recovery, recrystallization and restoration of microstructure lower the hardness, and the effect of precipitates disappears.

In order to study the relation between the formability and recrystallization – precipitation sequence, some additional measurements were performed. The free nitrogen content of the steel was measured at the beginning of the recrystallization (at $T_R = 525$ °C) at heating rates 20, 30, 55, 85 and 120 °C/h.

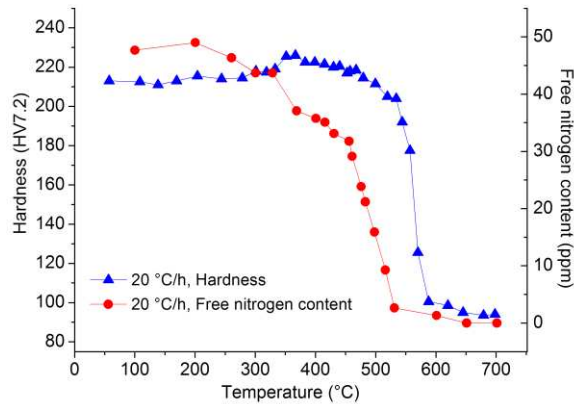


Figure 10

The change of free nitrogen content in continuously heated specimens

3.4 Formability test Results

The formability of heat treated sheets is characterized by the r -value determined using tensile tests and by the so-called cupping indices measured applying the conventional Erichsen-test. The results are presented in Fig. 11.

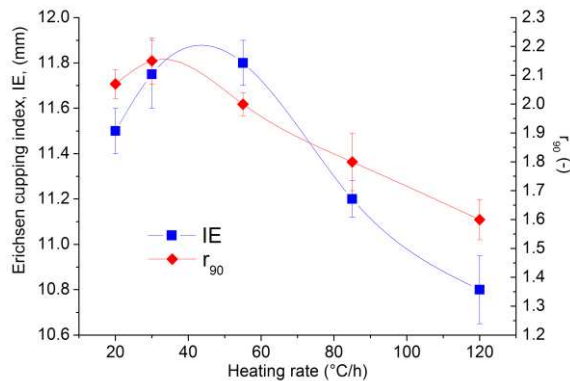


Figure 11

The change of the formability with heating rate during batch annealing

The formability reaches its maximum between heating rate 30 and 45 °C/h. The cupping indices measured at 30 and 55 °C/h heating rate are found to be almost the same (11.75 and 11.8). The correspondence between the nitride precipitation – recrystallization sequence and the optimal formability can be explained with the aid of Fig. 12. In this figure the precipitated nitride fraction was plotted against the heating rate at the beginning of recrystallization.

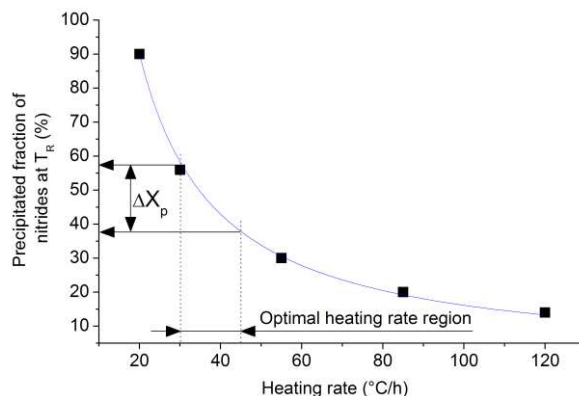


Figure 12

Effect of heating rate on the precipitated fraction of nitrides at the start temperature (T_R) of recrystallization

The precipitated nitride fraction at the beginning of the recrystallization depends on the heating rate. As it is revealed in Fig. 12, in the interval of the optimal heating rate (30-45 °C/h) the precipitated fraction of nitrides is ranging between 38 and 58%. According to the references [1, 3], the nitride precipitation can occur before or during the recrystallization. From the results presented in this section, it can be concluded that for ensuring good formability, the nitride precipitation should reach at least ~ 40% extent in the cold rolled sheet before the recrystallization process begins. On the basis of this observation, the industrial batch annealing process can be optimized by the adjustment of the heating rate during the heating up stage of the process.

Conclusions

The relationship between the formability and nitride precipitation – recrystallization sequence was investigated on 75% cold rolled low carbon aluminium killed steel. On the basis of the experiments, the following conclusions can be drawn:

- 1) The recrystallization process of 75% cold rolled sheet occurs in the temperature range 525-600 °C at heating rates between 20 and 120 °C/h. The shift of the recrystallization temperature is found to be 15 °C at 50% recrystallized fraction due to the heating rate change from 20 to 120 °C/h.
- 2) During the annealing treatment of the cold rolled strip, the nitride precipitation process occurs before the recrystallization at heating rate 20°C/h, concurrently the recrystallization at heating rate 55 °C/h and after the recrystallization at heating rate 120 °C/h.
- 3) The precipitation of 15 ppm nitrogen during heating up with 20 °C/h of the cold rolled steel results in a slight ($\sim 14 \pm 2$ HV7.2) hardness increase. The

possible further hardness increase due to the precipitation of nitrides is eliminated by the recovery and recrystallization.

- 4) The formability of cold rolled and annealed sheets reaches its maximum, if 30...45 °C/h heating rate is applied. In this case, $r_{90}=2.1$ and $IE=11.7...11.8$ mm was measured.
- 5) In order to obtain an optimal formability, the precipitated nitride fraction should reach ~38...58% at the beginning of the recrystallization.

Acknowledgement

The author wishes to express his sincere thanks to László Dévényi, for providing with all the necessary facilities. The author is also indebted to Gedeon Richter Talentum Foundation for its financial support.

References

- [1] R. K. Ray, J. J. Jonas, R. E. Hook, "Cold Rolling and Annealing Textures in Low Carbon and Extra Low Carbon Steels", *International Materials Reviews*, Vol. 39, No. 4, 1994, pp. 129-172
- [2] S. S. Satyam, B. J. Kishor, "Heating Rate Effects during Non-Isothermal Annealing of AIK Steel", *Journal of Materials Engineering and Performance*, Vol. 12, No. 2, 2003, pp. 157-164
- [3] F. G. Wilson, T. Gladman, "Aluminium Nitride in Steel" *International Materials Reviews*, Vol. 33, No. 5, 1988, pp. 223-286
- [4] V. Massardier, V. Guétaz, J. Merlin, M. Soler, "Kinetic and Microstructural Study of Aluminium Nitride Precipitation in a Low Carbon Aluminium-killed Steel", *Materials Science and Engineering A*, Vol. 355, No. 1, 2003, pp. 299-310
- [5] Y. Meyzaud, P. Parniere, "Etude du recuit des tôles mines d'acier extra-doux par resistivité électrique" *Mémoires Scientifiques de la Revue de Métallurgie*, Vol. 71, No. 7, 1974, pp. 415-434
- [6] H. F. Beeghly, "Determination of Aluminum Nitride in Steel", *Analytical Chemistry*, Vol. 21, No. 12, 1949, pp. 1513-1519
- [7] A. Brahmi, R. Borrelly, "Study of Aluminium Nitride Precipitation in Pure Fe-Al-N Alloy by Thermoelectric Power Measurements", *Acta Materialia*, Vol. 45, No. 5, 1997, pp. 1889-1897
- [8] J. P. Ferrer, T. de Cock, C. Capdevila, F. G. Caballero, C. G. de Andre's, "Comparison of the Annealing Behaviour between Cold and Warm Rolled ELC Steels by Thermoelectric Power Measurements", *Acta Materialia*, Vol. 55, No. 6, 2007, pp. 2075-2083

- [9] S. Carabajar, J. Merlin, V. Massardier, S. Chabanet, "Precipitation Evolution during the Annealing of an Interstitial-Free Steel", *Materials Science and Engineering A*, Vol. 281, No. 2, 2000, pp. 132-142
- [10] M. H. Biglari, C. M. Brakman, E. J. Mittemeijer, S. Van Der Zwaag, S., "The Kinetics of the Internal Nitriding of Fe- 2 At. Pct Al Alloy" *Metallurgical and Materials Transactions A*, Vol. 26, No. 4, 1995, pp. 765-776
- [11] R. Rana, S. B. Singh, O. N. Mohanty, "Thermoelectric Power Studies of Copper Precipitation in a New Interstitial-Free Steel" *Scripta Materialia*, Vol. 55, No. 12, 2006, pp. 1107-1110
- [12] V. Massardier, N. Lavaire, M. Soler, J. Merlin, "Comparison of the Evaluation of the Carbon Content in Solid Solution in Extra-Mild Steels by Thermoelectric Power and by Internal Friction" *Scripta Materialia*, Vol. 50, No. 12, 2004, pp. 1435-1439
- [13] L. C. Nordheim, J. Gorter, "Bemerkungen über Thermokraft und Widerstand", *Physica*, Vol. 2, No. 4, 1935, pp. 383-390
- [14] R. Rawlings, J. Tambini, "The Determination of α Phase Boundaries of the Iron-Nitrogen System by Internal Friction Methods", *Journal of Iron and Steel Institute*, Vol. 184, No. 11, 1956, pp. 302-308
- [15] L. Pokorádi, "Uncertainties of Mathematical Modeling", *Proc. of the 12th Symposium of Mathematics and its Applications*, 05-07 Nov. 2009, pp. 471-476
- [16] ISO 10113:2006 Metallic Materials - Sheet and Strip - Determination of Plastic Strain Ratio
- [17] ISO 20482:2003 Metallic Materials - Sheet and Strip - Erichsen Cupping Test

Increasing RSSI Localization Accuracy with Distance Reference Anchor in Wireless Sensor Networks

Ugur Bekcibasi¹, Mahmut Tenruh²

¹ Mugla S. K. University, Faculty of Technology, Department of Information Technology, 48000 Mugla, Turkey; e-mail: ugur@mu.edu.tr

² Mugla S. K. University, Department of Electrical and Electronics Engineering, 48000 Mugla, Turkey; e-mail: tmahmut@mu.edu.tr

Abstract: Localization is a prominent application and research area in Wireless Sensor Networks. Various research studies have been carried out on localization techniques and algorithms in order to improve localization accuracy. Received signal strength indicator is a parameter, which has been widely used in localization algorithms in many research studies. There are several environmental and other factors that affect the localization accuracy and reliability. This study introduces a new technique to increase the localization accuracy by employing a dynamic distance reference anchor method. In order to investigate the performance improvement obtained with the proposed technique, simulation models have been developed, and results have been analyzed. The simulation results show that considerable improvement in localization accuracy can be achieved with the proposed model.

Keywords: RSSI; Wireless Sensor Networks; WSN Localization

1 Introduction

The wireless sensor network (WSN) concept was first emerged in early 1980s. Since 1990s, it has been an important research area due to the progresses in micro electro-mechanic systems (MEMS) and wireless communication techniques. Although wireless sensor networks were initially used mainly in military applications, they have also been used in various applications in different areas. Depending on the hardware configurations, WSNs can be used to acquire data about various physical properties such as temperature, humidity, light, pressure, movement, soil composition, noise level, existence, weight, dimensions, velocity, direction, location [1]. WSNs can be deployed in various environments, where wired networks are impossible or impractical to deploy.

Due to their features such as reliability, flexibility, self-organization, and ease of deployment, WSNs have a wide range of present and possible future application areas. In the environment they are used, WSNs can interactively acquire data. WSNs have been an attractive research area, and therefore, experienced a rapid development, and found a variety of application areas such as military applications (C⁴ISRT) [2], environmental detection and monitoring [3], disaster prevention and rescue, medical applications, body network [4], smart house systems [5], smart fields [6], the cricket location support system [7], cooperative localization and tracking with a camera-based WSN [5] and resources tracking at building construction sites [8].

One of the important application areas of WSN is localization, on which several research studies have been realized, and several techniques have been developed. The common problem in localization is the additional hardware requirement and power consumption. The additional hardware and the resulting increased power consumption do not fit the energy-efficient WSN concept. The most power consuming component in a WSN node is the communication unit. Therefore, several research studies also investigate the ways to save energy. In addition, the environmental conditions make further studies necessary for better performance localization. Several studies investigated localization in WSNs with different techniques such as range-based [9], range-free [10], use of anchor and recursive solutions [11], MDS-based [12], centralized-distributed [9], mobile assisted [13], and cluster-based [14, 15].

In this study, a new method which uses a fourth anchor node as a measurement reference in received signal strength indication (RSSI) technique is introduced. In order to investigate the performance of the introduced method, simulation models have been designed and the results have been evaluated. According to the simulation results, the new method provides considerable performance improvement in localization.

The rest of the paper is organized as follows. In Section 2, a review of localization techniques in WSNs is provided. In this section, distance estimation, position computation, and localization algorithms are investigated. In addition, the factors affecting RSSI measurement and accuracy are also included. In Section 3, the simulation model is introduced. In order to compare performance improvements in localization, a second simulation model with the traditional method has also been designed. In Section 4, the simulation results are investigated and performance analysis is realized. The simulation results for the new model and traditional model are compared in graphs and tables. Finally, Section 5 provides the concluding remarks for the paper.

2 Localization In Wireless Sensor Networks

Localization is one of the main application areas in wireless sensor networks. Localization can be used in various applications such as determining coverage area of WSN, monitoring location changes, geographical area-based routing, and location directory services. Wireless sensor networks may contain hundreds of nodes; where it may cause a high cost to use the global positioning system (GPS) for each node [16]. Therefore, as stated in the study by Sheu et al (2008), such a solution is not suggested. In addition, as GPS receivers require relatively high energy, it is not suitable for the fundamental idea of energy-efficient WSNs.

In applications where only local location information is sufficient, there is no need for GPS. In this case, sensor nodes with known locations, called anchors, are used to determine the local coordinates of other nodes. In applications requiring global localization information, anchor nodes with GPS can be used, or anchor nodes can be located at known coordinates [16].

Several studies suggest different measurement techniques and localization algorithms. WSN localization techniques can be classified into several categories. The localization process is generally comprised of three phases. These are distance estimation; position computation; and localization algorithm [17].

Distance Estimation: In the distance estimation phase, the relative distances between the nodes are estimated via the measurement techniques. The four common measurement techniques can be classified as the angle of arrival (AoA), time of arrival (ToA), time difference of arrival (TDoA), and received signal strength indicator (RSSI). These are also known as range-based localization techniques.

Position computation: The coordinates of a node are calculated via the range or connectivity information. The main techniques used in localization are lateration, multilateration, and angulation. The lateration technique is used to compute the location of a node with the distance measurements obtained by three anchor nodes [9]. With the range information obtained by four anchors, it is also possible to realize three-dimensional localization. Trilateration is the process of lateration realized with three anchors. Lateration with more than three anchors is called multilateration. In angulation or triangulation method, the localization is computed based on the angle information obtained at least via three anchor nodes. In this method, the computation is realized by the node itself with the AoA information using trigonometric solutions [9].

Localization algorithms: WSN localization algorithms can be classified into several categories such as: single-hop or multi-hop based on the node connectivity and topology; range-based or range-free based on the dependency of the range measurement; distributed or centralized position computation [17].

Determining the distance between two communicating nodes is essential for localization in wireless sensor networks. In range-based algorithms, localization is realized with the distance information between two nodes obtained via several techniques such as angle of signal arrival, time difference of signal arrival, and received signal strength [9]. Since range-based algorithms require measurement at least via one anchor node, these techniques are also known as one-hop techniques [18].

2.1 Localization with Received Signal Strength Indication

In this study, the RSSI technique is used as the distance estimation method. The RSSI technique is based on the received signal strength indicator to estimate the distance between neighboring nodes. In free-space, the RSSI value is inversely proportional to the squared distance between the transmitter and the receiver. The radio signals attenuate with the increase of the distance. The propagation of the radio signals may be affected by reflection, diffraction, and scattering. Especially in indoor environments, such effects may impact the measurement accuracy. Therefore, this technique is more suitable for outdoor, rather than indoor applications.

This technique has the advantage of requiring no additional hardware since the RSSI feature exists in most wireless devices, and there is no significant impact on the local power consumption [11].

RSSI is affected from some factors that cause localization errors and reduce accuracy. These errors can be classified into two groups as environmental and device errors. Environmental errors are caused due to wireless communication channel. The causes are usually multi path, shadowing effect, and interference from other RF sources. Device errors are usually caused due to calibration errors, and the important issue here is to keep constant transmit power even under the circumstances of device differences and depleting batteries.

Signal samples, even with the same transmit power, show some standard deviations due to atmospheric conditions. Temperature, for example, has a little effect on a signal. However, rain can affect the signal considerably. Especially, in localization based on the received signal strength method, this will cause less accuracy and reliability [19].

2.2 Localization Process in the Introduced Model

In order to realize the localization with the introduced reference anchor node, which provides the dynamic coefficient for more accurate distance measurements, the following equations are used [20]. First, the RSSI value can be calculated with the Equation 1:

$$RSSI = -(10 \cdot \eta \cdot \log(d) + A) \quad (1)$$

where RSSI is the Received Signal Strength indicator measured by the receiving anchor node. In this case, the receiving node is the base node, and the sending node is the reference anchor node. η is the coefficient depending on the environmental conditions (which may change between 1.6 and 6). d is the distance between the receiving anchor node and the sending node, in this case, the base node and reference anchor node respectively, where the distance is already known. A is the absolute value of RSSI for the distance of 1 m. given by the producer, for example, $A = -51$ dBm for CC2420 radio communication chip by the TI.

Then, in order to compute the coefficient (η), also recomputed in every localization process according to the changing environmental conditions, the following equation is used:

$$\eta = \frac{RSSi + A}{-(10 \log d)} \quad (2)$$

The coefficient η is computed with the RSSI value obtained from the reference anchor by the base node. As the distance to the reference anchor is already known, this distance is used in the equation to compute the η coefficient. Then, the computed η is used to estimate more accurate distance values with the RSSI values transmitted by other three anchor nodes. In order to compute the distances of the anchor nodes to the node to be localized, the following equation is used.

$$d = 10^{-\left(\frac{RSSi+A}{10\eta}\right)} \quad (3)$$

After the distances of the anchor nodes to the localized node are computed by the base node, the trilateration method is applied to estimate the exact location. As this localization process is realized with the dynamically computed η coefficient according to the changing environmental conditions for each individual localization process, more accurate localization estimates are expected.

3 Material And Method

In this study, the RSSI method is applied in the simulation models. Due to the low computation capacity on WSN nodes, and the necessity to save energy, relatively low mathematical computation requiring circular localization technique is applied. The OMNEST 4.1 simulation software is used to develop the system models.

3.1 Simulation Model

The simulation model designed in this study includes mobile, reference, and anchor nodes. In the simulation, a square area with the dimensions of 100m x 100m has been modeled. In the model, a moving node continuously transmits existing information, and the anchor nodes located at the four corners of the area relay the signal strength information of the moving node to the base anchor node. The base anchor node computes the location of moving node. The location information produced in this process can be monitored with a computer connected to the base anchor. The simulation model components and the RSSI data flow can be seen in Figure 1.

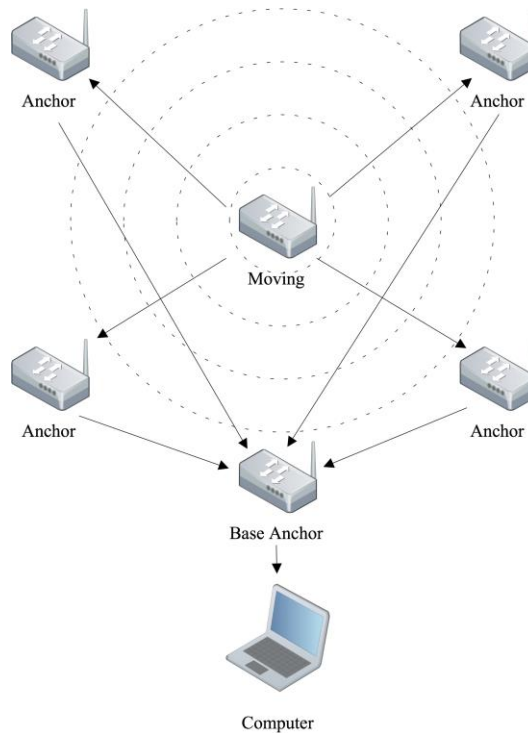


Figure 1

Simulation model functionality diagram

In this study, trilateration method is applied to compute localization. This is the method which requires the least computing power to find the intersection of three circles. Due to its computational simplicity, this method is suitable for the microcontroller in a WSN node. The trilateration method is depicted in Figure 2.

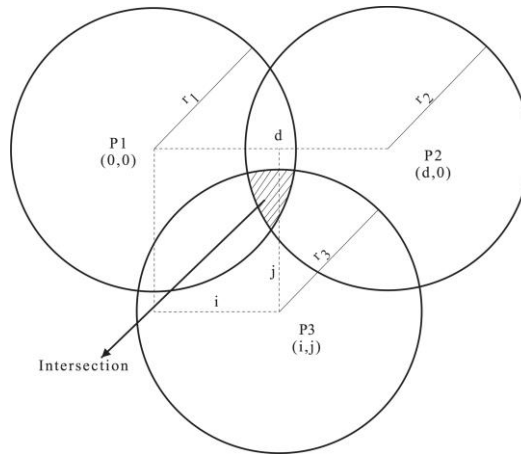


Figure 2
Trilateration method

This method finds the localization coordinates via intersection area of three circles with known radiuses on a coordinate plane by simplified equations. The equation group used in the method to compute the coordinates can be seen in Equation 4.

$$\begin{aligned}
 x &= \frac{r_1^2 - r_2^2 + d^2}{2d} \\
 y &= \frac{r_1^2 - r_3^2 + x^2 + (x-i)^2 + j^2}{2j} \\
 z &= \pm \sqrt{r_1^2 - x^2 - y^2}
 \end{aligned} \tag{4}$$

A distance of 100 m between two adjacent nodes is usually described as the coverage distance of a node with 10 mW transmit power under free space and direct line of sight conditions. Since the model is considered with two dimensions, the third dimension z is not required and excluded from computation.

The system model shown in Figure 3 includes four anchor nodes, where one node is added as a reference anchor to the traditional three anchor method.

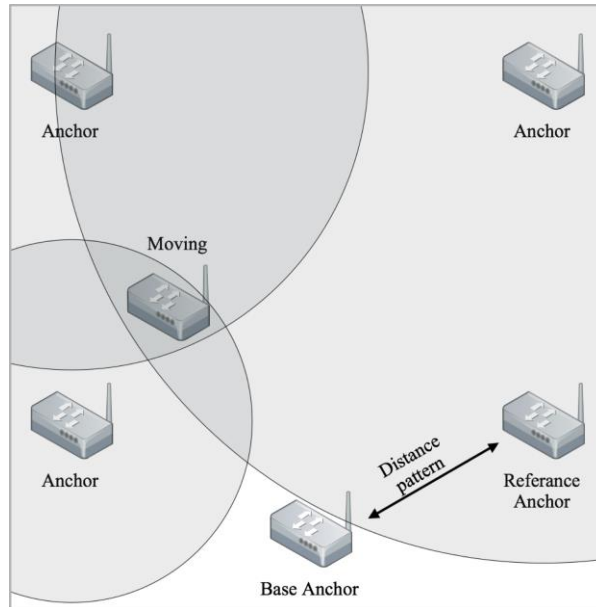


Figure 3

Four anchor measurement

In order to evaluate the performance improvement achieved with the introduced reference-anchor model, a traditional three anchor model has also been designed as seen in Figure 4.

In the proposed model, the moving node realizes periodic transmissions, and the signal strength indication (RSSI) information is produced separately at each receiving anchor node. Each anchor node transmits its RSSI information to the base node. At the base node, first three RSSI values are used to find coordinates of the moving node. Although the trilateration method is used for localization, a coefficient value obtained from the fourth anchor node is also used in localization process. The main contribution of the introduced model is that the fourth anchor node is used as a distance reference. The base node also acts as a dynamic distance coefficient producer. Since the fixed distance between the base station and the reference node is already known, the received signal strength from the reference node can be used to produce a distance coefficient at the base node. The coefficient value is determined dynamically according to changing environmental effects, such as atmospheric conditions, for every measurement. In this way, measurement errors originating from environmental effects, which result in varying RSSI values, can be eliminated considerably.

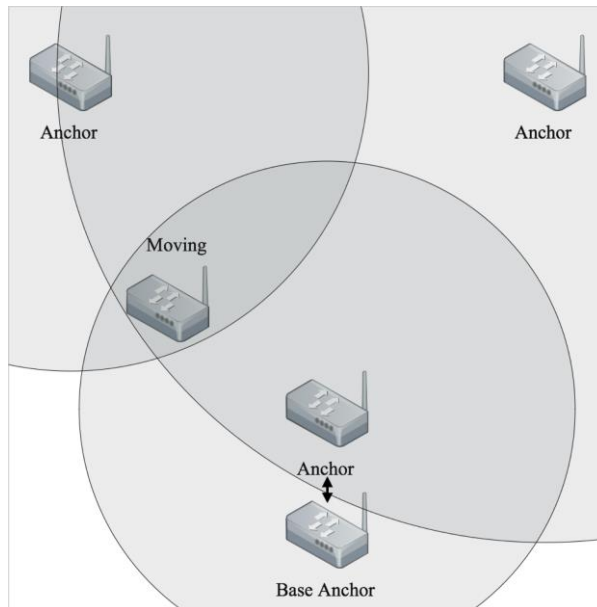


Figure 4
Three anchor measurement

The base station receives the RSSI values of the moving node from any three anchor nodes, and the fourth signal received from the last anchor is used to produce its RSSI value, which also determines the coefficient to be used in localization process. It can be argued that the coefficient value can also be produced from the received signal strength of an anchor node in the traditional three anchor model. In this concept, the fourth anchor node means an additional cost to the system. However, the fourth node also provides some advantages, such as more coverage and fault tolerance. If the moving node is outside the coverage area of one anchor, the other three anchors may still provide enough coverage. Especially in the case of one anchor node failure, the remaining three anchor nodes will still continue to function, and therefore, the system will also have fault tolerance. In this case, the coefficient is still produced by the base node with the last received signal of the three remaining nodes.

The main idea in this study is to investigate the performance improvement obtained with the reference anchor model against the traditional three anchor model. Since the focus is on the evaluation of the improvement provided by the new method, both model nodes are considered to be under the same environmental conditions. Performance improvement is based on the dynamically computed η environmental coefficient, in contrast to the constant η coefficient used in the traditional model. In order to evaluate the performance improvement, only the measurements with different fixed locations are covered. However, similar results

can be expected for moving nodes since the measurements are considered to be realized under the same conditions for both models. Figure 5 illustrates the simplified flow chart for the functionality of the system.

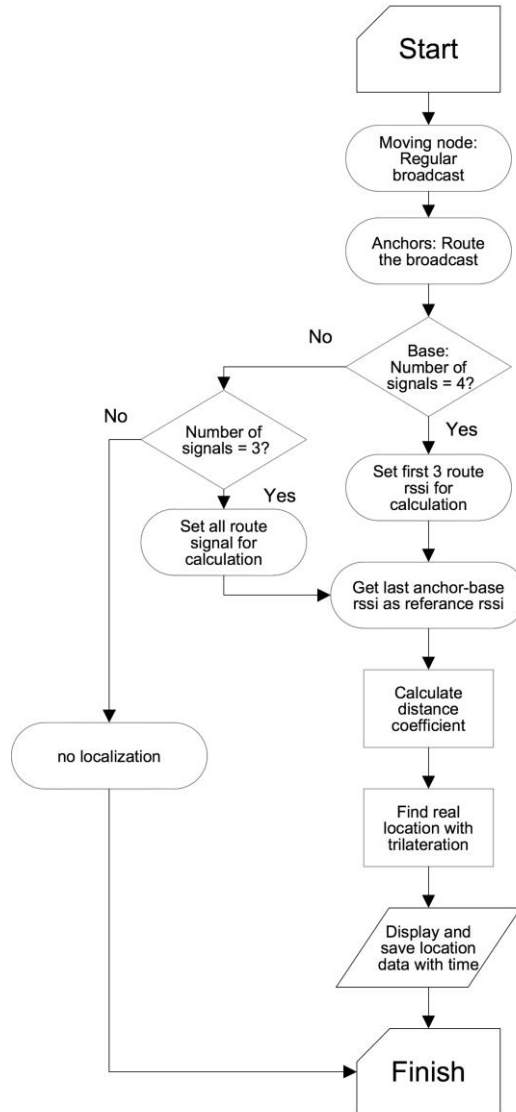


Figure 5
Simplified functionality flow chart diagram

4 Simulation Results And Performance Analysis

The simulation models have been operated with three different distance scenarios. In the first scenario, the moving node is located at the center of the area having (50;50) coordinates which have equal distances to all anchor nodes. In the second scenario, the moving node is located at the (28;37) coordinates which have different distances to the anchor nodes. The third scenario has the coordinate values of (75;50) for the moving node. These three different coordinates have been applied to both the traditional three anchor model, and the introduced fourth reference anchor model. Figure 6 and Figure 7 show the simulation models of three anchor nodes, and four anchor nodes respectively. These models aim to present the performance improvement obtained with the fourth node used as the measurement reference anchor. In the introduced model, before applying the trilateration method, the dynamic distance coefficient is used for scaling.

In the simulation studies, the localization processes have been realized repeatedly 100 times for all three coordinates. In every localization process, the coordinate values are kept constant in order to obtain the distribution of localization values for one point.

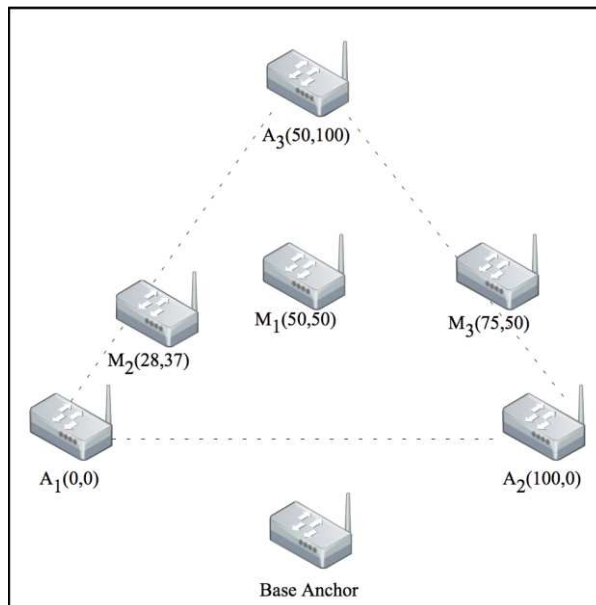


Figure 6
Simulation model for trilateration

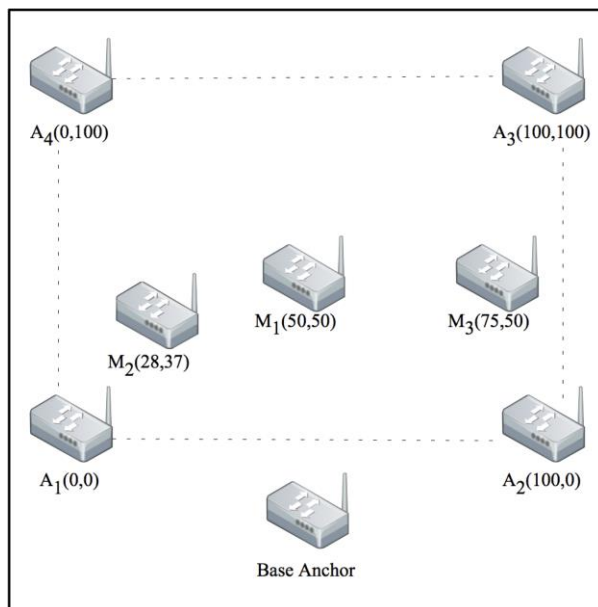


Figure 7

Simulation model for reference anchor

Simulation results for the coordinates of (50;50) can be seen in Figure 8. In this figure, the results for the both models are shown together for better comparison purposes. Table 1 provides the statistical minimum, maximum, average, and standard deviation values of the obtained measurements for both models. From the figure and table, it can be seen that although the traditional three anchor model provides a very close average value to the real point for the x axis, the y axis has a measurement error of about 2.88 meters. On the other hand, although the standard deviation value is slightly higher for the reference anchor model in y axis, the average values almost reach the exact coordinate values with only about 58.9 cm, and 61.9 cm differences on the x and y axes respectively. On the basis of the minimum and maximum measured values, although the y axis has more minimum measurement error for the introduced model, the other measurement values show better results. Moreover, as can be seen in Figure 8, the exact location coordinates are located in the center of the measured values with the reference anchor model. On the other hand, the traditional model values are scattered around a center beyond the exact location. These results show that the introduced new model produces better measurement results and has a higher performance over the traditional three anchor model.

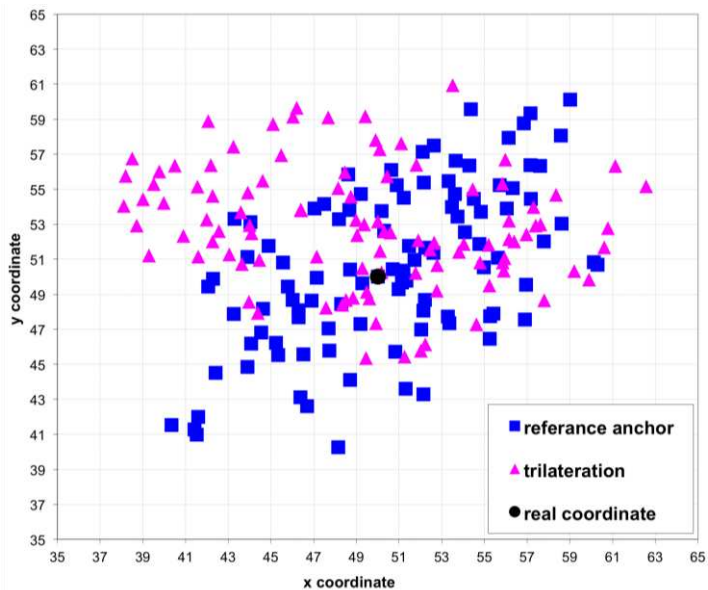


Figure 8

Measurement result for 50-50 coordinates

Table 1

Statistical values for 50-50 coordinates

(50;50)	3 anchor		Reference anchor	
	x	y	x	y
Mean	49.240	52.878	50.589	50.619
Maximum	62.572	60.936	60.289	60.106
Minimum	38.097	45.359	40.347	40.251
Standard Dev.	6.1650	3.362	4.905	4.5923

The simulation results of the both models for the (28;37) coordinates are also shown together in Figure 9. This location is chosen to be closer to the anchor node A1. As can be seen from the figure, for this location, the area of some scattered measurement results of the both models overlap. However, the exact location point is again in the center of the results obtained for the reference anchor model. Table 2 also shows the statistical results for both models. According to these results, it can be seen that the average measurement results for the reference anchor model show much better performance with the measurement differences in the order of centimeters (x: 0.073 m, y: 0.261 m), while the three anchor model produces measurement errors in the order of meters (x: 6.482 m, y: 3.199 m).

From the point of maximum and minimum measurement values, and standard deviation values, the proposed model mainly produces better results. These results show that the reference anchor model provides improved performance for also this location.

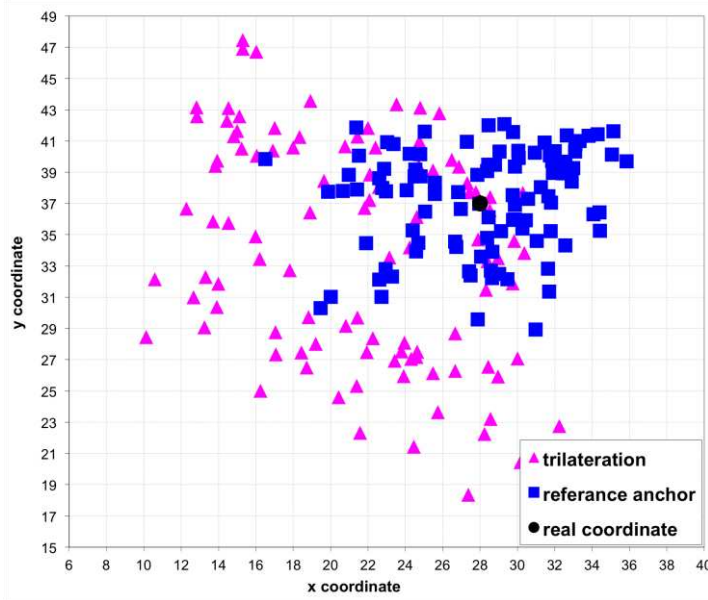


Figure 9
Measurement result for 28-37 coordinates

Table 2
Statistical values for 28-37 coordinates

(28;37)	3 anchor		Reference anchor	
	x	y	x	y
Mean	21.517	33.800	28.073	37.261
Maximum	32.240	47.457	35.852	42.079
Minimum	10.128	18.346	16.510	28.925
Standard Dev.	5.726	7.035	4.276	3.263

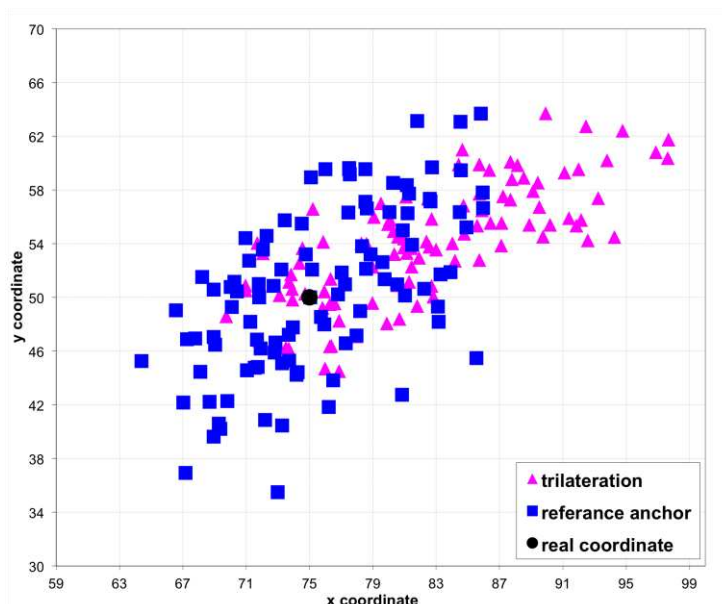


Figure 10
Measurement result for 75-50 coordinates

Table 3
Statistical values for 75-50 coordinates

(75;50)	3 anchor		Reference anchor	
	x	y	x	y
Mean	82.510	54.105	75.765	50.624
Maximum	97.675	63.725	85.964	63.694
Minimum	69.729	44.505	64.390	35.498
Standard Dev.	6.803	4.298	5.4186	6.109

Finally, the model performances are compared for the location coordinates (75;50), and the results are shown in Figure 10 and Table 3. From the figure, once more, it can be seen that the exact location point is in the center of distributed values obtained for the proposed model. The table shows that the average measurement values for the proposed model almost give the exact location coordinates with differences only in the order of centimeters (x: 76.5 cm, y: 62.4 cm), while the traditional model presents 7.51 meters, and 4.1 meters errors on the x and y axes respectively. From these results, it can be seen that the new model provides considerably better measurement performances.

Figure 11 shows all the statistical results together for comparison purposes. As seen in this figure, in all three cases the coordinates of exact points are located on the central point of value lines obtained for the proposed model. In some studies, averaging a few consequent measurements is used to obtain closer values to the exact location. From the simulation results, it is clear that a simple averaging process will produce very close values to the exact location with the proposed system.

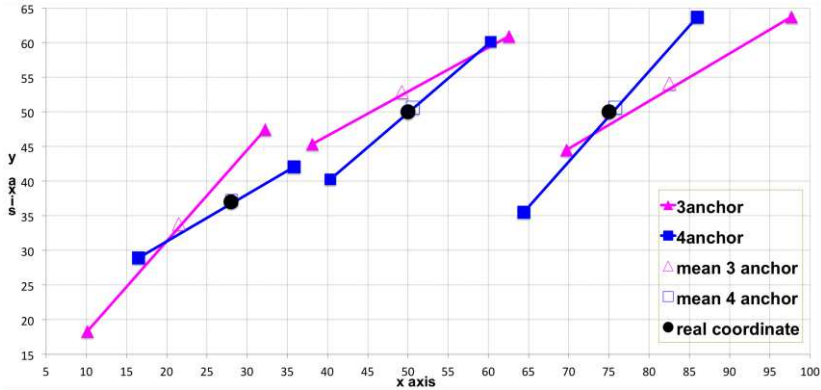


Figure 11
Measurement graphs

Conclusions

In this study, a new technique in RSSI localization method for wireless sensor networks has been introduced. The technique proposes a distance reference anchor node which provides a dynamic correction coefficient for every measurement. The distance reference anchor node provides a continuous feedback about the RSSI changes due to environmental effects. The base node uses the RSSI information from the reference anchor node to produce a correction coefficient. The coefficient is applied to the trilateration computation to find the location of a moving node. In this study, the reference node is arranged as a fourth anchor which is an additional node to the traditional trilateration model, which needs three anchor nodes for localization process. It has been explained that although adding a fourth anchor node to the system may cause an additional cost, it provides some benefits, such as more coverage area and fault tolerance.

In order to evaluate the performance improvement achieved with the proposed model, a three node traditional localization model has also been developed. Both models have been simulated for three different locations and statistical results have been obtained. The simulation results have been evaluated and the performances of the both models have been compared in graphs and tables. The simulation results showed that the proposed model with the reference anchor produced better measurement results than the traditional localization model. This

is because the proposed technique introduces the use of a correction coefficient in the localization process. The coefficient is produced dynamically according to the environmental conditions. As distance correction is realized dynamically for every localization process, the localization error is kept to a minimum. Therefore, environmental effects, such as atmospheric conditions, causing distance measurement errors, are eliminated considerably, and better localization results in WSN systems can be achieved. From the simulation results obtained in this study, it can be concluded that the proposed new technique provides considerable performance improvement in RSSI localization.

References

- [1] Akyildiz, I.: Wireless Sensor Networks: a Survey, *Computer Networks*, 38, 2002, pp. 393-422
- [2] Diamond S. M., Ceruti M. G.: Application of Wireless Sensor Network to Military Information Integration, in: 5th IEEE International Conference on Industrial Informatics, IEEE, 2007, pp. 317-322
- [3] Ma R. H., Wang Y. H., Lee C. Y.: Wireless Remote Weather Monitoring System Based on MEMS Technologies., *Sensors*, 11, 2011, pp. 2715-2727
- [4] Yang G. Z., Yacoub M.: *Body Sensor Networks*, 2006, Springer, London
- [5] Sanchez-Matamoros J. M., J. Martinez de Dios, Ollero A.: Cooperative Localization and Tracking with a Camera-based WSN, 2009 IEEE International Conference on Mechatronics, IEEE, 2009, pp. 1-6
- [6] Want R., Hopper A., Falcao V., Gibbons J.: The Active Badge Location System, *ACM Transactions on Information Systems* 10, 1992, pp. 91-102
- [7] Priyantha N. B., Chakraborty A., Balakrishnan H.: The Cricket Location Support System, 6th ACM International Conference on Mobile Computing and Networking, 2000, Boston, Massachusetts, USA
- [8] Shen X., Chen W., Lu M.: Wireless Sensor Networks for Resources Tracking at Building Construction Sites, *Tsinghua Science & Technology* 13, 2008, pp. 78-83
- [9] Mao G., Fidan B., Anderson B.: Wireless Sensor Network Localization Techniques, *Computer Networks*, 51, 2007, pp. 2529-2553
- [10] Bulusu N., Heidemann J., Estrin D.: GPS Less Low-Cost Outdoor Localization for Very Small Devices, *IEEE Personal Communications*, 7, 2000, pp. 28-34
- [11] Wang C., Xiao L.: Locating Sensors in Concave Areas, *IEEE INFOCOM 2006*, 25th IEEE Int. Conf. on Computer Communications, 2006, pp. 1-12
- [12] Ji X., Zha H.: Sensor Positioning in Wireless Ad-Hoc Sensor Networks using Multidimensional Scaling, *INFOCOM 2004*, 4, IEEE, 2004, pp. 2652-2661

- [13] Priyantha N., Balakrishnan H., Demaine E., Teller S.: Mobile-assisted Localization in Wireless Sensor Networks, 24th Annual Joint Conference of the IEEE Computer and Communications Soc., 1, IEEE, 2005, pp. 172-183
- [14] Medidi M.: Cluster-based Localization in Wireless Sensor Networks, Proceedings of SPIE, 6248, SPIE, 2006, pp. 62480J-62480J-9
- [15] Sheng X., Hu Y. H.: Collaborative Source Localization in Wireless Sensor Network System, IEEE Globecom, 2003
- [16] Sheu J. P., Member S., Chen P. C., Hsu C. S.: A Distributed Localization Scheme for Wireless Sensor Networks with Improved Grid-Scan and Vector-based Refinement, IEEE Transactions on Mobile Computing 7, 2008, pp. 1110-1123
- [17] Bal M., Liu M., Shen W.: H. Ghenniwa, Localization in Cooperative Wireless Sensor Networks: A Review, 2009, pp. 438-443
- [18] Hu L., Evans D.: Localization for Mobile Sensor Networks, MobiCom '04, October, ACM Press, New York, USA, 2004, p. 45
- [19] Clark M. P.: Radio Propagation, System Range, Reliability and Availability, Wireless Access Networks: Fixed Wireless Access and WLL Networks - Design and Operation, 2000, pp. 115-139
- [20] Wang X., Bischoff O., Laur R., Paul S.: Localization in Wireless Ad-hoc Sensor Networks using Multilateration with RSSI for Logistic Applications, Procedia Chemistry 1, 2009, pp. 461-464

Domain Specific Language Approach on Model-driven Development of Web Services

Viet-Cuong Nguyen, Xhevi Qafmolla, Karel Richta

Department of Computer Science and Engineering
Faculty of Electrical Engineering
Czech Technical University in Prague
Karlovo namesti 13, 121 35 Prague, Czech Republic
nguyevie@fel.cvut.cz, qafmoxhe@fel.cvut.cz, richta@fel.cvut.cz

Abstract: As modern distributed and cloud architecture keep gaining their popularity, web services have become the programmatic backbones of more and more systems. Developing web services requires gathering information from different aspects. Model-driven engineering promises to ease the burden of development and promote reuse of web services by focusing more on a higher level of abstraction. Current approach of modeling web services using UML is not well-suited since UML is created for multiple disciplines and is not specific for web service development. With current growing scale of distributed systems, the challenge is not only in development but also integration and maintenance of web services. Introducing a domain specific language (DSL) for modeling of web services promises to become a novel approach and could be the solution to the current problem with web service modeling and development. This article outlines the analysis as well as the current state of the problem domain and introduces an approach to model-driven development of web services by implementing a domain specific language called SWSM (Simple Web Service Modeling). This approach aims to solve problems that UML could not effectively resolve and promote efficiency with a non-complex language facility for modeling and code generation of web services. Our best practices and observation during the design of SWSM are also presented.

Keywords: web service; model-driven development; DSL; SWSM

1 Introduction

Cloud computing and distributed systems continue to gain more mainstream adoption as more companies move into the cloud. With mobile gradually taking over the desktop experience, cloud computing continues to accelerate and have more significance [17]. Model-driven Engineering methodologies have been applied (as a solution) for better reaction to market trends and aims to increase efficiency as well as bring more agility to the development life-cycle of cloud and

distributed systems. However, since there are many different applicable domains in web applications and distributed systems, it is unattainable to finalize a method or approach that would fit in every situation. This article is an effort towards the solution for this issue by analyzing the concepts involved in key aspects of web service design and introduces an approach to the development of web services by using model-driven techniques with domain specific language. As a result, a DSL for modeling of web services named SWSM (Simple Web Service Modeling) was developed and introduced. To demonstrate this approach, a case study of web service development from modeling to code generation is also illustrated with the associated techniques.

This article is structured as follows: In the next section, we review some knowledge of Model-driven Development (MDD) and domain specific language as background information. The subsequent section discusses the current state of web services development using model-driven techniques. We also highlight the features of the DSL that we aim achieve when designing a new DSL for modeling of web services. In the next section, we introduce SWSM (our designed DSL) for modeling and development of web services and how to apply it at a specific point during design phase. In the last section, we present some conclusions on web service development using SWSM and also related works of our research in the field of Model-driven Engineering.

2 Background

2.1 Model-driven Engineering

Model-driven engineering (MDE) is a software development methodology, which focuses on creating and exploiting domain models. Models can be perceived as abstract representations of the knowledge and activities that govern a particular application domain. Models are developed through-out various phases of the development life cycle with extensive communication among product managers, designers, developers and users of the application domain. MDE aims to increase productivity by maximizing compatibility between systems, simplifying the process of design and promoting communication between individuals and teams working on the system [16].

The Object Management Group's (OMG) initiatives on MDE contain the Model-driven Architecture (MDA) specification. MDA allows definition of machine-readable applications and data models that enable long-term flexibility with regards to implementation, integration, maintenance, testing and simulation [14] [15]. There are two main modeling classes in MDA:

- Platform Independent Models (PIMs): these are models of the structure or functionality, which are independent of the specific technological platform used to implement it.
- Platform Specific Models (PSMs): these are models of a software or business system, which are bound to a specific technological platform.

In the MDA, models are first-class artifacts which are later integrated into the development process through the chain of transformations from PIMs through PSMs to coded application. The mapping and transformation between PIMs and PSMs are based on meta-model concepts. These concepts can be described by technologies such as Unified Modeling Language (UML), Meta Object Facility (MOF) or Common Warehouse Meta-model (CWM) [22, 16]. These languages are considered as general-purpose modeling languages.

Currently, there are many challenges in implementing MDD due to the lack of standardization and tools. There are specific desired aspects for each application within its domain and this makes it difficult to design a tool that fits all.

2.2 Web Services

With the growing demands in recent years, distributed computing and cloud processing systems are made possible by adopting a new paradigm of Service-Oriented Computing (SOC). SOC integrates networks of connected business applications from many different locations. In the SOC paradigm, web services are currently considered one of the most dominant technologies. Web services are software systems designed to support interoperable machine-to-machine interaction over a network. The important components of web services know-how include XML technology, Web Services Description Language (WSDL), Universal Description, Discovery and Integration (UDDI) [21]. There are two popular classes of web services: REST-compliant web services and Simple Object Access Protocol (SOAP) web services [16]. Currently, the development of web services in MDD involves using UML to specify services precisely and in a technology-independent manner. However, UML is by far not the optimal way for modeling of web services. The efficiency could be improved by using a specific language to address the detailed nature of web services. Introducing a new DSL can set up the stage for automatic generation of a part of the XML and code, such as Java code, that implements the services. It also makes it easier to re-target the service(s) to use different web technologies when required.

2.3 Domain Specific Language

In software development and domain engineering, a domain specific language is a programming or specification language dedicated to a particular problem domain, a particular problem representation technique, and/or a particular solution

technique. The concept is not new. Special-purpose programming languages and all kinds of modeling or specification languages have always existed, but the term has become more popular due to the rise of domain specific modeling [19]. Adoption of domain specific language can be a solution to several problems encountered in various software development aspects. A DSL can reduce the costs related to maintaining software [5].

In comparison to other techniques, DSL is considered as one of the main solutions to software reuse [9]. On the other hand, using DSL also promotes program readability and makes its understanding easier, because it is often written at a good abstraction level. It enables users without experience in programming to create the models or programs as long as they possess knowledge of the targeted domain. Another advantage of a DSL for modeling is the ability to generate more verification on the syntax and semantics than a general modeling language. This can reduce errors (and burden) on the debugging process. DSL for modeling however also has several drawbacks. There is a long learning curve for a new language, even though as a specific language, it would be a lot easier to learn than a general programming language. Another disadvantage is the lack of capable human resources. Since a general language is adopted by more people and staff, it could be much easier to find staff capable of solving the problem using their language knowledge, rather than DSL.

2.4 Current Approaches in Web Services Development

Currently development of web services falls into two main categories associated with the order in which models are developed: bottom-up and top-down. In bottom-up development, the design process starts with a given prototype or presentation of a class. Other web service artifacts are generated from the given prototype. This means part of the implementation must be designed at the first stage. This approach implies that changes made during the first stage will propagate and require changes on all model artifacts. This can bring benefits only when there is an existing system that has a similar business logic, which was already implemented.

In top-down approach we first design the abstraction and description of a web service. After that, we add detail implementation(s) and business logic to it. In top-down process, modeling is a crucial part. A good design in this phase is very important to the overall quality of the web service. The UML approach during this phase has some drawbacks. UML is a tool for generic design, it is not conducive for addressing all aspects of web service. Besides, creating XML/WSDL is a complicated process with a lot of detail information. In contrast, modeling process at the first place is intended to abstract away unnecessary details and makes it easier to understand the system. Hence, there is a need to create a better mechanism to solely support the design of web services. Adopting a dedicated DSL for this purpose can turn into a promising approach in this situation.

3 Challenges

Advances on programming languages still cannot cover all aspects of the fast-growing complexity of web platforms. In a wide range of systems, especially distributed ones, more and more middle-ware frameworks are developed in languages such as Java or .Net, which contain thousands of classes and methods as well as their dependencies. This requires considerable effort to port systems to newer platforms when using these programming languages [17]. Therefore, general programming languages cannot be considered as first-class languages to describe system-wide and non-functional aspects of a system. There is a need to raise the level of abstraction while still providing specific domain attributes for modeling of such systems.

With mobile technology adoption continuing to gain momentum, in the next few years more cloud based and software-as-service (SaaS) systems will grow. As more systems migrate to the cloud, there is a big space for web services to continue gaining popularity. SaaS, and recently Platform-as-a-Service (PaaS), as different layers of cloud computing, require different approach to web service development and deployment. In these infrastructures, the so-called multi-tenancy becomes an essential factor. The multi-tenant architecture (as depicted in Fig. 1) ensures the customization of tenant-specific requirements while sharing the same code-base and other common resources. In this figure, four customizations of different tenants are built based on the shared service implementation and infrastructure. Web services in multi-tenant platforms need a way of abstracting away the configuration and make it possible for every part of the service to be customized for a specific tenant. These platforms are often built from the meta-data driven solution. This therefore means that the application logic can be based on meta-data which later can be customized [17].

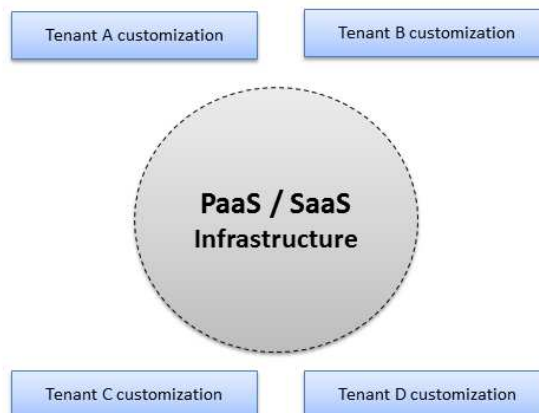


Figure 1

Multi-tenancy architecture: customizations of 4 tenant-specific requirements sharing the same base service implementation and infrastructure

The challenge in this architecture is to adopt or develop a modeling language at the appropriate abstraction level to separate the logical models from its technical aspects. This detaches the definition of service architectures independently from the used specific platforms. A modeling language raising the level of abstraction allows us to reuse models and keeps platform-specific artifacts at a separated tier in the development workflow. Having a modeling language based on services aspects with the ability to set aside technical concerns and still be able to tackle a problem in a specific platform is hard to come across.

There are existing general purpose modeling languages such as UML. UML is often used as a standard language for software systems modeling. It is able to represent various kinds of software systems, from embedded software to enterprise applications. In order to achieve this flexibility, UML provides a set of general elements applicable to any situation such as classes or relationships [1]. However, in the SaaS or PaaS architecture, the class systems in UML often force applications to be represented or surrounded by classes, this could make the models difficult to understand and use. In an effort to improve this, UML provides facilities to specialize for a specific domain, so-called UML profiles. Nevertheless, these mechanisms are not able to represent the semantics behind the domain concepts [1]. The challenge therefore remains in defining a domain specific language that can be suitable for the modeling and development of this infrastructure. In the case of modeling web services, the creation of a high-level DSL turns into a necessity for software reuse, higher development speed and better cost-effectiveness.

4 Features of a DSL as a Modeling Language

Introducing a new DSL with the support for modeling at a good abstraction level is crucial. This DSL can later be used for automatic generation of the model artifacts and code that implement the services. In theory, a general modeling language could also be used for this purpose but an appropriately designed DSL will perform the same job much more effectively. We define a set of features that are essential to the DSL design in model-driven development of web services. All of these features should be considered during the creation of a DSL to ensure the quality of the language.

Effectiveness: The language needs to be able to deliver useable output without having to re-tailor based on specific use case while being easy to read and to understand. This means that the language is able to bring up good solution on specific domain and focus on solving the particular range of problems. Effectiveness also needs to guarantee the unambiguity feature of language expressions and capability to describe the problem as a whole from a higher level.

Automation and Agility: As the modeling language can raise the level of abstraction away from programming code by directly using domain concepts, an important aspect is the ability to generate final artifacts from these high-level specifications. This automatic transformation has to fit the requirements of the specific domain. Agility ensures that models can adapt to changes efficiently. This changes from models described by the language are also propagated to the next phase of development automatically.

Support Integration: The DSL has to be able to provide support via tools and platforms. The DSL needs to be able to integrate with other parts of the development process. This means that the language is used for editing, debugging, compiling and transformation. It should also be able to be integrated together with other languages and platforms without a lot of effort.

When designing and implementing DSLs as executable languages, there is a need to choose the most suitable implementation approach. Related work from Mernik et al. [12] identifies different implementation patterns, all with different characteristics. These patterns provide another perspective to consider when making the design decisions of DSL. These options can be broken down to the following categories:

- *As interpreter:* In this method, DSL constructs are recognized and interpreted using a standard ‘fetch-decode-execute’ cycle. With this pattern no transformation takes place. The model is directly executable.
- *As compiler/application generator:* DSL constructs are translated to base language constructs and library calls. People are mostly talking about code generation when pointing at this implementation pattern.
- *Using pre-processor:* DSL constructs are translated to other constructs in an existing language (the base language). Static analysis is limited to that done by the base language processor.
- *Embedded design:* DSL constructs are embedded in an existing general purpose language (the host language) by defining new abstract data types and operators. A basic example is application library. This type of DSL is mostly called an internal DSL. The good side of this is that grammar, parsers and tools are immediately available. However, the challenge with an embedded DSL is to tactfully design the language so that the syntax is within the confines of what the host language allows, while still remaining expressive and concise [17].
- *Using extensible compiler/interpreter:* A general purpose language compiler/interpreter is extended by domain specific optimization rules and/or domain specific code generation. While extending interpreters is usually relatively easy, extending compilers is hard unless they were designed with extensibility in mind.

- *Commercial off-the-shelf*: existing tools and/or notations are applied to a specific domain. In this approach, it is not needed to define a new DSL, editor and implement them. One only needs to make use of a Model-driven Software Factory. One example is using the Mendix Model-driven Enterprise Application Platform targeted at the domain of Service-Oriented Business Applications.
- *Hybrid*: a combination of the above approaches [17].

The choice of the approach is very important because it can make a big difference in the total effort to be invested in DSL development. With the success of open source projects like Xtext, development of DSL is made affordable and the development is focused on building the grammar, while support for static analysis and validation of models are possible out of the box.

We aim to maintain the set of features defined in this section while designing SWSM. This allows us to provide automatic transformation, agility and integration to the development cycle. This ensures that the process of model-driven development of web services using SWSM is efficient.

5 Model-driven Development of Web Service using SWSM as a Domain Specific Language

Web service technologies depend on the use of XML, SOAP, WSDL. These standards are important, but they do not effectively support automation of code evolution at different phases in the development cycle. A DSL for modeling web services is therefore useful because it can effectively support automation in model-driven development. In the process of designing a suitable DSL for this purpose, we consider some valuable lessons described in the work of Wile [20]:

Lesson T2: You are almost never designing a programming language. Most DSL designers come from language-design backgrounds where the admirable principles of orthogonality and economy of form are not necessarily well-applied to DSL design. One must be careful not to embellish or over-generalize the language.

Lesson T2 Corollary: Design only what is necessary. Learn to recognize your tendency to over-design [17].

Keeping these principles as an effective approach during design, we created SWSM as a modeling language for web services at the appropriate abstraction level. As a proof of concept, this language aims to increase the efficiency of the development process by letting users focus only on modeling of the essential aspects that comprise the web service.

The syntax needs to be simple, yet expressive and concise. The possible set of simplified syntax diagrams for the components of this DSL can be depicted as follows:

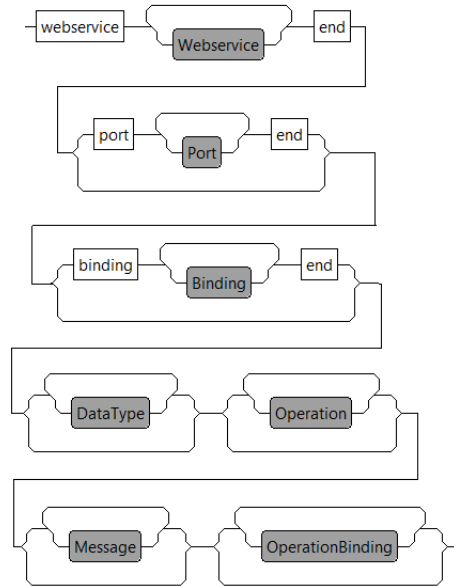


Figure 2

Simplified syntax diagram of web services with SWSM

To describe the service as an aggregation of several ports, the keyword *webservice* is used for modeling web services. Below is the syntax diagram for this model declaration:

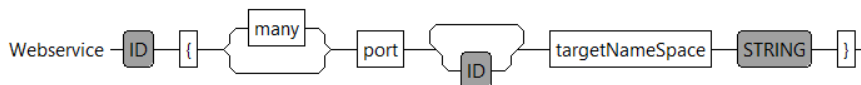


Figure 3

Web services syntax with SWSM

The semantics of the language expressions starts with the web service definition identified by its name (ID). There could be a number of ports associated with a web service and this mapping is described by the *port* keyword followed by a string identifier of a port. ID is a term representing the name (identification) of an element. The value of the target namespace is a string followed by *targetNamespace* keyword. This enables developers to specify the relationship between a port and a particular web service. In many cases, the association is a one-to-many mapping. The syntax diagram of ports can be depicted as follows:



Figure 4

Port syntax with SWSM

A port is identified by a name (ID term). It consists of one or many operations, each operation is then defined by input and output. This structure can be seen in the syntax diagram of an operation:

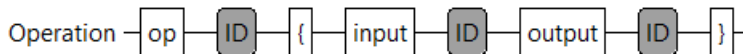


Figure 5

Operation syntax with SWSM

Each input and output of an operation is of the type *message*. The keywords *input* and *output* make the semantics of an operation signature easy to comprehend by describing the parameters for the operation with its returning type. The *message* element defines the data elements of an operation. Each message can consist of one or more fields (parts). These fields play the role of the parameters of a function call as in a traditional programming language. All modeled fields form the method signature for each operation.

Given a collection of operations $O_1 \dots O_n$ with associated input and output messages, we define the mapping to web services and ports:

- One or more operations ($O_1 \dots O_n$) are mapped to a port P1 to describe one function of a web service.
- P1 defines the connection point to a web service, one or more web services ($W_1 \dots W_n$) are modeled within an SWSM file.

The message format and protocol details for a web service are modeled via binding. A *binding* is identified by its name (ID on the diagram) and the mapping to a port is described by *port* attribute. The binding style is represented by *bindingStyle* attribute. Value of *transport* attribute has the direct semantics of defining which transportation protocol to use. For example, in the case of HTTP, we can simply assign "*http*" to transport. This is more convenient than the approach currently used in WSDL where "*http://schemas.xmlsoap.org/soap/http*" is assigned. To define the operations that the port exposes, the mapping *operationBinding* is used. For each operation binding, the corresponding SOAP action is described with its encoding type of input and output.

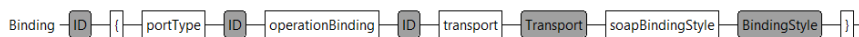


Figure 6

Binding syntax with SWSM

The best way of illustrating the syntax is to start modeling web services in a case-study. The first step in model-driven development of web services is designing the models. The output of this phase are models that conform to a web service meta-model, which can be represented in a textual format complying to the grammar of a DSL. Model artifacts are later used as input for the generation process. One of the important influencing factors is that any changes in the models will propagate changes in other stages. SWSM has a mechanism to support change propagation. To start modeling web services with SWSM, the process begins with representing the principal elements of a web service in the modeling language:

- **Types:** used to define the abstract elements in the description of the web service. They can be of a simple or complex type. They are identified by the keyword *type*.
- **Messages:** are units of information exchanged between the web service and the customer application (logically they are input/output messages and sometimes also fault messages). Each operation provided by a web service is described by at most, one input message and one output message. These messages relate to the parameters of the operation. In SWSM messages are identified by the *message* keyword.
- **Interfaces (or portTypes in WSDL1.0):** they constitute aggregations of operations provided by the service. In SWSM interfaces start with the keyword *interface*.
- **Bindings:** they specify in particular the protocol used to invoke the methods of an interface. In SWSM bindings start with the keyword *binding*.
- **Services and ports:** the service can constitute an aggregation of ports. A port is an endpoint enabling access to an interface through an URI address. Services are identified by the keyword *webservice* in SWSM. We can define multiple web services within one single design [18].

Utilizing MDD principles, web service development using SWSM can be decomposed into four steps:

1. Modeling the web service using SWSM language.
2. Enhancement and automatic validation of web service models.
3. Generating Java code using built-in code generation feature of SWSM.
4. Code refinement, refactoring and testing.

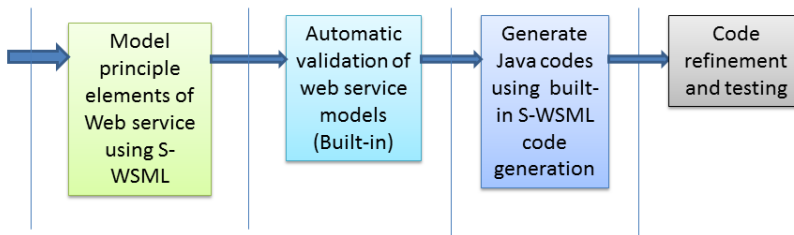


Figure 7

Stages in development of web services using SWSM language

To demonstrate the modeling syntaxes, we can see how SWSM is used to represent various essential elements of web services in an example. To model the service as an aggregation of several ports, the keyword *webservice* is used. The code below shows how the keyword *webservice* is used to define a service called DictionaryService:

```

webservice DictionaryService {
    port LookUpPort
    targetNameSpace "http://ws.mydictionary.net/lookUp"
}
end
  
```

The semantics of the *webservice* block indicates a web service, which can consist of one or many ports. This can be seen from the syntax diagram described above. However, on this dictionary look-up example, there is only one port named *LookUpPort* declared. In the next step, the ports associated to the service also need to be defined:

```

port
  LookUpPort {
    op LookUp
  }
end
  
```

In a port, there are operations involved, *LookUp* operation is the one in this case. A port is associated with an *interface* by the association *binding*. The meta-class *interface* constitutes an aggregation of several operations.

```

binding LookupBinding {
    portType LookUpPort
    operationBinding OpBinding
    transport http
    soapBindingStyle rpc
}
end
  
```

Each operation (identified by the keyword *op*) consists of *message(s)* which define(s) its inputs and outputs. A *message* naturally refers to a meta-class indicating its simple or complex type:

```
op LookUp {
    input Input
    output Output
}
message Input {
    username : String
    word: String
}

message Output {
    meaning : String
    wordType : String
    related : Integer
}
```

In addition, we can also define the action associated with an operation by using the keyword *opBinding*:

```
opBinding OpBinding {
    soapAction "http://ws.mydictionary.net/lookUpAction"
    inputSoapBody literal
    outputSoapBody literal
}
```

For the HTTP protocol binding of SOAP, the value of *soapAction* is required. For other SOAP protocol bindings, this value could be omitted. The *inputSoapBody* and *outputSoapBody* indicate whether the message parts are encoded using some encoding rules.

Putting all the pieces together gives us the information needed to model a simple web service. These models are later used as input for code generation. SWSM makes it possible to design web services by using simple and fast syntaxes. In contrast to other approaches, SWSM is uncomplicated, rapid and easy to adapt. The syntax used in SWSM is simple and more intuitive in comparison to the complex structure of UML. The order in which aspects of a web service are defined is the same as the logical order, when we design a web service. This makes the designing process more natural and perceptive. Using SWSM enables us to focus only on the essential aspects of the web service. This approach promotes model-driven development principles and makes the web service development process more efficient.

All of the SWSM language infrastructures can be packed as a plug-in for the Eclipse integrated development environment. This includes a text editor with autosuggestion and validation capabilities. This enables the development phase to be carried out seamlessly. We also built a code generation feature (Java language) based on a code template engine and embedded it into SWSM. Textual models created using SWSM are used as input for the generation of Java web services. Code generation can be executed right within the editor [18].

The role of MDA in this development process is to raise the level of abstraction in which we develop systems. This is aimed to improve productivity similarly as when we moved from assembly language to third-generation languages. At first, third-generation language compilers did not produce code as optimal as hand-crafted machine code. Over time, however, the productivity increase justified the changeover, especially as computers speeded up and compiler technology improved [7]. SWSM is similarly used at a different level of abstraction to third-generation programming languages, to tackle overall productivity.

6 Related Work

Model-driven development of web services is still evolving to address the problem of increasing complexity and fast-changing technologies in the software industry. Model-driven development of web-services is discussed in the work of Benguria *et al.* [1]. This approach focuses on building platform independent models for service oriented architectures. The solution provides a platform independent meta-model and a set of transformations that link the meta-model with specific platforms following the MDA approach. There are also existing UML-based approaches to modeling services. UML collaboration diagrams have been used extensively to model behavioral aspects, such as service collaboration and compositions in the work of Bezivin *et al.* [2]. In this approach, the Platform-Independent Model is created using UML. This PIM is transformed using Atlas Transformation Language (ATL) to generate the Platform-Specific Model based on three target platforms: Java, Web Service and Java Web Service Developer Pack (JWSDP). This approach showed that UML profiles allow the extension of the UML meta-model. However, UML profiles make the creation of transformation rules difficult.

The support for SaaS and Services Modeling has also been addressed by providing lightweight extensions to UML through Profiles. These approaches can be seen in the work of Fensel and Frankel *et al.* [6, 7, 3]. UML-profiles for services and SOA are proposed by Heckel *et al.* [8]. This effort developed a suitable syntax for this domain by sketching a UML profile for SOA based on UML 1.x standards with a direct mapping between WSDL 1.1 elements and their model elements. Once the profile is properly defined, its semantics can be given in terms of a graph

transformation. This approach has an advantage of UML generality, it can be used to model just about any type of application, running on any type and combination of hardware, operating system, programming language, and network. However, since UML is large and complex, using multiple models/diagrams makes it difficult to keep them consistent with each other and more code has to be added manually.

There are also other efforts to provide domain specific languages for modeling of web services and service-oriented architecture. A qualitative study that provides some analysis of a number of such approaches through a series of three prototyping experiments, in which each experiment has developed, analyzed, and compared a set of DSLs for process-driven SOAs, can be seen in the work of Oberortner et al. [13].

Maximilien et al. [11] developed a DSL for Web APIs and Services Mashups. This effort describes a domain specific language that unifies the most common service models and facilitates service composition and integration into end-user-oriented Web applications. A number of interesting design issues for DSLs are discussed including analysis on levels of abstraction, the need for simple and natural syntax as well as code generation.

On the track of non-UML-based modeling approaches, there are efforts also supporting modeling of services. The Web Services Modeling Framework (WSMF) [6] defines conceptual entities for service modeling. It is an effort to build the Web Service Modeling Framework (WSMF) that provides the appropriate conceptual model for developing and describing web services and their composition. Its philosophy is based on the following principle: maximal decoupling complemented by a scalable mediation service. Web-Service Modeling Ontology (WSMO) [10] provides a conceptual framework and a formal language for semantically describing all relevant aspects of Web services in order to facilitate the automation of discovering, combining and invoking electronic services over the Web. It has its foundations in WSMF but it defines a formal ontology to semantically describe web services. The Web Services Modeling Language (WSML) [4] provides a formal syntax and semantics for the WSMO based on different logical formalisms.

In general, approaches utilizing UML such as in [1], [2] and [8, 7, 3] make the creation of transformation rules challenging. On the other hand, non-UML-based modeling approaches as in [10, 6, 4] provide the conceptual models for web services but have limitation for code generation support. Existing DSL approaches such as [11] is rather complex. For model-driven development of web services, there is the need for simple and natural syntax that provide the support for code generation. Language such as SWSM is an effort aiming at making this possible.

Conclusions

MDD approach can be applied to web services in order to increase the resilience of implementations, as web services technologies change and evolve. The result of this research brings up the design theory and methodology for implementing and utilizing a domain specific language for model-driven development of web services. Adopting domain specific languages, such as the one we introduce, can increase productivity and ease the burden of development of web services as the backbone on SOA systems. SWSM also reduces the cost implied in maintaining the systems and provides a solution to software reuse.

SWSM was written at a good abstraction level. This improves code readability and makes program integration easier. SWSM enables users without experience in programming at a higher level to focus only on knowledge of their concerned domain. Hence under this approach, it is possible for different stakeholders such as business experts and IT experts to model web services during early stages of web services design. Another advantage of SWSM for modeling is the ability to generate more verification on the syntax and semantics than a general modeling language. This can reduce errors on the testing or debugging process. However, we also need to point out that this approach has several drawbacks. There is an extended learning curve for a new language, even though SWSM as a domain specific language proves to be a lot easier to learn than a general programming language. Additionally, as a general language is adopted by more people, it could be more feasible to find staff capable of solving the problem using their language knowledge. There are also spaces for improvement in the syntaxes of SWSM.

In practice, approach using SWSM can be applied to the web service development process in various environments. As members of our team are working with companies in the top global Fortune 500 dealing with large-scale web services for financial services and telecommunication industries, the outlined approach has started to gain adoption and initially has been applied successfully. Our future work will continue on the enhancement of SWSM and introduce a suitable model transformation for both SOAP and Representational State Transfer (REST) web services.

Acknowledgement

This work has been supported by the Department of Computer Science and Engineering, Faculty of Electrical Engineering and by the grant of Czech Technical University in Prague number SGS14/078/OHK3/1T/13.

References

- [1] Benguria, G., Larrucea, X., Elvesæter, B., Neple, T., Beardsmore, A., Friess, M.: A Platform Independent Model for Service-oriented Architectures. *Enterprise Interoperability*, pp. 23-32, 2007

-
- [2] Bezivin, J., Hammoudi, S., Lopes, D., Jouault, F.: Applying MDA Approach for Web Service Platform. In Proceedings of Enterprise Distributed Object Computing Conference, pp. 8-70, 2004
- [3] Bordbar, B., Staikopoulos, A.: Automated Generation of Metamodels for Web Service Languages. In Proceedings of Second European Workshop on Model-driven Architecture, 2004
- [4] De Bruijn, J., Lausen, H. (Ed.): The Web Service Modeling Language WSML. W3C Member Submission. Retrieved December 14, 2012, <http://www.w3.org/Submission/WSML/>, 2005
- [5] Deursen, A., Klint, P.: Little languages: Little maintenance. *Journal of Software Maintenance*, pp. 75-93, 1998
- [6] Fensel, D., Bussler, C.: The Web Service Modeling Framework WSMF, *Electronic Commerce. Research and Applications*, pp. 113-137, 2002
- [7] Frankel, D., Parodi, D.: Using Model-driven Architecture to Develop Web Services, IONA Technologies (2nd Ed.), 2002
- [8] Heckel, R., Lohmann, M., Thöne, S.: Towards a UML Profile for Service-Oriented Architectures. MDAFA, 2003
- [9] Krueger, C. W.: Software Reuse. *ACM computing Surveys*, pp. 131-183, 1992
- [10] Lausen, H., Polleres, A., Roman, D. (Ed.): Web Service Modeling Ontology (WSMO) W3C Member Submission. Retrieved December 14, 2012, <http://www.w3.org/Submission/WSMO/>, 2005
- [11] Maximilien, E. M., Wilkinson, H., Desai, N., Tai, S.: A Domain Specific-Language for Web APIs and Services Mashups, In Proceedings of 5th International Conference on Service Oriented Computing (ICSOC), LNCS 4749, Springer-Verlag, pp. 13-26, 2007
- [12] Mernik, M., Heering, J., Sloane, A. M.: When and How to Develop Domain Specific Languages. *ACM Computing Survey*, Vol. 37 No. 4, pp. 316-344, 1999
- [13] Oberortner, E., Zdun, U., Dustdar, S.: Domain specific Languages for Service-oriented Architectures: An Explorative Study. Towards a Service-Based Internet. Springer-Verlag Berlin, Heidelberg, pp. 159-170, 2008
- [14] Object Management Group (OMG): Meta Object Facility (MOF) Core. Retrieved March 20, 2012, <http://www.omg.org/spec/MOF/2.4.1/>, 2012
- [15] Object Management Group (OMG): The Architecture of Choice for a Changing World. Retrieved March 20, 2012, <http://www.omg.org/mda>, 2012
- [16] Qafmolla, X., Nguyen, V.: Automation of Web Services Development Using Model-driven Techniques. In Institute of Electronics Engineers, The

- 2nd International Conference on Computer and Automation Engineering (ICCAE 2010), pp. 190-194, 2010
- [17] The Enterprise Architect: Building an Agile Enterprise. Retrieved November 18, 2012, <http://www.theenterprisearchitect.eu>, 2012
- [18] Web Modeling Group - Czech Technical University in Prague (WMG): SWSM Language. Retrieved March 15 2013, from <http://webmodeling.net>, 2013
- [19] Wikipedia: Domain Specific Language. Retrieved January 12, 2012, from http://en.wikipedia.org/wiki/Domain_specific_language, 2012
- [20] Wile, D. S.: Lessons Learned from Real DSL Experiments. *Science of Computer Programming*, 51, pp. 265-290, 2002
- [21] World Wide Web Consortium (W3C): Web Services Architecture. Retrieved December 20, 2009, <http://www.w3.org/TR/ws-arch>, 2013
- [22] Yu, X., Zhang, Y., Zhang, T., Wang, L., Hu, J., Zhao, J., Li, X.: A Model-driven Development Framework for Enterprise Web Services. *Information Systems Frontiers*, pp. 391-409, 2007

Supervised Learning Based Multi-modal Perception for Robot Partners using Smart Phones

Dalai Tang, Janos Botzheim, Naoyuki Kubota

Graduate School of System Design, Tokyo Metropolitan University

6-6 Asahigaoka, Hino, Tokyo, 191-0065 Japan

tang@ed.tmu.ac.jp, {botzheim, kubota}@tmu.ac.jp

Abstract: This paper proposes a method for multi-modal perception of human-friendly robot partners based on various types of sensors built in a smart phone. The proposed method can estimate human interaction modes by fuzzy spiking neural network. The learning method of the spiking neural network based on the time series of the measured data is explained as well. Evolution strategy is used for optimizing the parameters of the fuzzy spiking neural network. Several experimental results are presented for confirming the effectiveness of the proposed technique. Finally, the future direction on this research is discussed.

Keywords: Robot Partners; Multi-modal Perception; Computational Intelligence; Human Robot Interaction

1 Introduction

Recently, the rate of elderly people rises in the super-aging society in many countries. For example, the rate is estimated to reach 23.8% in Tokyo in 2015 [1]. In general, the mental and physical care is very important for elderly people living home alone. Such elderly people have little chances to talk to other people and to perform daily physical activity. Human-friendly robots can be used as partners in daily communication to support the care of elderlies. Furthermore, various types of human-friendly robots such as pet robots, amusement robots, and robot partners have been developed to communicate with people [2-4]. However, it is difficult for a robot to converse with a person appropriately even if many contents of the conversation are designed beforehand, because the robot must have personal information and life logs required for daily conversation. Furthermore, in addition to verbal communication, the robot should understand non-verbal communication, e.g., facial expressions, emotional gestures, and pointing gestures. We have used

various types of robot partners such as MOBiMac, Hubot, Apri Poco, palro, miuro, and other robots for information support to elderly people, rehabilitation support, and robot edutainment [5-9]. In order to popularize robot partners, the price of a robot partner should be as low as possible. Therefore, we have also been developing on-table small sized robot partners called iPhonoid and iPadrone [10,11]. In this paper, we focus on how to use sensors that a smart phone or a tablet PC equipped with.

Various types of concepts and technologies on ubiquitous computing, sensor networks, ambient intelligence, disappearing computing, intelligent spaces, and other fields have been proposed and developed to realize information gathering, life support, safe and secure society [12-17]. One of the most important issues in the concepts and technologies is the structuralization of information. The structuralization of information means to give qualitative meaning to data and quantitative information in order to improve the accessibility and usability of information. We can obtain huge size of data through sensor networks, however useful, meaningful and valuable information should be extracted from such data.

We have proposed the concept of informationally structured space to realize the quick update and access of valuable and useful information for people and robots [18,19]. The sensing range of both people and robot is limited. If the robot can obtain the exact position of the robot itself, people, and objects in an environment, the robot does not need any sensors for measuring such information. As a result, the weight and size of the robot can be reduced, since many sensors can be removed from the robot. The received environmental information is more precise because the sensors equipped in the environment are designed suitable to the environmental conditions. Furthermore, if the robot can share the environmental information with people, the communication with people might become very smooth and natural. Therefore, we have proposed methods for human localization [20,21], map building [22], and 3D visualization [23]. Various types of estimation method of human state have been proposed. We applied spiking neural network [24,25] for localizing human position, estimating human transportation mode [26], and learning pattern of daily life of elderly people [27].

In this paper the sensors of a smart phone is used for estimating human interaction modes. As the computational power of a smart phone is not so high compared to a standard PC, we should reduce the computational cost as much as possible. Computational intelligence techniques are able to find good compromise between computational cost and solution accuracy. In this paper fuzzy spiking neural network is proposed for estimating human interaction modes. Additionally, evolution strategy is used for optimizing the parameters of the fuzzy spiking neural network. The performance of estimation is analyzed by several experimental results.

This paper is organized as follows. Section II explains the hardware specification of robot partners applied in this study, the interaction modes, and the sensory

inputs from a smart phone. Section III proposes the method of estimating human interaction modes. Section IV shows several experimental results. Finally, Section V summarizes this paper, and discusses the future direction to realize human-friendly robot partners.

2 Robot Partners using Smart Phones

2.1 Robot Partners

Recently, various types of smart phone and tablet PC have been developed, and their price is decreasing year by year [28]. Furthermore, the embedded system technology enables to miniaturize such a device and to integrate it with many sensors and other equipments. As a result, we can get a mechatronics device including many sensors, wireless communication systems, GPU and CPU composed of multiple cores with low price. Furthermore, elderly people unfamiliar with information home appliances have started using tablet PC [29], because touch panels and touch interfaces have been popularized at ticket machines and information services in public areas. Therefore, we started the development project on on-table small sized human-friendly robot partners called iPhonoid and iPadrone based on smart phone or tablet PC to realize information support for elderly people (Figs.1 (a) and (b)). Since iPhone is equipped with various sensors such as gyro, accelerometer, illumination sensor, touch interface, compass, two cameras, and microphone, the robot itself is enough to be equipped with only cheap range sensors. The mobile base is equipped on the bottom, however the mobile base is not used on the table for safety's sake. In order to control the actuators of a robot partner from the smart phone or tablet PC, wireless LAN and wireless PAN (Bluetooth) can be used in addition to a wired serial communication.

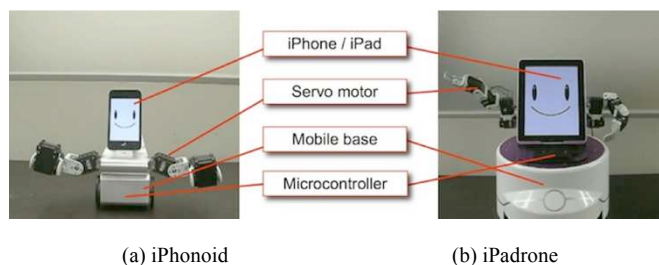


Figure 1

Robot partners using a smart phone and a tablet PC

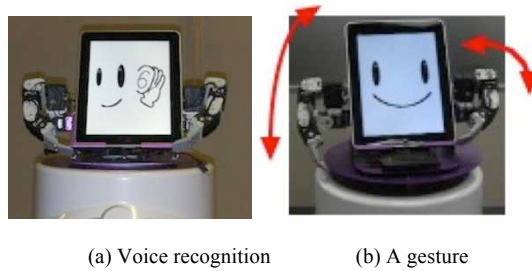


Figure 2

Robot behaviors for social communication with people

Basically, human detection, object detection, and voice recognition are performed by smart phone or tablet PC. Furthermore, touch interface is used as a direct communication method. The robot partner starts the multi-modal interaction after a smart phone is attached to the robot base. We use touch interface on the smart phone or tablet PC as the nearest interaction with the robot partner. The facial parts are displayed as icons for the touch interface on the display (Fig.2). Since the aim of this study is to realize information support for elderly people, the robot partner provides elderly people with their required information through the touch interface. The eye icon and mouth icon are used for providing the visual information and text information, respectively.

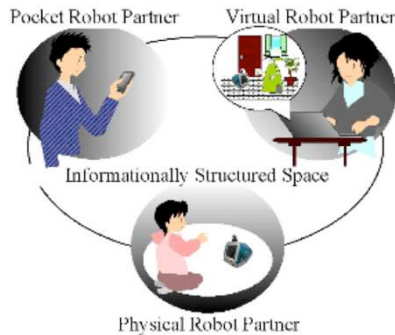


Figure 3

Interaction with robot partners from different view points

The ear icon is used for direct voice recognition because it is difficult to perform high performance of voice recognition in the daily communication with the robot partner. If the person touches the mouth icon, then the ear icon appears, and the voice recognition starts. The voice recognition is done by Nuance Mobile Developer Program (NMDP). NMDP is a self-service program for developers of iOS and Android application [30]. In this way, the total performance of multi-modal communication can be improved by combining several communication

modalities of touch interface, voice recognition, and image processing. The conversation system is composed of (A) daily conversation mode, (B) information support mode, and (C) scenario conversation mode [5-9].

2.2 Interaction Modes

We can discuss three different types of robot partners using a smart phone or a tablet PC from the interactive point of view: a physical robot partner, a pocket robot partner, and a virtual robot partner (Fig.3). These modes are not independent, and we interact with the robot partner based on several modes. Interaction modes mean the ways how we interact with the robot partner. We can interact with a physical robot partner by using multi-modal communication like with a human. The interaction is symmetric. The other one is a virtual robot partner. The virtual robot partner exists in the virtual space in the computer and can be considered as a computer agent, but we can interact with it through the virtual person or robot by immersing him or her in the virtual space. Therefore, the interaction is symmetric. The pocket robot partner has no mobile mechanism, but we can easily bring it everywhere and we can interact with the robot partner by touch and physical interface. Furthermore, the pocket robot partner can estimate the human situation by using internal sensors such as illumination sensor, digital compass, gyro, and accelerometer. The advantage of this device is in the compactness of integrated multi-modal communication interfaces in a single device.

Each style of robot partners is different, but the interaction modes depend on each other, and we interact with the robot partner with the same knowledge on personal information, life logs, and interaction rules.

In this paper, since we use the facial expression on the display for human interaction (see Figs.1 and 2), the robot partner should estimate the human interaction mode: (a) the physical robot partner mode (attached on the robot base), (b) the pocket robot partner mode (having removed from the robot base), or (c) other mode (on the table, in the bag, or others). In this paper 7 interaction modes are defined which will be detailed in the experimental section and depicted in Figs. 9 and 10.

2.3 Sensory Inputs from Smart Phones

We can use several sensory data measured by a smart phone. As depicted in Fig. 4, since iOS 4.0 there has been a Core Motion framework to deal with obtaining sensory data. The acceleration of human movement is calculated by using a high-pass filter for the measured data by the accelerometer. The angular velocity is calculated by using a low-pass filter for the measured data by the gyro sensor. The iPhone's attitude is calculated by the measured data of accelerometer, gyroscope, and magnetometer. The specification of the measured data is presented in Table 1. The data are updated in every 100 ms.

Table 1
Specification of iPhone's sensors

Sensor Name	Accelerometer	Gyro	Attitude
Acquired data	a_x, a_y, a_z	$\omega_x, \omega_y, \omega_z$	pitch, roll, yaw
Range of data	-/+2.3G	-/+90, -/+180, -/+180,	-/+90, -/+180, -/+180,
Time interval	100ms	100ms	100ms

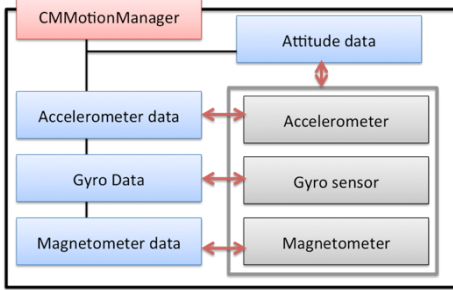


Figure 4

iOS Core Motion Framework for obtaining sensory data

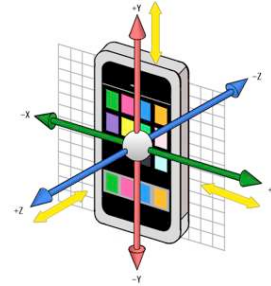


Figure 5

Acceleration data of iPhone

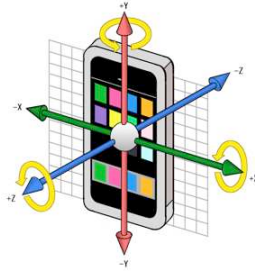


Figure 6

Angular velocity data of iPhone

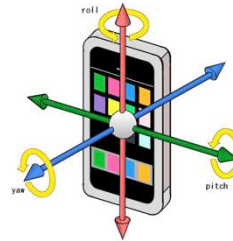


Figure 7

iPhone's attitude data

The acceleration can be calculated as (Fig. 5):

$$a(t) = \sqrt{a_x(t)^2 + a_y(t)^2 + a_z(t)^2}, \tag{1}$$

where $a_x(t)$, $a_y(t)$, and $a_z(t)$ are the components of the acceleration in the unit directions at time t .

The angular velocity is computed as (Fig. 6):

$$\omega(t) = \sqrt{\omega_x(t)^2 + \omega_y(t)^2 + \omega_z(t)^2}, \tag{2}$$

where $\omega_x(t)$, $\omega_y(t)$, and $\omega_z(t)$ are the angular velocities at time t in the X-axis, Y-axis, and Z-axis, respectively.

The iPhone's attitude is (Fig. 7):

$$\theta_x(t) = \left| \frac{\theta_x(t)}{90^\circ} \right|, \theta_y(t) = \left| \frac{\theta_y(t)}{180^\circ} \right|, \theta_z(t) = \left| \frac{\theta_z(t)}{180^\circ} \right|, \quad (3)$$

where $\theta_x(t)$, $\theta_y(t)$, and $\theta_z(t)$ are the pitch, roll, and yaw Euler angles at time t , respectively.

Since the measured data includes noise, we have to use some smoothing functions. Although there are many methods for decreasing the noise, in our application the computation complexity is an important issue. We realize our system in a smart phone which has limited computational power compared to a PC. Therefore, two simple weighted moving averages are applied as presented in Eqs. (4) and (5), where d is the window length. In Eq. (4) the weights increase from the smallest weight at time $(t-d+1)$ to the current data point at time t . In Eq. (5) the weights increase first, from the smallest weight at time $(t-d/2)$ to the current point at time t , after that they decrease till time $(t+d/2-1)$. In Eqs. (4) and (5) j indicates the input.

$$\tilde{x}_j(t) = \frac{1}{\sum_{k=0}^{d-1} \exp\left(-\frac{k}{d}\right)} \sum_{k=0}^{d-1} \exp\left(-\frac{k}{d}\right) x_j(t-k) \quad (4)$$

$$\tilde{x}_j(t) = \frac{1}{\sum_{k=0}^{d-1} \exp\left(-\frac{\left|k-\frac{d}{2}\right|}{d}\right)} \sum_{k=0}^{d-1} \exp\left(-\frac{\left|k-\frac{d}{2}\right|}{d}\right) \cdot x_j\left(t+k-\frac{d}{2}\right) \quad (5)$$

3 Fuzzy Spiking Neural Network for Estimation of Human Interaction Modes

3.1 Fuzzy Spiking Neural Network

We estimate the human interaction modes by fuzzy spiking neurons. One important feature of spiking neurons is the capability of temporal coding. In fact, various types of spiking neural networks (SNNs) have been applied for memorizing spatial and temporal context [31-33]. A simple spike response model is used in order to reduce the computational cost. In our model the SSN has fuzzy inputs, it is a fuzzy spiking neural network (FSNN) [25-27]. Figure 8 illustrates the FSNN model. We use evolution strategy to adapt the parameters of the fuzzy membership functions applied as inputs to the spiking neural network. Figure 9 depicts the detailed structure of the FSNN model. The inputs of the FSNN are the

sensory data, the outputs are the interaction modes. We use 7 interaction modes as presented in Fig. 9.

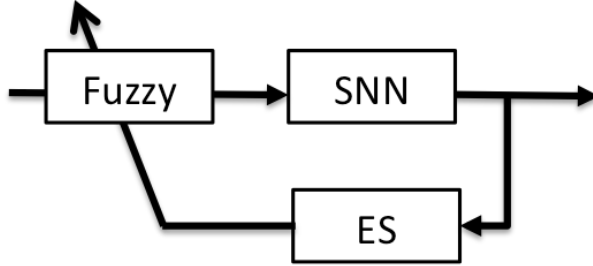


Figure 8
Fuzzy spiking neural network

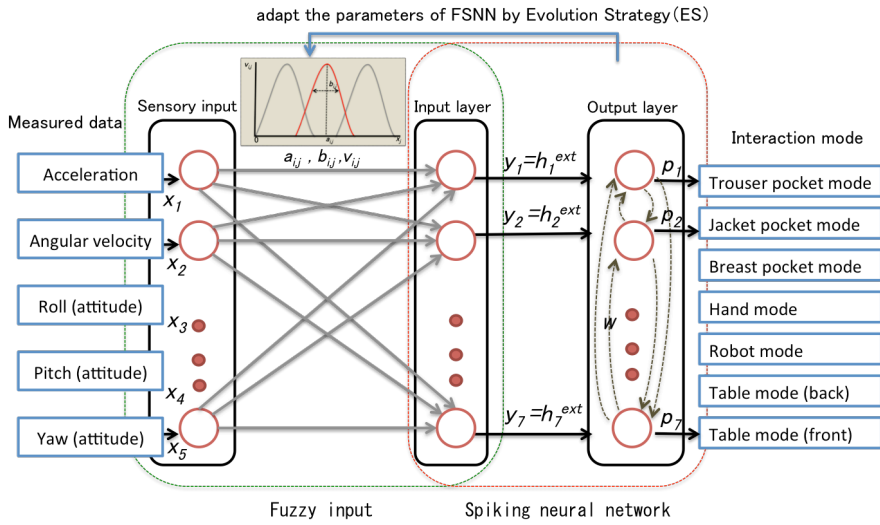


Figure 9
Detailed structure of fuzzy spiking neural network

On the sensory input fuzzy inference is performed by:

$$\mu_{A_{i,j}}(x_j) = \exp\left(-\frac{(x_j - a_{i,j})^2}{b_{i,j}}\right) \quad (6)$$

$$y_i = \prod_{j=1}^m v_{i,j} \cdot \mu_{A_{i,j}}(x_j) \quad (7)$$

where $a_{i,j}$ and $b_{i,j}$ are the central value and the width of the membership function $A_{i,j}$ and $v_{i,j}$ is the contribution of the j -th input to the estimation of the i -th human interaction mode. The result of fuzzy inference, y_i , will be the input of the spiking neurons.

The membrane potential, or internal state $h_i(t)$ of the i -th spiking neuron at the discrete time t is given by:

$$h_i(t) = \tanh(h_i^{syn}(t) + h_i^{ext}(t) + h_i^{ref}(t)), \quad (8)$$

where $h_i^{syn}(t)$ includes the pulse outputs from the other neurons, $h_i^{ref}(t)$ is used for representing the refractoriness of the neuron, $h_i^{ext}(t)$ is the input to the i -th neuron from the external environment. The hyperbolic tangent function is used to avoid the bursting of neuronal fires.

The external input, $h_i^{ext}(t)$ is calculated based on the fuzzy inference in Eqs. (6) and (7), and it is equal to y_i as illustrated in Fig. 9, thus:

$$h_i^{ext}(t) = \prod_{j=1}^M v_{i,j} \cdot \exp\left(-\frac{(x_j - a_{i,j})^2}{b_{i,j}}\right) \quad (9)$$

Furthermore, $h_i^{syn}(t)$ indicates the output pulses from other neurons presented by dashed arrows in Fig. 9 in the output layer:

$$h_i^{syn}(t) = \sum_{j=1, j \neq i}^N w_{j,i} \cdot h_j^{PSP}(t-1), \quad (10)$$

where $w_{j,i}$ is a weight coefficient from the j -th to the i -th neuron; $h_j^{PSP}(t)$ is the presynaptic action potential (PSP) approximately transmitted from the j -th neuron at the discrete time t ; N is the number of neurons. When the internal state of the i -th neuron is larger than the predefined threshold, a pulse is outputted as follows:

$$p_i(t) = \begin{cases} 1 & \text{if } h_i(t) \geq q^{pul} \\ 0 & \text{otherwise} \end{cases} \quad (11)$$

where q^{pul} is a threshold for firing. The outputs of FSNN are the p_i values as presented in Fig. 9. Thus, the output is the interaction mode i which for $p_i=1$. If there are more than one neuron with output pulse 1 (i.e., $\exists i, j \ i \neq j \ p_i = p_j = 1$), then the output will be that one which fired in the previous step, $t-1$. If none fired, then the output neuron will be selected randomly.

Furthermore, R is subtracted from the refractoriness value as follows:

$$h_i^{ref}(t) = \begin{cases} \gamma^{ref} \cdot h_i^{ref}(t-1) - R & \text{if } p_i(t-1) = 1 \\ \gamma^{ref} \cdot h_i^{ref}(t-1) & \text{otherwise} \end{cases} \quad (12)$$

where γ^{ref} is a discount rate and $R > 0$.

The spiking neurons are interconnected, and the presynaptic spike output is transmitted to the connected neuron according to the PSP with the weight connection. The PSP is calculated as follows:

$$h_i^{PSP}(t) = \begin{cases} 1 & \text{if } p_i(t) = 1 \\ \gamma^{PSP} \cdot h_i^{PSP}(t-1) & \text{otherwise} \end{cases} \quad (13)$$

where γ^{PSP} is the discount rate ($0 < \gamma^{PSP} < 1.0$). Therefore, the postsynaptic action potential is excitatory if the weight parameter, $w_{j,i}$ is positive, and inhibitory if $w_{j,i}$ is negative. In our case we set $w_{j,i} = -0.2$ in order to suppress the firing chance of other neurons when a given neuron fires.

In the equations describing the three components of the internal state simple functions are used instead of the differential equations proposed in the original model of spiking neural network [33]. By the proposed simple spike response model we can keep the computational complexity at low level.

3.2 Evolution Strategy for Optimizing the Parameters of FSNN

We apply $(\mu + \lambda)$ -Evolution Strategy (ES) for the improvement of the parameters of fuzzy spiking neural network in the fuzzy rules. In $(\mu + \lambda)$ -ES μ and λ indicate the number of parents and the number of offspring produced in a single generation, respectively [34]. We use $(\mu + 1)$ -ES to enhance the local hill-climbing search as a continuous model of generations, which eliminates and generates one individual in a generation. The $(\mu + 1)$ -ES can be considered as a steady-state genetic algorithm (SSGA) [35]. As it can be seen in Equations (6), (7), (9) and Figure 9, a candidate solution will contain the parameters of the fuzzy membership functions which play role in the input layer of the spiking neural network. These parameters are the central value ($a_{i,j}$), the width ($b_{i,j}$), and the contribution value ($v_{i,j}$):

$$\begin{aligned} \mathbf{g}_k &= [g_{k,1} \ g_{k,2} \ g_{k,3} \ \dots \ g_{k,l}] \\ &= [a_{k,1,1} \ b_{k,1,1} \ v_{k,1,1} \ \dots \ v_{k,n,m}] \end{aligned} \quad (14)$$

where n is the number of human interaction modes; m is the number of inputs; $l = n \cdot m$ is the chromosome length of the k -th candidate solution. The fitness value of the k -th candidate solution is calculated by the following equation:

$$f_k = \sum_{i=1}^n f_{k,i} \quad (15)$$

where $f_{k,i}$ is the number of correct estimation rates of the i -th human interaction mode. We compare the FSNN's each output in the time sequence with the corresponding desired output. If the FSNN's output is the same as the desired output, then we count this as a matching. The number of matchings for the i -th

interaction mode is $f_{k,i}$. Thus, the evaluation of the individual and consequently the learning process is performed in supervised manner.

In $(\mu+1)$ -ES, only one existing solution is replaced with the candidate solution generated by crossover and mutation. We use elitist crossover and adaptive mutation. Elitist crossover randomly selects one individual, and generates one individual by combining genetic information between the selected individual and the best individual in order to obtain feasible solutions from the previous estimation result rapidly. The newly generated individual replaces the worst individual in the population after applying adaptive mutation on the newly generated individual. In the genetic operators we use the local evaluation values of the human interaction mode estimation. The inheritance probability of the genes corresponding to the i -th rule of the best individual is calculated by:

$$p_i = \frac{1}{2} \cdot (1 + f_{best,i} - f_{k,i}) \quad (16)$$

where $f_{best,i}$ and $f_{k,i}$ are the part of the fitness value related to the i -th rule (i -th genes) of the best and the randomly selected k -th individuals, respectively. By Eq. (16) we can bias the selection probability of the i -th genes from 0.5 to the direction of the better individual's i -th genes among the best individual and the k -th individual. Thus, the newly generated individual can inherit the i -th genes (i -th rule) from that individual which the better i -th genes has. After the crossover operation, an adaptive mutation is performed on the generated individual:

$$g_{k,h} \leftarrow g_{k,h} + \alpha_h \cdot (1 - t/T) \cdot N(0,1) \quad (17)$$

where $N(0,1)$ indicates a normal random value; α_h is a parameter of the mutation operator (h stands for identifying the three subgroups in the individual related to a , b , and v); t is the current generation; and T is the maximum number of generations.

4 Experimental Results

This section shows comparison results and analyzes the performance of the proposed method. In the spiking neural network there are 5 inputs in the input layer: acceleration, angular velocity, and attitude of pitch, roll yaw. In the output layer there are 7 outputs related to the following 7 robot interaction modes (Fig. 10): (1) TableMode(front), (2) TableMode(back), (3) RobotMode, (4) HandMode, (5) BreastPocketMode, (6) JacketPocketMode, (7) TrouserPocketMode. The parameters of the neural network are as follows: the temporal discount rate for refractoriness (γ^{ref}) is 0.88, the temporal discount rate for PSP (γ^{PSP}) is 0.9, the threshold for firing (q^{pul}) is 0.9, and R is 1. Fourteen training datasets and 4 test datasets are used in the experiments. When obtaining the training set, in the case of BreastPocketMode, JacketPocketMode, and TrouserPocketMode the person

was walking for about 2 minutes, then standing for about 2 minutes. In the TableModes, RobotMode, and HandMode there was no motion.



Figure 10
Robot interaction modes

Figure 11 illustrates the experimental example of the measured smart phone mode. The cyan line is the high-pass filtered data measured by the accelerometer. The green line depicts the angular velocity calculated by the low-pass filtered data measured by the gyro sensor. The red line is the attitude of pitch data. The blue line is the attitude of roll data. The pink line is the attitude of yaw data. The second part of Fig. 11 shows the target output (blue line) and the estimated output by FSNN (red line). The number of spiking neurons is 5. These neurons are used for measuring the 7 robot interaction modes.

In the first experiment the sensor's raw data are used as input to the FSNN. Figure 11 shows experimental results by using the raw data of the second training dataset. In this case the phone is put on the table by the front side (a), and the person takes it in hand (b). Thereafter he/she puts the phone in jacket pocket (c) and takes out the phone putting it on the robot base (b,d). After that the person puts the phone in trouser pocket (b,e). Then he/she takes out the phone putting it on the table by the back side (b,f), and finally he/she takes the phone putting it in breast pocket (b,g). The number of fitting data is 16911 from 19213 training data in the case of second dataset. There are 14 training datasets, the total number of fitting data is 64936 from 72638 training data, and the running time is 4410 ms. The fitting rate is 89.4%. Figure 12 shows experimental results by using the raw data of second test dataset. The number of fitting data is 5966 from 7974 test data. There are 4 test datasets, the total number of fitting data is 31377 from 40096 test data, and the running time is 1688 ms. The fitting rate is 78.3%.

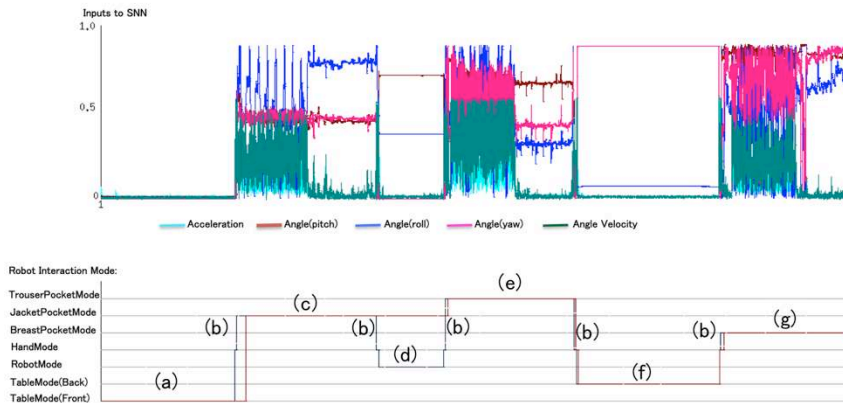


Figure 11
Experimental results by using the raw data for training dataset 2

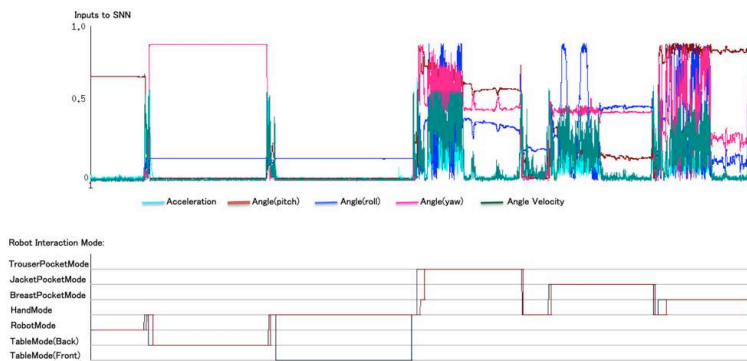


Figure 12
Experimental results by using the raw data for test dataset 2

In order to reduce the noise we have to use some smoothing functions as mentioned in Section 2. We apply two different kinds of weighted moving averages. In the second experiment we present results by using smoothing function described in Eq. (4). Figure 13 depicts the result for second training dataset. The number of fitting data is 18234 from 19213 training data. The total number of fitting data using all training datasets is 63659 from 72638 training data, the running time is 4445 ms, and the fitting rate is 87.6%. Figure 14 shows experimental results by using smoothing function in Eq. (4) for test dataset 2. The number of fitting data is 6911 from 7974 training data. The total number of fitting data using all test datasets is 34327 from 40096 test data, the running time is 1609 ms, the fitting rate is 85.6%.

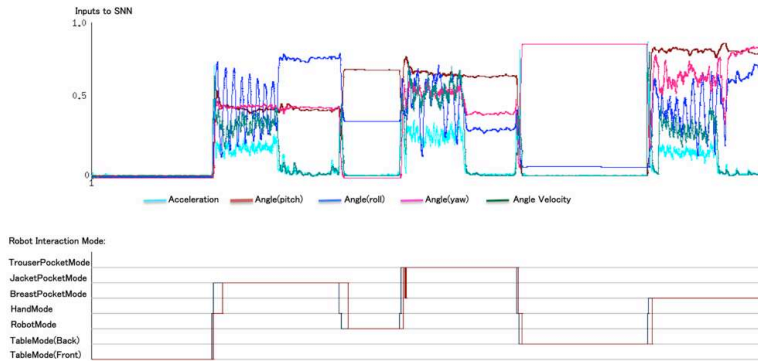


Figure 13

Experimental results by using the smoothing function in Eq. (4) for training dataset 2

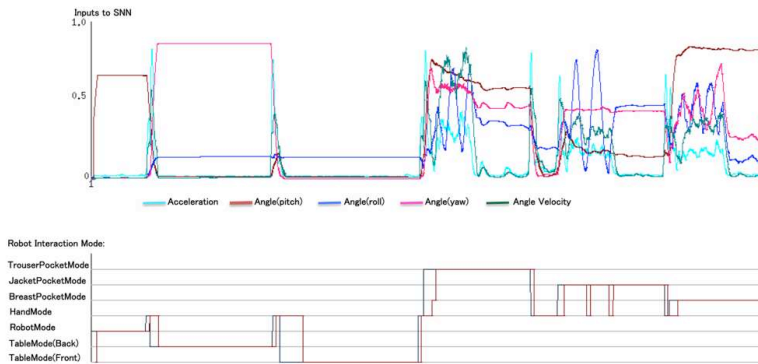


Figure 14

Experimental results by using the smoothing function in Eq. (4) for test dataset 2

In the third experiment, we present experimental result by the other smoothing function defined by Eq. (5). Figure 15 illustrates the results for second training dataset. In the case of second training dataset the number of fitting data is 18507 from 19213, and for all training datasets the total number of fitting data is 69356 from 72638, the running time is 4438 ms, the fitting rate is 95.5%. Figure 16 shows experimental results by using smoothing function in Eq. (5) for test dataset 2. The number of fitting data is 7499 from 7974 test data. The total number of fitting data for all test datasets is 36842 from 40096 test data, the running time is 1610 ms, the fitting rate is 91.9%.

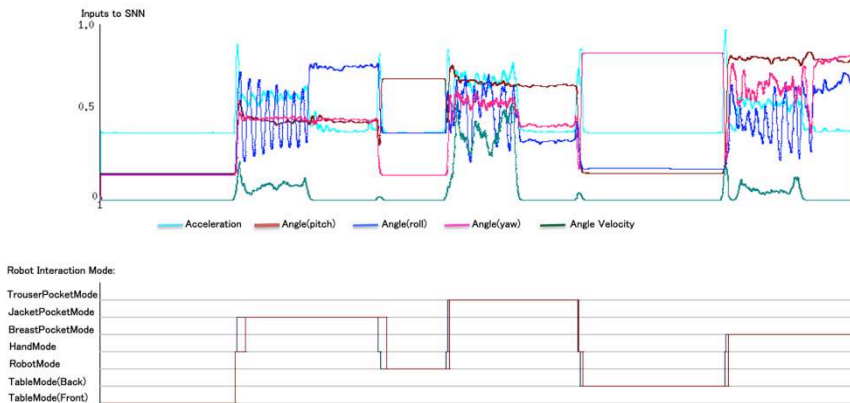


Figure 15

Experimental results by using the smoothing function in Eq. (5) for training dataset 2

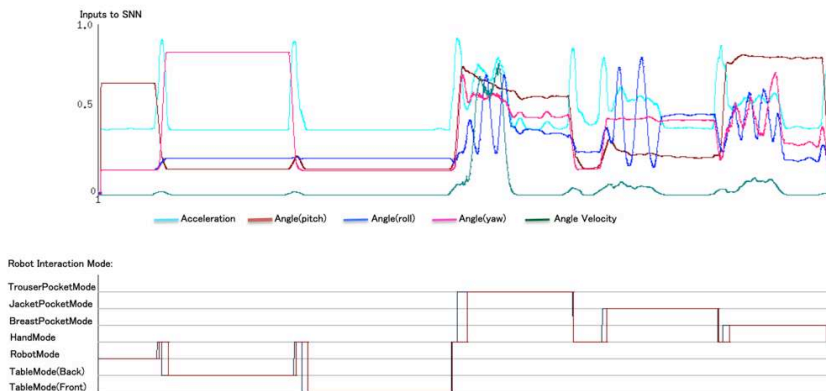


Figure 16

Experimental results by using the smoothing function in Eq. (5) for test dataset 2

In the fourth experiment we use evolution strategy for optimizing the parameters of FSNN. The population size is 100, the number of generations is 6000, and the evaluation time step is 1000, $\alpha_a=0.01$, $\alpha_b=0.005$, $\alpha_v=0.05$. Figure 17 illustrates the best results by ES for the raw data of second training dataset. The total number of fitting data using all training datasets is 68933 from 72638. The application of ES has an additional computational cost. The running time is 684259 ms, the fitting rate is 94.9%. Figure 18 shows the result for second test dataset after using evolution strategy for optimizing the parameters of FSNN based on training datasets. In the case of test datasets the total number of fitting data is 34842 from 40096 test data. The running time is 1810 ms, the fitting rate is 86.9%.

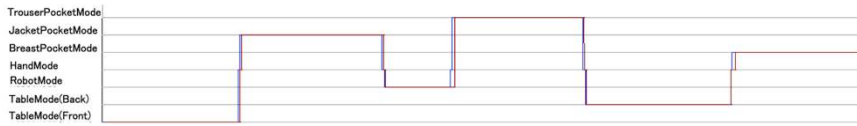


Figure 17

Experimental results by using ES for parameter optimization for training dataset 2 (for raw data)

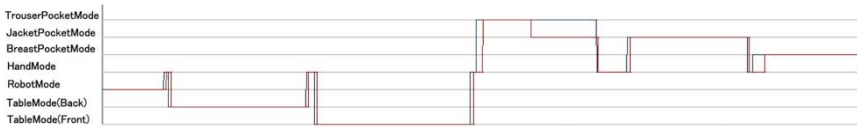


Figure 18

Experimental results by using FSNN for test dataset 2 after parameter optimization (for raw data)

Figure 19 depicts the best results by ES for training dataset 2 when using smoothing function in Eq.(4). The total number of fitting data using all training datasets is 69441 from 72638. The running time is 683293 ms, the fitting rate is 95.6%. Figure 20 shows the result for second test dataset when using smoothing function in Eq.(4) after using evolution strategy for optimizing the parameters of FSNN based on training datasets. In the case of test datasets the number of fitting data is 35805 from 40096 test data. The running time is 1743 ms, the fitting rate is 89.3%.



Figure 19

Experimental results by using ES for parameter optimization for training data set 2 (using smoothing function in Eq. (4))



Figure 20

Experimental results by using FSNN for test dataset 2 after parameter optimization (using smoothing function in Eq. (4))

Figure 21 presents the best results by ES for training dataset 2 when using smoothing function in Eq.(5). The total number of fitting data using all training datasets is 70604 from 72638. The running time is 654505 ms, the fitting rate is 97.2%. Figure 22 shows the result for second test dataset when using smoothing function in Eq.(5) after using evolution strategy for optimizing the parameters of FSNN based on training datasets. In the case of test datasets the number of fitting

data is 37730 from 40096 test data. The running time is 1586 ms, the fitting rate is 94.1%.



Figure 21

Experimental results by using ES for parameter optimization for training data set 2 (using smoothing function in Eq. (5))

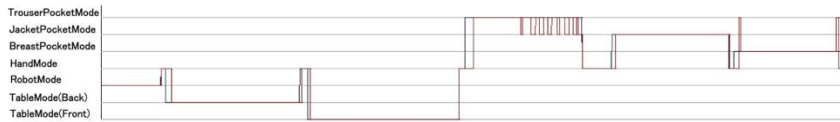


Figure 22

Experimental results by using FSNN for test dataset 2 after parameter optimization (using smoothing function in Eq. (5))

Table 2 summarizes the experimental results. The best results were obtained by evolution strategy.

Table 2
Summary of experimental results

Sensor Name	Experiment	Number of data	Number of fitting data	Fitting rate	Running time(ms)
Raw data	training	72638	64936	89.4%	4410
	test	40096	31377	78.3%	1688
Smoothing function Eq.(4)	training	72638	63659	87.6%	4445
	test	40096	34327	85.6%	1609
Smoothing function Eq.(5)	training	72638	69356	95.5%	4438
	test	40096	36842	91.9%	1610
ES for raw data	training	72638	68933	94.9%	684259
	test	40096	34842	86.9%	1810
ES for Smoothing function Eq.(4)	training	72638	69441	95.6%	683293
	test	40096	35805	89.3%	1743
ES for Smoothing function Eq.(5)	training	72638	70604	97.2%	654505
	test	40096	37730	94.1%	1586

5 Summary

In this paper, we proposed a method for estimating human interaction mode using accelerometer, gyro, and magnetometer. First, we introduced the robot partners applied in this paper. Next, we proposed an estimation method of human interaction modes using evolution strategy and fuzzy spiking neural network based on a simple spike response model. In the experimental results we showed, that the proposed method is able to estimate human interaction modes based on iPhone's sensors.

As a future work, we intend to improve the learning performance according to human life logs, and extend the method by combining it with the estimation of human transport modes which has been presented in [26].

Acknowledgement

This work is partially supported by MEXT Regional Innovation Strategy Support Program.

References

- [1] Statistics Bureau, Ministry of Internal Affairs and Communications, "Population estimates", September, 2012.
- [2] M. Pollack, "Intelligent Technology for an Aging Population: The Use of AI to Assist Elders with Cognitive Impairment," *AI Magazine*, 2005, vol. Summer.
- [3] T. Hashimoto, N. Kato, and H. Kobayashi, "Study on Educational Application of Android Robot SAYA: Field Trial and Evaluation at Elementary School," *ICIRA 2010, Part II, LNAI 6425*, pp. 505–516, 2010.
- [4] H. Ishiguro, M. Shiomi, T. Kanda, D. Eaton, and N. Hagita, "Field Experiment in a Science Museum with communication robots and a ubiquitous sensor network," *Proc. of Workshop on Network Robot System at ICRA2005*, 2005.
- [5] N. Kubota and T. Mori, "Conversation System Based on Boltzmann Selection and Bayesian Networks for A Partner Robot," *Robot and Human Interactive Communication (RO-MAN)*, Toyama, Japan, 2009.
- [6] H. Kimura, N. Kubota, and J. Cao, "Natural Communication for Robot Partners Based on Computational Intelligence for Edutainment," *MECATRONICS2010*, pp.610-615, Yokohama, Japan, 2010.
- [7] A. Yorita and N. Kubota, "Cognitive Development in Partner Robots for Information Support to Elderly People," *IEEE Transactions on Autonomous Mental Development*, Vol. 3, Issue 1, pp. 64-73, 2011.

- [8] N. Kubota, T. Mori, and A. Yorita, "Conversation System for Robot Partners based on Informationally Structured Space," IEEE Symposium Series on Computational Intelligence 2011 (SSCI2011), Paris, France, April 11-15, 2011.
- [9] D. Tang and N. Kubota, "Information Support System Based on Sensor Networks," Proc. of World Automation Congress (WAC) 2010, Kobe, Japan, September 19-23, 2010.
- [10] D. Tang, B. Yusuf, J. Botzheim, N. Kubota, and I. A. Sulistijono, "Robot Partner Development Using Emotional Model Based on Sensor Network," Proc. of IEEE Conference on Control, Systems and Industrial Informatics (ICCSII 2012), pp. 196-201, 2012.
- [11] N. Kubota and Y. Toda, "Multi-modal Communication for Human-friendly Robot Partners in Informationally Structured Space," IEEE Transaction on Systems, Man, and Cybernetics-Part C, Vol. 42, No. 6, pp. 1142-1151, 2012.
- [12] I. Khemapech, I. Duncan, and A. Miller, "A Survey of Wireless Sensor Networks Technology," Proc. of The 6th Annual PostGraduate Symposium on The Convergence of Telecommunications, Networking and Broadcasting, 2005.
- [13] I. Satoh, "Location-based Services in Ubiquitous Computing Environments," International Journal of Digital Libraries, Springer, 2006.
- [14] P. Remagnino, H. Hagaras, N. Monekosso, and S. Velastin, "Ambient Intelligence: A Gentle Introduction," In the book entitled "Ambient Intelligence A Novel Paradigm" (Eds: P. Remagnino, G. Foresti, T. Ellis), Springer Verlag, pp. 1-15, 2005.
- [15] V. Callaghan, M. Colley, H. Hagaras, J. Chin, F. Doctor, and G. Clarke, "Programming iSpaces: A Tale of Two Paradigms," In the book entitled "Intelligent Spaces: The Application of Pervasive ICT" (Eds: A. Steventon, S. Wright), Springer-Verlag, Chapter 24, pp. 389- 421, 2005.
- [16] K. Morioka, and H. Hashimoto, "Appearance Based Object Identification for Distributed Vision Sensors in Intelligent Space," Proc. of the 2004 IEEE/RSJ International Conference on Intelligent Robots and Systems (IROS'04), Vol.1, pp. 199-204, 2004.
- [17] K. Kemmotsu, T. Tomonaka, S. Shiotani, Y. Koketsu, and M. Iehara, "Recognizing Human Behaviors with Vision Sensors in Network Robot Systems," Proc. of The 1st Japan-Korea Joint Symposium on Network Robot Systems (JK-NRS2005), 2005.
- [18] N. Kubota and A. Yorita, "Topological environment reconstruction in informationally structured space for pocket robot partners," in Proc. of the 2009 IEEE International Symposium on Computational Intelligence in Robotics and Automation, CIRA, pp. 165-170, 2009.

- [19] N. Kubota, H. Sotobayashi, and T. Obo, "Human interaction and behavior understanding based on sensor network with iPhone for rehabilitation," in Proc. of the International Workshop on Advanced Computational Intelligence and Intelligent Informatics, 2009.
- [20] N. Kubota, D. Tang, T. Obo, and S. Wakisaka, "Localization of Human Based on Fuzzy Spiking Neural Network in Informationally Structured Space," in Proc. of 2010 IEEE World Congress on Computational Intelligence (WCCI 2010), Barcelona, Spain, pp. 2209-2214, 2010.
- [21] T. Obo, N. Kubota, and B. H. Lee, "Localization of Human in Informationally Structured Space Based on Sensor Networks," in Proc. of 2010 IEEE World Congress on Computational Intelligence (WCCI 2010), Barcelona, Spain, pp. 2215-2221, 2010.
- [22] N. Kubota, K. Yuki, and N. Baba, "Integration of Intelligent Technologies for Simultaneous Localization and Mapping," in Proc. of ICROS-SICE International Joint Conference 2009 (ICCAS-SICE 2009), Fukuoka, Japan, 2009.
- [23] M. Satomi, H. Masuta, and N. Kubota, "Hierarchical Growing Neural Gas for Information Structured Space," in Proc. of the IEEE Symposium Series on Computational Intelligence 2009.
- [24] N. Kubota, T. Obo, and T. Fukuda, "An Intelligent Monitoring System based on Emotional Model in Sensor Networks," in Proc. of the 18th IEEE International Symposium on Robot and Human Interactive Communication, pp. 346-351, 2009.
- [25] D. Tang and N. Kubota, "Human Localization by Fuzzy Spiking Neural Network Based on Informationally Structured Space," in Proc. of the 17th International Conference on Neural Information Processing (ICONIP 2010), Sydney, Australia, pp. 25-32, 2010.
- [26] D. Tang, J. Botzheim, N. Kubota, and T. Yamaguchi, "Estimation of Human Transport Modes by Fuzzy Spiking Neural Network and Evolution Strategy in Informationally Structured Space," IEEE International Workshop on Genetic and Evolutionary Fuzzy Systems (GEFS), Singapore, April 16-19, pp. 36-43, 2013.
- [27] J. Botzheim, D. Tang, B. Yusuf, T. Obo, N. Kubota, and T. Yamaguchi, "Extraction of Daily Life Log Measured by Smart Phone Sensors using Neural Computing," 17th International Conference in Knowledge Based and Intelligent Information and Engineering system - KES2013, Procedia Computer Science 22, pp. 883-892, 2013.
- [28] <http://www.letsgodigital.org/en/23646/smartphone-price/>
- [29] <http://green.tmcnet.com/news/2013/02/18/6929794.htm>

- [30] <http://www.nuance.com/for-partners/by-solution/mobile-developer-program/index.htm>
- [31] J. A. Anderson and E. Rosenfeld, Neurocomputing. The MIT Press, Cambridge, Massachusetts, US, 1988.
- [32] W. Gerstner, "Spiking Neurons," In the book entitled "Pulsed Neural Networks" (Eds: W. Maass and C. M. Bishop), Chapter 1, MIT Press, pp. 3-53, 1999.
- [33] W. Gerstner and W. M. Kistler, Spiking Neuron Models. Cambridge University Press, 2002.
- [34] H.-P. Schwefel, Numerical Optimization of Computer Models. John Wiley & Sons, New York, 1981.
- [35] G. Syswerda, "A Study of Reproduction in Generational and Steady-State Genetic Algorithms," In Foundations of Genetic Algorithms, Morgan Kaufmann Publishers, Inc., pp. 94-101, 1991.

The Role of Data Authentication and Security in the Audit of Financial Statements

László Szívós

Faculty of Economics and Social Sciences, Department of Finance
Budapest University of Technology and Economics
Magyar tudósok körútja 2, H-1117 Budapest, Hungary
E-mail: szivos@finance.bme.hu

István Orosz

Doctoral School of Applied Informatics
Óbuda University
Bécsi út 96/b, H-1034 Budapest, Hungary
E-mail: orosz.istvan@arek.uni-obuda.hu

Abstract: Fairly presented financial statements are factual, free from bias and any material misstatements, and reflect the commercial substance of the financial transactions at a company. These statements have a standardized format and should be prepared in accordance with the applicable financial reporting framework. External audits provide reasonable assurance to the owners of the business's on to what extent financial statements are free of material misstatement whether due to error or fraud. There is always a risk (control risk) that the business's internal control system cannot prevent, detect or correct misstatements. The necessary sources of the financial data are handled nowadays by ERP (Enterprise Resource Planning) systems, triggered out the manual handwork. The applied ERP systems are different in companies according to the size and the business flows of the company. When it comes to a small or middle sized company, many of them use one generic system, which operates both the OLAP (analysis) and the OLTP (transaction processing) functions. There is a common risk to overwrite the master data, which can influence the reliability of financial statements. Lot of control procedures assure that the contained data are valid and show the true and fair state of the business. In this paper, we review how control procedures in an ERP system can influence the level of control risk and thus the scope and quantity of the audit procedures performed by the financial auditor.

Keywords: financial audit; control risk; ERP; master data management; data migration; data consistency check

1 Introduction

In the audit of financial statements there is always a risk that a misstatement appears at the assertion level which is material either individually or when aggregated and could not be prevented, detected or corrected by the internal control of the company. This type of risk is called control risk and it plays an important role in the risk assessment of financial auditors.

The accuracy and relevance of master data and master files are essential for the fair presentation of financial statements. Today the application of ERP systems is quite common in business. It also means that ERP provides the platform where master data and master files are managed and maintained. There are transactions which increase the risk of misstatements in the financial statements. Such transactions are e.g. data migration, or unauthorized change of data in master files. These can have an adverse impact on the level of risk perceived by auditors who have to maintain the overall audit risk at an acceptable level.

The article is structured as follows. First, the authors define the risk assessment procedure of the financial auditors and then give a thorough literature review on the impact of information technology applications on the financial audit procedure and on risk assessment. Secondly, they prove the importance of master data management in the accuracy of financial statements and demonstrate an available tool in Microsoft Dynamics AX environment for checking the integrity and consistency of master data across all relations. In the conclusion section they investigate the interrelation between consistency check and the financial audit procedure.

2 The Risk¹ of Auditing Financial Statements

There is always a risk that the auditor expresses an inappropriate audit opinion about the financial statements, this is called audit risk. Risk assessment procedures are conducted by the auditor to understand the entity and its environment, including its internal control, to identify the risk of material misstatement either due to error or fraud. Audit risk is made up of two components: the material misstatement risk and the detection risk.

Material misstatement risk can be split to inherent risk and control risk (Figure 1). Inherent risk is the susceptibility of an assertion to a misstatement that could be material, either individually or when aggregated with other misstatements, assuming that there were no related internal controls. Control risk arises in an assertion that could be material, either individually or when aggregated with other

¹ Definitions are based on ISA 200 [8]

misstatements that will not be prevented, or detected and corrected on a timely basis by the entity's internal control. Detection risk is the risk when the procedures conducted by the auditor will not detect a misstatement. This derives from the fact that the auditor does not, and cannot examine all available evidence. The control risk and the inherent risk are the risks of business and exist independently from the audit procedure.

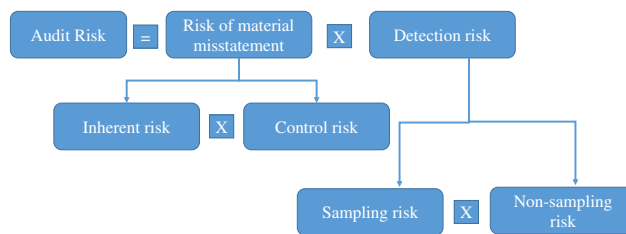


Figure 1

The components of audit risk

ISA 200 [8] states that in order to provide reasonable assurance the auditor should gather appropriate and sufficient audit evidence to keep audit risk at an acceptable level.

Our study investigates the control risk, which is one of the three above mentioned risk factors. Control risk depends on the effectiveness of internal control designed and implemented by the management of the entity. Efficient internal control, however, can only decrease but not totally eliminate the existence of control risk. This means that a certain level of control risk will always exist. The most common examples are human errors and mistakes, and examples when the management and those charged with governance override control.

Based on ISA 315 [8] definition, internal control is the process designed, implemented and maintained by those charged with governance, management and other personnel to provide reasonable assurance about the achievement of an entity's objectives with regard to the reliability of financial reporting, effectiveness and efficiency of operations and compliance with laws and regulations. Through a financial statement audit the auditor should acquire a reasonable understanding of the relevant aspects of the client's internal control system. This covers the identification of potential misstatements, the consideration of the factors that affect the risks of material misstatement, and based on the first two the design of the nature and timing of further audit procedures.

2.1 The Impact of Information System Applications at the Level of Control Risk

Companies can gain substantial benefits from using IT systems, however, this can also bring significant risks. The financial statement can be prepared based on IT systems which inaccurately process data or process inaccurate data, or in certain

cases both at the same time. If users have unauthorized access to data it might result in improper changes in data or in the record of unauthorized or non-existent transactions, or inaccurate recording of transactions.

ISA 315 [8] says that the auditor should understand the information systems applied by the company and all the related issues relevant to financial reporting. ISA 315 also says that the auditor shall overview the related accounting records, supporting information and specific accounts that are used to initiate, record, process and report transactions. It is also important for the auditor to understand the way the information system captures transactions and events that are significant to the financial statement.

Furthermore the auditor should understand how the company responds to the risks arising from the application of IT systems. The expected control an entity shall conduct can be split into two categories: 1) General IT controls and 2) Application controls. General IT controls are those policies and procedures which support the appropriate operations of an information system. General IT controls cover the following: 1) data centre and network operations, 2) system software acquisition, change and maintenance, 3) program change, 4) access security and 5) application system acquisition, development and maintenance. Application controls are procedures, either manual or automated, that run at business process level. The purpose of these controls is to maintain the integrity of accounting records. They are either preventive or detective. Most common application controls are: 1) controls over input: completeness, accuracy and authorization, 2) controls over processing, 3) controls over master file and standing data. The application of general IT controls and application controls are strictly interrelated in a way that they can either support or undermine each other. The strength of general controls can increase or decrease the reliability of application controls. For example the weaknesses in general control procedures, e.g. system development or software maintenance, or the authority of system users to sensitive data or system functions might result in a higher control risk as it can deteriorate the efficiency of application controls.

The level of control risk depends on the nature and characteristics of the company's information system. The company must manage the risk of using IT applications by setting up effective controls in respect of the nature of the information system.

2.2 The Response of Auditors to Increased Control Risk

As stated in ISA 200 the auditor is responsible for maintaining the audit risk at an acceptable level. As the audit risk is the function of the risk of material misstatement and the detection risk, if the internal control system fails to operate efficient and effective controls over the IT system it necessarily results in increased control risk and thus in increased material misstatement risk. In order to maintain the acceptable level of audit risk the auditor should outweigh this effect

by reducing the risk of detection. In this part we review what ISA 330 says about the auditor's required responses.

Based on ISA 330 [10] the auditor must design and apply appropriate responses to the assessed risk of material misstatement at the financial statement level. If the auditor reveals that the risk of material misstatement (including the control risk) is high, substantive procedures that respond to the assessed risk shall be conducted. The auditor can respond the assessed risk of material misstatement by means of:

- maintaining the professional scepticism in the engagement team,
- more experienced staff with more sophisticated skills should be appointed,
- the use of the work of experts,
- higher supervision over the audit process,
- higher unpredictability in the selection and application of audit procedures,
- general changes in the nature, timing and scope of the audit procedures.

The response of the auditor to the assessed risk highly depends on the auditor's opinion of the control environment. If the control environment is effective the auditor might put higher confidence in the internal control and the audit evidence gathered internally. Inefficiencies of the control environment, however, have the opposite impact on the procedures conducted by the auditor. The auditor's responses to the ineffective control environment are as follows:

- more audit procedures shall be conducted,
- gathering more audit evidence from substantive procedures,
- greater number of locations shall be included in the audit.

Any material misstatement revealed by the auditor is an indicator of the weakness in the internal control system. The auditor may decide to:

- perform only substantive analytical procedures as they are sufficient to reduce audit risk to the required level,
- conduct test of details only,
- use a combination of substantive analytical procedures and test of details.

As the assessment of the risk of material misstatement considers the characteristics and reliability of the internal control system, the extent of the substantive procedures should be increased if internal control turns to be inefficient.

However, it should be highlighted that the auditor's risk assessment is a matter of professional judgement, so might not take into consideration all risks of material misstatement and there are inherent limitations to internal control, i.e. management can override controls.

3 Literature Review

Both the function of audit and the required audit procedures (analytical and substantive) went through significant changes as a consequence of more intensive ERP system application among businesses. The research conducted by Wright and Wright (2002) [18] evidenced the fact that the application of ERPs significantly increases the control risk. They also stated that many of the risks come from inadequate training of personnel. However, efficient internal control procedures can outweigh the risk arising from the application. The companies must manage the control procedures properly as it costs approximately 50 to 100 times more to add functionality or to correct an error post-implementation than it would have cost to provide the proper functionality during the implementation (Goldberg and Godwin 2003) [6].

Bae and Aschroft (2004) [2] stated in their article that external auditors shall focus on two issues, on control activities and on information and communication, out of several components of an internal control system. Control activities are procedures to protect the company's assets and prevent the manipulation of accounting records. Information and communication are the timely identification, collection, processing and reporting of relevant data in a useful format, such that employees can effectively meet their responsibilities. It is essential for an external auditor to understand and document how the ERP system collects and processes data and what are the controls implemented in relation to the ERP system.

The research conducted by Messier *et al.* (2004) [14], surveying the six biggest public accounting firms in Norway, investigated the impact of IT on the audit procedures performed by external auditors. The research also examined whether the origins of misstatements revealed by the audit are different for computerized and non-computerized business processes. They found that control procedures were missing more often in computerized rather than non-computerized business processes and there is an increase in the cause of misstatements resulting from missing and poorly designed controls and audit test. They also found that as IT emerged in business, a deterioration of the control environment and excess workload of accounting staff could be observed. The authors identified that the main reason auditors could not rely on the internal control was their belief that substantive testing was more effective.

Some earlier researches indicated (e.g. Hunton *et al.*, 2004 [7]) that financial auditors recognize the risk associated with the ERP systems differently than IT auditors. Only certified public accountants were included in the research and the survey found that financial auditors were less concerned than IT auditors with the increased risk of the ERP implementation (e.g. business continuity, database security, application security). Financial auditors had a higher belief in their capabilities to evaluate risk in both computerized and non-computerized information systems. Financial auditors need the expertise of IT auditors and a strong cooperation between them is required. A study conducted by Brazel and

Agoglia in 2007 [3] showed that auditors having a higher information system expertise assessed higher control risk in the case of new information system (e.g. ERP) implementation than those not having previous IT experience and when internal control and computer assurance specialist competence was low, financial auditors planned more extensive substantive testing. As we evidenced above the relevant standard on auditing (ISA 315) requires the financial auditors to change their audit procedures and strategies in response to changes in the audit clients' information systems. However, some researches indicated (e.g. POB 2000 [16]) that the level of and the change in control risk sometimes are not reflected in the audit procedures performed by financial auditors.

As the consequence of using IT applications and ERP systems in businesses, the auditors were forced to cope with the challenges of providing audit in IT environment. Many professional bodies (IFAC – International Federation of Accountants, ISACA – Information System Audit and Control Association, AICPA – American Institution of Certified Public Accountants) have issued standards in this area. The survey of Yang and Guan in 2004 [19] examines the importance and advantages of using these standards in financial statement audits and emphasizes the importance of having a thorough understanding of these guidelines, standards by the auditors. Vendrzyk and Bagranoff in 2003 [17] investigated the impact of information system audit on the work of financial auditors. They found that in the last couple of decades the role of IT audit has shifted from a support tool towards an important pillar of financial audit. They also revealed that financial auditors found the test of general and application controls very important and the weaknesses of these controls have an impact on the scope of the audit procedures performed by financial auditors.

Based on reviewing all relevant literature Kanellou and Spathis 2011 [11] stated that ERP systems exert a significant impact on financial audit and internal audit. According to Kuhn and Sutton 2010 [12] in ERP environment errors might be undetected if there are no sufficient audit procedures performed, so internal control procedures shall be improved. Several risks appear and the most significant ones are related to information integrity, transaction errors, transparency of data and fraud.

4 Master Data Management

One of the first steps of keeping the system data validation is to secure the integrity and consistency of the Master Data. If Master Data records can be overridden, like the legal entity, this could lead to a serious problem. The area of the Master Data has to be first identified, and rules must be declared on how the change process will look like in this area. The area which will be called Master Data can be described on its way by interacting with other data areas. In ERP systems, the generally called Master Data is usually involved in each transaction

[5] [13]. For instance a customer can buy a product; a vendor can sell an accessory. Between the master data and the transactional data, these relationships can be examined. These are the main areas, which can be covered by this definition:

- Vendor and customer core data
- Global Address Book
- General Ledger
- Inventory
- Fixed Assets
- Open Financial Transactions (e.g. open purchase order, open sales orders etc.)
- Warehousing and transportation data
- Production data

There is another way of defining Master Data by its life cycle. These functions describe the following operations: create, read, update, delete, search, generally called SCRUD. When we define the Master Data this way, it will slightly change from company to company. It is a common experience that Master Data generally tends to be more volatile than transactional data, which means that it is important to keep the validity. The key usage of Master Data is reusability; we want to use the valid data as a basic of the transactions entered in the system. ERP's role is becoming more and more complex and the need is common for storing the Master Data only in one place and reuse it via a common channel. Proper Master Data Management could be vital (Figure 2), for instance a typing mistake in an invoice ship-to or bill-to address may cause loss of money. But we also mention the possibility of a mistyped price in the item master, an incorrect account number in account master – these actions can lead to even fraud-like actions. So maintaining the Master Data, and keeping the validity and consistency is very important to avoid these kind of issues when operating an ERP system.

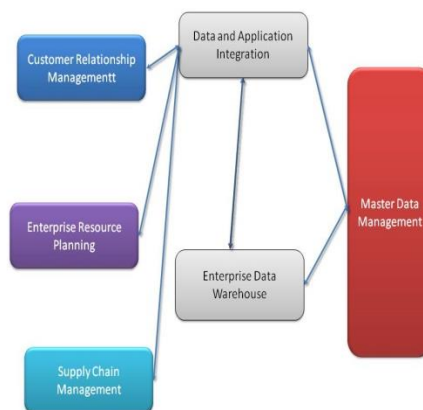


Figure 2

Data flow in the area of Master Data Management

Suppose that the current status of the Master Data does not contain any error. In this case, we should secure, that only one used entity exists, and no one uses local copies from cache, etc. An older and not up-to-date version of Master Data could cause exactly the same issues as mentioned in the previous section.

There are many companies, which are growing through mergers and/or acquisitions. Each time they acquire a company, the following problem occurs: the acquired company has its own Master Data and transactional data. This fact can lead to issues at merging: the structure of the data is different, sometimes came from different ERP, and there are possible duplicates. When the company acquired comes from a corresponding area of business, which is a possible situation, they likely to have the same customers, vendors. Transactional data have to be checked one by one for all of these vendors and customers. Items, attributes and inventory Master Data could be even harder to reconcile, when the corresponding parts were supplied by the same vendor, but probably with different item and vendor identifiers. Handling these kind of problems can be a part of the company's change management process (Figure 3).

Common data cleansing issue is to consolidate the different versions of the same data element. Let's get an example, the same vendor, who can have several business names, site addresses, phone and fax numbers. The name of the business responsible can be written as Mátyás Gábor, Gábor Mátyás, Gabor Matyas, Matyas Gabor, and in a lot of other versions. The data cleansing in this case needs a lot of manual handwork, because normal database data update queries cannot resolve this issue correctly [15].



Figure 3

Change management structure

At this stage it is important to estimate the amount of fully or partly invalid data. There are only limited tools for this estimation, only for the syntax issues. Right now the exact estimation needs a lot of handwork because of the hardships in semantic comparison automatization.

There are a lot of advantages, when a company has a clean, up-to-date and valid Master Data:

- can improve customer satisfaction,
- could save time and money in business operations,
- could reduce the danger of loss of revenue,
- could reduce the possibility of legal issues when preparing financial statements,
- reduces the time need of the database maintenance,
- minimizes the possible impact of having a corrupt database.

It is clear about these reasons, that having a real consistent and valid set of Master Data is vital for every ERP systems. All the policies, processes and systems, which are needed to achieve this is known as Master Data Management.

If Master Data Management is well defined, we should note, that it is just partly a technological problem, but the most difficult things to solve in this area are related to business processes and internal data flows.

Standardizing the data is often the most difficult part of making the right Master Data. On the technical side, at first the data structure has to be normalized to 4th normal form. After normalization the missing values have to be inserted, for instance the default values and the initial setups. Often there is a next step when standardizing the values, e.g. convert all dimensions to metric, all prices to a common currency. In this case at multinational companies there is a need to have a solution for cross-converting.

The future research direction will focus on the validation of Master Data. What kind of algorithms can be used to automatize the validation process, and how can the human factor be minimized? Future research efforts are needed on how can be determined the amount of invalid data, how can it be estimated?

5 Consistency Check, a Proposed Methodology to Reduce Control Risk

Consistency Check is one of the strongest tools in Microsoft Dynamics AX to secure the validity and consistency of the transactional data. Technically it is a batch processing tool, which validates every transactional data in the system, and checks the connections between the other transactions and Master Data as well.

The running time of this tool can be extremely long, depending on the number of the transactions in the system.

Tables in Dynamics AX can be divided into three categories: 1) master data tables like Customers, Ledger Accounts, Vendors, etc.; 2) transaction headers like Sales Orders, Purchase Orders and 3) transaction details like Sales Lines, PO Lines, etc. When a transaction is entered into Dynamics AX, the necessary indexes and keys are updated for connecting Sales Orders and Lines.

Sometime these records can be abandoned, which means, that the parent record was deleted while the child records still exist. These are called orphan records², because the transaction still exists, but either the parent or the child does not exist anymore.

If we have numerous orphan records, it can slow down the performance. To avoid these situations, AX2012 has a tool, which is called consistency check. The basic idea behind this tool is to go through the whole database and scan for orphan records. Keeping the transactional data up-to-date is vital for every ERP system, no matter what was the scenario because these records remained orphaned.

The ConsistencyCheck framework is the core of the Dynamics AX data migration process. If we want to use it as a whole integrity check for the database, more tables and rules can be inserted into the validation process. These modifications should be derived from the SysConsistencyCheck base class, and should make the following methods: executionorder(), run(), description(), helptext() (Figure 4). All the derived classes should overwrite these methods to specify the related tables and methods. The kernelCheckTable and kernelCheckRecords methods check the relation between these tables. The modifications are essential, because the standard consistency check which comes out of the box with dynamics AX does not contain the necessary areas for a specific implementation.

These customizations enable for example an Independent Solution Provider (ISV) to include their data area in the consistency and integrity check. This also prevents users from false positive checks.

There are standard tools for maintaining transaction integrity in Dynamics AX, like ttsLevel (SQL transaction level) checking and forUpdate checks within data manipulation codes. Although these are low level tools, we should mention them, as the right usage of them makes the consistency check cleaner on the technical side. If we check the functionality of forUpdate, we can see that it ensures that a record can be deleted or updated only if it was first selected for update.

² Orphan records are records of data that have no longer connection to other data.

```
Query                query;
QueryBuildDataSource qbds;
QueryRun             queryRun;

// LedgerTable
this.kernelCheckTable(tableNum(LedgerTable));

// LedgerJournalTable
query = new Query();
qbds = query.addDataSource(tableNum(LedgerJournalTable));
qbds.addRange(fieldNum(LedgerJournalTable,posted)).value(enum);
queryRun = new QueryRun(query);
this.kernelCheckRecords(queryRun);

// LedgerTableAlternative
this.kernelCheckTable(tableNum(LedgerTableAlternative));

// LedgerTableAlternativeTrans
this.kernelCheckTable(tableNum(LedgerTableAlternativeTrans));
```

Figure 4

LedgerConsistencyCheck.run() method

The `ttsLevel` check works similarly, ensures that a record can be updated or deleted only in the same transaction scope as it was selected for update. The transaction scope is bordered by the `ttsBegin` and `ttsCommit`. The first marks the beginning of the scope, and guarantees that all updates are consistent which are performed until the transaction ends. The second marks the successful end of a transaction, and commits all the changes. If there are any circumstances which deny the transaction to be consistent, the `ttsAbort` can discard all the changes and rolls back the database in the previous state. Maintaining referential integrity is a vital point for any ERP applications. In Dynamics AX 2012, we can model table relations with rich metadata content and express referential integrity. Dynamics AX 2012 does not represent table relations as SQL foreign table key constraints, because of the huge performance overhead in the SQL server. The application code can also violate referential integrity. In this case, referential integrity maintenance means that the data manipulating operations have to be performed in correct order. This is most vital when records are deleted and created. The parent record must be created first, before the child records can get the correct foreign key. And the following is also true; the child records must be deleted first before the parent records. Ensuring this from code can be hardly maintained, especially with the strongly normalized data structure of Dynamics AX 2012. That is the reason, why Dynamics AX 2012 provides a new programming concept, which is called Unit Of Work. This is basically a set of data manipulation methods, which are performed on the related data. The application code establishes the connection within the data in memory, modifies them, registers the modifications and then requests the Unit Of Work to perform the necessary operations in the correct sequence. For example, if the `RecId` of the header comes as a foreign key to the lines, we cannot insert lines first because we need the `RecId` of the header record.

Also we cannot insert the header first, if we need SUM from the lines. If we use the Unit Of Work class, all these are handled by the AX kernel itself.

Troubleshooting these data consistency issues during upgrading to a newer version of Dynamics AX or migrating to / from a different ERP system is vital part of the Data Migration process. In the first test after the migration, it is natural to have consistency errors both during and after the process. There are some guidelines to follow which can help quickly to find the root cause of the issues. At first, one has to check the generate mapping form to see if there are any mapping errors. After this it has to be determined if the issue is on the source or the target side of the process. Data Consistency Check can help this decision. There are two options:

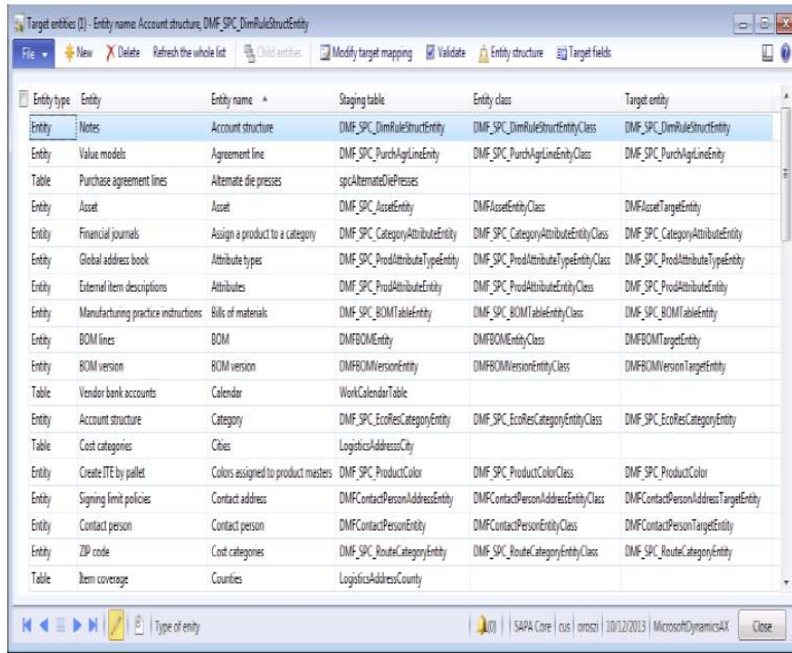
- The data looks corrupt: which means that the issue occurred in the source side. We have to determine the source table and the transformations made on this table. If the table is part of a transformation, one has to be sure which tables were populated and with what kind of outcomes?
- The data is ok: the issue is on the target side. If the data were copied correctly during the bulk copying, the script, which was used during the data migration, has to be determined. From this point, we can debug the script to determine the critical operation. It is also useful to check the dependencies of the script.

After this decision, the data migration process has to be corrected, rerun, and the consistency should be checked again. After the check, we can quickly determine if there are any modifications needed for the process.

The most important usage of the Data Consistency Check is carried out after a successful import of data, thus after the Data Migration. It assures that data are consistent through different relations and cross references. It prevents the system from becoming corrupted, and can warn for the underlying problems under the hood. If we cannot pay enough attention to these issues, they can seriously jeopardize the stability of the system.

There are some challenges with customizing complex business rules in integrity checks but the need for avoiding the manual checks is always stronger. Using Consistency Check with Data Migration is an essential step for a successful migration (Figure 5).

This tool provides a wide range of information, which needs to be evaluated by the data steward or master data track lead, because of the complexity of the field.



Entity type	Entity	Entity name	Staging table	Entity class	Target entity
Entity	Notes	Account structure	DMF_SPC_DimRuleStructEntity	DMF_SPC_DimRuleStructEntityClass	DMF_SPC_DimRuleStructEntity
Entity	Value models	Agreement line	DMF_SPC_PurchAgriLineEntity	DMF_SPC_PurchAgriLineEntityClass	DMF_SPC_PurchAgriLineEntity
Table	Purchase agreement lines	Alternate die presses	spcAlternateDiePresses		
Entity	Asset	Asset	DMF_SPC_AssetEntity	DMF_SPC_AssetEntityClass	DMF_SPC_AssetTargetEntity
Entity	Financial journals	Assign a product to a category	DMF_SPC_CategoryAttributeEntity	DMF_SPC_CategoryAttributeEntityClass	DMF_SPC_CategoryAttributeEntity
Entity	Global address book	Attribute types	DMF_SPC_ProdAttributeTypeEntity	DMF_SPC_ProdAttributeTypeEntityClass	DMF_SPC_ProdAttributeTypeEntity
Entity	External item descriptions	Attributes	DMF_SPC_ProdAttributeEntity	DMF_SPC_ProdAttributeEntityClass	DMF_SPC_ProdAttributeEntity
Entity	Manufacturing practice instructions	Bills of materials	DMF_SPC_BOMTableEntity	DMF_SPC_BOMTableEntityClass	DMF_SPC_BOMTableEntity
Entity	BOM lines	BOM	DMFBOMEntity	DMFBOMEntityClass	DMFBOMTargetEntity
Entity	BOM version	BOM version	DMFBOMVersionEntity	DMFBOMVersionEntityClass	DMFBOMVersionTargetEntity
Table	Vendor bank accounts	Calendar	WorkCalendarTable		
Entity	Account structure	Category	DMF_SPC_EcoResCategoryEntity	DMF_SPC_EcoResCategoryEntityClass	DMF_SPC_EcoResCategoryEntity
Table	Cost categories	Cities	LogisticsAddressCity		
Entity	Create ITE by pallet	Colors assigned to product masters	DMF_SPC_ProductColor	DMF_SPC_ProductColorClass	DMF_SPC_ProductColor
Entity	Signing limit policies	Contact address	DMFContactPersonAddressEntity	DMFContactPersonAddressEntityClass	DMFContactPersonAddressTargetEntity
Entity	Contact person	Contact person	DMFContactPersonEntity	DMFContactPersonEntityClass	DMFContactPersonTargetEntity
Entity	ZIP code	Cost categories	DMF_SPC_RouteCategoryEntity	DMF_SPC_RouteCategoryEntityClass	DMF_SPC_RouteCategoryEntity
Table	Item coverage	Countries	LogisticsAddressCountry		

Figure 5
Data Migration Framework entities

Conclusion

The aim of the Data Consistency Check is similar in every ERP system. With this tool, the system can guarantee that the master data is valid in all respects. If we develop the necessary parts for the customized code, it will also be true for those parts as well. The outcome of this function is a report, which contains all the table records with issues. If the report is empty, then it is a theoretically perfect database. Based on practical experience usually it is not the case, so after a migration cycle there are always consistency issues arising, so data inaccuracies and corruptions can be fixed immediately before transactional records start to use the corrupt data.

The application of Data Consistency Check is optional but not mandatory after data migration. Data migration carries the risk of data corruption and inconsistencies in master data and transactional data. In the absence of effective control procedures the reliability of the data from which the amounts in the statements are calculated is highly questionable. As a consequence, auditors should perform more extensive substantive procedures to check master data and transactional data accuracy in order to detect material misstatements at financial statement level. As many researches proved that it is 50 to 100 times more expensive to correct mistakes than to prevent them, the usage of control

procedures becomes more important. If effective general and application IT controls are in place, after these controls having been tested, financial auditors can rely on them. So the application and proper documentation of Data Consistency Check and other similar control procedures would decrease the control risk and as a consequence would result in:

- lower level of audit risk,
- less extensive substantive procedures,
- lower sample sizes,
- shorter audit procedure.

We can also conclude that the current methodology of the consistency check in Dynamics AX is useful for providing necessary information about the validity of transactional data, but it needs to have a broader validity area to be useful enough. We need to make a detailed description of the validity of a business rule, not just white and black. When it comes to enhancing the possibilities of this tool, we need to focus on advanced machine learning and intelligence techniques, e.g. fuzzy logic [4] [1]. Master Data management needs extensive standardization as it is heavily dependent on the methodology of the project.

References

- [1] Anil Kumar Gupta, "Quality Assurance for Dynamics AX-based ERP Solutions: Verifying Dynamics AX customization to the Microsoft IBI Standards Studies". Packt Publishing, 2002, ISBN-10: 1847192912
- [2] Bae, N. and Aschroft P.: "Implementation of ERP Systems: Accounting and Auditing Implications", Information System Control Journal, 2004, Vol. 5, pp. 43-8
- [3] Brazel, J. F. and Agoglia, C. P.: "An Examination of Auditor Planning Judgements in a Complex Accounting Information System Environment", Contemporary Accounting Research, 2007, Vol. 24, No. 4, pp. 1059-83
- [4] Fodor, J., Ósz, R., "Possible Applications of Fuzzy Methodology in the Educational Process", IEEE 11th International Symposium on Applied Machine Intelligence and Informatics (SAMi), DOI: 10.1109/SAMI.2013.6480992, ISBN: 978-1-4673-5927-6, pp. 37-40, 2013
- [5] Forrester, Jay Wright, "Industrial Dynamics". Waltham, MA: Pegasus Communications, 1961
- [6] Goldberg, S. and Godwin, J. H.: "Operational Reviews on Auditing ERP", The Journal of Corporate Accounting and Finance, 2003, Vol. 14, No. 4, pp. 63-5
- [7] Hunton, J. E., Wright, A. M. and Wright, S.: "Are Financial Auditors Overconfident in Their Ability to Assess Risk Associated with Enterprise

- Resource Planning System?”, *Journal of Information Systems*, 2004, Vol. 18, No. 2, pp. 7-28
- [8] International Standard on Auditing 200: Overall Objectives of the Independent Auditor and the Conduct of an Audit in Accordance with International Standards on Auditing, IFAC. <http://www.ifac.org/sites/default/files/downloads/a008-2010-iaasb-handbook-isa-200.pdf>
- [9] International Standard on Auditing 315: Identifying and Assessing the Risk of Material Misstatement through Understanding the Entity and Its Environment, IFAC. <http://www.ifac.org/sites/default/files/downloads/a017-2010-iaasb-handbook-isa-315.pdf>
- [10] International Standard on Auditing 330: The Auditor’s Response to Assessed Risks, IFAC. <http://www.ifac.org/sites/default/files/downloads/a019-2010-iaasb-handbook-isa-330.pdf>
- [11] Kanellou, A. and Spathis, C.: ”Auditing in Enterprise System Environment: a Synthesis”, 2011, *Journal of Enterprise Information Management*, Vol. 24, No. 6, pp. 494-519
- [12] Kuhn, J. R. and Sutton, S. G.: “Continuous Auditing in ERP System Environments: the Current State and Future Directions”, 2010, *Journal of Information Systems*, Vol. 24, No. 1, pp. 99-112
- [13] Maedche, Alexander, "An ERP-Centric Master Data Management Approach" (2010) AMCIS 2010 Proceedings. Paper 384. <http://aisel.aisnet.org/amcis2010/384>
- [14] Messier W. F., Eilifsen, A. and Austen, L. A.:”Auditor Detected Misstatements and the Effect of Information Technology”, *International Journal on Auditing*, 2004, Vol. 8, pp. 223-35
- [15] Osz, Rita; Fodor, Janos: “Possible Connecting Areas of Education and Intelligent Systems”, 2013 IEEE 9th International Conference on Computational Cybernetics (ICCC), Digital Object Identifier: 10.1109/ICCCyb.2013.6617560, Print ISBN:978-1-4799-0060-2, pp. 51-56
- [16] Public Oversight Board (POB): Panel on Audit Effectiveness: Report and recommendations, 2000, AICPA, Stamford, CT
- [17] Venzryk, V. P. and Bagranoff, N. A.: ”The Evolving Role of IS Audit: a Field Study Comparing the Perceptions of IS and Financial Auditors.” 2003, *Advances in Accounting*, Vol. 20, pp. 141-63
- [18] Wright, S. and Wright, A. M.: “Information System Assurance for Enterprise Resource Planning Systems: Unique Risk Considerations”, *Journal of Information Systems*, 2002, Vol. 16, pp. 99-113
- [19] Yang, D. C. and Guan, L.: “The Evolution of IT Auditing and Internal Control Standards in Financial Statement Audit. The Case of the United States”, 2004, *Managerial Auditing Journal*, Vol. 19, No. 4, pp. 544-55

Stability of the Classifications of Returns to Scale in Data Envelopment Analysis: A Case Study of the Set of Public Postal Operators

Predrag Ralevic¹, Momčilo Dobrodolac², Dejan Markovic², Matthias Finger³

¹ PhD Candidate at Faculty of Transport and Traffic Engineering, University of Belgrade, Vojvode Stepe Street 305, 11000 Belgrade, Serbia
E-mail: p.ralevic@sf.bg.ac.rs

² Faculty of Transport and Traffic Engineering, University of Belgrade, Vojvode Stepe Street 305, 11000 Belgrade, Serbia
E-mail: m.dobrodolac@sf.bg.ac.rs, mdejan@sf.bg.ac.rs

³ Ecole Polytechnique Fédérale de Lausanne (EPFL), Odyssea 215, Station 5, 1015 Lausanne, Switzerland
E-mail: matthias.finger@epfl.ch

Abstract: A significant theme in data envelopment analysis (DEA) is the stability of returns to scale (RTS) classification of specific decision making unit (DMU) which is under observed production possibility set. In this study the observed DMUs are public postal operators (PPOs) in European Union member states and Serbia as a candidate country. We demonstrated a sensitivity analysis of the inefficient PPOs by DEA-based approach. The development of this analytical process is performed based on real world data set. The estimations and implications are derived from the empirical study by using the CCR RTS method and the most productive scale size concept (MPSS). First, we estimated the RTS classification of all observed PPOs. After that, we determined stability intervals for preserving the RTS classification for each CCR inefficient PPO under evaluation. Finally, scale efficient inputs and output targets for these PPOs are designated.

Keywords: data envelopment analysis; returns to scale; stability; scale efficient targets; public postal operators

1 Introduction

Data envelopment analysis (DEA) is a non-parametric technique for evaluating the relative efficiency of multiple-input and multiple-output of a decision making units (DMUs) based on the production possibility set. DEA method is introduced

by Charnes *et al.* [1] and extended by Banker *et al.* [2]. There are various DEA models that are widely used to evaluate the relative efficiency of DMUs in different organizations or industries. Additionally, DEA is recognized as a powerful analytical research tool for modeling operational processes in terms of performance evaluations, e.g. [3], competitiveness, e.g. [4] and decision making e.g. [5]. A taxonomy and general model frameworks for DEA can be found in [6, 7].

The stability of the classifications of returns to scale (RTS) is an important theme in DEA and was first examined by Seiford and Zhu [8]. There are several DEA approaches considering this topic. One approach is the stability analysis of a specific DMU which is under evaluation [see 9, 10]. Another approach is the stability of a specific DMU which is not under evaluation [see 11, 12]. Additionally, some authors used free disposal hull (FDH) models (unlike the convex DEA models, FDH models are non-convex) for estimating RTS [see 13, 14, 15].

The stability of RTS and the methods for its estimating in DEA provides important information on the data perturbations in the DMU analysis. These information provide discussions that can be developed in performance analysis. This enables to determine the movement of inefficient DMUs on the frontier in improving directions. In [8, 16], the authors developed several linear programming formulations for investigating the stability of RTS classification (constant, increasing or decreasing returns to scale). These authors considered data perturbations for inefficient DMUs. The authors of [17] indicated that sometimes a change in input or output or simultaneous changes in input and output are not possible. In the papers of Jahanshahloo *et al.* [10] and Abri [18] developed an approach for the sensitivity analysis of both inefficient and efficient DMUs from the observations set.

The current article proceeds as follows: In Section 2, the determination of RTS in the CCR models is reviewed. Additionally, in this Section are introduced output-oriented RTS classification stability and scale efficient targets inputs and outputs of DMUs. In Section 3, we applied methods from Section 2 on real world data set of public postal operators (PPOs). Finally, conclusions are given in Section 4.

2 Methods

2.1 RTS Classification

In the DEA literature there are several approaches for estimating of returns to scale (RTS). Seiford and Zhu in [19] demonstrated that there are at least three

equivalent RTS methods. The first CCR RTS method is introduced by Banker [20]. The second BCC RTS method is developed by Banker *et al.* [2] as an alternative approach using the free variable in the BCC dual model. The third RTS method based on the scale efficiency index is suggested by Fare *et al.* [21]. The CCR RTS method is based upon the sum of the optimal lambda values in the CCR models of DEA, and is used in this study to the RTS classifications of observed PPOs.

The CCR is original model of DEA for evaluating the relative efficiency for a group of DMUs proposed by Charnes *et al.* [1]. The CCR stands for Charnes, Cooper and Rhodes which are the last names of this model creators. Suppose there are a set (A) of DMUs. Each DMU_j ($j \in A$) uses m inputs x_{ij} ($i = 1, 2, 3, \dots, m$) to produce s outputs y_{rj} ($r = 1, 2, 3, \dots, s$). The CCR model evaluates the relative efficiency of a specific DMU_o , $o \in A$, with respect to a set of CCR frontier DMUs defined $E_o = \{j \mid \lambda_j > 0 \text{ for some optimal solutions for } DMU_o\}$. One formulation of a CCR model aims to minimize inputs while satisfying at least the given output levels, i.e., the CCR input-oriented model (see the M1 model). Another formulation of a CCR model aims to maximize outputs without requiring more of any of the observed input values, i.e., the CCR output-oriented model (see the M1' model). The CCR models assume the constant returns to scale production possibility set, i.e. it is postulated that the radial expansion and reduction of all observed DMUs and their nonnegative combinations are possible and hence the CCR score is called overall technical efficiency. If we add

$\sum_{j \in E_o} \lambda_j = 1$ in the M1 and M1' models, we obtain the BCC input-oriented and the

BCC output-oriented models, respectively proposed by Banker *et al.* [2]. The name BCC is derived from the initial of each creator's last name (Banker-Charnes-Cooper). The BCC models assume that convex combinations of observed DMUs form the production possibility set and the BCC score is called local pure technical efficiency. It is interesting to investigate the sources of inefficiency that a DMU might have. Are they caused by the inefficient operations of the DMU itself or by the disadvantageous conditions under which the DMU is operating? For this purpose the scale efficiency score (SS) is defined by the ratio,

$SS = \frac{\theta_{CCR}^*}{\theta_{BCC}^*}$. This approach depicts the sources of inefficiency, i.e. whether it is

caused by inefficient operations (the BCC efficiency) or by disadvantageous conditions displayed by the scale efficiency score (SS) or by both.

M1 model

$$\theta^* = \min \theta \tag{1}$$

Subject to:

$$\sum_{j \in E_o} \lambda_j x_{ij} \leq \theta x_{io}, \quad i = 1, 2, 3, \dots, m$$

$$\sum_{j \in E_o} \lambda_j y_{rj} \geq y_{ro}, \quad r = 1, 2, 3, \dots, s$$

$$\lambda_j \geq 0, \quad j \in E_o$$

M1' model

$$\phi^* = \max \phi \tag{2}$$

Subject to:

$$\sum_{j \in E_o} \lambda_j x_{ij} \leq x_{io}, \quad i = 1, 2, 3, \dots, m$$

$$\sum_{j \in E_o} \lambda_j y_{rj} \geq \phi y_{ro}, \quad r = 1, 2, 3, \dots, s$$

$$\lambda_j \geq 0, \quad j \in E_o$$

If $E_o = A$, then the M1 model is original form of the input-oriented CCR model.

The DMU_j ($j \in E_o$) are called CCR efficient and form a specific CCR efficient aspect. These DMU_j ($j \in E_o$) appear in optimal solutions where $\lambda_j > 0$. The fact that $\lambda_j = 0$ for all $j \notin E_o$ in the M1 model when evaluating DMU_o enables performing the CCR model in form of M1 model or M1' model. By using the M1 or M1' model, we can estimate the RTS classification based on the following theorem by Banker and Thrall [22]:

Theorem 1. Let λ_j^* ($j \in E_o$) be the optimal values in M1 or M1' model, returns to scale at DMU_o can be determined from the following conditions:

(i) If $\sum_{j \in E_o} \lambda_j^* = 1$ in any alternate optimum then constant returns-to-scale (CRS) prevails.

(ii) If $\sum_{j \in E_o} \lambda_j^* > 1$ for all alternate optima then decreasing returns-to-scale (DRS) prevails.

(iii) If $\sum_{j \in E_o} \lambda_j^* < 1$ for all alternate optima then increasing returns-to-scale (IRS) prevails.

Seiford and Thrall in [23] derived the relationship between the solutions of the M1 model and M1' model. Suppose λ_j^* ($j \in E_o$) and θ^* is an optimal solution to M1 model. There exists a corresponding optimal solution λ_j^{**} ($j \in E_o$) and ϕ^*

to the M1' model such that $\lambda_j^* = \frac{\lambda_j^{**}}{\phi^*}$ and $\phi^* = \frac{1}{\theta^*}$.

A change of input levels for DMU_o in the M1 model or a change of output levels in the M1' model does not change the RTS nature of DMU_o . These models yield the identical RTS regions. However, they can generate different RTS classifications. In this study we chose the M1 model to determine the RTS classification.

2.2 Stability of the RTS Classifications

The stability of the RTS classifications provides some stability intervals for preserving the RTS classification of a specific DMU_o . It enables to consider perturbations for all the inputs or outputs of DMU_o . Input-oriented stability of RTS classifications allows output perturbations in DMU_o , and output-oriented stability of RTS classifications enables input perturbations.

In this study stability intervals of each CCR inefficient PPO under evaluation are derived from output-oriented RTS classification stability because we aim to consider input increases and decreases for each CCR inefficient PPO. Lower and upper limit of stability intervals determined by using two linear programming models (see the M2 and M2' models) where ϕ^* is the optimal value to the M1' model when evaluating DMU_o .

M2 model

$$\eta_o^* = \frac{1}{\min \sum_{j \in E_o} \lambda_j} \quad (3)$$

Subject to:

$$\sum_{j \in E_o} \lambda_j x_{ij} \leq x_{io}, \quad i = 1, 2, 3, \dots, m$$

$$\sum_{j \in E_o} \lambda_j y_{rj} \geq \phi^* y_{ro}, \quad r = 1, 2, 3, \dots, s$$

$$\lambda_j \geq 0, \quad j \in E_o$$

M2' model

$$\mu_o^* = \frac{1}{\max \sum_{j \in E_o} \lambda_j} \quad (4)$$

Subject to:

$$\sum_{j \in E_o} \lambda_j x_{ij} \leq x_{io}, \quad i = 1, 2, 3, \dots, m$$

$$\sum_{j \in E_o} \lambda_j y_{rj} \geq \phi^* y_{ro}, \quad r = 1, 2, 3, \dots, s$$

$$\lambda_j \geq 0, \quad j \in E_o$$

By using the M2 and M2' models, we can define lower and upper limit of stability intervals of DMUs based on the following theorems by Seiford and Zhu [8]:

Theorem 2. Suppose DMU_o exhibits CRS.

If $\gamma \in R^{CRS} = \{ \gamma : \min \{ 1, \mu_o^* \} \leq \gamma \leq \max \{ 1, \eta_o^* \} \}$. The CRS classification continues to hold, where γ represents the proportional change of all inputs, $\hat{x}_{io} = \gamma x_{io}$ ($i = 1, 2, 3, \dots, m$), and η_o^* and μ_o^* are defined in the M2 and M2' models, respectively.

Theorem 3. Suppose DMU_o exhibits DRS. The DRS classification continues to hold for $\xi \in R^{DRS} = \{ \xi : \eta_o^* < \xi \leq 1 \}$, where ξ represents the proportional decrease of all inputs, $\hat{x}_{io} = \xi x_{io}$ ($i = 1, 2, 3, \dots, m$), and η_o^* is defined in the M2 model.

Theorem 4. Suppose DMU_o exhibits IRS. Then the IRS classification continues to hold for $\zeta \in R^{IRS} = \{\zeta : \mu_o^* < \zeta \leq 1\}$, where ζ represents the proportional change of all inputs, $\hat{x}_{io} = \zeta x_{io}$ ($i = 1, 2, 3, \dots, m$), and μ_o^* is defined in the M2' model.

2.3 Scale Efficient Targets

Scale efficient targets (inputs and outputs) for DMUs can be derived by using the most productive scale size concept proposed by Banker [20]. This concept in DEA is known as acronym MPSS (see the M3 and M3' models). Both models are based on output-oriented CCR model. The M3 model produces the largest MPSS targets ($MPSS_{max}$), and the M3' model the smallest ($MPSS_{min}$).

M3 model

$$\mathcal{G}^* = \min \sum_{j \in E_o} \lambda_j \quad (5)$$

Subject to:

$$\sum_{j \in E_o} \lambda_j x_{ij} \leq x_{io}, \quad i = 1, 2, 3, \dots, m$$

$$\sum_{j \in E_o} \lambda_j y_{rj} \geq \phi^* y_{ro}, \quad r = 1, 2, 3, \dots, s$$

$$\lambda_j \geq 0, \quad j \in E_o$$

M3' model

$$\mathcal{V}^* = \max \sum_{j \in E_o} \lambda_j \quad (6)$$

Subject to:

$$\sum_{j \in E_o} \lambda_j x_{ij} \leq x_{io}, \quad i = 1, 2, 3, \dots, m$$

$$\sum_{j \in E_o} \lambda_j y_{rj} \geq \phi^* y_{ro}, \quad r = 1, 2, 3, \dots, s$$

$$\lambda_j \geq 0, \quad j \in E_o$$

The largest MPSS for $DMU_o(x_{io}, y_{ro})$ are $\hat{x}_{io} = \frac{x_{io}}{\phi^* \mathcal{G}^*}$ and $\hat{y}_{ro} = \frac{y_{ro}}{\mathcal{G}^*}$, and

the smallest MPSS for DMU_o are $\check{x}_{io} = \frac{x_{io}}{\phi^* \mathcal{V}^*}$ and $\check{y}_{ro} = \frac{y_{ro}}{\mathcal{V}^*}$. Seiford and

Thrall in [23] demonstrated that $MPSS_{\max}$ and $MPSS_{\min}$ remains the same under both orientations.

3 Results and Discussion

In this study we observed the sample of 27 DMUs. The observed DMUs are public postal operators (PPOs) in the countries of European Union (Austria, Bulgaria, Cyprus, Czech Republic, Denmark, Estonia, Finland, France, Germany, Great Britain, Greece, Hungary, Ireland, Italy, Latvia, Lithuania, Luxembourg, Malta, Netherlands, Poland, Portugal, Romania, Slovakia, Slovenia, Spain, Sweden) and the PPO in Serbia. We employed 3 inputs (the number of full-time staff (x_1), the number of part-time staff (x_2) and total number of permanent post offices (x_3)) and one output (the number of letter-post items, domestic services (y_1)) for evaluating the stability of the RTS classifications and scale efficient targets of PPOs. There are two types of reasons for selecting these particular input and output. The first and essential reason is that chosen input parameters (human capital and infrastructure) imply the largest part of the total costs for public postal operator functioning. On the other hand, the output that refers to the letter post produces the largest part of revenue. The second reason lies in the fact that we had an intention to use available data from the same database which was a constraint in the selection of input and output. Input and output data are listed in Table 1.

Table 1
Data of 27 public postal operators¹

PPO No.	PPO Name	x_1	x_2	x_3	y_1
PPO ₁	Austria	17233	3882	1880	621500000
PPO ₂	Bulgaria	8689	3796	2981	19159655
PPO ₃	Cyprus	714	1034	1082	58787116
PPO ₄	Czech Republic	28232	8020	3408	2574778260
PPO ₅	Denmark	12800	6200	795	800000000

¹ source: Universal Postal Union (2013),
http://pls.upu.int/pls/ap/spp_report.main?p_language=AN&p_choice=BROWSE

PPO ₆	Estonia	2290	502	343	25837400
PPO ₇	Finland	20077	7508	978	837000000
PPO ₈	France	204387	25900	17054	14900000000
PPO ₉	Germany	512147	0	13000	19784000000
PPO ₁₀	Great Britain	117206	38558	11818	18074291171
PPO ₁₁	Greece	9060	28	1546	446505500
PPO ₁₂	Hungary	28592	5368	2746	857056665
PPO ₁₃	Ireland	7825	1584	1156	614320000
PPO ₁₄	Italy	133426	11025	13923	4934317901
PPO ₁₅	Latvia	2438	2055	571	28886614
PPO ₁₆	Lithuania	2336	4226	715	36599075
PPO ₁₇	Luxembourg	950	547	116	110800000
PPO ₁₈	Malta	490	123	63	35123154
PPO ₁₉	Netherlands	13141	46590	2600	3777000000
PPO ₂₀	Poland	77548	16534	8207	822176000
PPO ₂₁	Portugal	11608	315	2556	868548000
PPO ₂₂	Romania	32630	1319	5827	292635204
PPO ₂₃	Slovakia	9650	5081	1589	425743495
PPO ₂₄	Slovenia	6344	161	556	1013027273
PPO ₂₅	Spain	65924	0	3183	5123200000
PPO ₂₆	Sweden	19222	2918	1924	2231000000
PPO ₂₇	Serbia	14659	280	1507	243130583

Given data were obtained from Universal Postal Union for the year 2011. Considering the 27 European Union member states, there is only one PPO that was not included in the research. It is PPO in Belgium for which there were no official data on the website of Universal Postal Union in the moment of this research. Beside that PPO in Serbia as a candidate country was included in observed production possibility set consisting of PPOs in European Union member states.

By reviewing the literature on Thomson Reuters Web of Science², considering years from 1996 to 2014, we have not found the examples of using a RTS in DEA in postal sector. This was an inspiration for the authors to demonstrate the applicability of this analytical process in this field.

All calculations in the study are performed by using the software DEA Excel Solver developed by Zhu [24]. It is a Microsoft Excel Add-In for solving data envelopment analysis (DEA) models.

² <http://apps.webofknowledge.com/>

By using the M1 and the Theorem 1 we derived RTS classification of observed PPOs. The M1 model evolved according to the selected input and output and applied to the sample from Table 1, e.g. the PPO in Czech Republic is:

$$\theta^* = \min \theta$$

Subject to:

$$\begin{aligned} &17233 \lambda_1 + 8689 \lambda_2 + 714 \lambda_3 + 28232 \lambda_4 + 12800 \lambda_5 + 2290 \lambda_6 + 20077 \lambda_7 \\ &+ 204387 \lambda_8 + 512147 \lambda_9 + 117206 \lambda_{10} + 9060 \lambda_{11} + 28592 \lambda_{12} + 7825 \lambda_{13} \\ &+ 133426 \lambda_{14} + 2438 \lambda_{15} + 2336 \lambda_{16} + 950 \lambda_{17} + 490 \lambda_{18} + 13141 \lambda_{19} + 77548 \lambda_{20} \\ &+ 11608 \lambda_{21} + 32630 \lambda_{22} + 9650 \lambda_{23} + 6344 \lambda_{24} + 65924 \lambda_{25} + 19222 \lambda_{26} \\ &+ 14659 \lambda_{27} \leq 28232 \theta \end{aligned}$$

$$\begin{aligned} &3882 \lambda_1 + 3796 \lambda_2 + 1034 \lambda_3 + 8020 \lambda_4 + 6200 \lambda_5 + 502 \lambda_6 + 7508 \lambda_7 \\ &+ 25900 \lambda_8 + 0 \lambda_9 + 38558 \lambda_{10} + 28 \lambda_{11} + 5368 \lambda_{12} + 1584 \lambda_{13} + 11025 \lambda_{14} \\ &+ 2055 \lambda_{15} + 4226 \lambda_{16} + 547 \lambda_{17} + 123 \lambda_{18} + 46590 \lambda_{19} + 16534 \lambda_{20} + 315 \lambda_{21} \\ &+ 1319 \lambda_{22} + 5081 \lambda_{23} + 161 \lambda_{24} + 0 \lambda_{25} + 2918 \lambda_{26} + 280 \lambda_{27} \leq 8020 \theta \end{aligned}$$

$$\begin{aligned} &1880 \lambda_1 + 2981 \lambda_2 + 1082 \lambda_3 + 3408 \lambda_4 + 795 \lambda_5 + 343 \lambda_6 + 978 \lambda_7 + 17054 \lambda_8 \\ &+ 13000 \lambda_9 + 11818 \lambda_{10} + 1546 \lambda_{11} + 2746 \lambda_{12} + 1156 \lambda_{13} + 13923 \lambda_{14} + 571 \lambda_{15} \\ &+ 715 \lambda_{16} + 116 \lambda_{17} + 63 \lambda_{18} + 2600 \lambda_{19} + 8207 \lambda_{20} + 2556 \lambda_{21} + 5827 \lambda_{22} \\ &+ 1589 \lambda_{23} + 556 \lambda_{24} + 3183 \lambda_{25} + 1924 \lambda_{26} + 1507 \lambda_{27} \leq 3408 \theta \end{aligned}$$

$$\begin{aligned} &6215000000 \lambda_1 + 19159655 \lambda_2 + 58787116 \lambda_3 + 2574778260 \lambda_4 \\ &+ 800000000 \lambda_5 + 25837400 \lambda_6 + 837000000 \lambda_7 + 14900000000 \lambda_8 \\ &+ 19784000000 \lambda_9 + 18074291171 \lambda_{10} + 446505500 \lambda_{11} + 857056665 \lambda_{12} \\ &+ 614320000 \lambda_{13} + 4934317901 \lambda_{14} + 28886614 \lambda_{15} + 36599075 \lambda_{16} \\ &+ 110800000 \lambda_{17} + 35123154 \lambda_{18} + 3777000000 \lambda_{19} + 822176000 \lambda_{20} \\ &+ 868548000 \lambda_{21} + 292635204 \lambda_{22} + 425743495 \lambda_{23} + 1013027273 \lambda_{24} \\ &+ 5123200000 \lambda_{25} + 2231000000 \lambda_{26} + 243130583 \lambda_{27} \geq 2574778260 \end{aligned}$$

$$\lambda_1, \lambda_2, \lambda_3, \dots, \lambda_{27} \geq 0$$

The optimal solution for this PPO is:

$$\theta^* = \theta_{CCR}^* = 0.25288$$

$$\phi^* = \frac{1}{\theta^*} = \frac{1}{\theta_{CCR}^*} = \frac{1}{0.25288} = 3.95444$$

$\lambda_1^* = 0.41428$, other $\lambda_j^* = 0 \Rightarrow \sum_{j=1}^{27} \lambda_j^* < 1 \Rightarrow$ the PPO in Czech Republic

exhibits IRS. Since $\lambda_1^* > 0$, the reference for this PPO is the PPO in Austria.

The BCC score (θ_{BCC}^*) is obtained by adding the following condition in the M1 model:

$$\lambda_1 + \lambda_2 + \lambda_3 + \dots + \lambda_{27} = 1$$

The BCC score for this PPO is:

$$\theta_{BCC}^* = 0.26107$$

In the same manner, the M1 model should be evolved for all other 26 PPOs. The CCR, BCC and returns to scale characteristics of each PPO are listed in Table 2.

Table 2
Analytical results derived from the M1 model

PPO No.	RTS Region	BCC	CCR				Scale Score (SS) $SS = \frac{\theta_{CCR}^*}{\theta_{BCC}^*}$
		Score (θ_{BCC}^*)	Score (θ_{CCR}^*)	Reference	$\sum_{j \in E_o} \lambda_j^*$	Input-oriented RTS	
PPO ₁	II	1.00000	1.00000		1.00000	Constant	1.00000
PPO ₂	I	0.05639	0.00611	PPO ₁	0.00308	Increasing	0.10842
PPO ₃	I	0.77607	0.22830	PPO ₁	0.00946	Increasing	0.29417
PPO ₄	VI	0.26107	0.25288	PPO ₁	0.41428	Increasing	0.96862
PPO ₅	I	0.36212	0.30440	PPO ₁	0.12872	Increasing	0.84059
PPO ₆	I	0.24353	0.03182	PPO ₁ , PPO ₂₄	0.00445	Increasing	0.13067
PPO ₇	I	0.30549	0.25888	PPO ₁	0.13467	Increasing	0.84744
PPO ₈	III	0.80392	0.30588	PPO ₁ , PPO ₂₄ , PPO ₂₅	2.70674	Decreasing	0.38048
PPO ₉	III	1.00000	0.94551	PPO ₂₅	3.86165	Decreasing	0.94551
PPO ₁₀	III	1.00000	0.46263	PPO ₁	2.90817	Decreasing	0.46263
PPO ₁₁	I	1.00000	0.56198	PPO ₂₄ , PPO ₂₅	0.16556	Increasing	0.56198
PPO ₁₂	VI	0.11309	0.09707	PPO ₁ , PPO ₂₅	0.13869	Increasing	0.85834
PPO ₁₃	I	0.28302	0.23249	PPO ₁ , PPO ₂₄	0.12627	Increasing	0.82146
PPO ₁₄	III	0.20119	0.17023	PPO ₁ , PPO ₂₄	2.93233	Decreasing	0.84611
PPO ₁₅	I	0.20098	0.03285	PPO ₁	0.00465	Increasing	0.16346
PPO ₁₆	I	0.21147	0.04344	PPO ₁	0.00589	Increasing	0.20543
PPO ₁₇	I	0.73492	0.32340	PPO ₁	0.01783	Increasing	0.44005
PPO ₁₈	I	1.00000	0.19875	PPO ₁	0.00565	Increasing	0.19875
PPO ₁₉	I	0.80875	0.79696	PPO ₁	0.60772	Increasing	0.98543

PPO ₂₀	VI	0.03610	0.03069	PPO ₁ , PPO ₂₅	0.13263	Increasing	0.85018
PPO ₂₁	VI	0.48475	0.46344	PPO ₁ , PPO ₂₄	0.84328	Increasing	0.95604
PPO ₂₂	VI	0.08887	0.05130	PPO ₁ , PPO ₂₄	0.25133	Increasing	0.57726
PPO ₂₃	I	0.16045	0.12233	PPO ₁	0.06850	Increasing	0.76245
PPO ₂₄	II	1.00000	1.00000		1.00000	Constant	1.00000
PPO ₂₅	II	1.00000	1.00000		1.00000	Constant	1.00000
PPO ₂₆	VI	0.41553	0.40714	PPO ₁ , PPO ₂₄ , PPO ₂₅	0.70363	Increasing	0.97983
PPO ₂₇	VI	0.34138	0.11897	PPO ₂₄ , PPO ₂₅	0.21345	Increasing	0.34851
Average		0.51441	0.34991				0.64940

Based on the results in Column 2 of Table 2 the PPOs are located in four RTS regions I, II, III and VI as shown in Figure 1. The regions IV and V are empty.

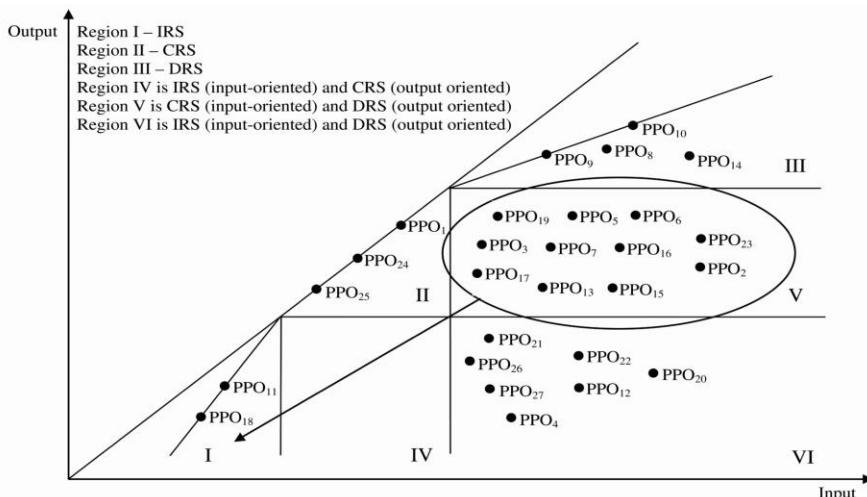


Figure 1
PPOs locating within the RTS regions

The results from Table 2 show that there are three PPOs which have the CCR score equal to 1. This score indicates overall technical efficiency when evaluated on the constant returns to scale assumption. These are PPOs in Austria, Slovenia and Spain. PPO in Austria is one of three best performers, and furthermore it is the PPO most frequently referenced for evaluating inefficient PPOs.

The BCC score provide efficiency evaluations using a local measure of scale, i.e. under variable returns to scale. In this empirical example four PPOs are accorded efficient status in addition to the three CCR efficient PPOs which retain their previous efficient status. These four PPOs are in Germany, Great Britain, Greece and Malta. For example, it can be concluded that PPO in Greece has the efficient operations ($\theta_{BCC}^* = 1$). Additionally, it can be considered that all PPOs having

the BCC score above average (0.51441) have the efficient operations. These are PPOs in Austria, Cyprus, France, Germany, Great Britain, Greece, Luxembourg, Malta, Netherlands, Slovenia and Spain.

Based on the results of scale scores from Table 2 the following PPOs operate in the advantageous conditions: Austria, Czech Republic, Denmark, Finland, Germany, Hungary, Ireland, Italy, Netherlands, Poland, Portugal, Slovakia, Slovenia, Spain and Sweden. Their scale scores are higher than average value (0.64940). Some of them although working in the advantageous conditions have the inefficient operations. We can notice the examples of PPOs in Czech Republic, Poland and Portugal. There are the opposite cases where PPOs work in the disadvantageous conditions but their operations are above average, for example PPOs in Cyprus and Luxembourg. Further there are PPOs operating in the disadvantageous conditions and having the inefficient operations such as PPOs in Bulgaria, Estonia, Latvia, Lithuania, Romania, Slovakia and Serbia.

By using the M2 and M2' models and the Theorem 2, 3 and 4 we derived lower and upper limit of stability intervals of PPOs. For example, the PPO in Czech Republic exhibits IRS, therefore it needs to use the Theorem 4 and the M2' model should be evolved:

$$\mu_o^* = \frac{1}{\max \lambda_1 + \lambda_2 + \lambda_3 + \dots + \lambda_{27}}$$

Subject to:

$$\begin{aligned} &17233 \lambda_1 + 8689 \lambda_2 + 714 \lambda_3 + 28232 \lambda_4 + 12800 \lambda_5 + 2290 \lambda_6 + 20077 \lambda_7 \\ &+ 204387 \lambda_8 + 512147 \lambda_9 + 117206 \lambda_{10} + 9060 \lambda_{11} + 28592 \lambda_{12} + 7825 \lambda_{13} \\ &+ 133426 \lambda_{14} + 2438 \lambda_{15} + 2336 \lambda_{16} + 950 \lambda_{17} + 490 \lambda_{18} + 13141 \lambda_{19} + 77548 \lambda_{20} \\ &+ 11608 \lambda_{21} + 32630 \lambda_{22} + 9650 \lambda_{23} + 6344 \lambda_{24} + 65924 \lambda_{25} + 19222 \lambda_{26} \\ &+ 14659 \lambda_{27} \leq 28232 \end{aligned}$$

$$\begin{aligned} &3882 \lambda_1 + 3796 \lambda_2 + 1034 \lambda_3 + 8020 \lambda_4 + 6200 \lambda_5 + 502 \lambda_6 + 7508 \lambda_7 \\ &+ 25900 \lambda_8 + 0 \lambda_9 + 38558 \lambda_{10} + 28 \lambda_{11} + 5368 \lambda_{12} + 1584 \lambda_{13} + 11025 \lambda_{14} \\ &+ 2055 \lambda_{15} + 4226 \lambda_{16} + 547 \lambda_{17} + 123 \lambda_{18} + 46590 \lambda_{19} + 16534 \lambda_{20} + 315 \lambda_{21} \\ &+ 1319 \lambda_{22} + 5081 \lambda_{23} + 161 \lambda_{24} + 0 \lambda_{25} + 2918 \lambda_{26} + 280 \lambda_{27} \leq 8020 \end{aligned}$$

$$\begin{aligned} &1880 \lambda_1 + 2981 \lambda_2 + 1082 \lambda_3 + 3408 \lambda_4 + 795 \lambda_5 + 343 \lambda_6 + 978 \lambda_7 + 17054 \lambda_8 \\ &+ 13000 \lambda_9 + 11818 \lambda_{10} + 1546 \lambda_{11} + 2746 \lambda_{12} + 1156 \lambda_{13} + 13923 \lambda_{14} + 571 \lambda_{15} \\ &+ 715 \lambda_{16} + 116 \lambda_{17} + 63 \lambda_{18} + 2600 \lambda_{19} + 8207 \lambda_{20} + 2556 \lambda_{21} + 5827 \lambda_{22} \\ &+ 1589 \lambda_{23} + 556 \lambda_{24} + 3183 \lambda_{25} + 1924 \lambda_{26} + 1507 \lambda_{27} \leq 3408 \end{aligned}$$

$$\begin{aligned}
 &6215000000 \lambda_1 + 19159655 \lambda_2 + 58787116 \lambda_3 + 2574778260 \lambda_4 \\
 &+ 800000000 \lambda_5 + 25837400 \lambda_6 + 837000000 \lambda_7 + 14900000000 \lambda_8 \\
 &+ 19784000000 \lambda_9 + 18074291171 \lambda_{10} + 446505500 \lambda_{11} \\
 &+ 857056665 \lambda_{12} + 614320000 \lambda_{13} + 4934317901 \lambda_{14} + 28886614 \lambda_{15} \\
 &+ 36599075 \lambda_{16} + 110800000 \lambda_{17} + 35123154 \lambda_{18} + 3777000000 \lambda_{19} \\
 &+ 822176000 \lambda_{20} + 868548000 \lambda_{21} + 292635204 \lambda_{22} + 425743495 \lambda_{23} \\
 &+ 1013027273 \lambda_{24} + 5123200000 \lambda_{25} + 2231000000 \lambda_{26} \\
 &+ 243130583 \lambda_{27} \geq 2574778260 * 3.95444
 \end{aligned}$$

$$\lambda_1, \lambda_2, \lambda_3, \dots, \lambda_{27} \geq 0$$

Inputs lower limit of stability interval of this PPO is $\mu_o^* = 0.6104066$. According to Theorem 4, inputs upper limit of stability interval of this PPO is equal to 1. Analogously, we can define stability region for inputs of all other 26 PPOs. The analytical results are shown in Table 3.

Table 3
Stability region for inputs of PPOs

PPO No.	Stability interval	PPO No.	Stability interval
PPO ₁	(1.0000000, 1.0000000)	PPO ₁₅	(1.0000000, 7.0684988)
PPO ₂	(1.0000000, 1.9833122)	PPO ₁₆	(1.0000000, 7.3771404)
PPO ₃	(1.0000000, 24.1358543)	PPO ₁₇	(1.0000000, 18.1400000)
PPO ₄	(0.6104066, 1.0000000)	PPO ₁₈	(1.0000000, 35.1693878)
PPO ₅	(1.0000000, 2.3647799)	PPO ₁₉	(1.0000000, 1.3113918)
PPO ₆	(1.0000000, 7.1535973)	PPO ₂₀	(0.2313787, 1.0000000)
PPO ₇	(1.0000000, 1.9222904)	PPO ₂₁	(0.5495740, 1.0000000)
PPO ₈	(0.1130049, 1.0000000)	PPO ₂₂	(0.2041303, 1.0000000)
PPO ₉	(0.2448462, 1.0000000)	PPO ₂₃	(1.0000000, 1.7858031)
PPO ₁₀	(0.1590794, 1.0000000)	PPO ₂₄	(1.0000000, 1.0000000)
PPO ₁₁	(1.0000000, 3.3943407)	PPO ₂₅	(1.0000000, 1.0000000)
PPO ₁₂	(0.6999022, 1.0000000)	PPO ₂₆	(0.5786327, 1.0000000)
PPO ₁₃	(1.0000000, 1.8412285)	PPO ₂₇	(0.5573724, 1.0000000)
PPO ₁₄	(0.0580535, 1.0000000)		

The results from Table 3 indicate that PPOs in Austria, Slovenia and Spain do not need input perturbations. PPOs in Czech Republic, France, Germany, Great Britain, Hungary, Italy, Poland, Portugal, Romania, Sweden and Serbia should consider decreasing inputs. PPOs in Bulgaria, Cyprus, Denmark, Estonia, Finland, Greece, Ireland, Latvia, Lithuania, Luxembourg, Malta, Netherlands and Slovakia should consider increasing inputs.

By using the M3 and M3' models we derived scale efficient inputs and output targets for each CCR inefficient PPOs. Thus, the M3 and M3' models for PPO in Czech Republic are:

M3 model

M3' model

$$\mathcal{G}^* = \min \lambda_1 + \lambda_2 + \lambda_3 + \dots + \lambda_{27} \quad \nu^* = \max \lambda_1 + \lambda_2 + \lambda_3 + \dots + \lambda_{27}$$

Subject to:

$$\begin{aligned} &17233 \lambda_1 + 8689 \lambda_2 + 714 \lambda_3 + 28232 \lambda_4 + 12800 \lambda_5 + 2290 \lambda_6 + 20077 \lambda_7 \\ &+ 204387 \lambda_8 + 512147 \lambda_9 + 117206 \lambda_{10} + 9060 \lambda_{11} + 28592 \lambda_{12} + 7825 \lambda_{13} \\ &+ 133426 \lambda_{14} + 2438 \lambda_{15} + 2336 \lambda_{16} + 950 \lambda_{17} + 490 \lambda_{18} + 13141 \lambda_{19} + 77548 \lambda_{20} \\ &+ 11608 \lambda_{21} + 32630 \lambda_{22} + 9650 \lambda_{23} + 6344 \lambda_{24} + 65924 \lambda_{25} + 19222 \lambda_{26} \\ &+ 14659 \lambda_{27} \leq 28232 \end{aligned}$$

$$\begin{aligned} &3882 \lambda_1 + 3796 \lambda_2 + 1034 \lambda_3 + 8020 \lambda_4 + 6200 \lambda_5 + 502 \lambda_6 + 7508 \lambda_7 \\ &+ 25900 \lambda_8 + 0 \lambda_9 + 38558 \lambda_{10} + 28 \lambda_{11} + 5368 \lambda_{12} + 1584 \lambda_{13} + 11025 \lambda_{14} \\ &+ 2055 \lambda_{15} + 4226 \lambda_{16} + 547 \lambda_{17} + 123 \lambda_{18} + 46590 \lambda_{19} + 16534 \lambda_{20} + 315 \lambda_{21} \\ &+ 1319 \lambda_{22} + 5081 \lambda_{23} + 161 \lambda_{24} + 0 \lambda_{25} + 2918 \lambda_{26} + 280 \lambda_{27} \leq 8020 \end{aligned}$$

$$\begin{aligned} &1880 \lambda_1 + 2981 \lambda_2 + 1082 \lambda_3 + 3408 \lambda_4 + 795 \lambda_5 + 343 \lambda_6 + 978 \lambda_7 + 17054 \lambda_8 \\ &+ 13000 \lambda_9 + 11818 \lambda_{10} + 1546 \lambda_{11} + 2746 \lambda_{12} + 1156 \lambda_{13} + 13923 \lambda_{14} + 571 \lambda_{15} \\ &+ 715 \lambda_{16} + 116 \lambda_{17} + 63 \lambda_{18} + 2600 \lambda_{19} + 8207 \lambda_{20} + 2556 \lambda_{21} + 5827 \lambda_{22} \\ &+ 1589 \lambda_{23} + 556 \lambda_{24} + 3183 \lambda_{25} + 1924 \lambda_{26} + 1507 \lambda_{27} \leq 3408 \end{aligned}$$

$$\begin{aligned} &6215000000 \lambda_1 + 19159655 \lambda_2 + 58787116 \lambda_3 + 2574778260 \lambda_4 \\ &+ 800000000 \lambda_5 + 25837400 \lambda_6 + 837000000 \lambda_7 + 14900000000 \lambda_8 \\ &+ 19784000000 \lambda_9 + 18074291171 \lambda_{10} + 446505500 \lambda_{11} \\ &+ 857056665 \lambda_{12} + 614320000 \lambda_{13} + 4934317901 \lambda_{14} + 28886614 \lambda_{15} \\ &+ 36599075 \lambda_{16} + 110800000 \lambda_{17} + 35123154 \lambda_{18} + 3777000000 \lambda_{19} \\ &+ 822176000 \lambda_{20} + 868548000 \lambda_{21} + 292635204 \lambda_{22} + 425743495 \lambda_{23} \\ &+ 1013027273 \lambda_{24} + 5123200000 \lambda_{25} + 2231000000 \lambda_{26} \\ &+ 243130583 \lambda_{27} \geq 2574778260 * 3.95444 \end{aligned}$$

$$\lambda_1, \lambda_2, \lambda_3, \dots, \lambda_{27} \geq 0$$

The optimal solution for this PPO is:

$$\mathcal{G}^* = \nu^* = 0.41428$$

The smallest inputs for the PPO are:

$$\tilde{x}_1 = \frac{x_{1o}}{\phi^* v^*} = \frac{28232}{3.95444 * 0.41428} = 17233$$

$$\tilde{x}_2 = \frac{x_{2o}}{\phi^* v^*} = \frac{8020}{3.95444 * 0.41428} = 4895$$

$$\tilde{x}_3 = \frac{x_{3o}}{\phi^* v^*} = \frac{3408}{3.95444 * 0.41428} = 2080$$

The largest output for the PPO is:

$$\hat{y}_{1o} = \frac{y_{1o}}{g^*} = \frac{2574778260}{0.41428} = 6215000000$$

Analogously, the M3 and M3' models should be evolved for all other 26 PPOs. The analytical results are shown in Table 4.

Table 4
Analytical results derived from M3 and M3' models

PPO No.	PPO Name	\tilde{x}_1	\hat{x}_1	\tilde{x}_2	\hat{x}_2	\tilde{x}_3	\hat{x}_3	\tilde{y}_1	\hat{y}_1
PPO ₂	Bulgaria	8689	17233	3796	7529	2981	5912	19159655	6215000000
PPO ₃	Cyprus	714	17233	1034	24956	1082	26115	58787116	6215000000
PPO ₄	Czech R.	17233	28232	4895	8020	2080	3408	2574778260	6215000000
PPO ₅	Denmark	12800	30269	6200	14662	795	1880	800000000	6215000000
PPO ₆	Estonia	2290	16382	502	3591	343	2454	25837400	5808328848
PPO ₇	Finland	20077	38594	7508	14433	978	1880	837000000	6215000000
PPO ₈	France	23097	204387	2927	25900	1927	17054	5504774313	14900000000
PPO ₉	Germany	125397	512147	0	0	3183	13000	5123200000	19784000000
PPO ₁₀	GB	18645	117206	6134	38558	1880	11818	6215000000	18074291171
PPO ₁₁	Greece	9060	30753	28	95	1546	5248	446505500	2696882321
PPO ₁₂	Hungary	20012	28592	3757	5368	1922	2746	857056665	6179865198
PPO ₁₃	Ireland	7825	14408	1584	2917	1156	2128	614320000	4865235527
PPO ₁₄	Italy	7746	133426	640	11025	808	13923	1682726646	4934317901
PPO ₁₅	Latvia	2438	17233	2055	14526	571	4036	28886614	6215000000
PPO ₁₆	Lithuania	2336	17233	4226	31176	715	5275	36599075	6215000000
PPO ₁₇	Luxem.	950	17233	547	9923	116	2104	110800000	6215000000
PPO ₁₈	Malta	490	17233	123	4326	63	2216	35123154	6215000000
PPO ₁₉	Nether.	13141	17233	46590	61098	2600	3410	3777000000	6215000000
PPO ₂₀	Poland	17943	77548	3826	16534	1899	8207	822176000	6199142219

PPO ₂₁	Portugal	6379	11608	173	315	1405	2556	868548000	1029965235
PPO ₂₂	Romania	6661	32630	269	1319	1189	5827	292635204	1164358279
PPO ₂₃	Slovakia	9650	17233	5081	9074	1589	2838	425743495	6215000000
PPO ₂₆	Sweden	11122	19222	1688	2918	1113	1924	2231000000	3170687665
PPO ₂₇	Serbia	8171	14659	156	280	840	1507	243130583	1139031351

Considering the results from Table 4, PPOs that need to perform input perturbations can be divided in three groups. The first group contains of PPOs with the input excess and the output deficit. Based on the results from Table 4 these PPOs are in Czech Republic, Hungary, Poland, Portugal, Romania, Sweden and Serbia. For example, PPO in Serbia has the input excess of the number of full-time staff, the number of part-time staff and total number of permanent post offices, $\hat{x}_1 - \check{x}_1 = 6488$, $\hat{x}_2 - \check{x}_2 = 124$, $\hat{x}_3 - \check{x}_3 = 667$, respectively. Additionally, this PPO has the output deficit of the number of letter-post items, domestic services, $\hat{y}_3 - \check{y}_3 = 895900768$. In the second group there are PPOs having the input excess. This means they could achieve the current output level with less inputs. The examples of this kind of PPOs are in France, Germany, Great Britain and Italy. The rest of PPOs are in the third group. The main characteristic of these PPOs is the possibility of increasing output by increased inputs. These PPOs are in Bulgaria, Cyprus, Denmark, Estonia, Finland, Greece, Ireland, Latvia, Lithuania, Luxembourg, Malta, Netherlands and Slovakia.

Obtained values from Table 4 should be considered conditionally having in mind the public expectations about postal systems, first of all the obligation to provide postal services on the whole territory of a state. Thus, in order to implement the proposed model further research should be performed for each specific country considering the legal limitations.

Conclusions

Many DEA researchers have studied the sensitivity analysis of efficient and inefficient decision making unit classifications. This study develops a RTS in DEA and the methods to estimate it in the postal sector. The sensitivity analysis is conducted for the CCR inefficient public postal operators in European Union member states and Serbia as a candidate country. The development of this analytical process is performed based on the public data obtained from the same source from Universal Postal Union.

The focus of this study was on the stability of the RTS classifications and scale efficient inputs and outputs targets of observed PPOs. It has been carried out by using the CCR RTS method and the MPSS. In order to determine lower and upper limit of stability intervals of the CCR inefficient PPOs we used output-oriented RTS classification stability when input perturbations occur in PPOs.

In order to implement the obtained results, PPOs should have in mind their legal obligations specific for the postal sector in their countries. This could be one of the possible guidelines for future research.

In this paper we used cross-section type of data. As a possible direction for the future research panel data could be used involving the efficiency measurement over time. This should be carried out in order to confirm the obtained results.

Acknowledgement

This research was supported by Serbian Ministry of Education, Science and Technological Development with project TR 36022.

References

- [1] Charnes, A., Cooper, W. W., Rhodes, E.: Measuring the Efficiency of Decision Making Units, *European Journal of Operational Research*, Vol. 2, No. 6, pp. 429-444, 1978.
- [2] Banker, R. D., Charnes, A., Cooper, W. W.: Some Models for Estimating Technical and Scale Inefficiencies in Data Envelopment Analysis, *Management Science*, Vol. 30, No. 9, pp. 1078-1092, 1984
- [3] Dalfard, V. M., Sohrabian, A., Najafabadi, A. M., Alvani, J.: Performance Evaluation and Prioritization of Leasing Companies Using the Super Efficiency Data Envelopment Analysis Model, *Acta Polytechnica Hungarica*, Vol. 9, No. 3, pp. 183-194, 2012
- [4] Kabok, J., Kis, T., Csuelloeg, M., Lendak, I.: Data Envelopment Analysis of Higher Education Competitiveness Indices in Europe, *Acta Polytechnica Hungarica*, Vol. 10, No. 3, pp. 185-201, 2013
- [5] Ertay, T., Ruan, D.: Data Envelopment Analysis-based Decision Model for Optimal Operator Allocation in CMS, *European Journal of Operational Research*, Vol. 164, No. 3, pp. 800-810, 2005
- [6] Gattoufi, S., Oral, M., Reisman, A.: A Taxonomy for Data Envelopment Analysis, *Socio-Economic Planning Sciences*, Vol. 38, No. 2-3, pp. 141-158, 2004
- [7] Kleine, A.: A General Model Framework for DEA, *Omega: International Journal of Management Science*, Vol. 32, No. 1, pp. 17-23, 2004
- [8] Seiford, L. M., Zhu, J.: Sensitivity and Stability of the Classification of Returns to Scale in Data Envelopment Analysis, *Journal of Productivity Analysis*, Vol. 12, No. 1, pp. 55-75, 1999
- [9] Cooper, W., Seiford, L., Tone, K., Thrall, R. M., Zhu, J.: Sensitivity and Stability Analysis in DEA: Some Recent Developments, *Journal of Productivity Analysis*, Vol. 15, No. 3, pp. 217-246, 2001

-
- [10] Jahanshahloo, G. R., Lotfi, F. H., Shoja, N., Tohidi, G., Razavian, S.: A One-model Approach to Classification and Sensitivity Analysis in DEA, *Applied Mathematics and Computation*, Vol. 169, No. 2, pp. 887-896, 2005
- [11] Charnes, A., Rousseau, J., Semple, J.: Sensitivity and Stability of Efficiency Classifications in Data Envelopment Analysis, *Journal of Productivity Analysis*, Vol. 7, No. 1, pp. 5-18, 1996
- [12] Seiford, L. M., Zhu, J.: Sensitivity Analysis of DEA Models for Simultaneous Change in all the Data, *Journal of the Operational Research Society*, Vol. 49, No. 10, pp. 1060-1071, 1998
- [13] Podinovski, V. V.: On the Linearization of Reference Technologies for Testing Returns to Scale in FDH Models, *European Journal of Operational Research*, Vol. 152, No. 3, pp. 800-802, 2004
- [14] Soleimani-damaneh, M., Jahanshahloo, G. R., Reshadi, M.: On the Estimation of Returns to Scale in FDH Models, *European Journal of Operational Research*, Vol. 174, No. 2, pp. 1055-1059, 2006
- [15] Lee, G., Yu, M. M., Wang, L. C.: Dea-based Integrated Relationship of Returns to Scale - An Application to Road Maintenance in Taiwan, *Journal of Civil Engineering And Management*, Vol. 18, No. 5, pp. 709-723, 2012
- [16] Jahanshahloo, G. R., Lotfi, F. H., Shoja, N., Abri, A. G., Jelodar, M. F., Firouzabadi, K. J.: Sensitivity Analysis of Inefficient Units in Data Envelopment Analysis, *Mathematical and Computer Modelling*, Vol. 53, No. 5-6, pp. 587-596, 2011
- [17] Charnes, A., Cooper, W. W., Golany, B., Seiford, L. M., Stutz, J.: Foundation of Data Envelopment Analysis for Pareto-Koopmans Efficient Empirical Production Functions, *Journal of Econometrics*, Vol. 30, No. 1-2, pp. 91-107, 1985
- [18] Abri, A. G.: An Investigation on the Sensitivity and Stability Radius of Returns to Scale and Efficiency in Data Envelopment Analysis, *Applied Mathematical Modelling*, Vol. 37, No. 4, pp. 1872-1883, 2013
- [19] Seiford, L. M., Zhu, J.: An Investigation of Returns to Scale Under Data Envelopment Analysis, *Omega: International Journal of Management Science*, Vol. 27, No. 1, pp. 1-11, 1999
- [20] Banker, R. D.: Estimating Most Productive Scale Size Using Data Envelopment Analysis, *European Journal of Operational Research*, Vol. 17, No. 1, pp. 35-44, 1984
- [21] Fare, R., Grosskopf, S., Lovell, C. A. K.: *Production Frontiers*, Cambridge University Press, Cambridge, 1994
- [22] Banker, R. D., Thrall, R. M.: Estimation of Returns to Scale Using Data Envelopment Analysis, *European Journal of Operational Research*, Vol. 62, No. 1, pp. 74-84, 1992

- [23] Seiford, L. M., Thrall, R. M.: Recent Developments in DEA: The Mathematical Programming Approach to Frontier Analysis, *Journal of Econometrics*, Vol. 46, No. 1-2, pp. 7-38, 1990
- [24] Zhu, J.: *Quantitative Models for Performance Evaluation and Benchmarking: Data Envelopment Analysis with Spreadsheets and DEA Excel Solver*, Kluwer Academic Publishers, Boston, 2003

Impact of the Glazing System on the U -Factor and Inside Surface Temperature of Windows

László Elek, Zsolt Kovács

University of West Hungary, Simonyi Károly Faculty of Engineering, Wood Sciences and Applied Art, Institute of Wood-base Products and Technologies, Bajcsy Zs u. 4, H-9400 Sopron, Hungary
laszlo.elek@skk.nyme.hu; zsolt.kovacs@skk.nyme.hu

Abstract: As a consequence of an increasing need for energy-efficiency, there is a growing interest on buildings with reduced energy consumption all over the world. Windows generally account for much higher proportion of the transmission losses through the building envelope, than their area fraction. Therefore, more attention is to be paid to the enhancement of the thermal insulation of fenestration products. In this article, the authors investigate the effect of the thermal performance of the glazing on the frame and edge-of glazing behaviour in a wooden-frame window commonly used in Central Europe. Windows' inside surface temperature with respect to condensation risk, as well as components of the total product U -factor according to both the European standard (ISO EN 10077-1 and -2) and the National Fenestration Rating Council (NFRC) were assessed by using THERM and WINDOW software packages to simulate respective U -factor and temperature distribution throughout the structure.

Keywords: U -factor; heat mirror; modelling; finite element model

Nomenclature

- b Dimension of the glass perpendicular to the direction of heat flow (mm),
 C_1 Coefficient (according to EN ISO 10077-2, 0.025 [W/(m·K)]),
 C_3 Coefficient (according to EN ISO 10077-2, 1.57 [W/(m²·K)]),
 C_4 Coefficient (according to EN ISO 10077-2, 2.11 [W/(m²·K)]),
 d Cavity length in the direction of heat flow [m],
 $emis_1$ Infrared (long-wave) emissivity of the shade material, exterior-facing side,
 $emis_2$ Infrared (long-wave) emissivity of the shade material, interior-facing side,
 h_a Convective heat transfer coefficient [W/(m²·K)],

h_r	Radiative heat transfer coefficient [$W/(m^2 \cdot K)$],
K_{eff}	Effective conductivity [$W/(m \cdot K)$],
R_S	Equivalent thermal resistance of the cavity [$m^2 \cdot K/W$],
SC	Shading coefficient,
$SHGC$	Solar heat gain coefficient,
T_{sol}	Solar transmittance of the shade material,
T_{vis}	Visible transmittance of the shade material,
U_c	Centre-of-glass U -factor [$W/(m^2 \cdot K)$], (NFRC),
U_e	Edge-of-glass U -factor [$W/(m^2 \cdot K)$], (NFRC),
U_f	Thermal transmittance of the frame [$W/(m^2 \cdot K)$], (ISO EN),
U_{fEN}	Frame U -factor determined according to EN ISO 10077-2 [$W/(m^2 \cdot K)$],
U_t	Total product U -factor [$W/(m^2 \cdot K)$], (NFRC),
U_w	Thermal transmittance of the window [$W/(m^2 \cdot K)$], (ISO EN),
λ_{eq}	Equivalent thermal conductivity of the cavity [$W/(m \cdot K)$],
Ψ	Linear thermal transmittance [$W/(m \cdot K)$].

1 Introduction

From the point of view of energy efficiency, windows are perhaps the most critical parts of a building, since the thermal performance of even a well-insulated window is inferior to the rest of the façade. Moreover, as a consequence of their structural complexity, and the environmental impacts they are exposed to, windows may be easily damaged over their service life resulting in significant degradation of their thermal performance.

One of the urgent tasks in our days is to find new possibilities for more efficient and rational energy consumption. The energy-efficiency of the existing stock of buildings in Hungary is rather low; the consumption index is twice as high as the average of the EU-15 countries [1]. The continuous decline of supplies of energy and the increase of their price justify the progression towards better thermal insulation of buildings. The European Union regulates the energy consumption of buildings through directives. From this follows the decree of 7/2006 that contains the requirements on the heat transfer coefficient (referred to as thermal transmittance in the standard EN ISO 10077-1) of fenestration products [1, 2]. Currently the allowable upper limit of the overall heat transfer coefficient (U -factor) for a wood-frame or PVC-frame window is $U_w=1.60$ [$W/(m^2 \cdot K)$]. Apart

from the ever more severe stipulations, the users of a building are interested in consuming the least possible energy, while sustaining the occupants' comfort. As shown in Figure 1, roughly 80 % of the energy consumption is due to heating; windows are responsible for a significant part of this, even if heat not only escapes, but a significant gain through the windows is generally realised.

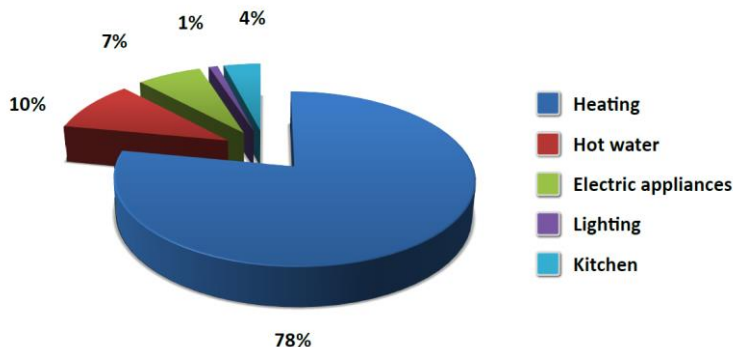


Figure 1

Energy consumption of households, according to use [3]

The primary objective of our investigation was to clarify the effect that modernisation of glazing may have on the components of the overall product *U*-factor and glazing indoor surface temperature in the case of a custom European wooden-frame windows of 68 mm profile depth.

Plenty of studies relating to the effect of glazing properties (gas type, gap thickness, coatings and films) on thermal performance were published during the last two decades. Apart from enhancing the performance of glazing, window design improvements over that period focused on spacer bar technology and frame details, including edge sealants. However, relatively little information can be found in the literature about the interaction of frame details and glazing properties and their contribution to thermal bridging and other additional effects; likewise, their consequences with regard to condensation are not fully explored.

2 Theoretical Background, Review of Literature

The resultant heat transmittance of a window is influenced by a number of factors: the glazing system, the material and profile of the frame and sashes, the way of fitting the sash to the frame, and by the method of joining the window to the wall. The heat flow directed outwards through a window is composed of the heat transfer by conduction, convection and radiation due to temperature difference (generally termed as transmission), and the convective flow due to air leakage.

A window's operation cannot be conceived without the presence of fitting surfaces with their inherent imperfectness, leading to gaps, through which air filtrates due to the pressure difference between the inside and the outside. This pressure difference results from the difference between the inside and outside air temperature and from the effect of wind; thus it can be purposefully influenced by the orientation of the windows with respect to the prevailing wind directions. Air filtration through a window is increased when due to environmental effects the sealing profiles (weather-strips) used for the frame-sash fitting become aged and get brittle, or wear in some other way, so that they cannot provide their function properly anymore. Further, locks and hinges wear in the course of use and their adjustment may be spoiled, leading to imperfect closing of the sash to the frame, hence increase of filtration heat loss [4].

As far as the thermal transmittance through the cavities of double or triple glazing is concerned, besides heat transfer by convection of the gas fill, which is slightly influenced by the thickness of the gap, an important part may happen due to radiant heat exchange between the warmer glass surface and the cooler one on the two sides of a cavity. Therefore, overall transmittance is largely influenced by the emissivity (ε) of those surfaces. Purposefully designed coatings applied to the glass surfaces reduce their emissivity in the long-wave infrared range, lowering thereby the heat transfer by radiation substantially.

A general method of calculating the net energy flux through the glazed area of a window has been worked out in the 1980s already [5]. Within the model, natural convection of the gas fill and emitted energy fluxes are calculated. The two-dimensional finite-volume analysis of vertical gaps, developed by Wright and Sullivan [6] proved to be capable of realistically modelling fill gas flow and heat transfer. The method of analysis was extended to simulate heat flux patterns and temperature profiles for a number of glazing systems [7]. Simulation results agreed well with guarded heater plate measurements. In a publication by Wright [8] a method has been presented for the extension of the two-dimensional frame and edge-glass numerical analysis to account for fill gas convective motion. The method requires computational fluid dynamics (CFD) calculation. Simulation results indicate the dominance of the influence of edge-seal conductance and gas motion over low-e coating and argon filling with respect to minimum indoor glass surface temperature. Three-dimensional CFD simulations were conducted and validated for window frame cavities by Gustavsen & al. [9]. Wright and McGowan [10] develop modifications to the "conventional" modelling concept used in the USA and Canada to determine the total product U -factors for windows. Modifications include modelling the convective motion of the fill gas and local variation of the indoor heat transfer coefficient at recessed corners. In order to be in line with highly insulating IGUs, Fang & al. [11] experimented with multi-material frame design consisting of skeleton framework and cavities filled with insulating material. Their simulations by two-dimensional finite element models, including evacuated glazing with low-emissivity coatings resulted in about 80% heat loss of that in a window of single material solid frame.

In a research project aimed at the improvement of thermal performance of light-weight construction wooden buildings, a resultant heat flow close to the value calculated in standing air was attained in the air cavity of the wall system. That was achieved by dividing the cavity in a number of parallel layers of small thickness with the use of thin aluminium foil [12]. This was possible because convection was almost non-existent in thin air layers; besides, due to the low emissivity of aluminium in the infrared range, heat transfer by radiation was also minimised.

3 Model Building, Material and Method

Product overall U -factor and the distribution of indoor glazing surface temperature was simulated for a 1230 mm by 1480 mm typical Central-European single casement, tilt-and-turn window with double thermal glazing. The 68 mm deep frame and sash profiles were made of laminated Scots pine wood (*Pinus sylvestris*). Taking the maximum available depth for glazing (24 mm) in the sash profile, a number of different configurations of glazing build-up analysed beforehand were selected for simulation (see Figure 2). The optimal cavity thicknesses in the case of the different gas fills can be identified in these curves. In the case of air and argon fill there was no significant difference between the optimum and the value at 16 mm, used in our model. With krypton as filling gas, a smaller cavity is justified. Xenon was shown the best and most insensitive to cavity thickness in these analyses; however, our study was not extended to that type of cavity fill, because it has an adverse effect on sound insulation.

In order to study the effect of the glazing build-up on the window's overall U -factor and on its components (frame U -factor, glazing edge U -factor), as well as on the inside glass surface temperature, we constructed three pairs of different models with air, argon and krypton fill respectively. In all three cases, in one of the two models the cavity thickness was divided in half by a film (0.08 mm thick heat mirror diaphragm). To allow studying the effect of glazing configuration only, total glazing thickness of 24 mm was used throughout the six resulting models, with a gas cavity thickness of 16 mm, or 7.96 mm + 7.96 mm, depending on the case. The 16 mm gas gap thickness was chosen in order to allow for reasonable cavity size when divided. It should be noted that in practice, 12 mm gap thickness is regarded as ideal in the case of air and argon fill, and 7 mm to 8 mm for krypton fill, as also reflected by the curves in Figure 2. It can be seen, that the change in thermal performance is small in the range of 12 mm to 16 mm gap thickness for all three fill types studied; however, air and argon exhibit more pronounced change when going down to 8 mm gap size. Table 1 summarises the glass and foil properties used in the models.

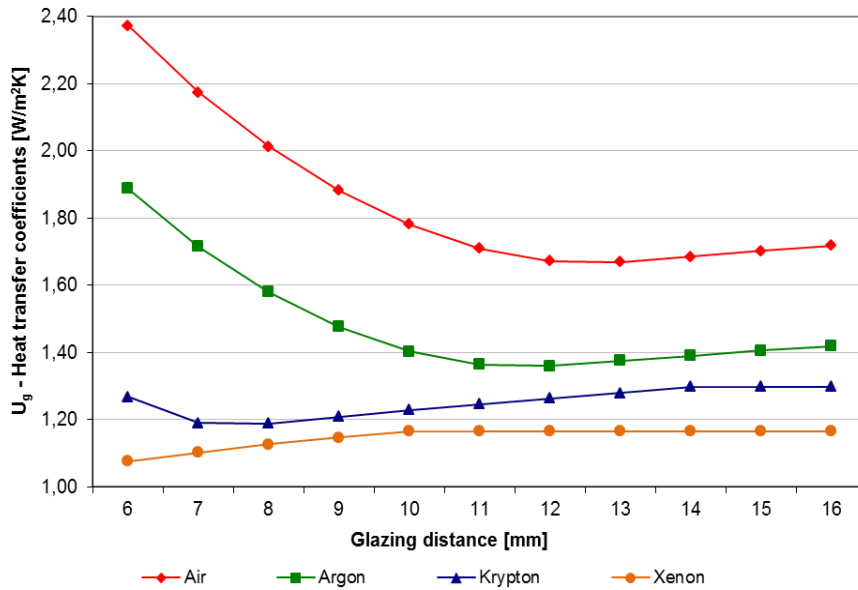


Figure 2

Change of U -factor of double glazing as a function of the gap size and the type of the fill [13]

Table 1

Properties of the components of the glazing with heat mirror

	Thickness [mm]	T_{sol}	T_{vis}	$emis_1$	$emis_2$	Cond
Float glass (7194)	4.00	0.84	0.900	0.837	0.837	1.000
Heat mirror (1518)	0.08	0.38	0.760	0.760	0.045	0.140
Low-E glass (7110)	4.00	0.59	0.890	0.037	0.837	1.000

Analysis of the window sections was performed by using THERM and WINDOW freeware packages developed at Lawrence Berkeley National Laboratories. THERM is based on Finite Element Method; WINDOWS uses Computational Fluid Dynamics (CFD) as a computation tool [14]. THERM was used by Hantos in a study to optimise a lightweight construction building [15]. In his case windows were taken into account with an average heat transfer coefficient, without analysing their effect in detail. In our case the calculation models were graphically defined; an AUTOCAD drawing of the window section was made (Figure 3) and used in THERM as an underlay for reproducing the geometry. Material properties could be assigned either by using library materials or defining custom materials with known thermal conductivity and surface emissivity.

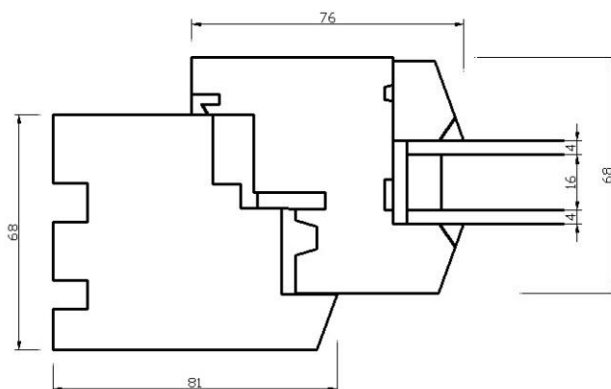


Figure 3

Horizontal section of the window studied (sizes in mm)

Thermal calculations were performed in two ways. First, we followed the procedure specified in the standard EN ISO 10077-2: 2004. Accordingly, we replaced the glazing unit in the model by an insulation panel with the prescribed thermal conductivity of $\lambda = 0.035$ [W/(m·K)], and calculated the thermal transmittance of the frame, U_{fEN} [W/(m²·K)] from the simulation results as stipulated in the above-mentioned standard. Then, after reinserting the glazing unit in its place, the linear thermal transmittance, Ψ [W/(m·K)] due to the combined thermal effects of glazing, spacer and frame, used in EN ISO 10077-1: 2006 was calculated from the simulation results as given in EN ISO 10077-2: 2003 [16, 17]. These two calculation results, along with the known U-value of the central area of glazing, allowed us to compute the window's overall thermal transmittance, U_w [W/(m²·K)]. Thereafter, the same model was also used for determining the values of frame and edge-of-glazing thermal transmittances, U_f [W/(m²·K)] and U_e [W/(m²·K)] respectively, as described in the international standard ISO 15099 [18]. This modelling concept is used by the National Fenestration Rating Council (NFRC) and is described in detail in the THERM6/WINDOW6 NFRC Simulation Manual [18].

For all simulations performed, glazing units were prepared and values of the centre-of-glazing U-factor, U_c [W/(m²·K)] were calculated using the software package WINDOW. In Table 2, properties of the glazing unit with krypton fill and heat mirror diaphragm are shown as calculated by WINDOW.

Table 2
Properties of the glazing unit with krypton fill and heat mirror

	Thickness of glazing [mm]	U-factor [W/(m ² ·K)]	SC	SHGC	Rel. Heat Gain [W/m ²]	T _{vis}	K _{eff} [W/(m·K)]
Glazing	24	0.829	0.4	0.346	258	0.62	0.0157

For a correct modelling of the conductance of frame cavity (formed along the frame and sash joining area), this cavity was divided according to the standard EN ISO 10077-2: 2004, see Figure 4. This division also met the criterion set in the NFRC 100-2001 document for the Nusselt numbers.

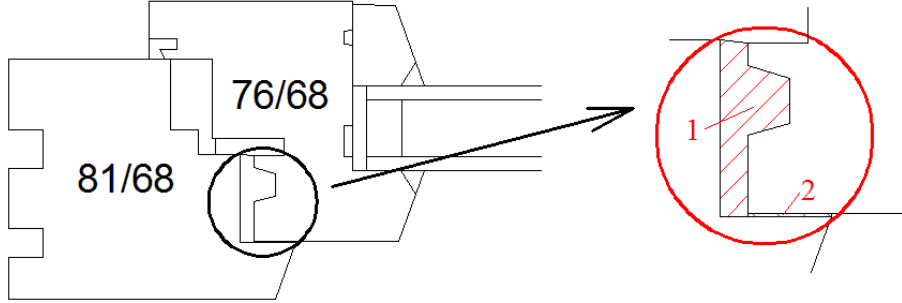


Figure 4

Division of the non-ventilated air cavity formed by the frame and sash profile in the exterior-facing side

Equivalent thermal conductivity values for the divided air gaps were calculated by using the equations below [17]:

$$\lambda_{eq} = \frac{d}{R_s} \quad (1)$$

$$R_s = \frac{1}{h_a + h_r} \quad (2)$$

$$h_a = \max \left\{ \frac{C_1}{d}; C_3 \right\} \quad (3)$$

$$h_r = C_4 \cdot \left(1 + \sqrt{1 + \left(\frac{d}{b} \right)^2} - \frac{d}{b} \right) \quad (4)$$

For cavity 1, see the calculation below:

$$h_a = 1.57 \left[\frac{W}{m^2 \cdot K} \right]$$

$$h_r = 2.11 \cdot \left(1 + \sqrt{1 + \left(\frac{0.025}{0.01} \right)^2} - \frac{0.025}{0.01} \right) = 2.52 \left[\frac{W}{m^2 \cdot K} \right]$$

$$R_s = \frac{1}{h_a + h_r} = \frac{1}{1.57 + 2.52} = 0.244 \left[\frac{m^2 \cdot K}{W} \right]$$

$$\lambda_{eq} = \frac{d}{R_s} = \frac{0.025}{0.244} = 0.102 \left[\frac{W}{m \cdot K} \right]$$

Calculations in the case of cavity 2 are next shown:

$$h_a = \frac{C_1}{d} = \frac{0.025}{0.0005} = 50 \left[\frac{W}{m^2 \cdot K} \right]$$

$$h_r = 2.11 \cdot \left(1 + \sqrt{1 + \left(\frac{0.0005}{0.012} \right)^2} - \frac{0.0005}{0.012} \right) = 4.134 \left[\frac{W}{m^2 \cdot K} \right]$$

$$R_s = \frac{1}{h_a + h_r} = \frac{1}{50 + 4.134} = 0.018 \left[\frac{m^2 \cdot K}{W} \right]$$

$$\lambda_{eq} = \frac{d}{R_s} = \frac{0.0005}{0.01847} = 0.027 \left[\frac{W}{m \cdot K} \right]$$

After specifying the boundary conditions on the inside and outside boundaries in the model as shown in Table 3, the calculations were performed.

Table 3
Boundary conditions according to EN ISO 10077:1 and EN ISO 10077:2

Inside temperature: θ_i	20 °C
Outside temperature: θ_e	0 °C
Inside surface resistance: (R_{si})	0.13 [m ² ·K/W]
Outside surface resistance: (R_{se})	0.04 [m ² ·K/W]

4 Results

The frame U -factor and the linear thermal transmittance, Ψ [W/(m·K)] due to the combined thermal effects of glazing, spacer and frame, defined in EN ISO 10077-1 and 2 are summarised in Table 4 for the individual models. Table 5 shows thermal transmittance values of frame, edge-of-glazing and central

glazing area, as well as total product U -factor calculated according to the NFRC model. The last column in table 5 contains the ratio of NFRC to EN ISO results for the windows in question.

Table 4
Thermal calculation results according to EN ISO 10077-1 and 2

Glazing type	EN ISO 10077		$U_{f(EN)}$ [W/(m ² ·K)]	Ψ [W/(m·K)]	U_w [W/(m ² ·K)]
1	Air	Normal	1.375	0.0862	1.8706
2		HM	1.375	0.0902	1.7508
3	Ar	Normal	1.375	0.0915	1.7253
4		HM	1.375	0.0951	1.5988
5	Kr	Normal	1.375	0.0931	1.6651
6		HM	1.375	0.1003	1.4328

Table 5
Thermal calculation results according to the NFRC model

Glazing type	ISO 15099		U_f [W/(m ² ·K)]	U_g [W/(m ² ·K)]	U_c [W/(m ² ·K)]	U_t [W/(m ² ·K)]	U_t/U_w
1	Air	Normal	1.8160	2.3481	1.792	1.8734	1.0015
2		HM	1.8103	2.1703	1.602	1.7438	0.9960
3	Ar	Normal	1.8074	2.1417	1.559	1.7159	0.9946
4		HM	1.8019	1.9586	1.360	1.5810	0.9889
5	Kr	Normal	1.8040	2.0589	1.465	1.6523	0.9923
6		HM	1.7930	1.7320	1.097	1.4043	0.9801

It should be noted that the simulation model does not contain hardware parts; isotherms obtained in the frame and sash profile would be somewhat different in reality for that reason too. Because of the changing geometry of hardware components along the frame length, their contribution to thermal bridging could only be truly assessed by three-dimensional modelling. Temperature distributions in the modelled section exhibit themselves similar with all three fill gases. Figures 5 to 7 demonstrate the isotherms and colour IR visualisation for air, argon and krypton fill respectively. It should be noted that these isotherms in a window will be different depending on whether the section modelled is a head, sill or jamb part, and will change depending on the cavity height, which is by default 1 m in THERM.

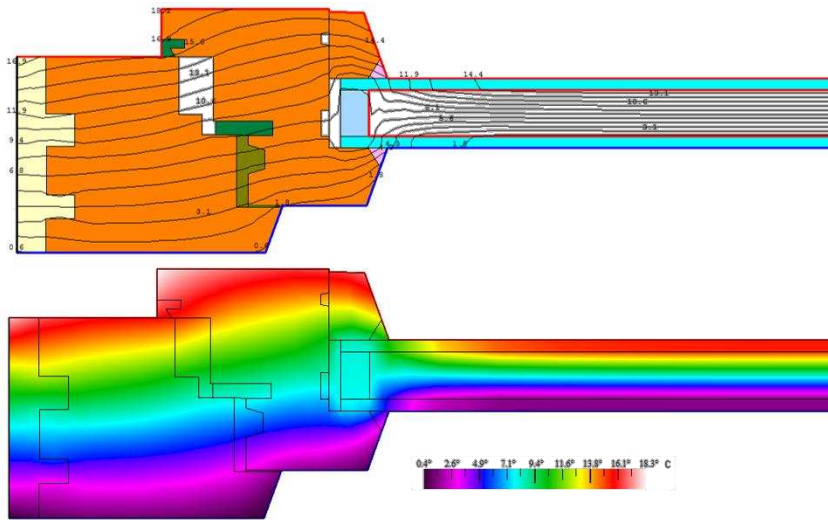


Figure 5

Isotherms and continuous temperature distribution diagram in the window section in the case of air fill.
(Temperature in °C)

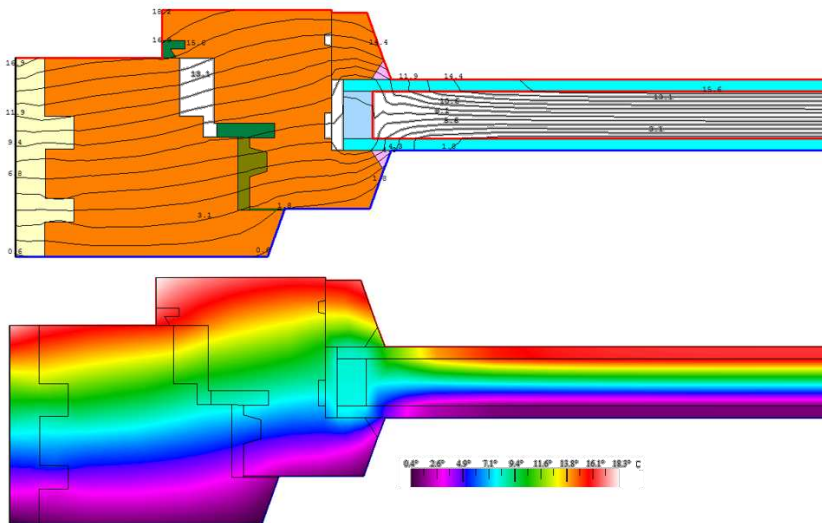


Figure 6

Isotherms and continuous temperature distribution diagram in the window section in the case of argon fill.
(Temperature in °C)

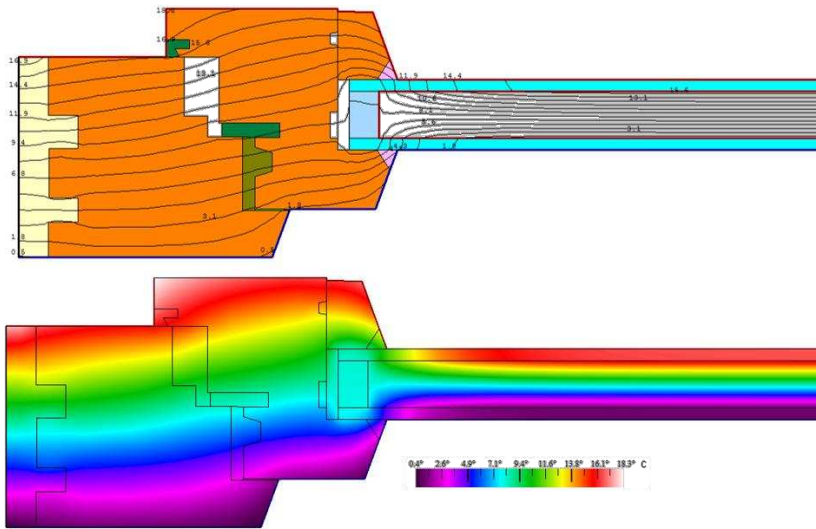


Figure 7

Isotherms and continuous temperature distribution diagram in the window section in the case of krypton fill. (Temperature in °C)

Division of the cavity by heat mirror film resulted more favourable values in all three cases (Figures 8 to 10).

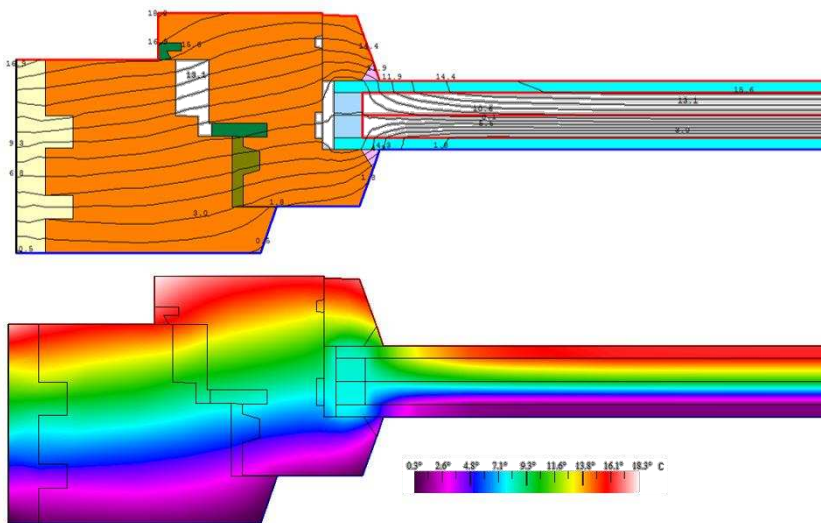


Figure 8

Isotherms and continuous temperature distribution diagram in the window section in the case of air fill and heat mirror. (Temperature in °C)

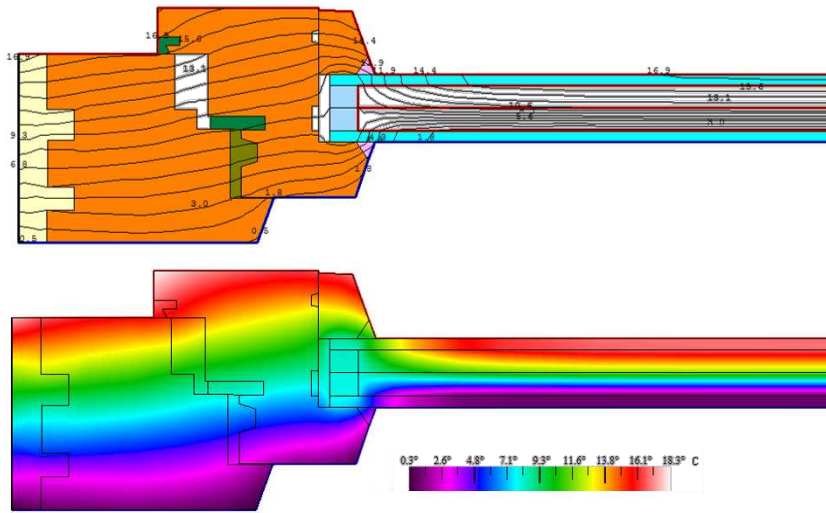


Figure 9

Isotherms and continuous temperature distribution diagram in the window section in the case of argon fill and heat mirror. (Temperature in °C)

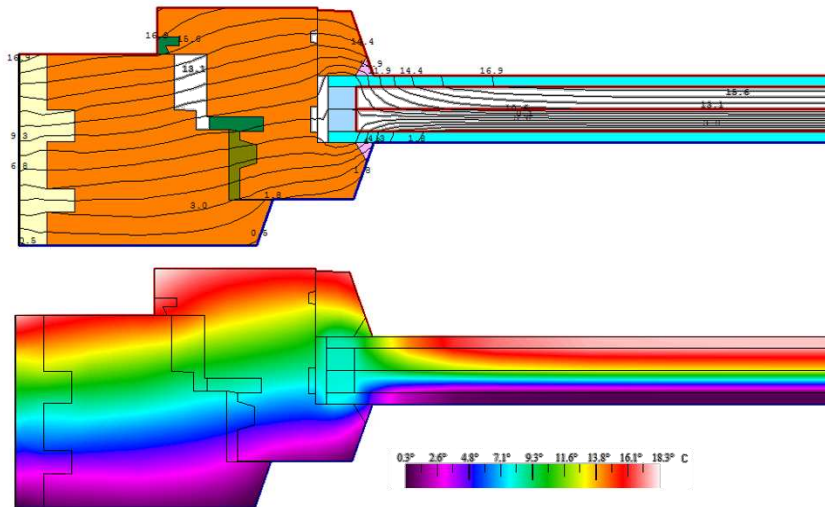


Figure 10

Isotherms and continuous temperature distribution diagram in the window section in the case of krypton fill and heat mirror. (Temperature in °C)

It is apparent in the figures that there are no important differences in the resulting temperature distributions. The point of interest for us was how condensation risk is influenced by improving glazing insulation with unchanged frame. We took the

dew-point temperature corresponding to a room temperature of 20 °C and relative humidity of 65% as a basis for comparison, which turns out to be 13.2 °C. On the basis of the location of the 13.2 °C isotherm on the interior glass surface, it can be established that the extension of the edge effect caused by the steel spacer considerably was reduced by the application of the heat mirror diaphragm. The observed values of the distance of the 13.2 °C isotherm from the inside edge of the sash are summarised in Table 6.

Table 6
Distance of the 13.2 °C isotherm from inside edge on the glass surface

Type of gas fill	Normal double glazing [mm]	Double glazing with heat mirror [mm]	Improvement [%]
Air	30	23	13
Argon	21	18	14
Krypton	20	14	30

As a result, the distance of the 13.2 °C isotherm from the inside edge reduced from 14 mm to 7.2 mm with a resultant thermal transmittance of the window of 1.27 [W/m²·K].

5 Discussion

A summary of the simulation results is given in Tables 4 to 6. Table 7 summarises the ratios of the total product U -factors and glazing U -factors, as well the improvement of U -factors due to heat mirror for the different glazing types investigated. In terms of the thermal transmittance of the window as a whole, it could be expected that values higher than those determined for the central area of glazing (column U_c in table 5) will result. In the case of a normal double glazing window with argon fill the increase is 10% to 16%, while with krypton fill it attains almost 13% to 28% depending on the lack or presence of heat mirror. On the contrary, with air fill, this increase was only 4.5% to 8.9%, due to the comparatively higher thermal transmittance of the glazing unit.

When the cavity is divided by a heat mirror diaphragm, results are more remarkably different with different gas fills. The most pronounced improvement of thermal transmittance was observed in the case of krypton fill; that can be explained by the fact that the optimal thickness of krypton-filled cavity is 6 mm to 8 mm (as our divided cavities) rather than 16 mm, see Figure 2. From this, it follows that the window's resultant U -factor in the case of krypton fill exceeds glazing U -factor more (by 28%), than with other glazing configurations investigated. The effect of heat mirror can also be evaluated through the ratio of U_{iHM} to $U_{inormal}$, see the last column in Table 7, where the subscript _{HM} refers to heat mirror. The values in the table tell us, that the gain attained by the application

of heat mirror is enhanced with the use of thermally superior fill gas. This is the good part of using high-performance glazing with unchanged frame systems; the bad part being the fact, the higher the thermal performance of the glazing, the less remains the rate of its exploitation in the total product U -factor.

As an effect of the application of heat mirror, the distance of the 13.2 °C isotherm from the frame's inner edge (in other words the spread of low surface temperature) was reduced by nearly 14% in the case of argon fill, while with krypton fill an improvement of 30% could be justified, as can be read in table 6. The trend is similar to that of the ratio of U_{tHM} to U_{normal} .

Table 7

Ratios of U -factors for glazing and total product and with and for windows with and without heat mirror

Glazing type	Description		U_c [W/(m ² ·K)]	U_t [W/(m ² ·K)]	U_t/U_c	U_{tHM}/U_{normal}
1	Air	Normal	1.792	1.873	1.045	0.931
2		HM	1.602	1.744	1.089	
3	Ar	Normal	1.559	1.716	1.101	0.921
4		HM	1.360	1.581	1.163	
5	Kr	Normal	1.465	1.652	1.128	0.850
6		HM	1.097	1.404	1.280	

Conclusions

Thermal transmittance of the glazing not only defines thermal transmittance of the window with a given frame system, but influences the spread of the low surface temperature zone along the inside glazing perimeter. Among the available low-e coated glazing types those with krypton fill provide the best results that also depend on gas cavity thickness. Further improvements can be attained by the use of heat mirror diaphragms within the glazing system.

However, higher cost of glazing units of extremely low emissivity and or those equipped with heat mirror, as well as and an important decrease of visible light transmittance with their use obstacle the spread of such glazing units. On the other hand, these low-e glazing systems with gas fills of increased thermal resistance, when used with current framing systems, seem to approach the upper limits of attainable thermal performance. Major improvements in the thermal performance of window framings, and/or new concepts of fitting together movable and fix parts in window systems may become necessary in the future. In other words, the less we can approach the thermal resistance of glazing around the glazed area of a window, the less the enhancement of the glazing's thermal properties can be exploited.

Acknowledgements

This research was supported by the European Union and co-financed by the European Social Fund in the frame of the project „Talentum - Development of the complex condition framework for nursing talented students at the University of West Hungary”, project ID: TAMOP 4.2.2.B-10/1-2010-0018.

Special thanks are due to Dr. Levente Csoka associate professor, UWH, for his valuable contribution to this paper.

References

- [1] Prohaszka, R.: State-of-the-art of Building Energetics in Hungary. In: Hungarian Construction Technology, a periodical of the National Association of Building Entrepreneurs XLV/6 – 2007/6
- [2] Ministerial Decree about Calculation Methods and Energetical Properties of Buildings, Budapest, (TNM rendelet az épületek energetikai jellemzőinek meghatározásáról. in: Magyar Közlöny 2006/62. Magyar Hivatalos Közlönykiadó), 2006
- [3] <http://www.gaz-piezzo.hupont.hu/12/solar-avagy-a-napenergia-felhasznalasa>, 2012
- [4] Bencsik, B., Kovacs, Zs., Denes, L.: Performance Characteristics of Windows in the Course of Their Service Life; 2nd International Joint Conference on Environmental and Light Industry Technologies, 21-22 November 2011, Budapest, Hungary, Óbuda University
- [5] Rubin, M.: Calculating Heat Transfer through Windows Energy Research, Vol. 6, 1982, 341-349
- [6] Wright, J. L., Sullivan, H. F.: A Two-Dimensional Numerical Model for Natural Convection in a Vertical Rectangular Window Cavity Ashrae Transactions, Vol. 100, Pt. 2, 1994, pp. 1193-1206
- [7] Wright, J. L., Sullivan H. F.: A Two-Dimensional Numerical Model for Glazing System Thermal Analysis Ashrae Transactions: Symposia, Vol. 101, Pt. 1, 1995, pp. 819-831
- [8] Wright, J. L.: A Simplified Numerical Method for Assessing the Condensation Resistance of Windows Ashrae Transactions, Vol. 104, Pt. 1, 1998, pp. 1222-1229
- [9] Gustavsen, A., Brent T. Griffith and Dariush: Arasteh Three-Dimensional Conjugate CFD Simulations of Internal Window Frame Cavities Validated Using IR Thermography Reprinted by permission from Ashrae Transactions Vol. 107, Part 2, pp 538-549 ©2001 American Society of Heating, Refrigerating and Air-Conditioning Engineers, Inc.

-
- [10] Wright, J. L., McGowan, A. G.: A Comparison of Calculated and Measured Indoor side Window Temperature Profiles Ashrae Transactions, Vol. 109, Pt. 2, 2003, pp. 857-870
- [11] Fang, Y., Philip C. Eames, Trevor J. Hyde, Norton, B.: Complex Multimaterial Insulating Frames for Windows with Evacuated Glazing Received 5 December 2003; received in revised form 8 October 2004; accepted Solar Energy 79, 2005, 245-261
- [12] Pasztory, Z.: Possibilities of Enhancing Thermal Insulation in Wooden Houses. In Hungarian. NymE, Sopron, 2007
- [13] Elek, L., Kovacs, Zs., Denes, L.: Wood Windows in the 21st Century: End User Requirements, Limits and Opportunities; The Future of Quality Control for Wood & Wood Products, The final conference of COST Action E53: 'Quality control for wood & wood products'; Edinburgh, 2010
- [14] WINDOW 6.3 / THERM 6.3: Research Version User Manual For Analyzing Window Thermal Performance, Windows & Daylighting Group, Building Technologies Program, Environmental Energy Technologies Department Lawrence Berkeley National Laboratory Berkeley, CA 94720 USA, 2009
- [15] Hantos, Z.: Thermal Optimisation of a Wooden Frame Lightweight Construction System; Dissertation in Hungarian, University of West Hungary, Sopron, 2008
- [16] EN ISO 10077-1:2000: Thermal Performance of Windows, Doors and Shutters - Calculation of Thermal Transmittance - Part 1: Simplified Method
- [17] EN ISO 10077-2:2004: Thermal Performance of Windows, Doors and Shutters - Calculation of Thermal Transmittance - Part 2: Numerical Method for Frames
- [18] ISO 15099: Thermal Performance of Windows, Doors and Shading Devices – Detailed Calculations, 2003

Modeling of Stress-Strain State of Road Covering with Cracks

Shahin G. Hasanov, Vagif M. Mirsalimov

Azerbaijan Technical University
Baku, Azerbaijan
E-mail: iske@mail.ru, mir-vagif@mail.ru

Abstract: The stress-strain state of road covering in the course of operation is considered. It is assumed that the cross section of the covering has arbitrary number of rectilinear cracks. Force interaction of the wheel (roller) and road covering with rough upper surface is investigated. Using the perturbation method and the method of singular integral equations the contact problem of the pressing of the wheel (roller) in the road surface was solved. The stress intensity factors for the vicinity of the cracks vertices are found.

Keywords: road covering; elastic base; rectilinear cracks; stress intensity factors; rough surface

1 Introduction

Timely detection of various damages of road covering is of particular importance for providing reliable and safe functioning of road transport. In this connection the defects as cracks are of significant interest. Setting of the norms of admissible presence of defects, choice of the methods and periodicity of defectoscopic control of road is an important problem for increasing durability of road covering. While evaluating durability of road covering of motor roads it is necessary to proceed from possibility of presence of the most dangerous unrevealed defects in coverings. In this connection, the initial defects should be accepted to be equal to sensitivity limit of the used defectoscopic device.

Real surfaces of roads differ by the presence of roughnesses that are the unavoidable consequence of technological process. In spite of smallness of geometric distortions in the form of surface roughness, their role in friction, wear and fracture and etc. is very great [1-3]. Therefore, investigation of the roughness geometry itself for strength and the relation of roughness with the characteristics of physical-technical phenomena (friction, wear, fracture) generated by it are very significant. In this connection development of design models of investigation of parameters of road covering fracture is a very urgent problem [4-12].

2 Formulation of the Problem

Consider the stress-strain state of road covering during operation process. Let the cross section of the road covering have N rectilinear internal cracks of length $2l_k$ ($k=1,2,\dots,N$) (Fig. 1). It is assumed that the cracks are open and not filled.

For calculating the stress-strain state of the road covering near the rolling surface, in this case we arrive at the following contact problem of fracture mechanics.

Let us consider force interaction of the wheel and covering. Taking into account that the sizes of the contact area while contacting with covering are small compared with typical linear size of road covering in the plan, in the statement and solution of the contact problem the covering may be replaced by an elastic strip of thickness h situated on an elastic base in the form of elastic half-plane.

We model the material of the covering by an elastic medium with mechanical characteristics E_1 (elasticity modulus), μ_1 (Poisson ratio). Accordingly, we model the elastic base by elastic medium with mechanical characteristics E_2 , μ_2 . As a rule, the external surface of road covering has roughnesses of rolling surface.

Let us consider the following contact problem for an elastic strip with elastic base in the form of a half-plane. A wheel under the arbitrary system of forces is pressed into an elastic strip with internal cracks and rough upper surface. We can assume that normal force P_k (clip force) and moment M is applied to each unit of the length of the contact area. The base of the hard wheel is characterized by a rather smooth function $f_*(x)$.

It is required to determine the laws of contact stress and stress intensity factors distribution in the vicinity of the cracks tips.

Denote by $q(x)$ and $\tau(x)$ normal and tangential stresses, respectively, applied to the boundary of the half-plane (base of the covering). Denote the wheel's pressure on the covering by $p(x)$, the segment $[a_1, a_2]$ will be the contact area. In addition to normal forces (pressure) $p(x) = -\sigma_y(x, 0)$, the tangential stresses $\tau_{xy}(x, 0)$ connected with contact pressure by the Amonton-Coulomb law

$$\tau_{xy} = f p(x)$$

where f is the friction factor of the pair wheel-road covering, are also act in the contact area $a_1 \leq x \leq a_2$.

Consider some realization of the roughness of the external surface of the road rolling L'_1 . Represent the boundary of the external contour L'_1 , in the form

$$y = \delta(x)$$

We will assume the contour L'_1 close to the rectilinear form assuming only small deviations of the line L_1 from the straight line $y = 0$.

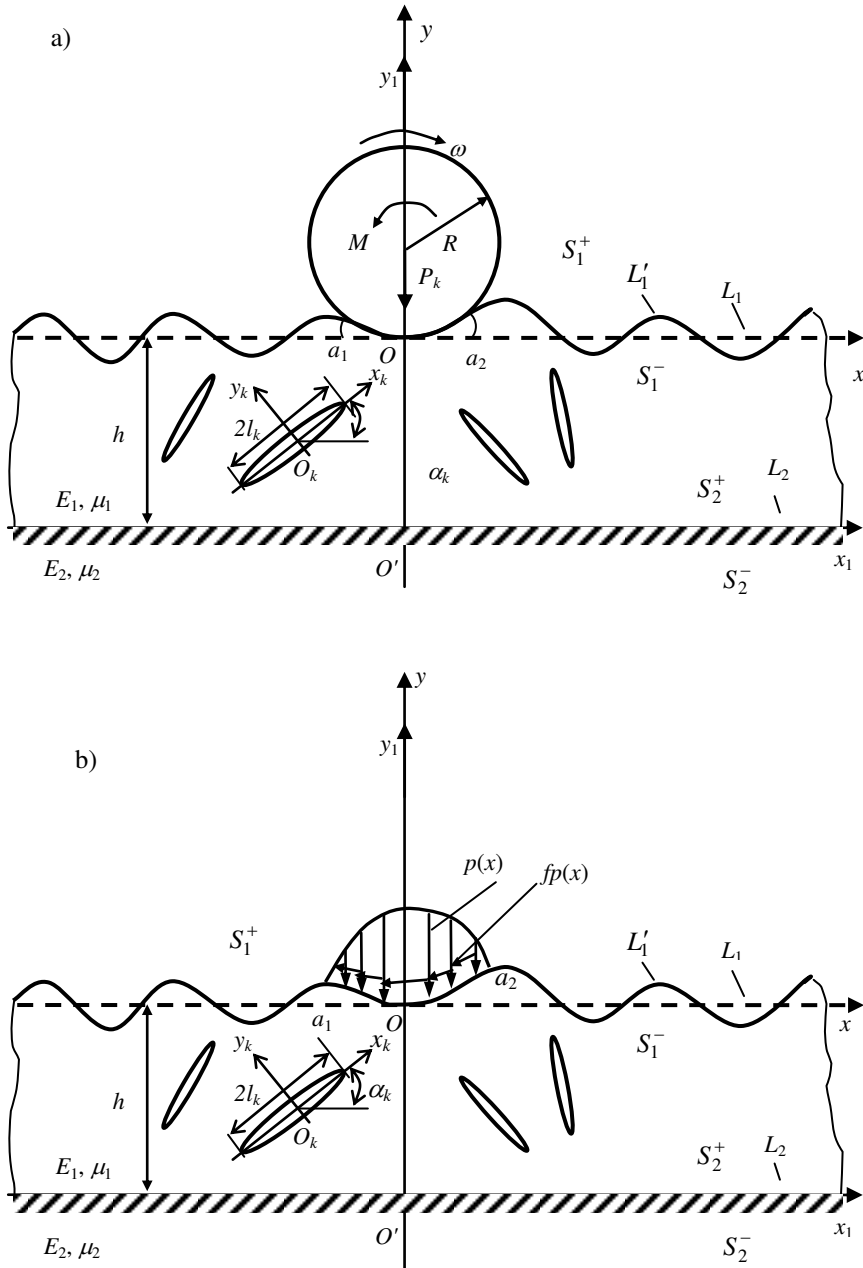


Figure 1
 Calculation scheme of a contact fracture mechanics problem

On the base what has been said above, we write the boundary conditions of the considered contact problem of fracture mechanics in the form

$$\text{for } y = \delta(x) \quad \sigma_n = 0, \quad \tau_{nt} = 0 \quad \text{exterior to the contact area} \quad (1)$$

$$\text{for } y = \delta(x) \quad v_n = f(x) + \alpha x + C, \quad \tau_{nt} = f\sigma_n \quad \text{on the contact area} \quad (2)$$

$$\text{for } y = -h \quad (\sigma_y - i\tau_{xy})_I = (\sigma_y - i\tau_{xy})_{II}, \quad (u + iv)_I = (u + iv)_{II} \quad (3)$$

$$\sigma_n = 0; \quad \tau_{nt} = 0 \quad \text{on the cracks faces}$$

Here it is accepted that in the external surface area of the covering where the wheel is pressed, the dry friction forces occur; exterior to the contact area the surface of covering is free from external forces. The cracks faces are free from external loads. Stresses and displacements (perfect coupling conditions) are equal on the interphase of medium (covering and elastic base); $i = \sqrt{-1}$ is an imaginary unit; C is the translation of penetration (wheel), α is a turning angle of the penetrator; $f(x) = f_*(x) + \delta(x)$. Furthermore, the following additional conditions hold:

$$P_k = \int_{a_1}^{a_2} p(t) dt, \quad M = \int_{a_1}^{a_2} t p(t) dt \quad (4)$$

3 The Case of One Crack

As it was accepted that the functions $\delta(x)$ and $\delta'(x)$ are small quantities, we can write the equation of the upper contour of the covering as follows:

$$y = \delta(x) = \varepsilon H(x) \quad (5)$$

where ε is a small parameter for which we can accept the greatest height of the roughness of the upper surface of the road covering related to the thickness of the covering.

Expand the stress tensor components σ_x , σ_y , τ_{xy} in series in small parameter of ε

$$\sigma_x = \sigma_x^{(0)} + \varepsilon\sigma_x^{(1)} + \dots, \quad \sigma_y = \sigma_y^{(0)} + \varepsilon\sigma_y^{(1)} + \dots, \quad \tau_{xy} = \tau_{xy}^{(0)} + \varepsilon\tau_{xy}^{(1)} + \dots \quad (6)$$

Expanding in series the expressions for the stresses in the vicinity $y = 0$, we find the values of the stress tensor components for $y = \delta(x)$.

Using the perturbations method, allowing what has been said, we get the following conditions: for the covering in a zero approximation

$$\text{for } y = 0 \quad \sigma_y^{(0)} = 0, \quad \tau_{xy}^{(0)} = 0 \quad \text{exterior to the contact area} \quad (7)$$

$$\sigma_y^{(0)} = -p^{(0)}(x), \quad \tau_{xy}^{(0)} = -fp^{(0)}(x) \quad \text{on the contact area}$$

$$\sigma_n^{(0)} = 0, \quad \tau_{nt}^{(0)} = 0 \quad \text{on the cracks faces} \quad (8)$$

$$\text{for } y = -h \quad \sigma_y^{(0)} = q^{(0)}(x), \quad \tau_{xy}^{(0)} = \tau^{(0)}(x) \quad (9)$$

for the covering in a first approximation

$$\text{for } y = 0 \quad \sigma_y^{(1)} = N, \quad \tau_{xy}^{(1)} = T \quad \text{exterior to the contact area} \quad (10)$$

$$\sigma_y^{(1)} = N - p^{(1)}(x), \quad \tau_{xy}^{(1)} = T - fp^{(1)}(x) \quad \text{on the contact area}$$

$$\sigma_n^{(1)} = 0, \quad \tau_{nt}^{(1)} = 0 \quad \text{on the cracks faces} \quad (11)$$

$$\text{for } y = -h \quad \sigma_y^{(1)} = q^{(1)}(x), \quad \tau_{xy}^{(1)} = \tau^{(1)}(x) \quad (12)$$

for elastic base in a zero approximation

$$\text{for } y = -h \quad \sigma_y^{(0)} = q^{(0)}(x), \quad \tau_{xy}^{(0)} = \tau^{(0)}(x) \quad (13)$$

in a first approximation

$$\text{for } y = -h \quad \sigma_y^{(1)} = q^{(1)}(x), \quad \tau_{xy}^{(1)} = \tau^{(1)}(x) \quad (14)$$

$$\text{Here} \quad N = 2\tau_{xy}^{(0)} \frac{d\Delta}{dx} - H \frac{\partial \sigma_y^{(0)}}{\partial y}, \quad T = (\sigma_x^{(0)} - \sigma_y^{(0)}) \frac{dH}{dx} - H \frac{\partial \tau_{xy}^{(0)}}{\partial y}, \quad (15)$$

the quantities N and T are known on the base of zero solution $\sigma_x^{(0)}$, $\sigma_y^{(0)}$, $\tau_{xy}^{(0)}$ and the function $H(x)$ describing the rough contour of the upper surface of road covering.

Because of smallness of the small parameter ε , in what follows we will be restricted in expansions (6) by the terms to the first order of smallness inclusively, with respect to ε .

Knowledge on the stress intensity factor allowing in the considered case to investigate the ultimate state of road covering and their durability on their base is of significant interest for predicting fracture.

According to perturbations method, the stress intensity factors for the vicinity of the cracks tip are found as follows

$$K_I = K_I^{(0)} + \varepsilon K_I^{(1)} + \dots, \quad K_{II} = K_{II}^{(0)} + \varepsilon K_{II}^{(1)} + \dots$$

Here $K_I^{(0)}$, $K_{II}^{(0)}$ are the stress intensity factors for a zero approximation, $K_I^{(1)}$, $K_{II}^{(1)}$ for a first approximation, respectively.

In the center of the rectilinear crack locate the origin of the local system of coordinates $x_1 O_1 y_1$ whose axis x_1 coincides with the linear crack and forms the angle α_1 with the axis x (Fig. 1). The stress-strain state of road covering, at each approximation satisfies the system of differential equations of plane theory of elasticity.

Use the superposition principle. Then we can represent the stress and strain state of a two-layer body with a crack in the form of the sum of two states. The first state will be determined from the solution of contact problem (1)-(3) for a two-layer body in unavailability of a crack. The second state is determined from the solution of a boundary value problem for a cracked covering with forces on the faces determined by the first stress state. The first state for each approximation in unavailability of a crack is known [13].

The boundary conditions of the second problem are of the form:

in a zero approximation

$$\text{for } y_1 = 0 \quad \sigma_{y_1}^{(0)} = -p_*^{(0)}(x_1), \quad \tau_{x_1 y_1}^{(0)} = -p_1^{(0)}(x_1) \quad (|x_1| \leq l_1) \quad (16)$$

$$\text{for } y = 0 \quad \sigma_y^{(0)} = 0, \quad \tau_{xy}^{(0)} = 0$$

$$\text{for } y = -h \quad \sigma_y^{(0)} = 0, \quad \tau_{xy}^{(0)} = 0 \quad (|x| < \infty) \quad (17)$$

in a first approximation

$$\text{for } y_1 = 0 \quad \sigma_{y_1}^{(1)} = -p_*^{(1)}(x_1), \quad \tau_{x_1 y_1}^{(1)} = -p_1^{(1)}(x_1) \quad (|x_1| \leq l_1) \quad (18)$$

$$\text{for } y = 0 \quad \sigma_y^{(1)} = 0, \quad \tau_{xy}^{(1)} = 0$$

$$\text{for } y = -h \quad \sigma_y^{(1)} = 0, \quad \tau_{xy}^{(1)} = 0 \quad (|x| < \infty) \quad (19)$$

Here $p_*^{(0)}(x_1)$, $p_1^{(0)}(x_1)$ and $p_*^{(1)}(x_1)$, $p_1^{(1)}(x_1)$ are normal and tangential stresses arising in continuous covering along the axis x_1 in zero and first approximations, respectively, from the application of the given loads relieving stress on the covering boundary. The quantities $p_*^{(0)}(x_1)$, $p_1^{(0)}(x_1)$ and $p_*^{(1)}(x_1)$, $p_1^{(1)}(x_1)$ are determined from the relations of [13]. The boundary conditions of problem (16)-(17) are written by means of Kolosov-Muskhelesvili formulas [14] in the form of a boundary value problem for finding two analytic functions $\Phi(z)$ and $\Psi(z)$

$$\text{for } y = 0 \quad \Phi_0(z) + \overline{\Phi_0(z)} + z\overline{\Phi_0'(z)} + \overline{\Psi_0(z)} = 0 \quad (20)$$

$$\text{for } y = -h \quad \Phi_0(z) + \overline{\Phi_0(z)} + z\overline{\Phi_0'(z)} + \overline{\Psi_0(z)} = 0$$

$$\text{for } y_1 = 0 \quad \Phi_0(x_1) + \overline{\Phi_0(x_1)} + x_1\overline{\Phi_0'(x_1)} + \overline{\Psi_0(x_1)} = f^{(0)}(x_1),$$

$$\text{where } f^{(0)}(x_1) = -(p_*^{(0)}(x_1) - ip_1^{(0)}(x_1)).$$

We will seek the complex potentials $\Phi_0(z)$ and $\Psi_0(z)$ in the form [15]

$$\Phi_0(z) = \frac{1}{2\pi} \sum_{k=0}^2 \int_{-l_k}^{l_k} \frac{g_k^0(t) dt}{t - z_k} \quad (21)$$

$$\Psi_0(z) = \frac{1}{2\pi} \sum_{k=0}^2 e^{-2i\alpha_k} \int_{-l_k}^{l_k} \left[\frac{\overline{g_k^0(t)}}{t - z_k} - \frac{\overline{T_k} e^{i\alpha_k}}{(t - z_k)^2} g_k^0(t) \right] dt$$

where $T_k = te^{i\alpha_k} + z_k^0$, $z_k = e^{-i\alpha_k}(z - z_k^0)$, $\alpha_0 = \alpha_1 = 0$, $z_0^0 = 0$, $z_2^0 = -ih$, $l_0 = \infty$, $l_2 = \infty$.

Satisfying by functions (21) boundary conditions (20), after some transformations we get the system of three integral equations

$$\int_{-\infty}^{\infty} \left[\frac{g_0^0(t)}{t - x} + g_2^0(t) K_{0,2}(t - x) + \overline{g_2^0(t)} L_{0,2}(t - x) \right] dt = \quad (22)$$

$$= - \int_{-l_1}^{l_1} \left[g_1^0(t) K_{0,1}(t, x) + \overline{g_1^0(t)} L_{0,1}(t, x) \right] dt \quad |x| < \infty$$

$$\int_{-\infty}^{\infty} \left[\frac{g_2^0(t)}{t-x} + g_0^0(t) K_{2,0}(t-x) + \overline{g_0^0(t)} L_{2,0}(t-x) \right] dt = \quad (23)$$

$$= - \int_{-l_1}^{l_1} \left[g_1^0(t) K_{2,1}(t,x) + \overline{g_1^0(t)} L_{2,1}(t,x) \right] dt \quad |x| < \infty$$

$$\int_{-l_1}^{l_1} \frac{g_1^0(t)}{t-x} + \left[\int_{-l_1}^{l_1} g_1^0(t) K_{1,1}(t,x) + \overline{g_1^0(t)} L_{1,1}(t,x) \right] dt + \quad (24)$$

$$+ \int_{-\infty}^{\infty} \left[g_0^0(t) K_{1,0}(t,x) + \overline{g_0^0(t)} L_{1,0}(t,x) \right] dt +$$

$$+ \int_{-\infty}^{\infty} \left[g_2^0(t) K_{1,2}(t,x) + \overline{g_2^0(t)} L_{1,2}(t,x) \right] dt = \pi f^0(x), \quad |x| \leq l_1$$

The quantities K_{nk} , L_{nk} ($k, n=0,1,2$) are not cited because of their bulky form. From the system of three singular integral equations (22)-(24) we exclude the two functions $g_0^0(t)$ and $g_2^0(t)$. Substituting the functions $g_0^0(x)$ and $g_2^0(x)$ found from the solution of integral equations (22) and (23), after some transformations we get one complex singular integral equation for the unknown function $g_1^0(x)$

$$\int_{-l_1}^{l_1} \frac{g_1^0(t) dt}{t-x} + \int_{-l_1}^{l_1} \left[g_1^0(t) R_{11}(t,x) + \overline{g_1^0(t)} S_{11}(t,x) \right] dt = \pi f^0(x) \quad |x| \leq l_1 \quad (25)$$

We don't cite expressions for the functions $R_{11}(t,x)$ and $S_{11}(t,x)$ because of their bulky form (they have the form similar to (V. 41) in the book [16]).

To the singular integral equation (25) for the internal crack we add the additional condition

$$\int_{-l_1}^{l_1} g_1^0(t) dt = 0 \quad (26)$$

providing the uniqueness of displacements in tracing the contour of the crack in a zero approximation.

Under additional condition (26), the complex singular integral equation (25) is reduced to the system of M algebraic equations with respect to approximate values of the desired function $g_1^0(x_1)$ at the nodal points. For obtaining the system of algebraic equations at first in integral equation (25) and condition (26) we reduce all the integration intervals to one interval $[-1, 1]$ by means of change of variables $t = l_1\tau$, $x = l_1\xi$ ($|\tau| < 1$, $|\xi| < 1$). Look for the solution of the singular integral equation in the form

$$g_1^0(\eta) = \frac{g_1^*(\eta)}{\sqrt{1-\eta^2}} \quad (27)$$

where $g_1^*(\eta)$ is a function bounded in the interval $[-1, 1]$.

Using the quadrature formulae of Gauss type [16, 17], the singular integral equation (25) with condition (26) reduces to the system of M algebraic equations for defining the M unknowns $g_1^*(t_m)$ ($m=1, 2, \dots, M$)

$$\frac{1}{M} \sum_{m=1}^M l_1 \left[g_1^*(t_m) R_{11}(l_1 t_m, l_1 x_r) + \overline{g_1^*(t_m)} S_{11}(l_1 t_m, l_1 x_r) \right] = f^0(x_r) \quad (28)$$

$$\sum_{m=1}^M g_1^*(t_m) = 0, \quad t_m = \cos \frac{2m-1}{2M} \pi, \quad x_r = \cos \frac{\pi r}{M} \quad (r=1, 2, \dots, M-1)$$

For the stress intensity factors in a zero approximation, we have

$$K_{10}^{\pm} - iK_{110}^{\pm} = \mp \sqrt{\pi d_1} g_0^*(\pm 1) \quad (29)$$

$$\text{where } g_0^*(1) = \frac{1}{M} \sum_{m=1}^M (-1)^m g_0^*(t_m) \cot \frac{2m-1}{4M} \pi$$

$$g_0^*(-1) = \frac{1}{M} \sum_{m=1}^M (-1)^{M+m} g_0^*(t_m) \tan \frac{2m-1}{4M} \pi$$

In a first approximation

$$\frac{1}{M} \sum_{m=1}^M l_1 \left[g_1^*(t_m) R(lt_m, lx_r) + \overline{g_1^*(t_m)} S(lt_m, lx_r) \right] = f_1(x_r) \quad (30)$$

$$\sum_{m=1}^M g_1^*(t_m) = 0, \quad g_1'(\xi) = \frac{g_1^*(\xi)}{\sqrt{1-\xi^2}}$$

For the stress intensity factors in a first approximation we have

$$K_{10}^{\pm} - iK_{110}^{\pm} = \mp \sqrt{\pi d_1} g_1^*(\pm 1) \quad (31)$$

$$\text{where } g_1^*(1) = \frac{1}{M} \sum_{m=1}^M (-1)^m g_1^*(t_m) \cot \frac{2m-1}{4M} \pi$$

$$g_1^*(-1) = \frac{1}{M} \sum_{m=1}^M (-1)^{M+m} g_1^*(t_m) \tan \frac{2m-1}{4M} \pi$$

Knowing the stress intensity factors, by means of brittle fracture criterion [18, 19], for the generalized normal discontinuity

$$\cos^2 \frac{\theta_*}{2} \left(K_{I} \cos \frac{\theta_*}{2} - 3K_{II} \sin \frac{\theta_*}{2} \right) = K_{Ic}, \quad \theta_* = 2 \arctg \frac{K_{I} \mp \sqrt{K_{I}^2 + 8K_{II}^2}}{4K_{II}^2} \quad (32)$$

where the K_{Ic} is a characteristic fracture toughness of the material and is determined experimentally; the sign “+” corresponds to the values of $K_{I} < 0$, the sign “-” to the values of $K_{I} > 0$.

Find the limit values of the external load by attaining of which the crack will be in limit-equilibrium state.

While solving algebraic systems by the Gauss method with the choice of the principal element, the number of Chebyshev nodal points was assumed to be equal to $M=30$.

Asphalt concrete covering of road of type 1 was accepted in place of an example of calculation. Calculations on definition of stress intensity factors were carried out. The graph of dependence of stress intensity factors on dimensionless length of the crack were represented in Figs. 2-3. Here the curve I corresponds to the

smooth contour of road; curve 2 for $\delta(x) = A_1 \left(\cos \frac{2\pi}{L_p} x - 1 \right) + A_2 \left(\cos \frac{4\pi}{L_p} x - 1 \right)$,

where A_1, A_2 are the amplitudes of the constituents of two-hump roughness, $x = Vt$, V is the velocity of motion in road with the components of length L_p and joining roughnesses, t is time; the curve 3 for

$$\delta(x) = \sum_{n=0}^{\infty} \left(A_n \cos \frac{n\pi}{L_p} x + B_n \sin \frac{n\pi}{L_p} x \right),$$
 where A_n, B_n are non-correlated random variables satisfying the conditions $\langle A_n \rangle = 0, \langle B_n \rangle = 0, D\langle A_n \rangle = D\langle B_n \rangle = D_n$.

At calculations it was accepted $E_1 = 3.2 \cdot 10^3$ MPa, $\mu_1 = 0.16, \alpha_1 = \pi/4$, and the crack's center at the point $O_1 (0.05h; -0.25h)$.

The results of calculations of stress intensity factors for the crack of opening mode (mode I) $\alpha_1 = 0$ from dimensionless length of the crack for different combinations of materials of covering and base are represented in Fig. 4. The road's surface is assumed to be smooth.

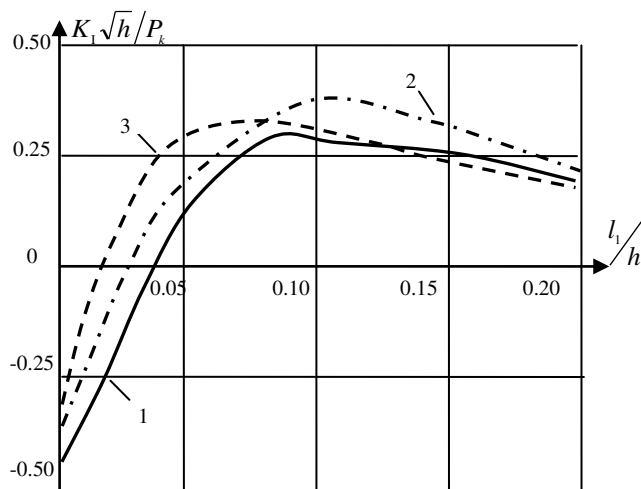


Figure 2

Dependences of the stress intensity factor K_I , on dimensionless length of the crack l_1/h

The analysis of calculations allow to make the following conclusions: a) if $G_1/G_2 > 1$ (G is shear modulus of the material), then for constant external load P_k and for the fixed values of other parameters of the problem, the stress intensity factor K_I increases according to increase of the crack's length. In this case there may happen fracture of the covering if the external load is such that the critical length of the crack is less than the length of the crack of the layer containing it. b) if $G_1/G_2 < 1$, then under constant external load and fixed values of other parameters of the problem, the dimensionless stress intensity factor $K_I / (P_k / \sqrt{\pi h})$ at first increases according to increase of the crack's length, and then beginning with some value l_1/h , it slowly decreases.

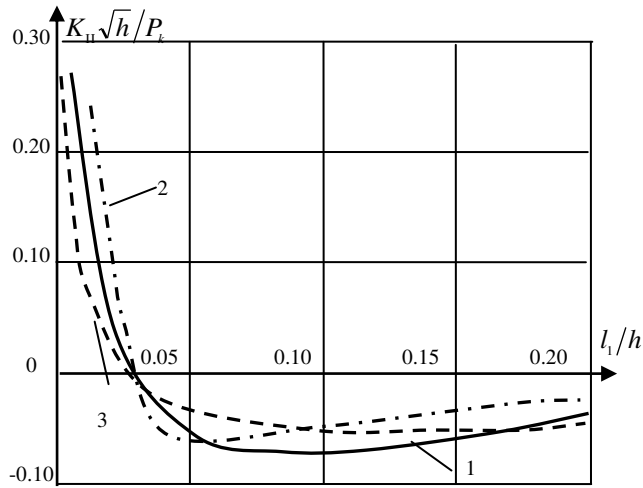


Figure 3

Dependences of the stress intensity factor K_{II} , on dimensionless length of the crack l_1/h

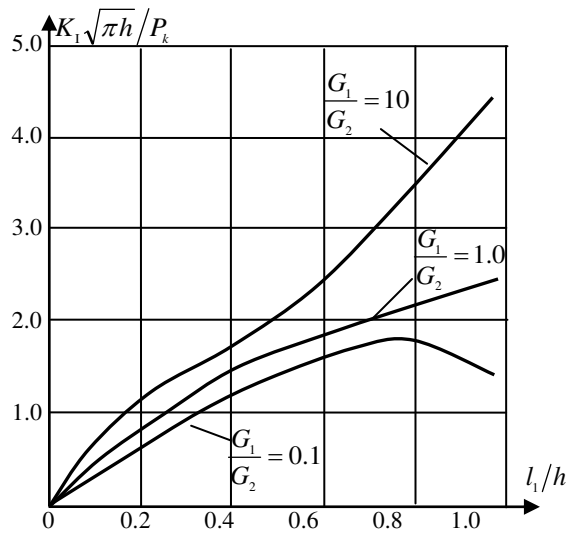


Figure 4

Dependence of the stress intensity factor K_I , on dimensionless length l_1/h of the longitudinal crack

In this case, there may happen retardation or arrest of the crack. The indicated event happens when the crack's vertex is close to the interface of media since in this case the influence of elastic base shows itself.

4 The Case of Arbitrary Number of Cracks in the Road Covering Cross Section

In the center of cracks (Fig. 1) locate the origin of local systems of coordinates $x_k O_k y_k$ whose axes x_k coincide with the lines of cracks and from angles α_k with the axis x . It is accepted that the cracks faces are free from external loads. The boundary conditions for the case under consideration are of the form (1)-(4). The stated problem is reduced to the sequence of boundary value problems in zero and first approximations.

At each approximation we use the superposition principle. We can represent the stress-strain state of a two-layer body with cracks in the form of the sum of two states. The first state will be determined from the solution of a wear contact problem on pressing out of a wheel into the road covering surface at unavailability of cracks. The second state is determined from the solution of a boundary value problem for a strip weakened by an arbitrary system of rectilinear cracks with the forces on the faces determined by the first stress state.

In a zero approximation, the boundary conditions of the second problem have the form

$$\text{for } y_k = 0 \quad \sigma_{y_k}^{(0)} = -\sigma_k^{(0)}(x_k), \quad \tau_{x_k y_k}^{(0)} = -\tau_k^{(0)}(x_k) \quad (k=1,2,\dots,N) \quad (33)$$

$$\text{for } y = 0 \quad \sigma_y^{(0)} = 0, \quad \tau_{xy}^{(0)} = 0$$

$$\text{for } y = -h \quad \sigma_y^{(0)} = 0, \quad \tau_{xy}^{(0)} = 0$$

in a first approximation

$$\text{for } y_k = 0 \quad \sigma_{y_k}^{(1)} = -\sigma_k^{(1)}(x_k), \quad \tau_{x_k y_k}^{(1)} = -\tau_k^{(1)}(x_k) \quad (k=1,2,\dots,N) \quad (34)$$

$$\text{for } y = 0 \quad \sigma_y^{(1)} = 0, \quad \tau_{xy}^{(1)} = 0$$

$$\text{for } y = -h \quad \sigma_y^{(1)} = 0, \quad \tau_{xy}^{(1)} = 0$$

Here $\sigma_k^{(0)}(x_k)$ and $\tau_k^{(0)}(x_k)$ are normal and tangential stresses arising in the continuous strip along the axis y_k in a zero approximation from the application of the given loads; $\sigma_k^{(1)}(x_k)$ and $\tau_k^{(1)}(x_k)$ also arise in the continuous strip along the axis y_k in a first approximation from the given loads on road covering.

The quantities $\sigma_k^{(0)}(x_k)$ and $\tau_k^{(0)}(x_k)$ and $\sigma_k^{(1)}(x_k)$, $\tau_k^{(1)}(x_k)$ are found from the relations of [13].

Consider zero approximation (33). We look for the complex potentials in the form

$$\Phi^{(0)}(z) = \frac{1}{2\pi} \sum_{k=0}^{N+1} \int_{-l_k}^{l_k} \frac{g_k^0(t) dt}{t - z_k} \quad (35)$$

$$\Psi^{(0)}(z) = \frac{1}{2\pi} \sum_{k=0}^{N+1} e^{-2i\alpha_k} \int_{-l_k}^{l_k} \left[\frac{\overline{g_k^0(t)}}{t-z_k} - \frac{\overline{T_k} e^{i\alpha_k}}{(t-z_k)^2} g_k^0(t) \right] dt \quad (36)$$

where $T_k = te^{i\alpha_k} + z_k^0$, $z_k = e^{-i\alpha_k}(z - z_k^0)$.

Having defined the stresses on the axis x_n from Kolosov-Muskhelesvili formula [14], and substituting them into boundary conditions (33), after some transformations we get the system of $N + 2$ integral equations

$$\int_{-\infty}^{\infty} \left[\frac{g_0^0(t)}{t-x} + g_{N+1}^0(t) K_{0,N+1}(t-x) + \overline{g_{N+1}^0(t)} L_{0,N+1}(t-x) \right] dt = \quad (37)$$

$$= - \sum_{k=1}^N \int_{-l_k}^{l_k} \left[g_k^0(t) K_{0,k}(t,x) + \overline{g_k^0(t)} L_{0,k}(t,x) \right] dt \quad |x| < \infty$$

$$\int_{-\infty}^{\infty} \left[\frac{g_{N+1}^0(t)}{t-x} + g_0^0(t) K_{N+1,0}(t-x) + \overline{g_0^0(t)} L_{N+1,0}(t-x) \right] dt = \quad (38)$$

$$= - \sum_{k=1}^N \int_{-l_k}^{l_k} \left[g_k^0(t) K_{N+1,k}(t,x) + \overline{g_k^0(t)} L_{N+1,k}(t,x) \right] dt \quad |x| < \infty$$

$$\int_{-l_k}^{l_k} \frac{g_n^0(t)}{t-x} + \sum_{k \neq n} \left[\int_{-l_k}^{l_k} g_k^0(t) K_{nk}(t,x) + \overline{g_k^0(t)} L_{nk}(t,x) \right] dt + \quad (39)$$

$$+ \int_{-\infty}^{\infty} \left[g_0^0(t) K_{n,0}(t,x) + \overline{g_0^0(t)} L_{n,0}(t,x) \right] dt +$$

$$+ \int_{-\infty}^{\infty} \left[g_{N+1}^0(t) K_{n,N+1}(t,x) + \overline{g_{N+1}^0(t)} L_{n,N+1}(t,x) \right] dt = \pi f_n^0(x) \quad |x| < l_n$$

$$\text{Here } K_{0,N+1}(x) = K_{N+1,0}(x) = \frac{x}{x^2 + h^2}, \quad L_{0,N+1}(x) = \overline{L_{N+1,0}(x)} = \frac{ih}{(x+ih)^2} \quad (40)$$

$$K_{0,k}(t,x) = \frac{e^{i\alpha_k}}{2} \left(\frac{1}{T_k - x - ih/2} + \frac{1}{\overline{T_k} - x + ih/2} \right)$$

$$K_{n,0}(t,x) = \frac{1}{2} \left(\frac{1}{t + ih/2 - X_n} + \frac{e^{-2i\alpha_n}}{t - ih/2 - \overline{X}_n} \right)$$

$$L_{0,k}(t,x) = \frac{e^{-i\alpha_k} (\bar{T}_k - T_k + ih)}{2 (\bar{T}_k - x + ih/2)^2}, \quad L_{N+1,k}(t,x) = \frac{e^{-i\alpha_k} (\bar{T}_k - T_k - ih)}{2 (\bar{T}_k - x - ih/2)^2}$$

$$L_{n,0}(t,x) = \frac{1}{2} \left(\frac{1}{t - ih/2 - \bar{X}_n} - \frac{t + ih/2 - X_n}{(t - ih/2 - \bar{X}_n)^2} e^{-2i\alpha_n} \right)$$

$$L_{n,N+1}(t,x) = \frac{1}{2} \left(\frac{1}{t + ih/2 - \bar{X}_n} - \frac{t - ih/2 - X_n}{(t + ih/2 - \bar{X}_n)^2} e^{-2i\alpha_n} \right)$$

$$K_{N+1,k}(t,x) = \frac{e^{i\alpha_k}}{2} \left(\frac{1}{T_k - x + ih/2} + \frac{1}{\bar{T}_k - x - ih/2} \right)$$

$$K_{n,N+1}(t,x) = \frac{1}{2} \left(\frac{1}{t - ih/2 - X_n} + \frac{e^{-2i\alpha_n}}{t + ih/2 - \bar{X}_n} \right)$$

$$K_{nk}(t,x) = \frac{e^{i\alpha_k}}{2} \left(\frac{1}{T_k - X_n} + \frac{e^{-2i\alpha_n}}{(\bar{T}_k - \bar{X}_n)^2} \right)$$

$$L_{nk}(t,x) = \frac{e^{-i\alpha_k}}{2} \left(\frac{1}{\bar{T}_k - \bar{X}_n} - \frac{T_k - X_n}{(\bar{T}_k - \bar{X}_n)^2} e^{-2i\alpha_n} \right), \quad X_n = xe^{i\alpha_n} + z_n^0$$

For convenience, in (37), (38), (39) and in what follows the index x_n is omitted. From the system of $N+2$ singular integral equations we exclude the two unknown functions $g_0^0(t)$ and $g_{N+1}^0(t)$.

After some transformations we get a system N singular integral equations of the problem under consideration in a zero approximation

$$\int_{-l_k}^{l_k} \frac{g_k^0(t) dt}{t-x} + \sum_{k=1}^N \int_{-l_k}^{l_k} \left[g_k^0(t) R_{nk}(t,x) + \overline{g_k^0(t) S_{nk}(t,x)} \right] dt = \pi f_n^0(x_n) \quad |x| \leq l_n \quad (41)$$

($n=1,2,\dots,N$)

$$R_{nk}(t,x) = (1 - \delta_{nk}) K_{nk}(t,x) + r_{nk}(t,x), \quad S_{nk}(t,x) = (1 - \delta_{nk}) L_{nk}(t,x) + s_{nk}(t,x) \quad (42)$$

$$r_{nk}(t,x) = \int_{-\infty}^{\infty} \left[K_{n,0}(\tau,x) M_{0,k}(t,\tau) + L_{n,0}(\tau,x) \overline{N_{0,k}(t,\tau)} + \right. \quad (43)$$

$$\left. + K_{n,N+1}(\tau,x) M_{N+1,k}(t,\tau) + L_{n,N+1}(\tau,x) \overline{N_{N+1,k}(t,\tau)} \right] d\tau$$

$$s_{nk}(t, x) = \int_{-\infty}^{\infty} \left[K_{n,0}(\tau, x) N_{0,k}(t, \tau) + L_{n,0}(\tau, x) \overline{M_{0,k}(t, \tau)} + \right. \\ \left. + K_{n,N+1}(\tau, x) N_{N+1,k}(t, \tau) + L_{n,N+1}(\tau, x) \overline{M_{N+1,k}(t, \tau)} \right] d\tau$$

After substituting functions $M_{0,k}(u, x)$, $N_{0,k}(u, x)$, $M_{N+1,k}(u, x)$, $N_{N+1,k}(u, x)$ into (43), the kernels $r_{nk}(t, x)$ and $s_{nk}(t, x)$ will be represented by triple integrals. After integration these expressions may be represented by one-fold integrals.

Omitting very bulky calculations, finally for the kernels $r_{nk}(t, x)$ and $s_{nk}(t, x)$ we find

$$r_{nk}(t, x) = \int_0^{\infty} \left[\left(\frac{1}{shhs + hs} + \frac{1}{shhs - hs} \right) H_{nk}(X_n, T_k, s, \alpha_n, \alpha_k) + \right. \\ \left. + \left(\frac{1}{shhs + hs} - \frac{1}{shhs - hs} \right) G_{nk}(X_n, T_k, s, \alpha_n, \alpha_k) \right] ds \quad (44)$$

$$s_{nk}(t, x) = \int_0^{\infty} \left[\left(\frac{1}{shhs + hs} - \frac{1}{shhs - hs} \right) H_{nk}(X_n, \bar{T}_k, s, \alpha_n, -\alpha_k) + \right. \\ \left. + \left(\frac{1}{shhs + hs} + \frac{1}{shhs - hs} \right) G_{nk}(X_n, \bar{T}_k, s, \alpha_n, -\alpha_k) \right] ds$$

$$\text{Here } H_{nk}(X_n, \bar{T}_k, s, \alpha_n, -\alpha_k) = \frac{e^{i\alpha_k}}{4} \left\{ \sin(X_n - \bar{T}_k) s - \sin(T_k - \bar{X}_n) s \langle hs + \right. \quad (45)$$

$$+ e^{-2i\alpha_n} [1 - hs + s^2(T_k - \bar{T}_k)(\bar{X}_n - X_n) + h^2 s^2] \rangle + \langle s(T_k - \bar{T}_k) - \\ - e^{-2i\alpha_n} [(T_k - \bar{T}_k) + hs^2(\bar{X}_n - X_n - T_k + \bar{T}_k)] \rangle \cos(T_k - \bar{X}_n) s + \\ + e^{-hs} [\sin(T_k - X_n) s + e^{-2i\alpha_n} \sin(\bar{T}_k - \bar{X}_n) s] \};$$

$$G_{nk}(X_n, T_k, s, \alpha_n, \alpha_k) = \frac{e^{i\alpha_k}}{4} \left\{ -[1 + e^{-2i\alpha_n}(-1 + hs)] \sin(\bar{T}_k - \bar{X}_n) s - \right. \\ - hs \sin(T_k - X_n) s - s(T_k - \bar{T}_k) \cos(T_k - X_n) s - \\ - e^{-2i\alpha_n} (\bar{X}_n - X_n) s \cos(\bar{T}_k - \bar{X}_n) s + e^{-hs} [\sin(T_k - \bar{X}_n) s - \\ \left. - e^{-2i\alpha_n} \sin(T_k - \bar{X}_n) s + e^{-2i\alpha_n} \sin(\bar{X}_n - X_n - T_k + \bar{T}_k) s \cos(T_k - \bar{X}_n) s] \right\}$$

Note that the functions $r_{nk}(t, x)$ and $s_{nk}(t, x)$ are regular. They determine the influence of the boundaries of the strip on stress state near the cracks vertices. To the system of singular integral equations (41) for the internal cracks we should add the following additional conditions

$$\int_{-l_k}^{l_k} g_k^0(t) dt = 0 \quad (k = 1, 2, \dots, N) \quad (46)$$

Using the procedure for converting a system to an algebraic [16, 17], the system of singular integral equations (41) with conditions (46) is reduced to a system of $N \times M$ algebraic equations for determining the $N \times M$ unknowns $g_k^0(t_m)$:

$$\frac{1}{M} \sum_{m=1}^M \sum_{k=1}^N l_k \left[g_k^0(t_m) R_{nk}(l_k t_m, l_n x_r) + \overline{g_k^0(t_m)} S_{nk}(l_k t_m, l_n x_r) \right] = f_n^0(x_r^0) \quad (47)$$

$$\sum_{m=1}^M g_n^0(t_m) = 0 \quad (n, k = 1, 2, \dots, N; m = 1, 2, \dots, M)$$

If in (47) we pass to complexly conjugate values, we get one more $N \times M$ algebraic equations.

For the stress intensity factors in the vicinity of the cracks tips, in a zero approximation we find:

at the right vertex of the crack

$$K_{In}^{(0)} - iK_{In}^{(0)} = \sqrt{\pi l_n} \frac{1}{M} \sum_{m=1}^M (-1)^m g_n^0(t_m) \cot \frac{2m-1}{4M} \pi \quad (48)$$

at the left vertex of the crack

$$K_{In}^{(0)} - iK_{In}^{(0)} = \sqrt{\pi l_n} \frac{1}{M} \sum_{m=1}^M (-1)^{M+m} g_n^0(t_m) \tan \frac{2m-1}{4M} \pi \quad (49)$$

Now consider the solution of problem (34) in a first approximation.

Behaving as above, we get a system of singular integral equations of a first approximation

$$\int_{-l_k}^{l_k} \frac{g_k^1(t) dt}{t-x} + \sum_{k=1}^N \int_{-l_k}^{l_k} \left[g_k^1(t) R_{nk}(t, x) + \overline{g_k^1(t)} S_{nk}(t, x) \right] dt = \pi f_n^1(x_n) \quad |x| \leq l_n \quad (50)$$

To the system of singular integral equations (50) we should add the additional equalities

$$\int_{-l_k}^{l_k} g_k^1(t) dt = 0 \quad (k = 1, 2, \dots, N) \quad (51)$$

As in a zero approximation, the system of complex singular equations (50) with conditions (51) by means of the algebraization procedure [16, 17] is reduced to the system of $N \times M$ algebraic equations with respect to $N \times M$ unknown $g_k^1(t_m)$ ($k=1,2,\dots,N; m=1,2,\dots,M$):

$$\frac{1}{M} \sum_{m=1}^M \sum_{k=1}^N l_k \left[g_k^1(t_m) R_{nk}(l_k t_m, l_n x_r) + \overline{g_k^1(t_m)} S_{nk}(l_k t_m, l_n x_r) \right] = f_n^1(x_r^0) \quad (52)$$

$$(r = 1, 2, \dots, M-1)$$

$$\sum_{m=1}^M g_n^1(t_m) = 0$$

If in (52) we pass to complexly conjugate values, we get one more $N \times M$ algebraic equations.

For the stress intensity factors in the vicinity of the cracks tips in a first approximation we get

at the right vertex of the crack

$$K_{\text{rn}}^{(1)} - iK_{\text{lrn}}^{(1)} = \sqrt{\pi l_n} \frac{1}{M} \sum_{m=1}^M (-1)^m g_n^1(t_m) \cot \frac{2m-1}{4M} \pi \quad (53)$$

at the left vertex of the crack

$$K_{\text{rn}}^{(1)} - iK_{\text{lrn}}^{(1)} = \sqrt{\pi l_n} \frac{1}{M} \sum_{m=1}^M (-1)^{M+m} g_n^1(t_m) \tan \frac{2m-1}{4M} \pi \quad (54)$$

Finally, for the stress intensity factors we have

$$K_{\text{rn}} = K_{\text{rn}}^{(0)} + \varepsilon K_{\text{rn}}^{(1)} + \dots, \quad K_{\text{lrn}} = K_{\text{lrn}}^{(0)} + \varepsilon K_{\text{lrn}}^{(1)} + \dots$$

Conclusions

Experimental data of practice of exploitation of the pair “road covering-elastic base” convincingly shows that by designing new constructions of motor roads it is necessary to take into attention the cases when in road covering there may arise cracks. The existing methods of strength analysis of road coverings ignore this circumstance. Such a situation makes impossible to design road coverings of minimal specific consumption of materials under guaranteed reliability and durability. In this connection, it is necessary to realize the limiting analysis of the pair “road covering-base” in order to establish that the presupposed initial cracks located unfavorably will not grow to catastrophic sizes and will not cause fracture during the rated service life. The size of the initial minimal crack should be considered as a design characteristics of the covering material.

Based around the suggested design model taking into account crack-like defects in road covering, a method for calculating the fracture parameters of road covering

with regard to real roughness surface of the road is developed. The elaborated calculation method, by means of definition of stress intensity factors, allows to predict the growth of available cracks in road covering, to take into account not only separately each realization of the roughness profile (deterministic approach) and also to carry out statistic description of surface roughnesses of the road by realization of a random function, to evaluate different factors (constructive, technological, operational) for road covering strength.

Numerical realization of the obtained dependences allows to solve the following practically important problems:

- 1) definition of critical sizes of a crack under known loads, stresses and fracture toughness. These informations may be used by developing requirements to decision abilities of the used methods of defectoscopy.
- 2) definition of critical level of stresses depending on external loads and parameters of brittle strength.

These informations may be used by developing technological processes for lowering the level of residual stresses.

References

- [1] Thomas T. R.: 'Rough surfaces' Longman, London, 1982
- [2] Aykut Ş.: 'Surface Roughness Prediction in Machining Castamide Material Using ANN', Acta Polytechnica Hungarica, Vol. 8, No. 2, pp. 21-32, 2011
- [3] Zolgharnein E., Mirsalimov V. M.: 'Nucleation of Crack under Inner Compression of Cylindrical Bodies', Acta Polytechnica Hungarica, Vol. 9, No. 2, pp. 169-183, 2012
- [4] Hasanov Sh. H.: 'Influence of Elastic Foundation Surface Roughness on Stress-Strain State of Road Covering', Engineering and Automation Problems, No. 4, pp. 61-64, 2008
- [5] Tukashev J. B. and Adilhanova L. A.: 'Investigation of Stress-Strain State of Road Covering', Geology, Geography and Global Energy, No 2(37), pp. 163-165, 2010
- [6] Hasanov Sh. H.: 'Calculated Method of Research of Fatigue Fracture of the Road Covering', Structural Mechanics of Engineering Constructions and Buildings, No. 2, pp. 14-20, 2010
- [7] Chernous D. A., Shilko S. V., Kravchenko S. E.: 'Prediction of Mechanical Characteristics of Asphalt Concrete', Mechanics of Machines, Mechanisms and Materials, No. 1(18), pp. 72-74, 2011
- [8] Tschegg E. K., Jamek M., Lugmayr R.: 'Fatigue Crack Growth in Asphalt and Asphalt-Interfaces', Engineering Fracture Mechanics, Vol. 78, Issue 6, pp. 1044-1054, 2011

-
- [9] Ameri M., Mansourian A., Heidary Khavas M., Aliha M. R. M., Ayatollahi M. R.: 'Cracked Asphalt Pavement under Traffic Loading – A 3D Finite Element Analysis', *Engineering Fracture Mechanics*, Vol. 78, Issue 8, pp. 1817-1826, 2011
- [10] Lavrushina E. G., Lavrushin G. A., Blinova O. S., Plaksin M. V., Gneduk D. S.: 'Experimental Determination of Crack Resistance of Road Coating', *Vologdinskies Reading*. pp. 40-41, 2012
- [11] Hasanov Sh. H.: 'Cohesive Crack with Partially Contacting Faces in Section of the Road Covering', *Mechanics of Machines, Mechanisms and Materials*, No. 2(19), pp. 58-64, 2012
- [12] Hasanov Sh. H.: 'Solution of Fracture Mechanics for the Transverse Crack in the Cross Section of Road Cover', *Mechanics of Machines, Mechanisms and Materials*, No. 2(23), pp. 35-40, 2013
- [13] Hasanov Sh. G.: 'Modelling of Stress-Strain State in Road Covering', *Sci. proc. of Azerbaijan Architecture and Building University*, Baku, No. 2, pp. 151-159, 2007
- [14] Muskhelishvili N. I.: 'Some Basic Problems of Mathematical Theory of Elasticity' Amsterdam: Kluwer, 1977
- [15] Panasyuk V. V., Savruk M. P. and Datsyshyn A. P.: 'A General Method of Solution of Two-Dimensional Problems in the Theory of Cracks', *Eng. Fract. Mech.*, Vol. 9, No. 2, pp. 481-497, 1977
- [16] Panasyuk V. V., Savruk M. P. and Datsyshyn A. P.: 'Stress Distribution around Cracks in Plates and Shells' Kiev: Naukova Dumka (in Russian), 1976
- [17] Mirsalimov V. M.: 'Non-One-Dimensional Elastoplastic Problems' Moscow: Nauka (in Russian), 1987
- [18] Cherepanov G. P.: 'Mechanics of Brittle Fracture' N-Y.: Mc Graw-Hill, 1979
- [19] Panasyuk V. V.: 'Mechanics of Quasibrittle Fracture of Material' Kiev: Naukova Dumka (in Russian) 1991

Comparative Analysis of Tuning a PID Controller using Intelligent Methods

Vikram Chopra¹, Sunil K. Singla², Lillie Dewan³

^{1&2} Department of Electrical & Instrumentation Engineering, Thapar University, Patiala, Punjab-147004, India
e-mails: vikram.chopra@thapar.edu; ssingla@thapar.edu

³ Department of Electrical Engineering, NIT Kurukshetra-136119, India
e-mail: l_dewan@nitkkr.ac.in

Abstract: A proportional integral derivative (PID) controller is the most commonly used controller in controlling industrial loops due to its simple structure, robust nature and easy implementation. Tuning a PID controller is an important task. The conventional methods for tuning a PID controller have certain limitations. These limitations can be taken care by tuning the PID controller using intelligent techniques. This paper presents the intelligent methods based on fuzzy logic, artificial neural network (ANN), adaptive neuro fuzzy inference system (ANFIS) and genetic algorithms (GA) for tuning a PID controller. The controller tuned by the given methods has been used for concentration control of a continuous stirred tank reactor (CSTR). Simulation results reveals that intelligent methods provide better performance than the conventional Zeigler Nichols (ZN) method in terms of various performance specifications.

Keywords: PID controller; Fuzzy logic controller (FLC); ANN; ANFIS; GA; CSTR

1 Introduction

PID controllers are the most commonly used controllers in process industries. About 90% of industrial loops use PID controllers. This is because of its simple structure, easy implementation, robust nature and less number of tuning parameters [1]. The control signal provided by PID controller is dependent upon three terms and is given by [2]:

$$u(t) = K_p e(t) + K_i \int_0^t e(t) dt + K_d \frac{de(t)}{dt} \quad (1)$$

$u(t)$ is the control signal, $e(t)$ the error signal which is the difference between the reference signal $r(t)$ and the system output $y(t)$. K_p , K_i and K_d are the proportional gain, the integral gain and the derivative gain respectively. These are the parameters to be tuned. There are various conventional methods for PID controller tuning. One of them is the Ziegler–Nichols (ZN) method [3]. In this method the parameters of the PID controller are determined by finding out the proportional gain at which the output becomes oscillatory corresponding to a step input. This gain is called as the critical gain and the frequency of oscillation as critical frequency. The downside of the ZN method is that it results in high value of maximum overshoot. In processes such as plastic glove manufacturing it is undesirable to have high overshoot. Therefore, the ZN method cannot be used for such systems. The other tuning method that appears in the literature is the Cohen–Coon technique [4], where the main design criterion is related to disturbance rejection but it can only be used for first order models including large process delays. The relay auto-tuning method [5] eliminates the possibility of driving the plant close to the stability limit. But the method is difficult to apply in case of processes with large time delays [6]. Morari [7] proposed the internal model control (IMC) based method for tuning a PID controller but it is hard to implement for systems with first order plus dead time. Tunings methods based on optimization has been discussed by Astrom [3]. In these methods the design criterion is based on minimization of certain performance criterion such as integral of square error (ISE) or integral of time multiplied by absolute error (ITAE). Another method for tuning a PID controller is the pole placement method [3] in which the tuning is based on keeping the closed loop poles at desired locations. However the method is not suitable for higher order systems.

In this paper the intelligent methods based on fuzzy logic, ANN, ANFIS and GA for tuning a PID controller have been compared. The controller tuned by the various methods has been used for concentration control of a CSTR. The intelligent methods provide better performance in terms of various performance specifications than the conventional Zeigler Nichols method while the steady state error remains same at zero.

This paper is organized in 4 sections. Section 1 gives the general introduction of the paper. Section 2 represents the problem formulation. In Section 3 the tuning of PID controller using various intelligent methods such as fuzzy logic, ANN, ANFIS and GA has been discussed. The results, comparison and discussion are given in Section 4. At the end conclusion and brief list of references is given.

2 Problem Formulation

The aim of this paper is to tune a PID controller using various intelligent methods for concentration control of a continuous stirred tank reactor. The input output transfer function of the reactor is given by [4]:

$$G(s) = \frac{-1.1170s + 3.1472}{s^2 + 4.6429s + 5.3821} \quad (2)$$

The reactor transfer function is a second order system with right half plane (RHP) zero. The control objective is to keep the various performance specifications such as rise time t_r , settling time t_s , maximum overshoot M_p , maximum undershoot M_u and steady state error e_{ss} within desirable limits.

3 Intelligent Methods for Tuning a PID Controller

3.1 Fuzzy Logic

Conventional PID controller does not give acceptable performance for systems with uncertain dynamics, time delays and non-linearity [8]. Hence it is necessary to automatically tune the PID parameters for obtaining satisfactory response. The automatic tuning of PID controller has been done using fuzzy logic. Based on expert knowledge a fuzzy logic system transforms a linguistic control strategy into an automatic control strategy [9]. Figure 1 shows the block diagram of a fuzzy PID controller. The fuzzy PID controller has been implemented using fuzzy logic toolbox in MATLAB [11].

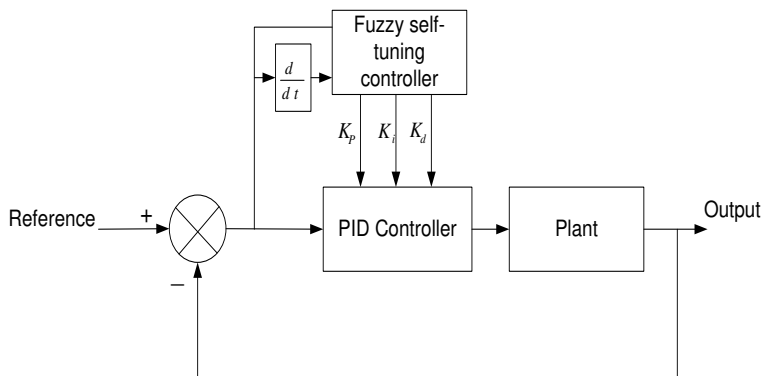


Figure 1
Block diagram of a fuzzy-PID controller [10]

The inputs to the controller are the error (e) and the rate of change of error (Δe) while the outputs are controller gain K_p , K_i & K_d . The structure of fuzzy-PID controller is a two input-three output structure as shown in Figure 2. For finding the range or the universe of discourse of the input and output membership functions the PID controller has been tuned using the conventional Zeigler Nichols method. From there the range of the input as well as output membership functions have been found. The membership functions of these inputs fuzzy sets are shown in Figure 3. The linguistic variable levels are assigned as: negative big (NB), negative small (NS), zero (Z), positive small (PS) and positive big (PB). Similarly, the fuzzy set for error change (Δe) is presented as NB, NS, Z, PS, PB. The ranges of these inputs are from -1.44 to 1.56 and -15.7 to 4.3 respectively.

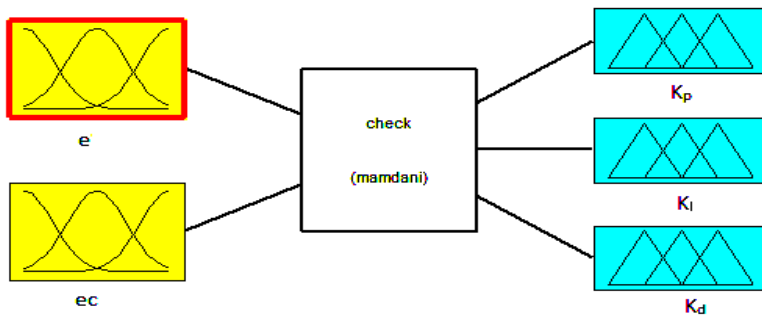
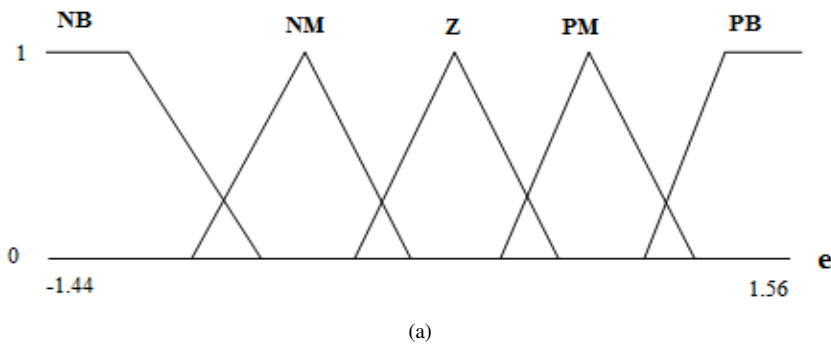
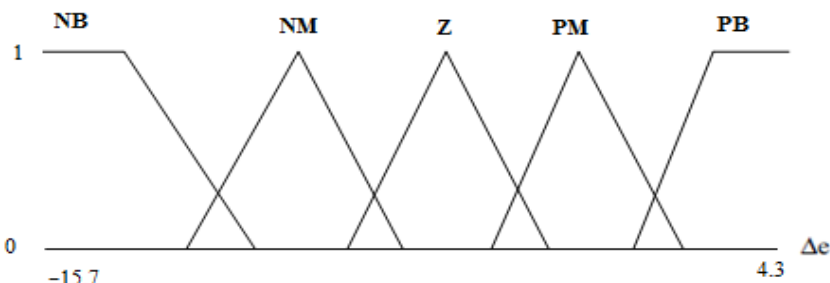


Figure 2
Two input three output FLC structure





(b)

Figure 3

Input fuzzy sets (a) error (e) (b) Change of error (Δe)

The output membership functions are shown in Figure 4. For the output fuzzy sets the scaling of range has been done corresponding to the formulas given below [10-12]:

$$\begin{aligned}
 K_p' &= \frac{K_p - K_{p \min}}{K_{p \max} - K_{p \min}} \\
 K_i' &= \frac{K_i - K_{i \min}}{K_{i \max} - K_{i \min}} \\
 K_d' &= \frac{K_d - K_{d \min}}{K_{d \max} - K_{d \min}}
 \end{aligned}
 \tag{3}$$

The minimum and the maximum values of various gains have been obtained by analyzing the step response of the given process using Zeigler Nichols method.

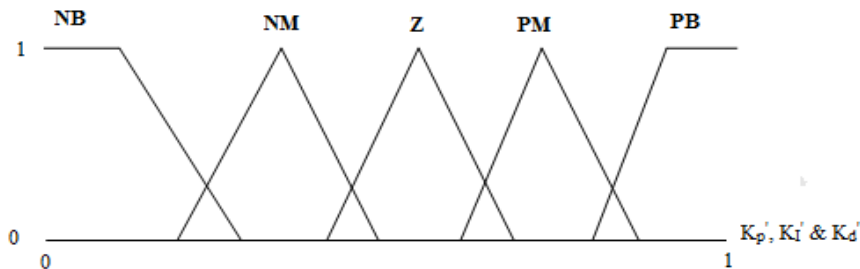


Figure 4

Output fuzzy sets $K_p', K_i' & K_d'$

The rule base for the fuzzy-PID controller is shown in Table1 [12] which can be implemented for tuning the PID controller.

Table1
Rule base for fuzzy-PID controller

$\Delta e \backslash e$	NB	NM	Z	PM	PB
NB	NB	NB	NM	NM	Z
NM	NB	NM	NS	Z	PM
Z	NM	NM	Z	PM	PM
PM	NM	Z	PM	PM	PB
PB	Z	PM	PM	PB	PB

The simulink blockset for fuzzy PID controller implemented for concentration control of a CSTR is shown in Figure 5.

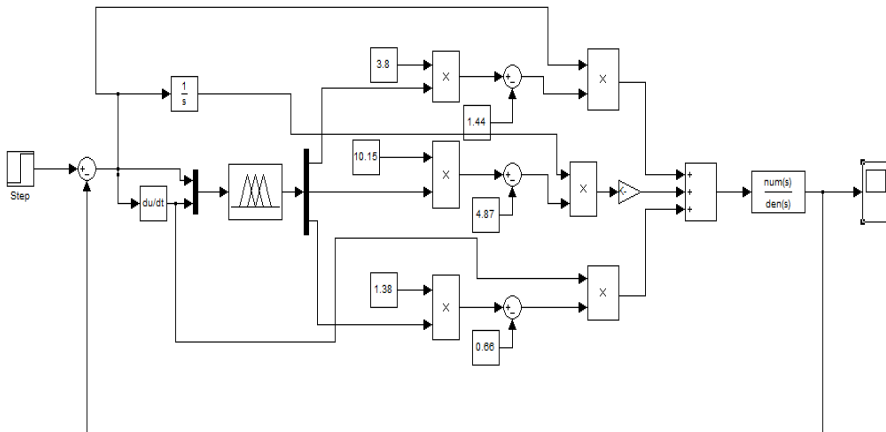


Figure 5
Fuzzy-PID controller implementation in MATLAB Simulink

3.2 Artificial Neural Networks

An ANN is a computational model comprising of artificial neurons operating as a unit for processing information from input to output. [13]. Figure 6 shows the block diagram of PID controller tuning using neural network. The ANN structure used is a single neuron structure [14].

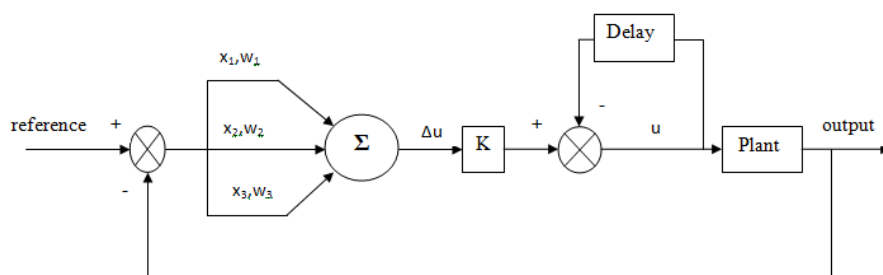


Figure 6

Closed loop control system with single neuron ANN structure [14]

The neuron weights w_1 , w_2 & w_3 will act as the gains of the PID controller. With the help of some learning algorithm the weights of the neural network are modified to attain the desired goal. The proportional error $x_1(k)$, the integral error $x_2(k)$ and the derivative error $x_3(k)$ are given by:

$$x_1(k) = e(k) - e(k-1)$$

$$x_2(k) = e(k)$$

$$x_3(k) = e(k) - 2e(k-1) - e(k-2) \quad (4)$$

These error signals are multiplied with their corresponding weights and act as the input to the single neuron.

The neuron output is given by [14]:

$$u(k) = u(k-1) + K \sum_{i=1}^3 w_i(k) x_i(k) \quad (5)$$

K is a constant for speeding up or slowing down the closed loop response,

The various steps in tuning a PID controller using ANN are as follows:

Step 1: Choose random values for the weights.

Step 2: Calculate the error which is the difference between the reference input and the output.

Step3: The gains of PID controller are decided by supervised delta learning method, using the error signal.

Step 4: The output of the single neuron i.e. Δu is multiplied with a gain K to obtain a better closed loop response.

Step 5: The updated weights will act as the proportional gain, the integral gain and the derivative gain respectively.

Supervised delta learning algorithm for updating the weights has been given by [14]:

$$\begin{aligned}w_1(k) &= w_1(k-1) + \eta_p e(k-1)u(k-1) \\w_2(k) &= w_2(k-1) + \eta_i e(k-1)u(k-1) \\w_3(k) &= w_3(k-1) + \eta_D e(k-1)u(k-1)\end{aligned}\tag{6}$$

η_p, η_i and η_D are the proportional, integral and the derivative learning speeds. Based upon the above steps ANN with single neuron has been implemented on CSTR for tuning of PID controller.

3.3 Adaptive Neuro Fuzzy Inference System (ANFIS)

ANFIS is a special type of neural network which combines the features of both neural networks and fuzzy logic. ANFIS develops a Takagi Sugeno fuzzy inference system (FIS) with the help of an input output data set [15-16]. By using error back propagation algorithm the membership functions of the ANFIS are developed. The inputs to the proposed adaptive neuro fuzzy controller are the error (e) and the rate of change of error (de/dt) while the outputs are the proportional gain K_p , the integral gain K_i and the derivative gain K_d . The input output data set has been taken from a PID controller tuned using conventional method. The proposed approach has been implemented using ANFIS editor in MATLAB as shown in Figure 7. The ANFIS model structure is a two input single output feed-forward structure having three hidden layers as shown in Figure 8 [17]. The simulink implementation of the given method is shown in Figure 9.

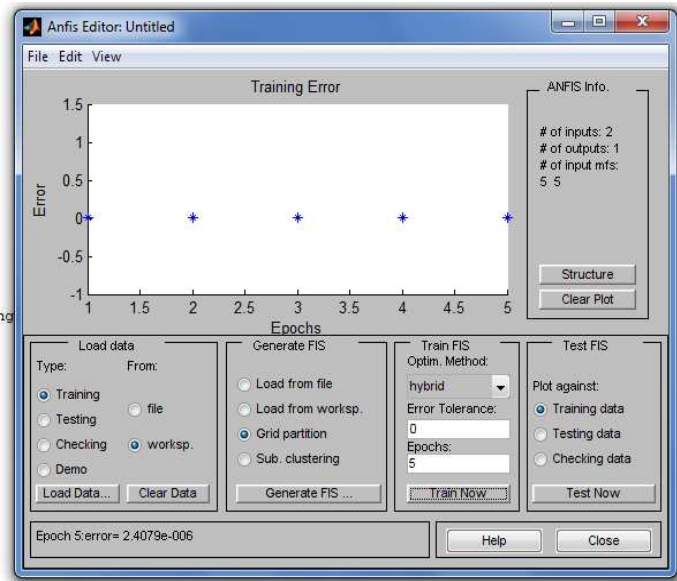


Figure 7
ANFIS Editor

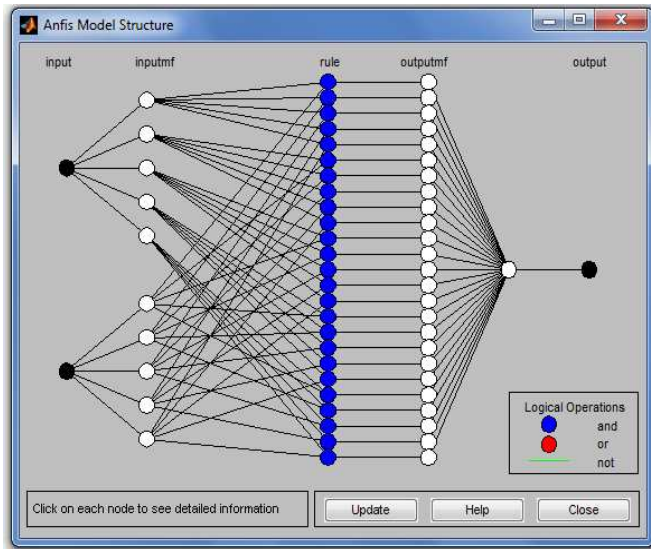


Figure 8
ANFIS structure

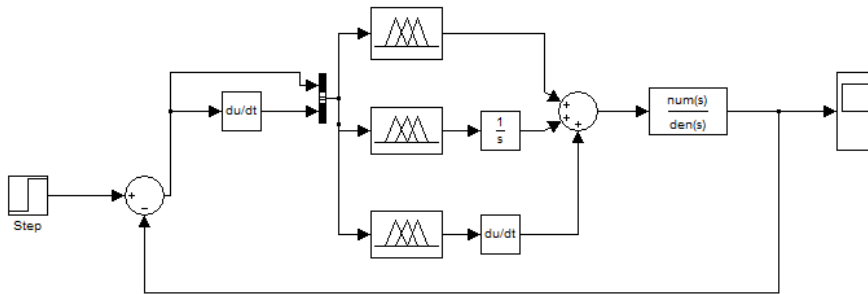


Figure 9

Adaptive neuro fuzzy controller implementation using MATLAB simulink

3.4 Genetic Algorithms

GA is a derivative free random optimization technique based on the ideas of natural selection and evolutionary processes. The fundamental components of GA are encoding, reproduction, crossover and mutation [13]. GA encodes a number into a binary string called chromosomes. Depending upon the value of evaluation function also called the fitness function the parents are selected from a group of binary strings to perform the operations of crossover and mutation. Figure 10 shows the block diagram for tuning of PID parameters using GA [18-19].

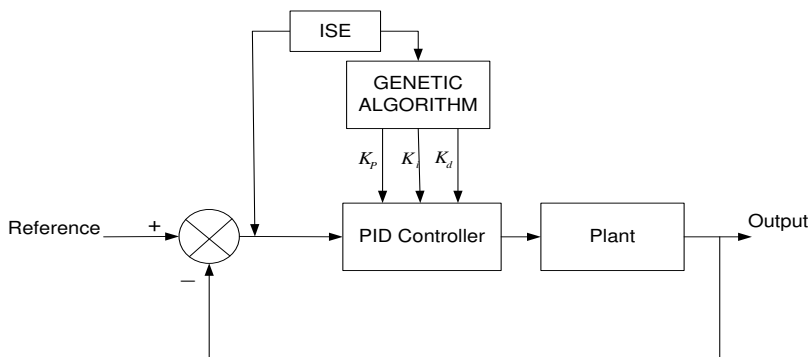


Figure 10

Block diagram of PID controller tuning using GA [17]

Auto-tuning of the PID controller has been done using GA by minimizing the integral of square error (ISE). The ISE criterion is defined as $ISE = \int (r(t) - y(t))^2 dt$. The various steps in finding the parameters of a PID controller are:

Step 1: Define the Plant transfer function.

Step 2: Initialize K_p, K_i & K_d and calculate ISE.

Step 3: Obtain pbest and gbest values.

Step 4: Calculate new population using mutation.

Step 5: Obtain pbest1 and gbest1.

Step 6: Compare pbest and pbest1.

Step 7: Compare gbest and gbest1.

Step 8: Obtain the new values of K_p, K_i & K_d and find out the step response for the closed loop system.

4 Results, Comparison and Discussions

The closed loop response of the reactor transfer function subjected to a step input with the different methods has been shown in Figure 11 to Figure 14 using different tuning methods.

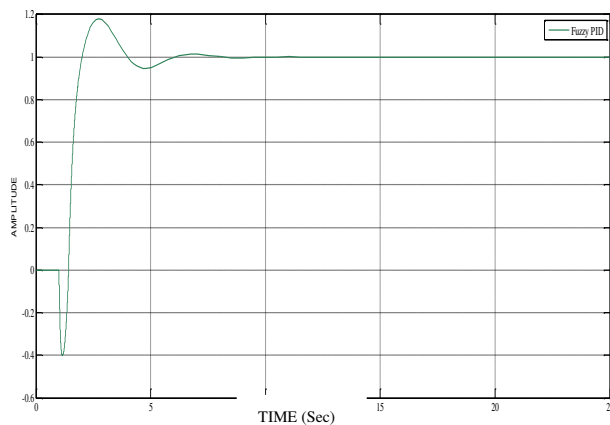


Figure 11
Step response using Fuzzy based PID controller

Due to RHP zero the system shows inverse response behavior.

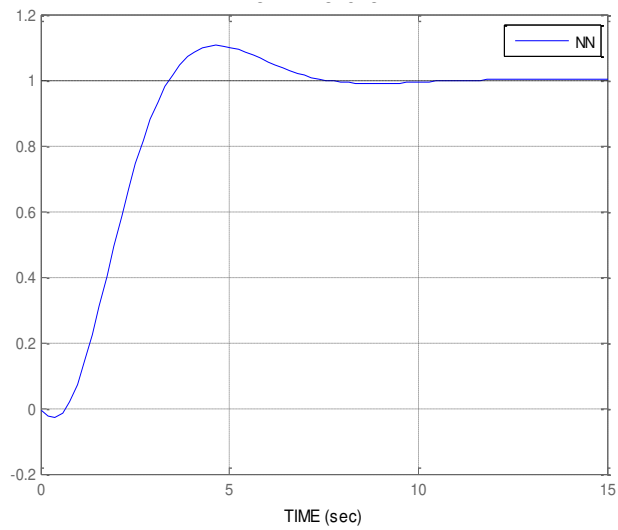


Figure 12
Step response using ANN based PID controller

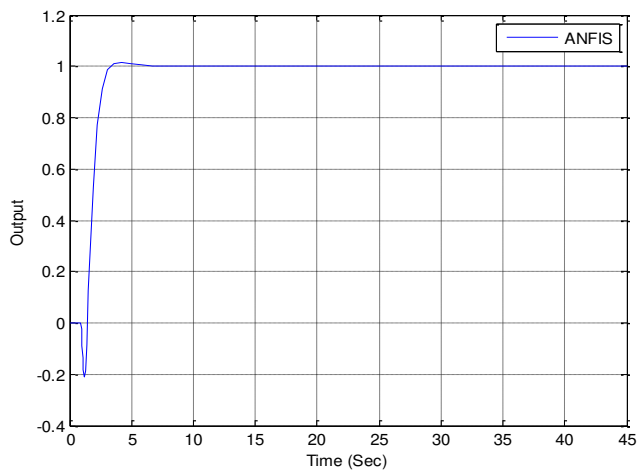


Figure 13
Step response using ANFIS based PID controller

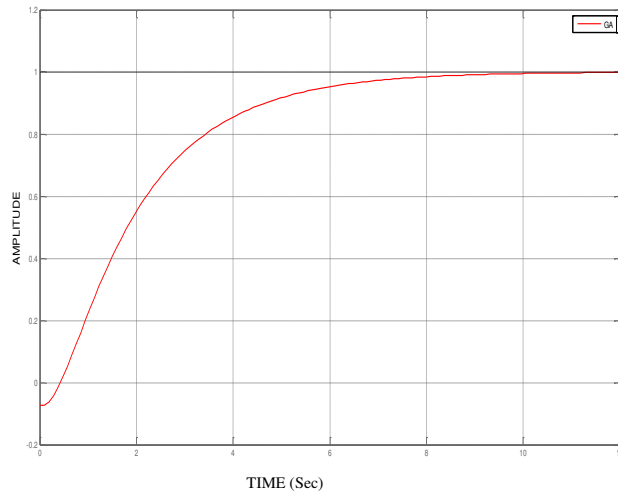


Figure 14

Step response using GA based PID controller

The comparison among different tuning methods in terms of various performance specifications such as rise time, settling time, overshoot, undershoot and steady state error using the intelligent and conventional tuning methods has been shown in Table 2.

Table 2

Comparison among different methods for tuning a PID controller

Parameters	Tuning Methods				
	ZN	Fuzzy	ANN	ANFIS	GA
Rise time t_r (sec)	1.789	1.865	2.98	2.578	4.84
Settling time t_s (sec)	3.745	5.624	6.85	3.425	7.12
Overshoot M_p (%)	20.05	17.95	10.47	1.0149	0
Undershoot M_u (%)	44.46	39.98	2.948	21.2	7.2923
Steady state error e_{ss}	0	0	0	0	0

From Table 2 it can be concluded that:

- The various performance specifications have been improved greatly using the intelligent methods except the rise time which is less in case of ZN method.
- The best performance in terms of settling time and overshoot has been given by ANFIS. Moreover undershoot in case of ANFIS method is less than the ZN and fuzzy PID methods. This is due to the fact that ANFIS

uses the combined features of neural networks and fuzzy logic in a single structure.

- The performance of ANN based PID controller is better than the ZN, fuzzy and GA based PID controller in terms of overshoot and undershoot. The maximum undershoot in case of ANN is even less than ANFIS based method.
- The steady state error remains zero in all the tuning methods.

Conclusion

In this paper the intelligent methods for tuning a PID controller have been compared. The different methods include fuzzy logic, artificial neural network, adaptive neuro fuzzy inference system and genetic algorithm. The controller tuned by the different methods has been used for concentration control of a continuous stirred tank reactor (CSTR) which is a second order system with right half plane zero. Simulation results show that the best performance has been achieved by ANFIS in terms of settling time and overshoot while the moderate performance has been given by ANN tuned PID controller as it reduces the overshoot and undershoot to a great amount in comparison to the Zeigler Nichols method.

References

- [1] Meng Joo Er, and Ya Lei: Hybrid Fuzzy Proportional–Integral Plus Conventional Derivative Control of Linear and Nonlinear Systems, *IEEE Transactions on Industrial Electronics*, Vol. 48, No. 6, December 2001, pp. 1109-1117
- [2] J. C. Basilio and S.R. Matos: Design of PI and PID Controllers with Transient Performance Specification, *IEEE Transactions on Education* Vol. 45, No. 4, November 2002, pp. 364-370
- [3] K. J. Astrom and T. Hagglund: *PID Controllers: Theory, Design and Tuning*, Instrument Society of America, 2 edition, 1995
- [4] B. Wayne Bequette: *Process Control: Modeling, Design and Simulation*, Prentice Hall, January 2003
- [5] David I. Wilson: *Relay-based PID Tuning*, *Automation & Control*, March 2005
- [6] D. Seborg, T. F. Edgar & D. A. Mellichamp: *Process Dynamics & Control*, Wiley India Edition, 2005
- [7] D. E. Rivera, M. Morari & S. Skogestad (1986) Internal Model Control 4: PID Controller Design. *Industrial and Engineering Chemistry Process Design and Development*, 25, 252-265
- [8] K. S. Tang, K. F. Man, G. Chen, and S. Kwong: An Optimal Fuzzy PID Controller, *IEEE Transactions On Industrial Electronics*, Vol. 48, No. 4, August 2001, pp. 757-765

-
- [9] T. J. Ross, *Fuzzy Logic with Engineering Applications*, Wiley India Edition 2009
- [10] K. Sinthipsomboon, W. Pongaen & P. Pratumswan: A Hybrid of Fuzzy and Fuzzy self-tuning PID Controller for Servo Electro-hydraulic System, 6th IEEE Conference on Industrial Electronics and Applications, 2011, pp. 220-225
- [11] *MATLAB™ fuzzy toolbox user guide* (www.mathworks.com)
- [12] Zulfatman and M. F. Rahmat: Application of Self Tuning Fuzzy PID Controller On Industrial Hydraulic Actuator Using System Identification Approach, *International Journal On Smart Sensing and Intelligent Systems*, Vol. 2, No. 2, June 2009, pp. 246-261
- [13] J. S. R Jang, C. T. Sun & E. Mizutani: *Neuro Fuzzy and Soft Computing*, PHI Learning, 2009
- [14] X. Liu: Single Neuron Self-tuning PID Control for Welding Molten Pool Depth, *Proceedings of the 7th World Congress on Intelligent Control and Automation* June 25-27, 2008, Chongqing, China
- [15] N. Nedjah & L. Mourelle: *Studies in Fuzziness and Soft Computing*, Germany, Springer Verlag
- [16] J. Shing & R. Jang: ANFIS: Adaptive Network Based Fuzzy Inference System, *IEEE Transactions on Systems, Man, and Cybernetics*, Vol. 23, No. 3, May/June 1993
- [17] Y. J. Mon, C. M. Lin & I. J. Rudas: ANFIS-based Wireless Sensor Network (WSN) Applications for Air Conditioner Control, *Acta Polytechnica Hungarica*, Vol. 10, No. 3, May 2013, pp. 5-16
- [18] K. S. Tang, G. R. Chen, K. F. Man & S. Kwong: *Fuzzy Logic and Genetic Algorithm Methods in PID Tuning*, Springer, 2005
- [19] M. Chebre, A. Meroufel, Y. Bendaha: Speed Control of Induction Motor Using Genetic Algorithm-based PI Controller, *Acta Polytechnica Hungarica*, Vol. 8, No. 6, November 2011, pp. 141-153